

DISS. ETH NO. 25336

Active collision zones:

Morphotectonic analysis, cosmogenic nuclide evidence and kinematic
modelling of the Turkish-Iranian Plateau and Caucasus Regions

Amaneh Kaveh Firouz

2018



DISS. ETH NO. 25336

Active collision zones: Morphotectonic analysis, cosmogenic nuclide
evidence and kinematic modelling of the Turkish-Iranian Plateau and
Caucasus Regions

A dissertation submitted to attain the degree of
Doctor of Sciences of ETH Zurich

Presented by

AMANEH KAVEH FIROUZ

M.Sc. in Geology. Azad University, Science and Research branch (Tehran, Iran)

Born on *09.02.1981*

Citizen of *Iran*

Accepted on the recommendation of

Prof. Dr. Jean-Pierre Burg

ETH Zurich

Supervisor

Dr. Laurentiu Danciu

ETH Zurich

Co-Examiner

Prof. Dr. Sébastien Castelltort

University of Geneva

Co-Examiner

2018

*I slept, and dreamed that life was Beauty;
I woke, and found that life was Duty.*

(Ellen Sturgis Hooper, Life a Duty)

To My Parents and Teachers

Summary

The main motivation and goal of this study is to investigate landscape evolution and ongoing crustal deformation in active collisional zones. To do so, this study concentrates on the Turkish-Iranian Plateau and Caucasus because it is a region of ongoing deformation and active seismicity that is situated between the Arabian and Eurasian plates. This region is complex due to different tectonic processes including post-collisional volcanism and active faulting. Quantitative information on uplift, incision and erosion from surface features can address landscape evolution such as where and how the high relief was developed and whether relief is in transient or steady state. In addition, exploring the location of maximum strain accumulation indicates how deformation is accommodated in the crust. To identify the indicators and signals of tectonic activity and their relationship with catchment-average erosion rates and to estimate strain rate and active long-term deformation with spatial-temporal distribution, this study applies a combination of quantitative topographic analysis based on digital elevation model data, catchment-averaged erosion rates measured from ^{10}Be concentrations in river sands, and using kinematic modelling across the western part of Turkish-Iranian Plateau and south Caucasus Region.

The first part of this thesis consist of quantitative morphometric/topographic analysis and indicates that the drainage networks of the “Qezel-Owzan and Kura-Arax” rivers in the study area are not in an equilibrium state. This is specifically documented in the lower catchment of Qezel-Owzan River and upper catchment of Kura-Arax Rivers. The disequilibrium is associated with drainage divide reorganization and captures, which display the ongoing dynamics and migration of the river basin drainage divides towards the internal plateau. The second part of this thesis consists of quantification of short-term landscape erosion rates derived from river sand ^{10}Be content across three distinct tectono-stratigraphic zones from the upper to lower catchments of the Qezel-Owzan River in the north Iranian Plateau and west Alborz Mountain Range. The lower catchment has higher erosion rates/higher topographic metrics and annual precipitation compared to the upper/middle catchments in the plateau. This suggests that a different state exists between the lower and upper/middle parts of the catchment. Comparison between long-term exhumation

rates (AFT/He data) and short-term erosion rates in the lower catchment suggest that the region has experienced a steady erosion rate since ~5 Ma, indicating a stability between erosion rate and regional shortening. The final part of this thesis presents the results of kinematic modelling in the frame of estimated long-term slip rates of the active faults and strain rates. The best fit of the kinematic model, with geodetic, geologic data and stress direction inputs, displays that crustal deformation is mostly accommodated by the active fault systems. Active faulting is primarily accommodated by right-lateral strike slip faults in the western part of Turkish-Iranian Plateau and Lesser Caucasus, but a high degree of shortening associated with the deformation is partly due to active thrust faults within the Talesh and Bitlis regions, with supplementary shortening in the Alborz and Greater Caucasus fold and thrust systems.

Résumé

L'objet de cette thèse est l'évolution du relief en réponse à la déformation de la croûte terrestre dans une zone de collision active. L'étude se concentre sur le plateau Turco-Iranien et le Caucase qui se situe entre les plaques arabe et eurasienne où différents processus tectoniques sont en jeux, y compris le volcanisme post-collisionnel. L'évolution du paysage, par exemple où et comment les hauts reliefs ont été développés et s'ils sont dans un état transitoire, peut être évaluée en quantifiant l'évolution de la topographie par les taux de soulèvement, d'incision et d'érosion. De plus, l'identification des zones d'accumulation de contrainte illustre comment la déformation crustale est distribuée. Cette étude combine l'analyse géomorphologique quantitative basée sur les modèles numériques de terrain pour estimer les taux d'érosion moyens dans les zones de drainage fluviales à partir de la concentration de ^{10}Be dans les sables fluviaux. Ceci permet d'identifier les zones d'activité tectoniques et leurs relations avec les taux d'érosion moyens à long terme sur le plateau Turco-Iranien et le Caucase.

La première partie de cette thèse consiste en une analyse morphométrique/topographique quantitative et montre que les réseaux de drainage des rivières « Qezel-Owzan » et « Kura-Arax » ne sont pas dans un état stationnaire. Ceci est particulièrement prononcé dans le bassin inférieur de la rivière Qezel-Owzan et dans le bassin supérieur des rivières Kura-Arax. Le déséquilibre morphologique est associé à la réorganisation des lignes de partage des eaux et la capture de réseaux de drainage. Ceci met en évidence la dynamique en cours de la migration des lignes de partage des eaux vers le plateau interne.

La deuxième partie de cette thèse est consacrée à la quantification des taux d'érosion à court terme obtenus en mesurant la teneur en ^{10}Be des sables de rivière. La rivière Qezel-Owzan draine trois zones tectono-stratigraphiques correspondant aux bassins supérieurs et inférieurs de la rivière qui traverse le nord du plateau Iranien et la chaîne de l'Ouest Alborz. Le bassin inférieur présente des taux d'érosion, des indices topographique et des précipitations annuelles plus élevées que ceux des bassins supérieurs/intermédiaires du plateau. Ces mesures révèlent des situations

géomorphologiques et tectoniques différents. La comparaison entre les taux d'exhumation à long terme (données AFT/He) et les taux d'érosion à court terme dans le bassin versant inférieur suggère que l'Ouest Alborz a connu un taux d'érosion stable depuis ~5 Ma, indiquant un équilibre entre l'érosion et la déformation de raccourcissement à l'échelle régionale.

La dernière partie de cette thèse présente les résultats de la modélisation cinématique dans le cadre de l'estimation des vitesses de déplacement des failles actives et des vitesses de déformation régionales. L'ajustement optimal du modèle cinématique avec les données géodésiques, géologiques et les directions des contraintes principales montre que la déformation crustale est principalement accommodée, de nos jours, par les systèmes de failles actives. La fracturation active s'exprime essentiellement sur des failles décrochantes dextres dans la partie ouest du plateau Turco-Iranien et du Petit Caucase, mais une partie significative du raccourcissement se fait aussi sur des failles inverses dans les régions de Talesh et de Bitlis, avec un raccourcissement supplémentaire par plissement dans les chaînes de l'Alborz et du Grand Caucase.

Contents

Summary	i
Résumé	iii
1 Introduction	1
1.1 General introduction	1
1.2 Aims of the thesis	2
1.3 Method	3
1.3.1 Quantitative morphometric analysis	3
1.3.2 Cosmogenic nuclide	4
1.3.3 Kinematic modelling	4
1.4 Study area	5
1.4.1 Tectonic, geologic, and geomorphic setting	5
1.4.2 Geodynamics and seismicity	8
1.4.3 Overview of previous work	8
1.5 Thesis structures and outline.....	9
2 Evolution of large-scale drainage networks in orogenic plateaus: Insights from quantitative morphometric analysis of the Kura-Arax and Qezel-Owzan River Basins	11
Abstract	11
2.1 Introduction.....	12
2.2 Study area	13
2.2.1 Geological setting	13
2.2.2 Geomorphological and climate settings	15
2.2.3 Drainage system	17

2.3	Analytical methods	18
2.3.1	Swath profile.....	18
2.3.2	Local relief map.....	18
2.3.3	Longitudinal profile, steepness (ksn) map and paleo-river profile	18
2.3.4	Chi (χ) analysis	19
2.4	Results.....	20
2.4.1	Swath profiles	20
2.4.2	Local relief analysis.....	23
2.4.3	Stream profile, steepness map and paleo-profile reconstruction	25
2.4.4	Chi maps and plots	31
2.5	Discussion	36
2.6	Conclusion	38

3 Spatial variability of ¹⁰Be erosion rates in the north Iranian Plateau and margin: Insight from landscape evolution across different tectono-stratigraphic zones..... 55

	Abstract.....	55
3.1	Introduction.....	56
3.2	Study area.....	58
3.2.1	Geological, geomorphological and seismic setting	58
3.2.2	Climatic and hydrologic setting.....	60
3.3	Data and methods.....	61
3.3.1	¹⁰ Be-derived erosion rates.....	61
3.3.2	Climatic and topographic analysis.....	63
3.3.3	Exhumation rate.....	64
3.4	Results.....	64
3.4.1	Catchment-averaged erosion rates	64
3.4.2	Erosion rates and climatic gradients	65
3.4.3	Erosion rates and topographic metrics.....	65
3.4.4	Correlation between short-term erosion rates and long-term exhumation rates	67
3.5	Discussion	67
3.6	Conclusion	71

4 Present-day crustal deformation of the Turkish-Iranian Plateau: insights from kinematic modelling.....	77
Abstract.....	77
4.1 Introduction.....	78
4.2 Regional background: tectonics, geology and seismicity	80
4.3 Kinematic model: method, assumptions and input data	81
4.3.1 Method and assumptions	81
4.3.2 Input data	83
4.4 Kinematic model: model details and tuning parameters	88
4.5 Results and discussion	91
4.5.1 Estimation of fault slip rates	91
4.5.2 Tectonic strain field.....	99
4.6 Conclusion	104
5 Conclusion, outlook and work in preparation.....	105
5.1 Conclusion	105
5.2 Outlook	106
5.3 Work in preparation.....	107
5.3.1 Introduction	107
5.3.2 Methodology.....	109
5.3.3 Prior results and ongoing work.....	109
Bibliography	111
Acknowledgements.....	119
Curriculum Vitae	121
Appendix	123

1 Introduction

1.1 General introduction

Identifying temporal-spatial patterns of ongoing deformation in the landscape is one of the main research on active tectonics (e.g. Whipple, 2009; Wobus et al., 2006a). Several processes control the landscape state on different tectono-geomorphologic features, which can record the response of the landscape evolution with respect to the boundary conditions (Fig. 1.1). Geomorphic features such as stream channels can record the response of landscapes to climate and tectonic conditions (e.g. Whipple, 2004; Wobus et al., 2006b). To understand landscape evolution, erosion rates complement information from to climate/topographic metrics. Therefore, a region with a complex tectonic setting may display changes in erosional regime consistent with changes in tectonic regime. If the region is tectonically active, distinguishing the tectonic impact is important and understanding whether strain is localized or operates diffusely is crucial (e.g. Houseman and England, 1993).

The landscape of the Turkish-Iranian Plateau and the Caucasus Mountain Range have different Late Miocene to Quaternary deformation patterns. These regions are situated within the collisional zone between the Arabian and Eurasian plates and expose different tectono-stratigraphic zones (e.g. Pirouz et al., 2017; Şengör and Kidd, 1979).

Investigation of landscape evolution and ongoing crustal deformation across the Turkish-Iranian Plateau and Caucasus Regions (Fig. 1.2) is the main goal of this thesis.

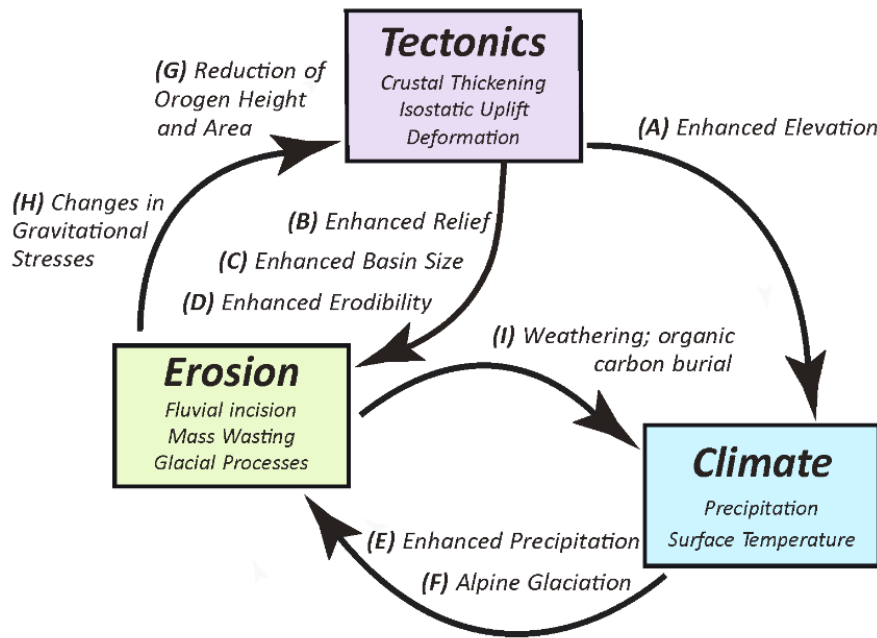


Fig. 1.1: Interaction and response between tectonics, climate, and erosional processes (modified after Willett, 2006).

1.2 Aims of the thesis

The Turkish-Iranian Plateau and Caucasus is the region of ongoing deformation and seismicity situated between Arabia to the south and Eurasia to the north (Fig. 1.2; Golonka, 2004; Pirouz et al., 2017; Şengör and Kidd, 1979). This region is active and complex due to various tectonic processes including post-collisional volcanism and active faulting. We decided to produce quantitative information on “uplift, incision and erosion” and drainage networks. On a regional scale, comparison with previous morphotectonic studies, understanding of dominant boundary conditions on surface processes and their relationship can emphasize where and how the high relief was developed and whether relief is in transient or steady state. Investigating the location of maximum strain accumulation indicates how deformation is accommodated in the crust.

This study applies different methods to (1) identify the indicators and signals of tectonic activity from drainage network, (2) measure catchment-average erosion rates and their relationship with climatic/topographic metrics, (3) estimate strain rate and active long-term deformation with spatial-temporal distribution, including quantitative topographic/climatic and morphometric analysis, ^{10}Be cosmogenic nuclides and long term fault slip rates derived from the kinematic model “neokinema” reference. Since drainage networks are sensitive features to surface movements, this work focuses on the largest river catchments “Kura-Arax and Qezel-Owzan” in the study area.

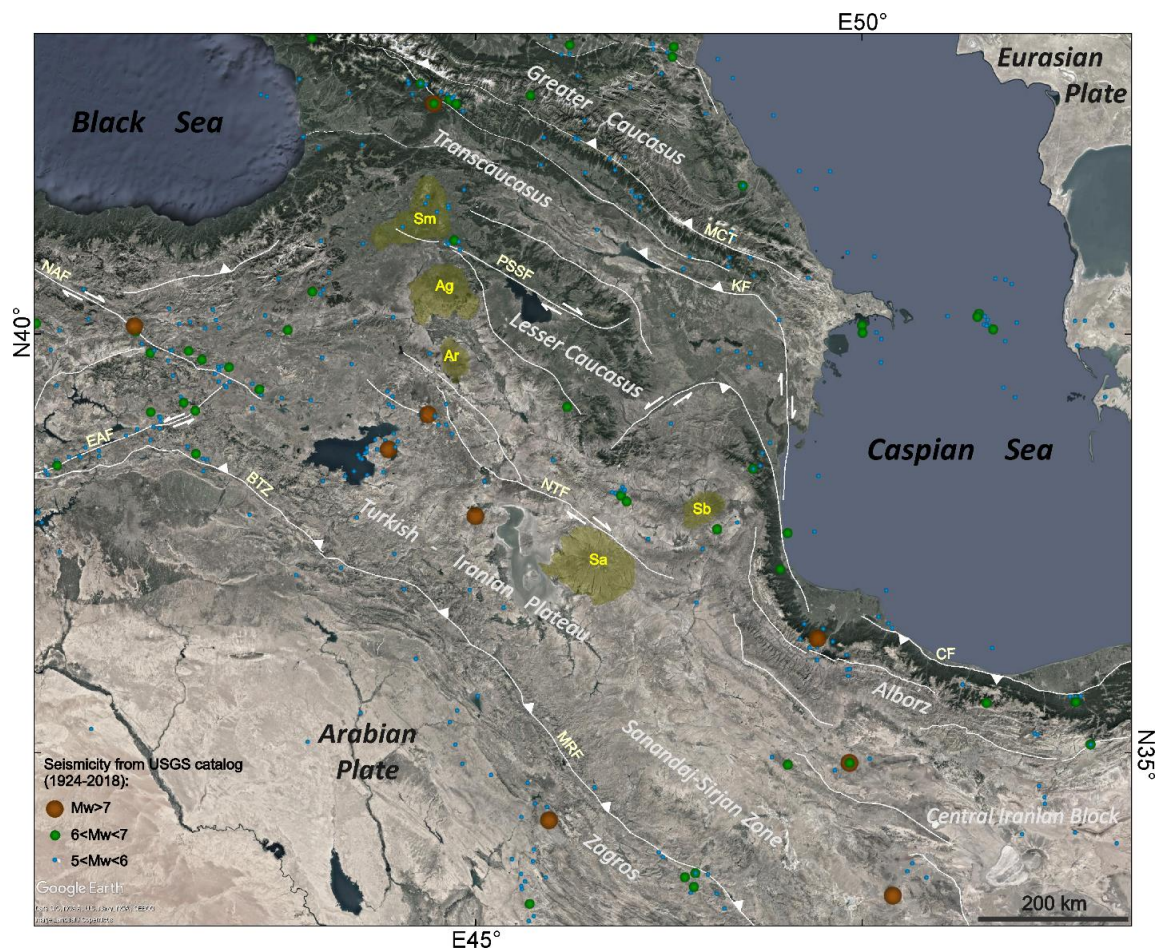


Fig. 1.2: Topographic overview of the Turkish-Iranian Plateau and Caucasus Region from a Google Earth image, major active faults (white lines), and seismicity (USGS earthquake catalogue). The light yellow abbreviations are active fault names: BTZ=Bitilis; CF=Caspian Fault; KF= Kura Fault; MCT=Main Caucasus Thrust; MRF=Main Recent Fault; NTF=North Tabriz Fault; PSSF=Pambak-Sevan-Sunik Fault. Explanation of the Neogene-Quaternary volcanoes (yellow polygons): Ag: Aragats, Ar: Ararat, Sa: Sahand, and Sb: Sabalan, Sm: Samsari Volcanoes.

1.3 Method

We used following techniques to solve the main questions of this research:

1.3.1 Quantitative morphometric analysis

To provide evidence for active tectonic processes in the drainage network, we used geomorphological and river profile analysis as a first indicator of ongoing tectonic activity. Drainage network reorganization in response to lithology, tectonics, base-level fall, and climate can be defined by a chi analysis. This analysis was carried out using the Digital Elevation Models (DEM) with ~90 m resolution produced by the Shuttle Radar Topography Mission (SRTM; Jarvis et al., 2008). We used the MATLAB software package 'TopoToolbox' Version 2 (Schwanghart and Kuhn, 2010; Schwanghart and Scherler, 2014) to extract geomorphic/topographic metrics from DEM.

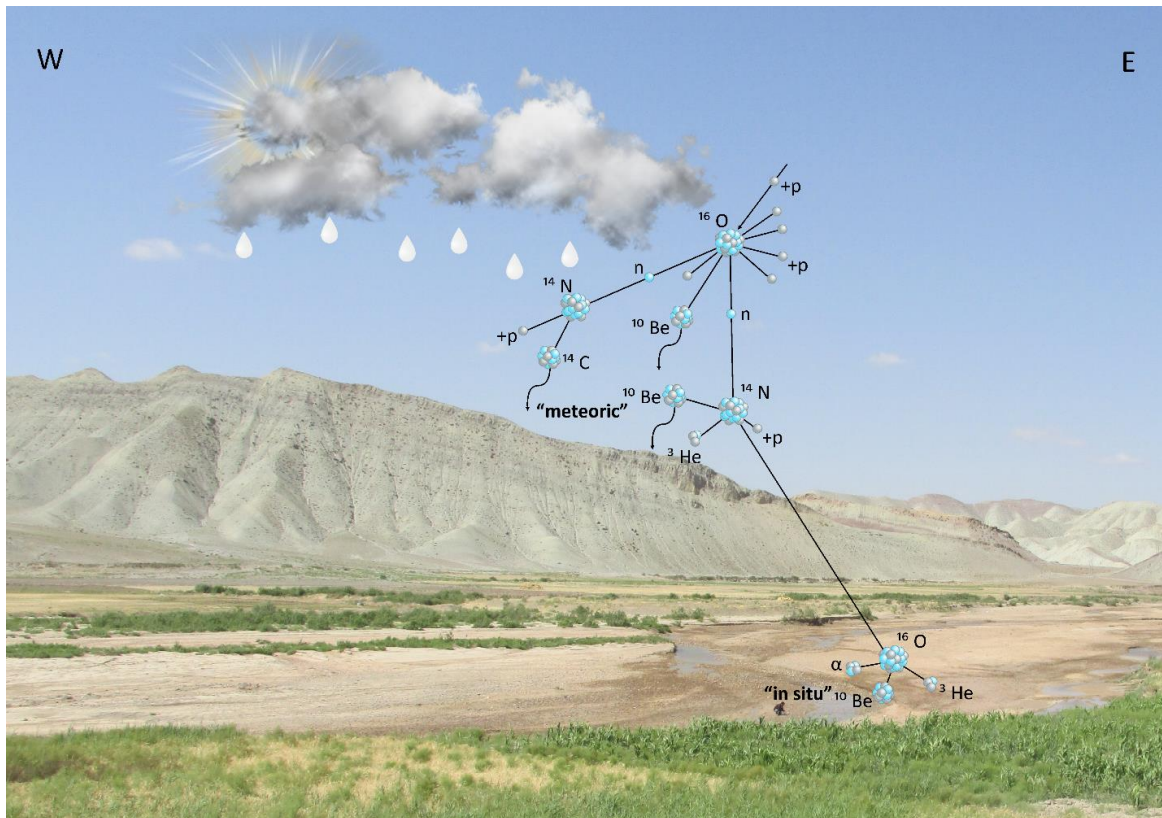


Fig. 1.3: Cosmogenic nuclides generation in galaxy and cosmic radiation on earth-surface (von Blanckenburg and Willenbring, 2014) on the background of Qezel-Owzan River tributary adjacent to the Folded Miocene Belt in Mianeh Basin.

1.3.2 Cosmogenic nuclide

To document spatial-temporal variations of erosion rates across the river basins, we constrained the quantitative morphometric analysis with short-term erosion rates using ^{10}Be cosmogenic nuclides from river sands (Fig. 1.3). Sands were collected from tributaries and along the trunk channel of the Qezel-Owzan River, purified to quartz grains by standard analytical procedures (Lupker et al., 2012) at ETH Zurich and dissolved in concentrated HF (40%). “TANDY” AMS (Accelerator Mass Spectrometer) measured $^{10}\text{Be}/^9\text{Be}$ ratios at the ETH Zurich (Christl et al., 2013). These ratios were converted to erosion rates by using the CRONUS-Earth online calculator version 2.3 (Balco et al., 2008; <https://hess.ess.washington.edu/>). In addition, we investigated relationships between climatic/topographic parameters and ^{10}Be -delivered erosion rates in catchment-averaged scale to identify the main controls on landscape erosion in the river basins.

1.3.3 Kinematic modelling

Long-term fault slip rates and spatial distribution of ongoing crustal deformation within the plateau and mountain ranges were estimated by applying the kinematic finite-element model “Neokinema” (Bird and Liu, 2007). This model combines geological information (plate boundary,

fault traces and slip-rates), geodetic measurements, and principal stress directions. We performed a sensitivity analysis of three primary adjustable parameters to support the model construction process and find the best-fit model. The adjustable, tuning parameters are A_0 “area of continuum”, L_0 “length of fault trace” and μ “the uncertainty of continuum deformation rate”.

1.4 Study area

1.4.1 Tectonic, geologic, and geomorphic setting

The Turkish-Iranian Plateau is bounded by the Eastern Pontide arc and the Lesser Caucasus to the north, and the Bitlis and the Sanandaj–Sirjan massifs in Turkey and Iran to the south (Fig. 1.2). The plateau is composed of a series of continental blocks and Late Cretaceous to Early Tertiary ophiolites and ophiolitic mélanges, which are covered by Neogene-Quaternary volcanic rocks and sediments (e.g. Dilek et al., 2010; Şengör, 1990).

The Greater Caucasus is bounded by the Scythian platform of Eurasia to the north and the Transcaucasus to the south. This zone is composed of Late Paleozoic crystalline rocks overlain by tightly folded, Jurassic-Eocene shelf carbonate and turbiditic sequences (Gamkrelidze, 1986; Zonenshain and Pichon, 1986).

The Transcaucasus is an intermountain depression between the Greater and Lesser Caucasus. The Paleozoic rocks of Transcaucasus are unconformably overlain by Mesozoic-Cenozoic shallow marine to continental clastic rocks and carbonate sequences (e.g. Adamia et al., 1981; Yilmaz et al., 2000).

The Lesser Caucasus is separated from Transcaucasus depression by the Sevan–Akera suture zone and bounded by the Turkish-Iranian Plateau to the south (e.g. Golonka, 2004; Khain and Koronousky, 1997). This zone comprises Cretaceous island arc and ophiolitic series, and widespread Eocene and Plio-Quaternary volcanic and plutonic rocks on the surface (e.g. Golonka, 2007; Knipper, 1975; Robinson et al., 1995; Sosson et al., 2010).

The recent geological history of Turkish-Iranian Plateau and Caucasus Regions happened during the Late Miocene (Fig. 1.4) with eliminated oceanic lithosphere between the Arabian and Eurasian continents at the Bitlis/Zagros suture zones (e.g. Şengör and Kidd, 1979). Convergence of the two continental plates has continued until the Present and resulted in intracontinental shortening of the plateau (e.g. Golonka, 2004; Pirouz et al., 2017; Şengör and Kidd, 1979).

Post-collisional volcanism is present in the western Caucasus and as isolated volcanoes in the Turkish-Iranian Plateau since the Late Miocene (Okay et al., 2010). Volcanism of the studied segment of Turkish-Iranian Plateau formed the Ararat, Sabalan and Sahand volcanoes

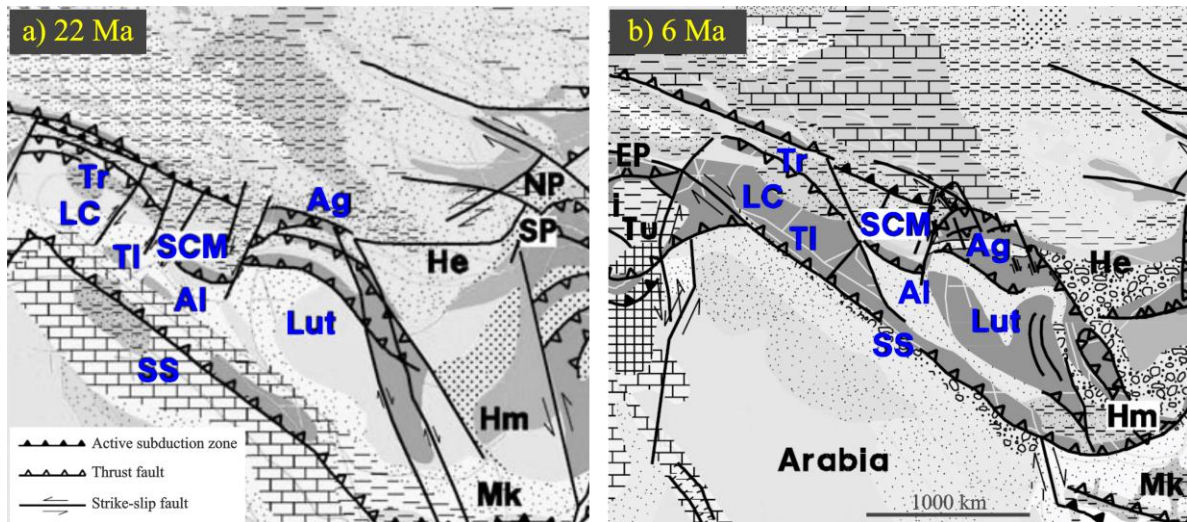


Fig. 1.4: Paleogeographic reconstruction of the southern margin of Eurasia, between Arabian and Eurasia Plates (a) Early Miocene, (b) Late Miocene (Modified after Golonka, 2004). Blue abbreviations are related plate names within the Turkish-Iranian Plateau and Caucasus Regions. Ag: Aghdarband (southern Kopet Dag), Al: Alborz, EP: Eastern Pontide, He: Herat, Hm: Helmand, LC: Lesser Caucasus, Lut: Lut block, Mk: Makran, NP: North Pamir, SCM: South Caspian Microcontinent, SP: South Pamir, SS: Sanandaj-Sirjan, TI: Talysh, and Tr: Transcaucasus. Tu: Turan.

(Fig. 1.2; e.g. Keskin, 2005). The Aragats and Samsari ridge series are the youngest and most elevated volcanoes in the Lesser Caucasus (Lebedev et al., 2003).

Another recent geological event is attributed to changes in tectonic regime and deformation patterns from folding/ thrusting to strike-slip faulting in the plateau and Lesser Caucasus after Late Miocene. The evidence for these changes in the tectonic regime are seen along fault which cuts across Late Miocene geological structures such as dykes, sills, fold axes, and displacement in drainage networks that range from 100 m to 7 km (e.g. Koçyiğit et al., 2001).

On the basis of topography and regional geomorphology, the Turkish-Iranian region is a high plateau (about 2 km) with steep mountain ranges (more than 3-4 km height) along its margins. The area is relatively semi-arid due to orographic barriers between Iranian Plateau and Caspian/Mediterranean/Black Seas. The presence of undeformed Early Miocene shallow-water lacustrine deposits on the plateau interior shows that the plateau is a relatively young morphotectonic feature (Ballato et al., 2016). Caucasus Regions can be divide into E-W striking high relief mountain ranges (Greater and Lesser Caucasus) and low relief intermountain basins (Transcaucasus). The mean relief elevation in Caucasus mountain range is higher than Turkish-Iranian Plateau. The area experiences a varied range of climate and precipitation from north to south and west to east, as a result of prevailing westerly winds (Gobejishvili et al., 2011).

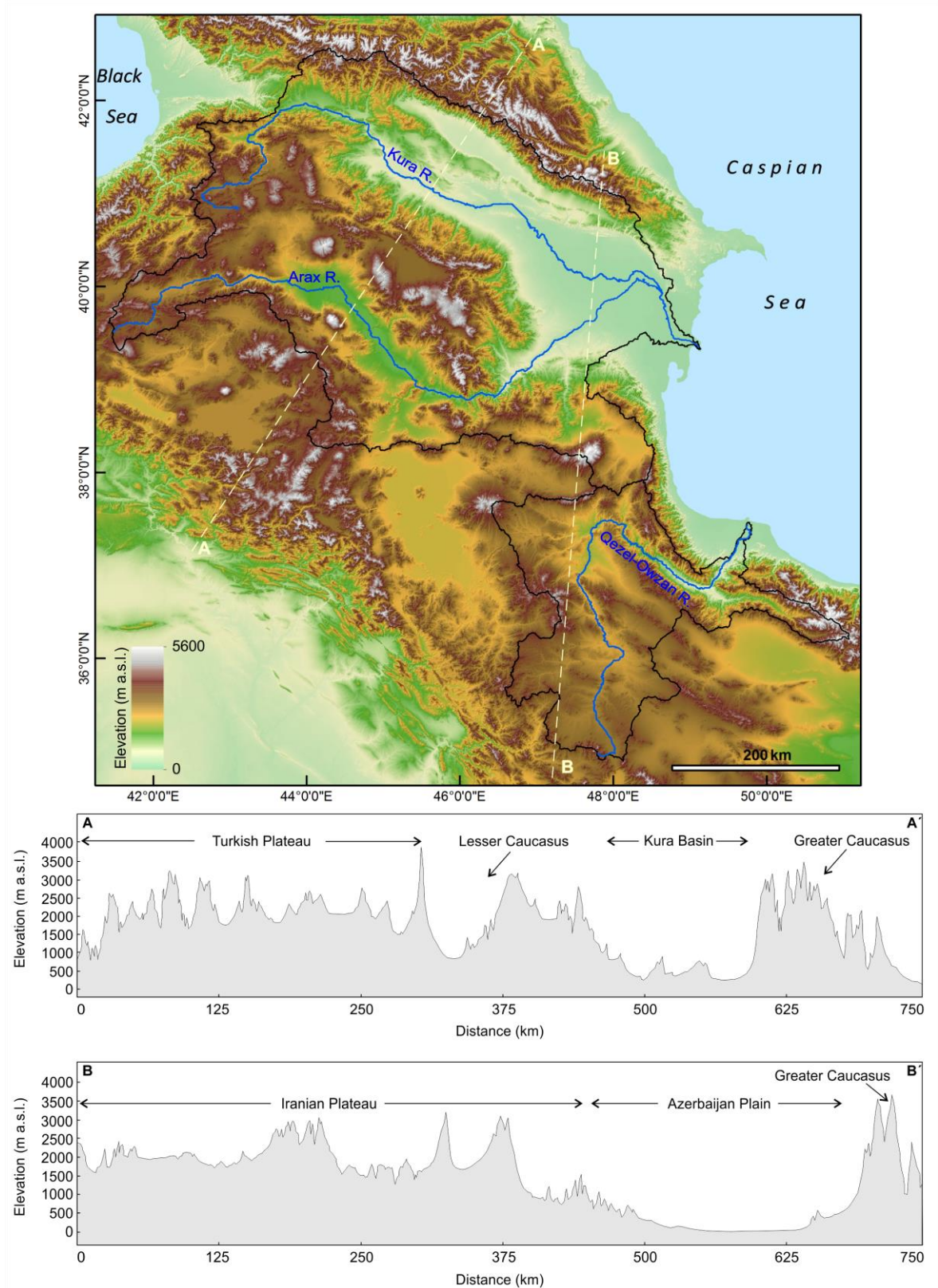


Fig. 1.5: Overview of drainage basins and topographic cross sections (AA', BB') through the study area. Black lines: drainage divide; Blue line: main rivers from DEM SRTM 90 m.

Moreover, the Kura-Arax and Qezel-Owzan are the main river basins in the studied part of Turkish-Iranian Plateau and south Caucasus regions which are discharging to the Caspian Sea (Fig. 1.5). We applied geomorphological studies on these river basins to address where there is more potential of erosion, incision, uplift rates and landscape modifications from the drainage networks.

1.4.2 Geodynamics and seismicity

Collisional forces caused crustal deformation and seismicity (Fig. 1.2) with complex interactions between active strike-slip and thrust faults (e.g. Ambraseys and Melville, 2005; Berberian, 2014; Copley and Jackson, 2006). GPS measured crustal motions can be divided into several areas: nearly N-S shortening in NW Iran, NE-SW shortening in Caucasus Regions and NW-SE shortening in east Anatolia at mean rates of 14, 10, 14 mm/yr with respect to fixed Eurasia, respectively (e.g. Reilinger et al., 2006b; Vernant and Chery, 2006). A large part of crustal deformation is accommodated along the strike-slip faults such as North Tabriz, North Anatolian, East Anatolian and Pambak-Sevan-Sunik Faults in the Turkish-Iranian Plateau and Lesser Caucasus (e.g. Karakhanian et al., 2004; Rizza et al., 2013; Stein et al., 1997). Moreover, part of shortening is concentrated in thrust faults such as Main Caucasus Thrust and Kura Faults (e.g. Philip et al., 1989; Reilinger et al., 2006b). Therefore, faulting is defined as a main expression of neo-tectonics in this region. However, some fault slip rates and contribution of distributed seismic sources in the study area have remained partly unknown. Better understanding of distribution of strain and active faults slip rate requires extensive work and research in the study area.

1.4.3 Overview of previous work

Few regional studies have been done to discover the interaction between active tectonics and erosion in the Turkish-Iranian Plateau and Caucasus Regions. In the topic of regional quantitative geomorphological analysis, some work has been done in NW Iran (Allen et al., 2011b; Ballato et al., 2015; Heidarzadeh et al., 2017), and Caucasus Region (Forte et al., 2014; Forte et al., 2016; Forte et al., 2015b). Some of this research was focused on long-term exhumation and erosion rates using thermochronometry in the west Alborz and Talesh Mountain Ranges (Madanipour et al., 2017; Madanipour et al., 2013; Rezaeian et al., 2012), NW Iran (Behyari et al., 2017; Reichenbacher et al., 2011) and Caucasus (Avdeev and Niemi, 2009; Cavazza et al., 2017). However, the analysis of cosmogenic nuclide (^{10}Be) to calculate the short-term erosion rates has not been done in this area. This method is useful to understand the Quaternary geochronology and landscape evolution (Ivy-Ochs and Kober, 2008) and was applied in several research across collisional zones such as Alps (e.g. Delunel et al., 2010; Olivetti et al., 2012), Himalaya (e.g.

Lupker et al., 2012; Portenga et al., 2015; Scherler et al., 2014), Tibet (e.g. Wang et al., 2017), western Greater Caucasus (Vezzoli et al., 2014), and Zagros (Oveisi et al., 2009). Since ^{10}Be cosmogenic nuclides and topographic metrics can address short-term deformations of topography, we also applied a kinematic model to estimate the long-term and current crustal deformation, which is independent from earthquake catalogs. This model was applied by Khodaverdian et al. (2015) at large-scale for entire Iran.

1.5 Thesis structures and outline

This PhD thesis includes three main chapters, this introduction, a conclusion and appendix. Applied methods are described separately in each chapter.

Chapter 2 reports the results of a regional geomorphological analysis along the two largest catchments in the study area: the “Kura-Arax” and “Qezel-Owzan” river basins. The main aim is to achieve the first overview of surface dynamics and topographic expression of tectonic, climate and volcanic activity using river markers. Various knickpoints/knickzones extracted using long stream profile analysis tools led us to classify them into three groups: (1) lithology changes, (2) fault-related, and (3) regional knickpoints at similar elevations. Moreover, the “chi analysis” is used to investigate the geometry of drainage networks in the studied catchment as an indicator of steady-state or transient landscape. The “Chi” analysis displays the geometric disequilibrium produced by drainage reorganization and plateau area integration in both river basins. The geomorphological study addresses where erosion, incision, uplift rates and landscape modifications are dominant.

Chapter 3 presents catchment-averaged erosion rates across the Qezel-Owzan River Basin using ^{10}Be content in river sediments from tributaries and along trunk channel of the Qezel-Owzan River. We used ALOS World 3D-30m DEM to calculate the topographic metrics including local relief, hillslope angle, and channel steepness for each sampled catchment. Moreover, we used 1 km resolution Worldclim (<http://worldclim.org/version2>) precipitation data as a proxy for climatic variability within the studied catchments to better understand the relationship between climate and erosion rates. This study allows to better understand the landscape evolution under uniform climatic conditions in different tectono-stratigraphic zones from upper to lower catchment including Sanandaj-Sirjan, Central Iran zones and Alborz Mountain Range.

Chapter 4 presents a kinematic finite-element model “Neokinema” to specify deforming areas and long-term forecast of seismicity in the Turkish-Iranian Plateau and Caucasus Regions. This model includes fault traces and slip rates, principal stress azimuths, geodetic velocities, and

velocity boundary conditions. The best fit of the Neokinema model is an estimation of long-term and current crustal deformation, fault slip rates, and distribution of strain rates between active faults (Howe and Bird, 2010).

Chapter 5 is a short conclusion, outlook and work in preparation (the Kura-Arax River erosion rates).

Appendix: Appendix A includes supplementary data for chapter 4.

2 Evolution of large-scale drainage networks in orogenic plateaus: Insights from quantitative morphometric analysis of the Kura-Arax and Qezel-Owzan River Basins

Amaneh Kaveh Firouz^a, Jean-Pierre Burg^a, Emanuele Giachetta^a

^a *Department of Earth Sciences, ETH Zurich, Someggstrasse 5, 8092 Zurich, Switzerland*

This chapter is in preparation for submission to Earth Surface Processes and Landforms

Abstract

We investigate the recent landscape evolution of the orogenic Turkish-Iranian Plateau (TIP), and the Lesser and Greater Caucasus Ranges by performing a regional analysis of morphometric indices, river profiles, and χ analysis. We show that a combination of enhanced aridity, rapid uplift of orographic barriers along the TIP margins, and exposure of resistant rocks associated to the regional volcanic activity preserved the low-relief plateau landscapes in the upper catchment of the Kura-Arax and Qezel-Owzan Rivers. However, high local relief in the flanks, downstream increase in channel steepness, and perturbations in the χ plots of the three main rivers indicate that the topography is in a transient state. The reconstruction of the paleo-river profiles from the relict section of the upper Kura-Arax and Qezel-Owzan rivers shows that the Quaternary eustatic oscillations in Caspian Sea level do not explain the incision of ~700-1000 m gorges (i.e. Amardos) below major knickpoints. The regional analysis of the χ parameter and the asymmetry of main drainage divides reveals that incision of the river gorges and disequilibrium in the plan-form geometry of the drainage networks are produced by persistent migration of drainage divides towards the plateau interior and integration of plateau areas into the external fluvial system. We found that other factors, such as neotectonic activity along regional structures, contrasts in rock strength, and Quaternary volcanic activity controlled the orientation of the river courses and drainage divides, and contribute to the persisting disequilibrium conditions in the landscapes of the TIP and Caucasus Ranges.

2.1 Introduction

River morphology provides quantitative constraints on landscape evolution (Pritchard et al., 2009; Whittaker, 2012; Wobus et al., 2006b). As they flow, rivers erode the underlying bedrock and shape landscapes. River channel geometry is a response to local erosion rates and boundary conditions such as tectonic uplift, climate conditions and underlying rock type variability (e.g. Burbank and Anderson, 2011; Howard, 1994; Kirby and Whipple, 2012). The rate of these responses is a function of magnitude and direction of the tectonic perturbation, as well as of the processes that control incision into bedrock (Niemann et al., 2001; Whipple and Tucker, 2002). Studies of tectonic and climate signals from rivers have classically been based on the stream power model, which is a function of upstream drainage area and channel gradient (Howard and Kerby, 1983; Whipple and Tucker, 1999). A sharp change in river channel slope, i.e. “knickpoints/knickzones,” can form in response to tectonic or climatic perturbation, rock strength contrast, river capture, or increase in base-level fall rate. In transient river profiles, an increase in surface uplift rate produces an increase in the channel steepness downstream and an upstream migrating “knickpoint”. The knickpoint separates the downstream part of the channel that is adjusted to the new uplift rate from the upstream part in balance with the old uplift rate (Rosenbloom and Anderson, 1994; Whipple and Tucker, 1999).

The analysis of topography in active orogens enables correlation of recent rock uplift and erosion modulated by climate changes (e.g. Kirby and Whipple, 2012). Our case study is located in the active Turkish-Iranian Plateau (TIP) and Caucasus collision zone between the Arabian and Eurasian plates (Fig. 2.1). A large portion of regional shortening is accommodated by thrust faults, particularly active in the Alborz and Greater Caucasus Mountain Ranges. The high Turkish-Iranian plateau (TIP) makes up the rest of the study region, where relief is linked to scattered Neogene-Quaternary volcanoes. Active faults in the TIP and lesser Caucasus are dominantly strike-slip (Fig. 2.2; Table 2.1; e.g. Donner et al., 2015; Karakhanian et al., 2002; Ritz et al., 2016). The Kura-Arax River (KAR) and the Qezel-Owzan River (QOR) are the two main river basins in the TIP and Caucasus Region (Fig. 2.1). Both catchments discharge into the Caspian Sea, but are underlain by relatively different lithologies in complex tectonic settings and different mean annual precipitations (Fig. 2.1). These drainage basins include Neogene-Quaternary volcanoes, which affected the landscapes by changing the local erosional base-level (Hayakawa and Matsukura, 2003). The Kura and Arax drainage networks developed subsequent to the volcanism and associated lava flows that created an elevated base-level in the upper and middle catchments. Additionally, the Caspian Sea experienced several base-level fluctuations during the last 7 million years (Forte and Cowgill, 2013; Miller et al., 2005). All of these processes initiated knickpoints

that can be used to investigate and compare the influence of volcanoes on landform evolution, topography and river basins in the studied catchments. Therefore, as a first overview of surface dynamics and topographic expression river markers (i.e., knickpoints) can help understand the steady/transient states of river basins in terms of tectonic, climate, and volcanic activity.

Few regional quantitative geomorphological analyses have been conducted to explore the relative activity of tectonic, volcanic and erosion processes in the Greater Caucasus (Allen et al., 2011b; Forte et al., 2016) and in the TIP (Copley and Jackson, 2006; Heidarzadeh et al., 2017). In this study, we applied quantitative geomorphological analysis (swath profiles, local relief distribution, and longitudinal stream profiles analysis) and field observations to understand which/where boundary conditions and surface process are controlling the recent landscape evolution of the TIP and Caucasus regions. In addition, we used the integral method to test for equilibrium of river networks in the northwestern TIP.

2.2 Study area

2.2.1 Geological setting

The study area is located in NW Iran, Eastern Turkey and the southern Caucasus (Fig. 2.1). Present-day kinematics calculated from GPS measurements with respect to a fixed Eurasia, indicate northward crustal motion of 13–15 mm/yr in the TIP and 10 mm/yr in the Caucasus (Fig. 2.1). The convergence rate increases eastward from ~2mm/yr near the Black Sea to the ~15 mm/yr near the Caspian Sea (Fig. 2.1; Kadirov et al., 2012; Reilinger et al., 2006b). Several moderate ($M_w > 4$) to strong ($M_w > 7$) earthquakes strike regularly the area. Earthquake fault plane solutions indicate essentially strike-slip and thrust faulting (Copley and Jackson, 2006).

The TIP is composed of Precambrian continental fragments, Late Cretaceous to Early Tertiary sedimentary sequences and ophiolites in the west, and a cover of Cenozoic-Quaternary volcanic rocks and Plio-Quaternary sediments in the west (e.g. Şengör, 1990).

The Caucasus Region is divided from north to south into the Greater Caucasus, the Trans-Caucasus and the Lesser Caucasus (Fig. 2.1). The Greater Caucasus is an anticlinorium with a Paleozoic core overlain by folded, Jurassic-Eocene shelf carbonate and turbiditic sequences (Gamkrelidze, 1986; Koçyiğit et al., 2001; Zonenshain and Pichon, 1986). The Trans-Caucasus is dominated by a Paleozoic basement unconformably overlain by Mesozoic-Cenozoic shallow marine to continental clastic rocks and carbonate sequences (Adamia et al., 1981; Koçyiğit et al., 2001; Yilmaz et al., 2000). Folds, thrust faults and ramp basins are prominent due to N-S shortening (Jackson, 1992a; Koçyiğit et al., 2001). The Lesser Caucasus consists of a Late Albian-

Early Campanian island arc and a Middle Jurassic-Lower Cretaceous ophiolitic series (e.g. Adamia et al., 1977; Golonka, 2007; Knipper, 1975; Lordkipanidze, 1980; Robinson et al., 1995; Sosson et al., 2010; Yilmaz et al., 2000; Zakariadze et al., 1983).

The widely distributed Neogene-Quaternary volcanoes (e.g. Ararat, Sabalan and Sahand, Fig. 2.2) created high local relief on the TIP (e.g. Dilek and Altunkaynak, 2010). The Aragats and Samsari series ridges are the highest and youngest volcanoes in Lesser Caucasus (Lebedev et al., 2003).



Fig. 2.1: Topography of the Turkish-Iranian Plateau and Caucasus Region from a SRTM 90m DEM (Jarvis et al., 2008). Yellow Square in inset includes the study area. Black arrows: GPS velocity vector respect to stable Eurasia reference frame (Reilinger et al., 2006a). Colored circles: seismicity of the area based on USGS earthquake catalogue. Black polygons: studied rivers catchment boundaries discharging to the Caspian Sea: (I) Kura-Arax and (II) Qezel-Owzan. White dash-lines: swath profiles location (A–A', B–B', C–C' and D–D' displayed in Fig. 2.3).

2.2.2 Geomorphological and climate settings

The growth of the TIP and Caucasus Mountains has affected local and regional air circulation and climate (e.g. Dettman et al., 2003; Garzzone et al., 2008; Mulch et al., 2010). The Tibetan plateau and the growth of the mountain ranges north of it might have additionally affected the paleoclimatic conditions in northern Iran (Ballato et al., 2010).

The TIP is characterized by marked topographic and climatic contrasts. The mean elevation of western TIP increases from less than 500 m a.s.l. in the western lowlands to 2000 m a.s.l. in the east, with an average annual precipitation of 500-700 mm. The present-day climate is arid to semi-arid with a strong seasonality in precipitation including wet winters and dry summers (Ballato, 2009). The heterogeneous distribution of precipitation across the TIP is caused by the orographic barriers of the Zagros and Alborz preventing moist air from the Caspian, Mediterranean, and Black Sea from entering the plateau interior (Kehl, 2009). The South Caspian lowlands receive annual precipitations of up to 2000 mm/yr (Ballato, 2009). The mean annual precipitation in the Iranian Highlands is less than 350 mm/y (Kehl, 2009). During the winter, only the highest peaks of the volcanoes and mountain chains in the western TIP are glaciated (e.g. Mount Ararat 5137 m a.s.l.; Fig. 2.2; Çiner, 2004; Kurter and Sungur, 1980).

The climate of the Caucasus Region is cold and dry during winter, and warm and dry during summer (e.g. Berg, 1950; Borisov and Halstead, 1965; Joannin et al., 2014; Lydolph and Landsberg, 1977). The region experiences wide ranges of climate variations from N to S and W to E that are related to the elevation and exposition of the mountain range to the prevailing westerly winds. Rain precipitation decreases from the high topographic areas in the west to the low topographic areas in the east.

Quaternary climate changes in the northwestern TIP were reconstructed from lake sediments (e.g. Djamali et al., 2009), loess-soil sequences (e.g. Kehl et al., 2005), and alluvial sediments (e.g. Vita-Finzi, 1969). During the Pleistocene and Holocene, the climate conditions in northern and western Iran shifted from dry and cold glacial to relatively warm and moist interglacial (Kehl, 2009). Evidence of Holocene climate fluctuations were also recognized in the varve sediments of Lake Van (Fig. 2.2). Three main phases of past glaciation were recognized: between 12600 and 10400 yr BP the area was affected by arid and cold climate, followed by continental and dry climate with decreasing precipitations and lake level fall between 4200 and 3000 yr BP. A more humid climate with lake level rise was recorded between 3000 and 2000 yr BP (humid climate with lake level rise; Lemcke and Sturm, 1997). Oxygen, hydrogen and carbon isotopes of the Neor Lake sediments in NW Iran (Fig. 2.2) indicate that dry climate conditions prevailed during the last glacial event and were followed by a wet interval during the early Holocene (Sharifi et al., 2015).

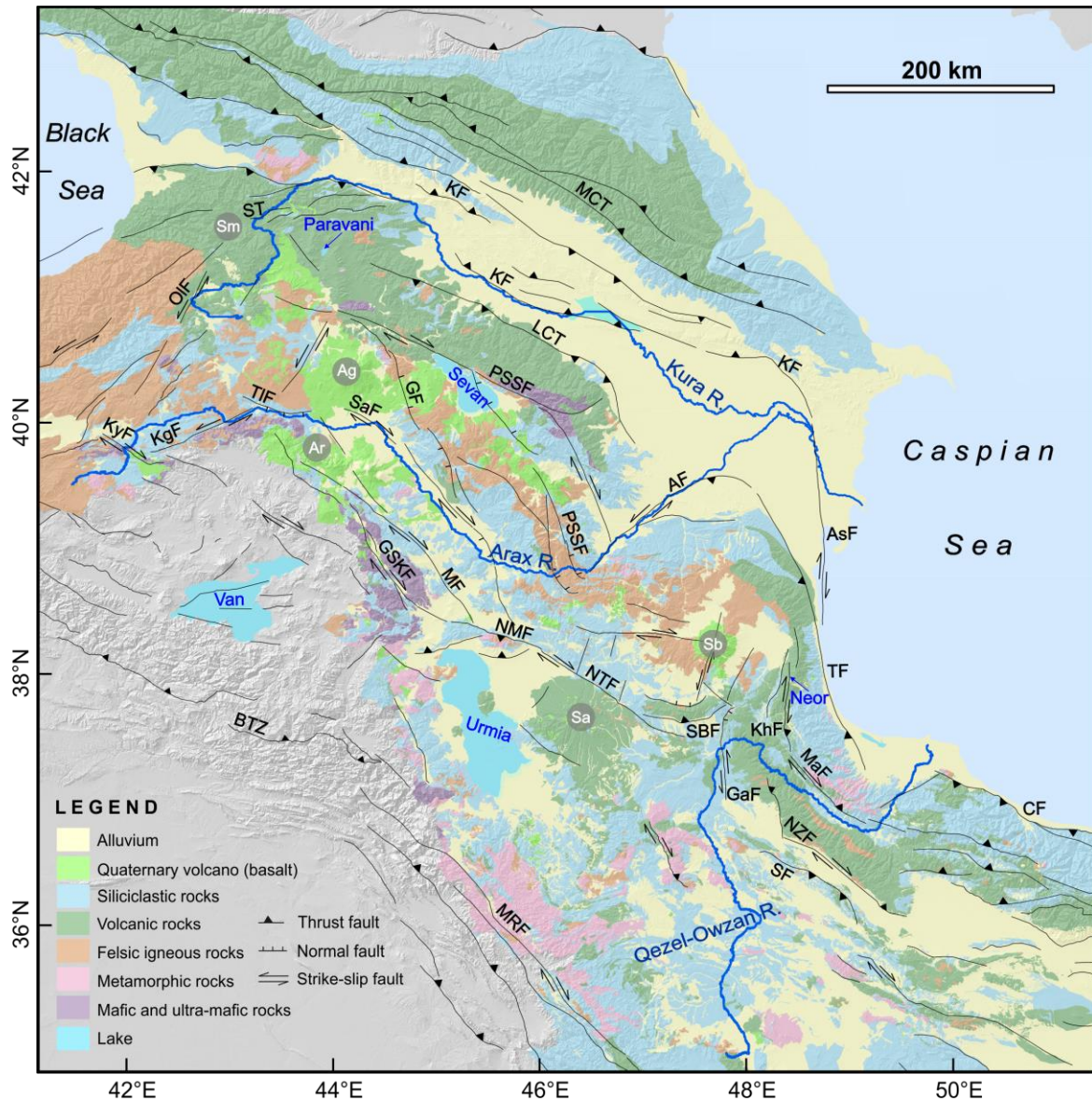


Fig. 2.2: Simplified geological map of the area, based on Geological maps of NW Iran (scale: 1:250,000, Geological Survey of Iran, 1969-1994), Turkey (1:500,000 and 1:1,250,000, General Directorate of Mineral Research and Exploration, 2002 and 2011), Armenia (1:500,000, Geological Agency of Armenia, 2005), Azerbaijan Republic (1:500,000, National Academy of Sciences, 2008), and Georgia (1:500,000; Georgian National Academy of Sciences, 2013). Grey Circles: quaternary volcanoes (Sm:Samsari, Ag:Aragats, Ar:Ararat, Sa:Sahand, and Sb:Sabalan Volcanoes). Explanation of the active faults and major structures name from active fault map of Iran (Hessami et al., 2003), NW Iran (Nazari et al., 2013; Faridi et al., 2017), Turkey (Emre et al., 2012; Dhont and Chorowicz, 2006; Koçyiğit et al., 2001), Armenia (Karakhanian et al., 2004), Georgia (Forte et al., 2014; Gudjabidze and Gamkrelidze, 2003): AF=Arax Fault; AsF=Astara; BTZ=Bitilis Thrust Zone; CBF=Cobandede Fault; CF=Caspian Fault; GF=Garni Fault; GSKF=Gisakan-Siahcheshmeh-Khoy Fault; KF= Kura Fault; KgF=Kagizman Fault; KhF=Khalkhal Fault; KyF=Karayazi Fault; LCT=Lesser Caucasus Thrust; MaF=Masuleh Fault; MF=Maku Fault; Fault; MCT=Main Caucasus Thrust; MRF=Main Recent Fault; NMF=North Mishu Fault; NTF=North Tabriz Fault; NZF=North Zanjan Fault; OIF=Olur Fault; PSSF=Pambak-Sevan-Sunik Fault; SaF=Sardarapat Fault; SBF=South Bozghush Fault; SF=Soltanieh Fault; TF=Talesh Fault; TIF=Tuzluca Fault.

Evidence of both paleo and modern glaciations are located in the western Caucasus (e.g. Gobejishvili et al., 2011) where palynological record from Lake Paravani (Fig. 2.2) indicates 3

main phases of climate change during the Late Quaternary: the period between the Early Holocene and 8500 yr BP was characterized by dry climate; a second phase was recognized between 8500 and 3000 yr BP with humid climate and increasing vegetation cover; the last phase between 3000 BP to present-day was characterized by dry climate. Moraine deposits in the lake sediments indicate local glaciers reaching the lake level (2077 m) during the Last Glacial periods (Messenger et al., 2013).

2.2.3 Drainage system

The most important drainage basins of the study area are the Kura-Arax and the Qezel-Owzan.

2.2.3.1 *The Kura-Arax River Basin*

The Kura-Arax River Basin (KARB) flows from northeastern Turkey in the west to the Caspian Sea in the east (Figs. 2.1, 2.2; Table 2.1). The Kura is the main stream and the Arax its major tributary with confluence in the Azerbaijan plain. The bedrock of the KARB predominantly consists of ophiolite in northeastern Turkey and northwestern Iran, and volcanic rocks around the Ararat and Aragats Volcanoes and volcanoclastic and carbonate sediments in the Iranian Plateau and Lesser Caucasus. Fig. 2.2 displays the major geological structures in the basin.

2.2.3.1 *The Qezel-Owzan River Basin*

The Qezel-Owzan River (QOR) sources at an elevation of 2200 m in the Zagros Mountains, flows from south to north through the Iranian Plateau and, after bending its course to the southeast near the city of Mianeh, the river flows through a 1000 m deep gorge between the Tarom and Talesh Ranges (Figs. 2.1, 2.2; Table 2.1). The Qezel-Owzan River joins the Shahrud River near Manjeel and forms the Sefidrood River, which flows to the north through the 1900 m deep Rudbar gorge in the Talesh Mountains and ultimately discharges into the Caspian Sea. The Sefidrood River discharges a high volume of sediment load and forms a large delta in the southern Caspian lowland. Analysis of sediment cores indicated that the Sefidrood delta initiated during the Early Pleistocene (around ~1 Ma) after the opening of the Rudbar gorge and river capture of the Qezel-Owzan and Shadrood Rivers (Kazancı and Gulbabazadeh, 2013). A recent study suggested that fluvial connectivity between the Iranian Plateau and the Caspian Sea through the Amardos gorge initiated at ~4 Ma (Heidarzadeh et al., 2017). The main active faults of the area strike NW-SE. Exposed lithologies mostly consist of conglomerate, sandstone and evaporitic sediments in the Iranian Plateau, and tuffs and andesitic tuff in the Alborz Mountain. The Folded Miocene Belt (FMB), the Masuleh Fault (MaF) and North Zanjan Fault (NZF) are the most important structures (Fig. 2.2).

River Basin	Local name of river	Length (km)	Basin area (km ²)	Source	Flow direction	Discharge
Kura	Mtkvari	1130	193577	Mount Kisirindađı (Eastern Anatolia, Ardahan)	W-E	Caspian Sea
Arax	Araz/Aras	1030		Bingöl Mt. (Eastern Anatolia, Bingöl)	W-E	Kura River
Qezel-Owzan	Qizil-Üzan	750	58623	Chehelcheshmeh Mt. (Iranian Zagros Mt.)	S-N	Caspian Sea

Table 2.1: The main drainage basins of the study area

2.3 Analytical methods

The regional morphometric analysis was carried out using the Digital Elevation Models with ~90 m resolution produced by the Shuttle Radar Topography Mission (SRTM; Jarvis et al., 2008). The 30 m resolution DEM extracted from digitized 1:25,000 scale topographic maps of the region of interest was too noisy. The MATLAB software package 'TopoToolbox' Version 2 was used to carry out topographic and basin analyses (Schwanghart and Kuhn, 2010; Schwanghart and Scherler, 2014).

2.3.1 Swath profile

Swath profiles have been widely used in the geomorphological analysis of large orogens, typically with a band width of 10-100 km (e.g. Kühni and Pfiffner, 2001; Telbisz et al., 2013). We extracted three swath profiles with a 50 km swath width to identify regional topographic variability. This width is sufficient to include the mountain chain and part of the adjacent basins. The swath profiles of average annual precipitation data at 1km resolution (Hijmans et al., 2005) was carried out over the same topographic swath profiles.

2.3.2 Local relief map

We produced a local relief map using a circular sampling window with a radius of 4 km, which is large enough to include at least two major envelopes and/or sub-envelopes of the maximum and minimum elevations and displays the characteristics of valley-to-ridge relief patterns (Yildirim et al., 2011). The minimum and maximum elevation envelopes are consistent with valley bottom and peak (or ridges) elevations, respectively.

2.3.3 Longitudinal profile, steepness (ksn) map and paleo-river profile

Longitudinal stream profiles were extracted from the DEM for the main streams and their tributaries. Sudden changes of elevation along bedrock rivers indicate varying bedrock incision

due to tectonic or climate perturbation, change of base-level fall rate, and rock strength. Knickpoints or knickzones correspond to sharp changes in the slope-area scaling that is observed for most bedrock rivers (Flint, 1974; Hack, 1960; Howard and Kerby, 1983):

$$S = k_s A^{-\theta} \quad (\text{Eq. 1})$$

where S is the local channel slope, k_s is the channel steepness index ($\text{m}^{2\theta}$), A is the upstream drainage area (m^2), and θ is the channel concavity index (Flint, 1974). The normalized steepness index is the local channel steepness calculated using a reference concavity $\theta_{\text{ref}} = 0.45$ (Whipple, 2004). Assuming a steady-state river profile under uniform uplift and bedrock erodibility and setting $\theta = \theta_{\text{ref}}$, the normalized channel steepness index, k_{sn} , can be used as a proxy for uplift or erosion rate (DiBiase et al., 2010; Kirby and Whipple, 2012). Changes in the slope-area scaling can be identified from the analysis of both longitudinal profiles and slope-area plots (e.g. Whittaker, 2012; Wobus et al., 2006a). For this study, longitudinal profiles and slope-area data were extracted from the DEM and analyzed using the stream profiler toolbar for ArcGIS Desktop version 10.0 (Wobus et al., 2006b).

We used the results of the slope-area analysis to reconstruct paleo-river profiles and estimate the average long-term river incision from the equation of the stream-power model for river erosion (Howard, 1994; Howard and Kerby, 1983; Whipple and Tucker, 1999):

$$E = K A^m S^n \quad (\text{Eq. 2})$$

where E is the river erosion rate, S is the local channel slope, K ($\text{m}^{1-2m} \text{yr}^{-1}$) is a dimensional parameter of bedrock erodibility, and the exponents m , n are positive constants.

2.3.4 Chi (χ) analysis

At steady state, the slope-area scaling predicted by equation (1) can also be expressed in an integral form:

$$z(x) = z_b + A_0 \frac{m}{n} k_s \chi, \quad (\text{Eq. 3})$$

where z_b is the elevation at a base level, A_0 is an area scaling factor, and m , n are the exponents in the stream-power equation (2). The integral term, χ , is defined as (Perron and Royden, 2013):

$$\chi = \int_{x_b}^x \left(\frac{A_0}{A(x')} \right)^{\frac{m}{n}} dx' \quad (\text{Eq. 4})$$

where A is downstream drainage area, m/n is the river channel concavity index, θ , and integration is performed in the upstream direction starting from the river outlet. Calculation of channel slope from noisy topographic data produces considerable scatter in log slope-log area plots and reduces the accuracy of the derived channel steepness (Perron and Royden, 2013). Such problems are reduced by using the integral method, which is based on the integration of drainage area (equation 4; Perron and Royden, 2013). When a scaling area of $A_0 = 1 \text{ m}^2$ is used, the steady-state river

profile is transformed into a straight line and the slope of the line is the channel steepness (equations (2) and (3)), allowing us to easily identify knickpoints. In addition, geometric equilibrium in channel networks implies that a χ map network exhibits equal values across all water divides (the ridges separating river basins; Willett et al., 2014). A joint analysis of χ -z plots (χ -plots) and maps of χ (χ -maps) allows identification of geometric disequilibrium produced by tectonic or climatic perturbation, and provides a dynamic view of river network geometry.

For the construction of χ -plots and χ -maps, we selected an arbitrary scaling area $A_0 = 1 \text{ m}^2$ (Yang et al., 2015), which gives χ units of length, and set the ratio m/n to the reference, equilibrium value of 0.45. We choose this value because it has been constrained in previous work (e.g. Heidarzadeh et al., 2017). Channel pixels were identified in the DEM by using a threshold area of 10^6 m^2 (Montgomery and Foufoula-Georgiou, 1993; Tarboton et al., 1989; Wobus et al., 2006a).

2.4 Results

2.4.1 Swath profiles

Fig. 2.3 shows swath profiles of the TIP, nearly normal to the general NW-SE structural trend of the northern TIP and south Caucasus Region. Each profile shows maximum, minimum and mean elevations obtained from a 90m SRTM DEM and a swath width of 50 km centered on the profile line. These profiles were placed to cross the flanks of the TIP and highlight possible orographic effects on precipitation.

1) The ~330 km long swath profile AA' shows the variation of the elevations in the TIP compared to the mountain ranges (Caucasus Mountains) north of it (Fig. 2.3) and is divided into two segments: the SW segment includes the region between the northern flank of the TIP and the drainage divide of the Lesser Caucasus Range. This segment of the swath profile crosses Quaternary andesitic volcanic, igneous and pyroclastic rocks and Quaternary sediments incised by the Arax River and its tributaries. In the TIP, the mean elevation is nearly constant at ~2200 m, except for a narrow structural depression corresponding to the Maku fault trace, and drops rapidly to ~1000 m with a mean slope of 0.06 along the northern flank of the plateau. The mean elevation of the swath profile increases with a mean slope of 0.025, from ~1000 in the Arax River basin up to ~2000 m at the drainage divide of the Lesser Caucasus, which corresponds to the Pambak-Sevan-Sunik Fault (segment 1, PSSF1; Fig. 2.3A). The highest peak at 4000 m in the maximum elevation profile corresponds to the Aragats volcano (Fig. 2.3A). A high local relief (the difference between maximum and minimum elevations in a swath profile) is observed around the Aragats volcano and in the Lesser Caucasus. The Arax River valley exhibits the minimum

local relief. The mean annual precipitation (Hijmans et al., 2005) is higher in the Lesser Caucasus (~600 mm/yr), drops to less 300 mm/yr in the Arax River basin, and slightly increases in the TIP (Fig. 2.3A). The NE segment of the profile shows the valley-ridge topography across the Kura River basin and the Greater Caucasus Range. This profile segment crosses Mesozoic limestone, Cenozoic pyroclastic and Pleistocene-Quaternary sediments. The mean elevation varies between few hundred meters in the Kura River valley and ~3000 m in the Greater Caucasus. The southern flank of the Greater Caucasus shows a marked topographic change corresponding to the MCT (Fig. 2.3A), where mean elevations increase with a slope of 0.05. The maximum local relief is observed in the Greater Caucasus (Fig. 2.3A); the Kura River valley is bounded by the KF and LCT and displays relatively low local relief. The mean annual precipitation is higher in the Greater Caucasus (~900 mm/yr) and drops to ~300 mm/yr in the Kura River basin (Fig. 2.3A). In general, the profile AA' shows that major topographic changes occur at important tectonic structures and volcanic edifices and that precipitation decreases from northeast to southwest.

2) The swath profile BB' is ~500 km long (Fig. 2.2) and is subdivided into two segments: the SW segment, from the Zagros Mountain to the Arasbaran Mountains (Fig. 2.1), includes baserock of Cretaceous ophiolites, Paleozoic sandstones and shales and Quaternary deposits (Figs. 2.2, 2.3B). The mean elevation shows a plateau topography with mean elevation of ~1500 m corresponding to the internally drained basin of the Urmia Lake. The peaks in the maximum elevations and the high local relief correspond to the Main Recent Fault in the Zagros to the SW, and to the North Mishu Fault system in the Arasbaran Mountains to the NE (Fig. 2.3B). The transition to the northeastern segment is marked by a step change in the elevations occurring at the divide between the internal drainage of Lake Urmia and the Arax River basin. The difference between maximum and minimum elevations rapidly increases across the northern flank of the TIP, highlighting the transition from internally drained topography in the plateau interior to the externally drained region of the Arax and Kura Rivers. In the NE segment, the mean elevation decreases from ~2500 m in the Arasbaran Mountains to ~500 m in the Kura River basin, with a mean slope of 0.013. The section of the profile corresponds to the Arax River valley and is characterized by high local relief across the PSSF. The NE segment represents the topographic profile from the Arasbaran Mountain to the Kura Basin, and includes granite, granodiorite, conglomerate and sandstones incised by the Arax and Kura Rivers (Fig. 2.3B). The mean precipitation is ~400 mm/yr along most of the profile segment and increases slightly in the Zagros Mountains and southern Caucasus. The swath profile BB' shows the overall control of structural boundaries on the locations of both high local relief and major drainage divides separating internally drained and fluvially integrated areas.

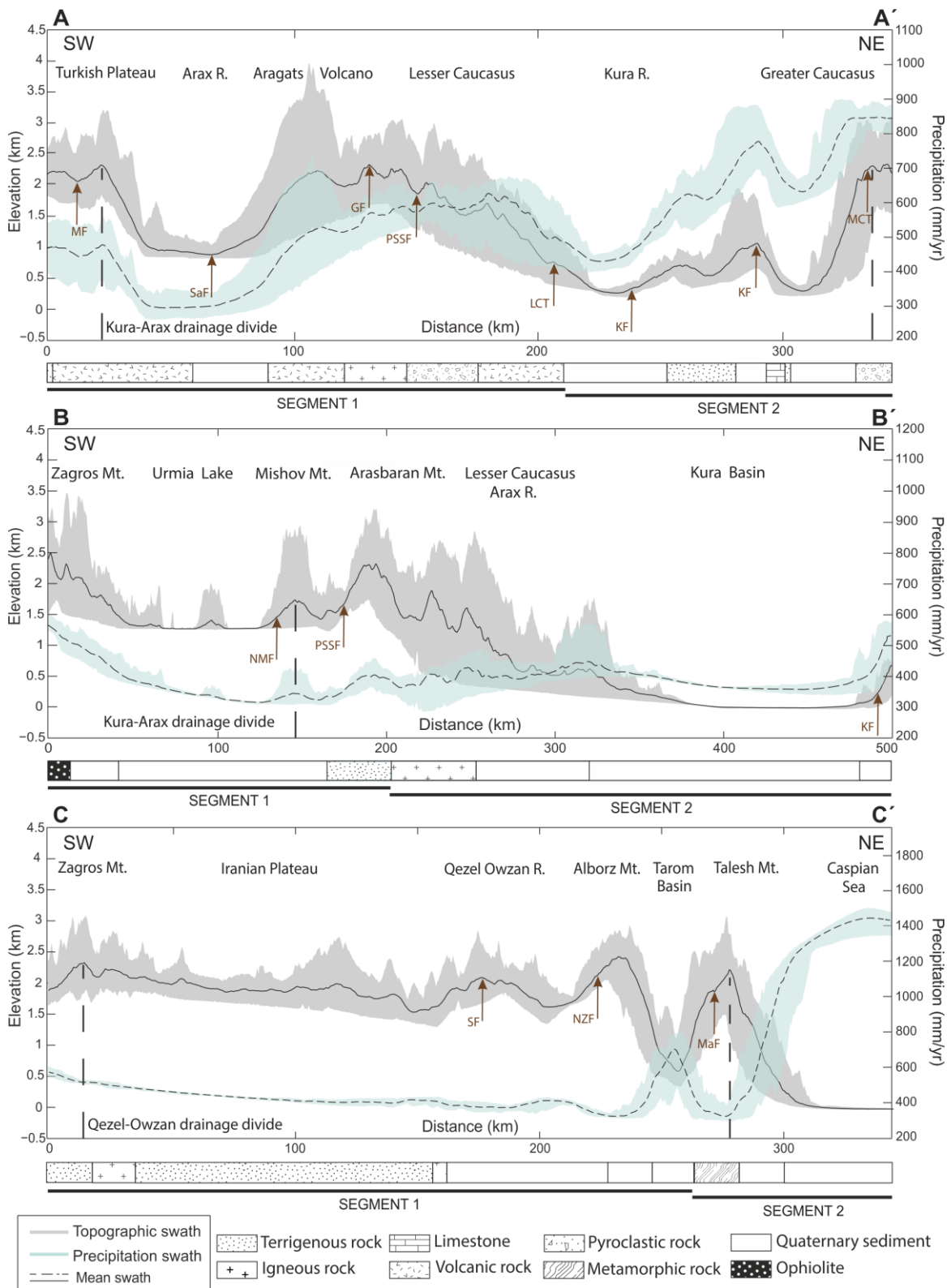


Fig. 2.3: Topographic (grey color) and precipitation (green color) swath profiles (located in Fig. 2.1) along (A-A', B-B', C-C'; 50 km width). Bounds of the colored regions: upper = maximum elevation, lower = minimum elevation, and Mean elevation = black line. Brown lines = active faults (names as in Fig. 2.2). Bedrock lithology indicated below each swath profile. Precipitation swath extracted from a global dataset with 1 km resolution (Hijmans et al., 2005).

3) The ~330 km long swath profile CC' and includes the topography from the Zagros to the Alborz Mountains. The southwestern and central profile sections show higher mean elevations of the plateau topography (~2000 m) compared to the profile BB', and a tilt of the plateau surface toward the NE with a mean slope of 0.0012. The peaks in the maximum elevations occur at the Main Recent Fault in the Zagros, and at the NZF and MaF in the Alborz Mountains. Rock type along this segment includes terrigenous and igneous Eocene rocks (Fig. 2.3C). In the northeastern section of the profile, two step changes in the elevations correspond to the Tarom basin, a ~1000 m deep gorge (Amardos gorge) incised by the Qezel-Owzan River, and to the lowland between the southern coast of the Caspian Sea and the Talesh Mountains. High difference between maximum and minimum elevations is observed in the Alborz and Talesh Mountains and correspond to the NZF and MaF traces. There is a steep precipitation gradient between the southern coast of the Caspian Sea (~1400 mm/yr) and the Talesh Mountains (~600 mm/yr). The mean precipitation drops to less than 400 mm/yr in the Iranian Plateau and slightly increases in the Zagros Mountains (~600 mm/yr; Fig. 2.3C). The NE section of the profile includes metamorphic and terrigenous rocks and Quaternary sediments incised by the Qezel-Owzan River (Fig. 2.3C). The profile CC' suggests a regional tilting of the TIP that is not apparent in profiles AA' and BB', and confirms that high local relief occurs at major fault systems and in regions of low to moderate seismicity (Fig. 2.1). The Talesh and Alborz Mountains act as orographic barriers along the northeastern flank of the TIP, resulting in widespread aridity and subdued fluvial relief in the plateau interior.

2.4.2 Local relief analysis

The local relief maps of Fig. 2.4 was computed as the residual relief between maximum and minimum elevations averaged over a sampling window of 4 km, and illustrates the distribution of fluvial incision in the TIP compared to the surrounding mountain ranges. The values of local relief vary between 0 m (valley bottoms) and 3400 m, and in general local relief is very low in the TIP compared to the Greater and Lesser Caucasus Ranges. In the Greater Caucasus, high local relief corresponds to the Main Caucasus Thrust (MCT), while volcanic edifices and intrusive rocks, which are more resistant to fluvial erosion, result in the high local relief observed in the Lesser Caucasus Region (Fig. 2.4).

Low local relief is also observed in the downstream part of the Arax and Kura River basins, reflecting alluvial deposition. In the central part of the Arax River basin and in close proximity of Pambak-Sevan-Sunik Fault the local relief values change rapidly from 600 m to 3400 m within a distance of ~10 km (Figs. 2.2, 2.5B). Local relief is high on the northeastern and southwestern

flanks of the TIP, with higher values to the east in the Talesh Mountains and Tarom Basin. The highest value of local relief is in the lower Qezel-Owzan catchment, where the river incised a ~1000 m deep gorge (Fig. 2.5C). The boundary of the low-relief topography in the northern Tarom Basin coincides with the sudden decrease in precipitation behind orographic barriers observed along the swath profile CC'. The marked variation in local relief between the upper and lower Qezel-Owzan catchment indicates that the topography of the plateau interior represents a transient feature, which was integrated into the external fluvial system by higher precipitation and efficient head-ward erosion on the northeastern flank.

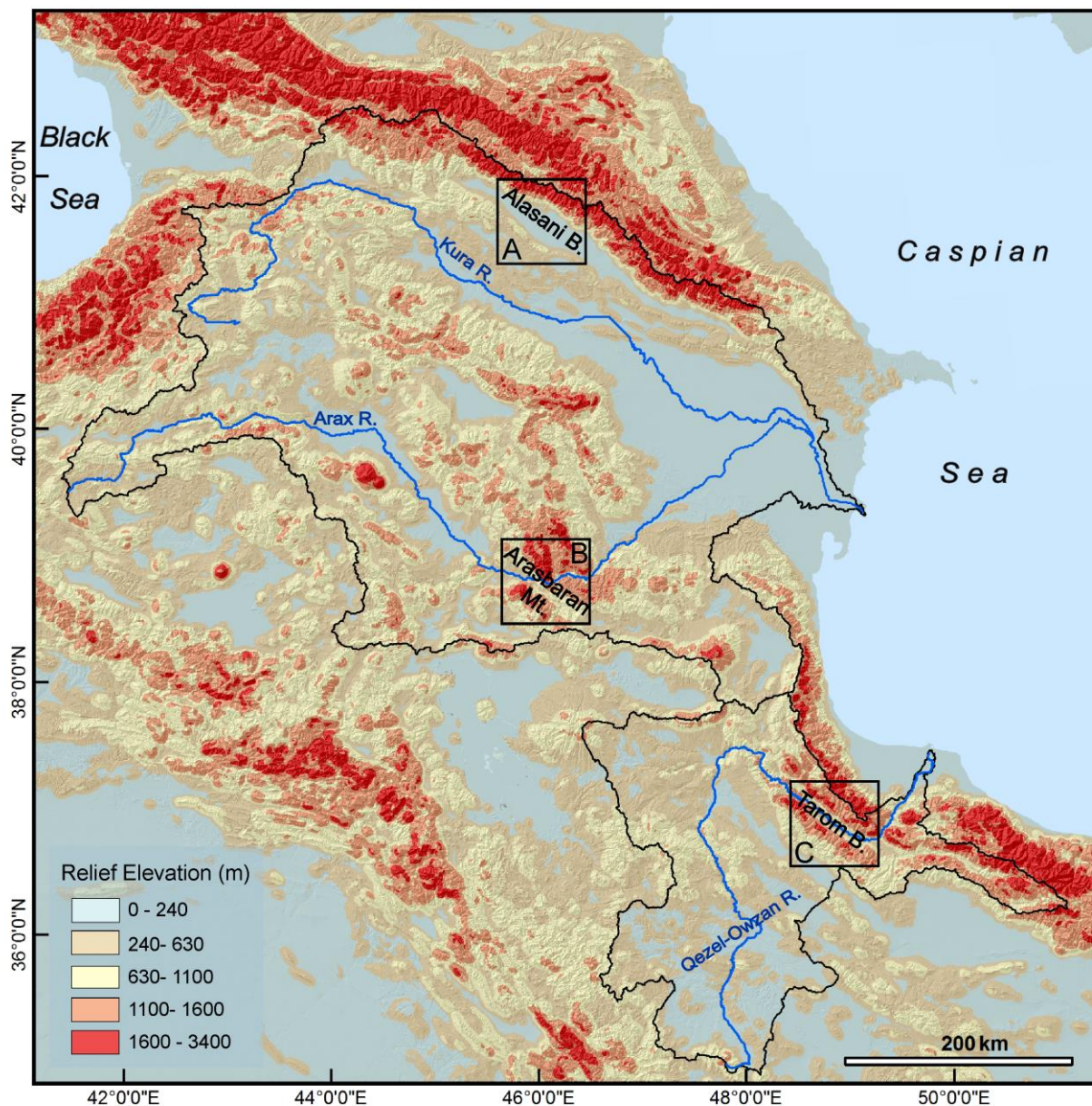


Fig. 2.4: Local relief map calculated with a 4 km radius sampling window over the Turkish-Iranian Plateau and Caucasus Regions (explanation in text). Black rectangles A=Alasani Basin; B=Arasbaran Mountain (Ghareh-Dagh) and C=Tarom Basin, point out sharp local relief variation.

2.4.3 Stream profile, steepness map and paleo-profile reconstruction

We extracted longitudinal river profiles of the Kura, Arax and Qezel-Owzan Rivers and calculated the steepness and concavity indices by linear regression analysis from log-log plots of drainage area, A , and channel slope, S . Knickpoints were identified on longitudinal profiles and, based on geological maps and Google Earth imagery, they were classified as 1) lithology contacts, 2) active faults and 3) regional knickpoints. In addition, we calculated a regional map of normalized steepness index to investigate the spatial variation in channel steepness throughout the TIP and the surrounding areas.

2.4.3.1 Kura River

The longitudinal profile of the Kura River shows a smooth, concave-up shape between its outlet to the Caspian Sea and ~1000 km from the mouth, where channel steepness gradually increases. This deviation in channel slopes coincides with a major knickpoint at ~1800 m elevation, separating the steep downstream channel segment from the low relief topography in the headwaters of the Kura River. Below this major knickpoint, the Kura River flows through a sequence of volcanic rocks forming the Kars plateau. The map of normalized channel steepness suggests that marked variations in channel slopes could be coincident with the more resistant volcanic units that outcrop in the upper Kura River basin. High values of ksn (90->120) are observed below the major knickpoint in the Akhalkalaki Basin (Fig. 2.5A), whereas ksn is very low near the headwaters of the Kura River, within the Kars plateau (<30). The downstream portion of the Kura profile also displays low ksn values (<60) within the alluvial plain of the Kura Basin. Fig. 2.5D shows the Kura slope-area data and the results of the linear regression analysis. The normalized channel steepness index is anomalously high in the middle segment of the Kura River between the Samsari Thrust Fault and where the bedrock consists of volcanic rocks. The ksn values decrease in the upper segments of the Kura River and reach a value of 11.3 in the Kars plateau, indicating the presence of a relict landscape in the headwaters adjusted to an old base-level. The concavity indices calculated for the channel segments of the Kura River show positive values higher than 0.6, and suggest disequilibrium of the profile in response to change of base-level, onset of uplift, climate shift, or a combination of these factors (Whipple, 2004). A paleo-profile reconstruction was obtained by using the concavity and steepness indices calculated for the channel segment above the ~1550 m knickpoint, and projecting the elevations along the downstream distance. The reconstruction of the Kura paleo-profile indicates that the total river incision into the volcanic units is ~800 m (Fig. 2.5B).

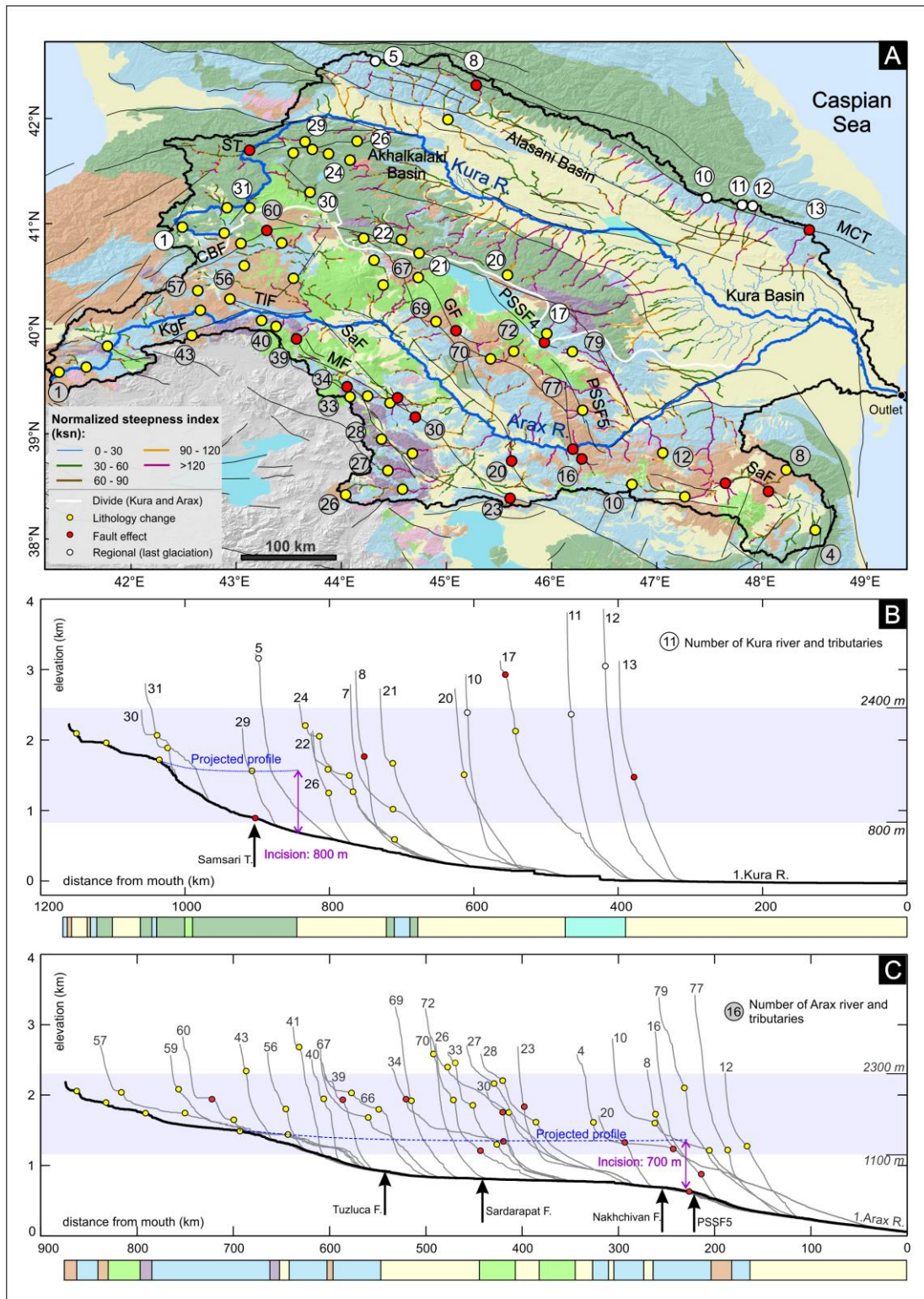


Fig. 2.5: A: channel steepness indices map that are normalized (ksn) to a reference concavity (θ_{ref}) of 0.45 thru the Kura-Arax River Basin. This is calculated by the stream profiler tool (www.geomorphptools.org) with a smoothing window of 500 m. simplified geological map of bedrocks from different scale maps (NW Iran; Turkey; Georgia; Armenia; Azerbaijan Republic). B, C: Long stream profiles with major knickpoints marked by colored circles in term of knickpoint types based on boundary conditions in Kura and Arax rivers. Below the profile is indicated by bedrock lithology. Active faults name explained in Fig. 2.2. The blue colored rectangles are most distribution of knickpoints. D, E: Log slope versus log area plots of the Kura and Arax Rivers (trunk channel), respectively. –Continued on next page.

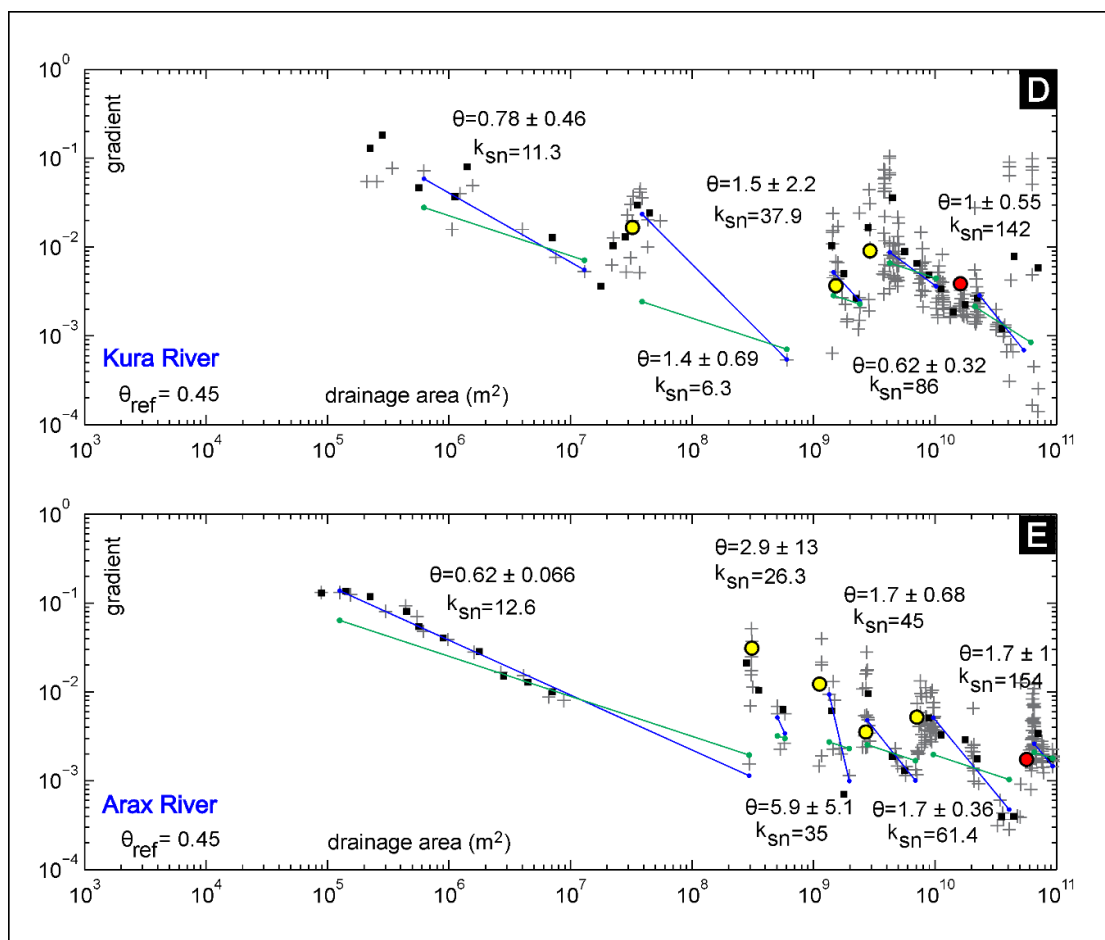


Fig. 2.5: -Continued from previous page.

The longitudinal profiles of 32 tributaries of the Kura River show knickpoint elevations between 100 and ~3200 m. Most knickpoints occurring between 800 and 2400 m are related to lithology changes (Figs. 2.5A, 2.7A). We identified four knickpoints coincident with active faults: the Samsari Thrust, below the major knickpoint in the Kura trunk channel, the Main Caucasus Thrust in the left tributaries 8 and 13, and the Pambak-Sevan-Sunik Fault (PSSF) in the right tributary 17 (Figs. 2.5A, 2.5B). Regional knickpoints display similar elevations and are identified in the upper portion of the Kura tributaries draining the southern flank of the Greater Caucasus Mountains (white circles with number 5, 10, 11, 12 in Figs 2.5A, 2.5B): given their high elevations, these knickpoints could reflect different erosion processes on the river profile caused by glacial erosion. The channel steepness and concavity indices calculated for the tributaries of the Kura River and they show variation (Table 2.2 and 2.3; Fig. 2.5D). Tributary number 24 displays the highest k_{sn} and θ values within volcanic rocks of the Samsari Volcano (Fig. 2.5A). The left tributaries show higher local relief values compared to the right tributaries, which are attributed to less erodible rocks combined with high uplift rates along the Main Caucasus Thrust fault (Fig. 2.4).

2.4.3.2 *Arax River*

The Arax River displays a longitudinal profile composed of 6 smooth, concave-up channel segments, separated by 5 major knickpoints (Fig. 2.5C). Three of these major knickpoints correspond to strike-slip or thrust faults, whereas two major knickpoints near the headwaters are related to lithology changes. Three major knickpoints in the upper longitudinal profiles of both the Kura and Arax Rivers display very similar elevations (Figs. 2.5B, 2.5C), indicating a common origin and could be attributed to a change in regional surface uplift, common base-level fall, or climate shift. The results of the linear regression analysis of the Arax slope-area plot reveals values of concavity higher than 0.6, and ksn values one order of magnitude higher in the middle channel segment than in the upper segments. Both results suggest a state of disequilibrium of the Arax River profile and that the upper catchment represents a relict landscape adjusting to changes in boundary conditions. We reconstructed the plaeo-profile of the Arax from the ksn and θ values calculated from channel segment above the knickpoint at ~1300 m, and indicate that for the middle channel segment the total river incision in response to the change in base-level is ~700 m (Fig. 2.5C).

We analyzed the longitudinal profiles of 82 tributaries of the Arax River. Knickpoint elevations are distributed between 500 and 3500m (Table 2.4). The knickpoints showing elevations between 1100 and 2300 m in 28 tributaries are related to lithological changes from igneous to ophiolitic, and from igneous to sedimentary rocks (Figs. 2.5A, 2.7B, 2.7C). Thirteen knickpoints along the trunk channel and ten tributaries are related to active faults (Fig. 2.5A). High channel steepness and concavity are observed in the tributaries flowing through the volcanic units of the Aragats volcano in the Lesser Caucasus, and suggest low erodibility of this bedrock. The highest channel steepness and concavity also occur around other volcanoes and suggest the effect of resistant lithologies on local channel steepness. In addition, the ksn map reveals that the tributaries draining the upper and middle catchment display steeper lower reaches, which indicates transient profile evolution in response to base-level fall. High fluvial relief (>1000) is observed around volcanic edifices and in areas surroundings the major faults (Figs. 2.4, 2.5A).

2.4.3.3 *Qezel-Owzan River*

The longitudinal profile of the Qezel-Owzan River displays 3 major knickpoints at ~1000 m, ~1500 m, and ~1900 m elevations, separating concave-up channel segments (Fig. 2.6). In fact, the shape of this profile is similar to folded river. Relatively steep slopes characterize the channel segment of the Qezel-Owzan River below the ~1000 m knickpoint, which occurs downstream of the Gamachay Fault and does not correspond with any lithology change. Previous work has

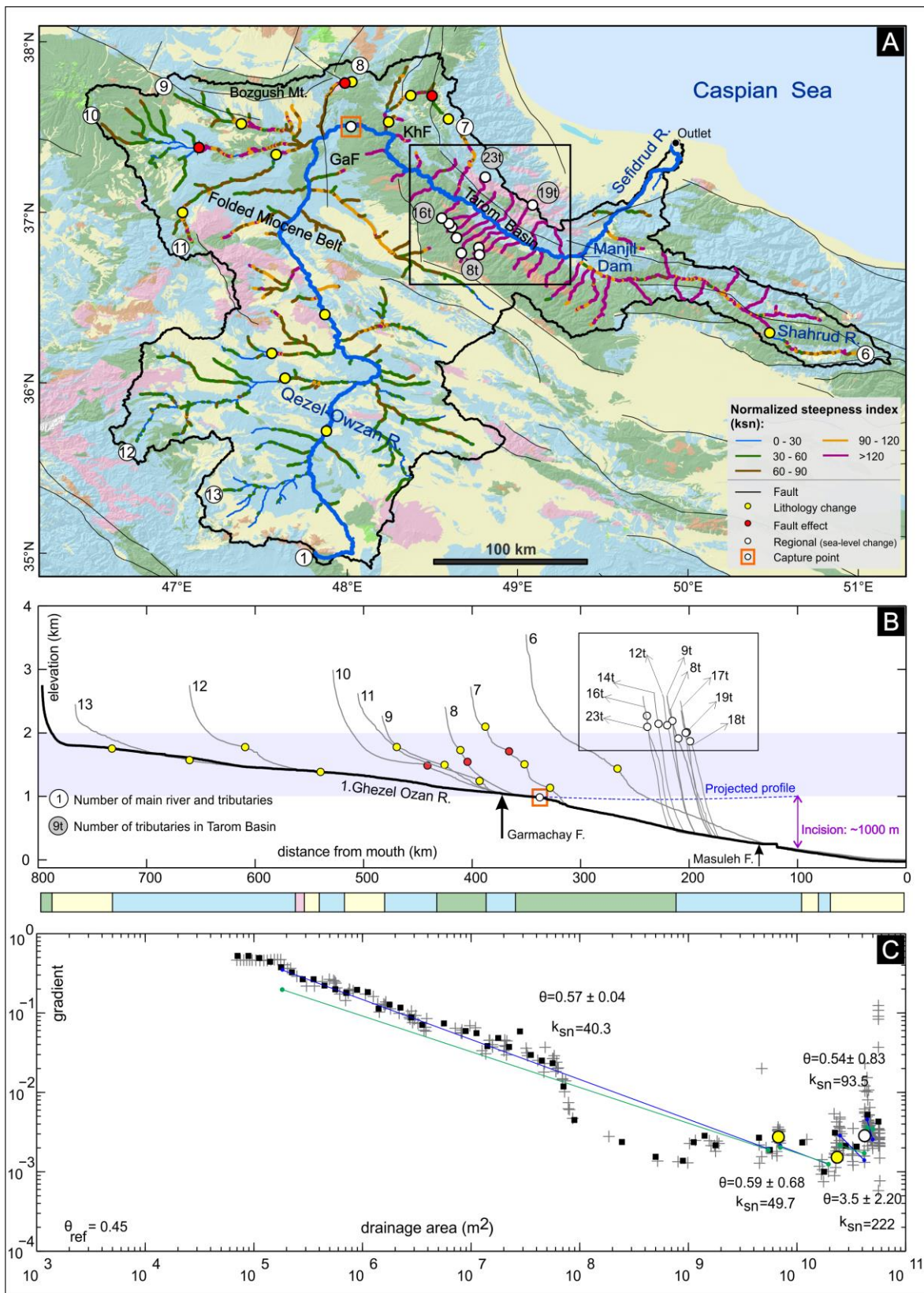


Fig. 2.6: A: Ksn map of the Qezel-Owzan River Basin with θ ref. of 0.45. B: Longitudinal stream profiles of the Qezel-Owzan (folded shape) with major knickpoints (different colors) and inset frame indicates tributaries with evidence of Caspian Sea-level changes. C: Log slope versus log area plots of the trunk channel in upper/middle catchment.

suggested that the major knickpoint at ~1000 m represents the capture point of a former internally drained area (Heidarzadeh et al., 2017), which was reintegrated into the external drainage of a paleo-Qezel-Owzan River by headward erosion (Ballato et al., 2016; Kazancı and Gulbabazadeh, 2013). The Qezel-Owzan River cut the ~1000 m Amardos gorge within the Tarom Basin following the increase in drainage area. However, the two knickpoints identified at higher elevations within the TIP are also related to lithology changes (Figs. 2.6A, 2.6B). The results of the slope-area regressions (Fig. 2.6C) show high steepness and concavity in the lower Qezel-Owzan River basin, confirming that the profile is in a transient state of disequilibrium. Conversely, the upper portion of the slope-area plot displays low channel steepness and a concavity of 0.57 (Fig. 2.6C), suggesting that the relict plateau landscape is near steady-state conditions.

The longitudinal profiles of 23 tributaries of the Qezel-Owzan River display knickpoints between ~1000 and ~3300 m elevation (Fig. 2.6; Tables 2.2, 2.5). Major knickpoints with elevations between ~1000 and ~2000 m are mostly related to lithological changes (Figs. 2.6B, 2.7D). Three major knickpoints correspond to active faults: Khalkhal Fault in tributary 7, Garmachay Fault in tributary 8 and a fault according to geological maps (Mianeh and Hashtrud geological maps, scale: 1:250,000 and 1:100,000, Geological Survey of Iran) in tributary 10. Analysis of small tributaries in the Amardos gorge shows a regional knickpoint between 2000 m and 2200 m elevations (Fig. 2.6B inset). This regional knickpoint was not observed in exterior rivers draining the Talesh Mountains and flowing directly into the Caspian Sea, and indicates river incision following a catchment specific event, such as an increase of drainage area by plateau capture in the upper Qezel-Owzan River basin. The *ksn* map shows that the Qezel-Owzan River and its tributaries are characterized by higher channel steepness in the Tarom Basin ($ksn > 120$) compared to the upstream portion of the catchment ($ksn < 60$; Fig. 2.6A), confirming that the river network is not in equilibrium.

River Basin	Channel steepness (<i>ksn</i>), $m^{0.9}$		Concavity index (θ)		
	Min.	Max.	Min.	Max.	Mean
Kura	2	217	0.09	4	0.89
Arax	~5	381	-0.05	6	1.15
Qezel-Owzan	11.6	286	0.018	5	1.41

Table 2.2: The maximum and minimum of the channel steepness and concavity index within the studied river basins.



Fig. 2.7: Field evidence corresponding to lithology changes knickpoints in the Kura tributaries (Alasani, A); Arax (Ordobad-Chay, B; Klisa-Kandy, C) and Qezel-Owzan tributary (Dagah, D).

2.4.4 Chi maps and plots

Interactions between the drainage network and the regional-scale faults in the TIP can result in continuous drainage reorganization and drainage area exchange along shared drainage divides, and persistent state of disequilibrium of drainage basins (e.g. Goren, 2016). A map of the χ parameter is useful to investigate the effects of river basin dynamics (Beeson et al., 2017; Willett et al., 2014) in the TIP. For steady-state river networks, under the assumptions of uniform uplift and bedrock erodibility, χ scales linearly with elevation. Thus, cross-divide differences in χ can be used to identify disequilibrium of drainage divides.

The χ map of the TIP reveals large differences in χ values across the main drainage divides, suggesting that the Kura-Arax and Qezel-Owzan drainage basins are not in equilibrium (Fig. 2.8). Perturbations resulting from drainage reorganization can be detected from χ plots by deviation from the linear trend predicted by equation (3). The χ profiles of the Arax and Qezel-Owzan Rivers are near-linear and display similar steepness in their downstream sections (Fig. 2.8A). The

upper tributaries of the Arax and Qezel-Owzan Rivers display shallower χ -plots, but tributaries of the latter display higher steepness (Fig. 2.8A). The difference in channel steepness is consistent with the difference in χ across the shared drainage divide, and indicates relatively high erosion rates in the Qezel-Owzan basin and migration of the main drainage divide toward the Arax River basin.

In the upper Arax River catchment, the χ map exhibits large χ differences along internal drainage divides and suggests disequilibrium in the drainage network. Fig. 2.8B shows the χ profiles of tributaries draining the internal drainage divide along the Kars plateau escarpment. The χ plots of the tributaries draining the Kars plateau interior (red χ plots) are shifted toward low χ values compared to the exterior tributaries (blue χ plots). This configuration is consistent with recent gain of drainage area, and suggests that the Kars plateau landscape has been integrated into the external drainage of the Arax River by head-ward erosion.

The χ map of the Arax River reveals also large χ differences along the main divide shared with the internal drainage of the Urmia Lake. The χ profiles of the Arax tributaries display different steepness in their upper reaches that is consistent with cross-divide differences in the χ map, and give evidence for disequilibrium and internal drainage reorganization.

The χ profiles of the Qezel-Owzan River and its tributaries display higher steepness than the exterior rivers draining the Talesh Range. Previous work suggested that the Qezel-Owzan River has carved the Amardos gorge in response to an increase of drainage area by plateau capture. Assuming that U and K are uniform in the Qezel-Owzan River basin, the shift of the trunk profile toward lower χ values confirms that this perturbation is related to the drainage area capture from the TIP.

Differences in erosion rates across divides could be used to confirm the state of disequilibrium and interpretations of direction of divide migration from χ maps. Where cross-divide erosion rates are not available, stability of river networks can also be checked by comparing χ maps with topographic asymmetry across main drainage divides (Beeson et al., 2017; Giachetta and Willett, 2018). Examples from the Arax and Qezel-Owzan main drainage divides are provided in Fig. 2.9 using the Google Earth topography. The topographic asymmetry of drainage divides, the different steepness of paired channels, and geomorphic evidence of drainage area exchange (e.g., wind-gaps in the headwaters) are illustrated in these examples, and validate the χ proxy as a good metric for direction of local divide motion in the TIP.

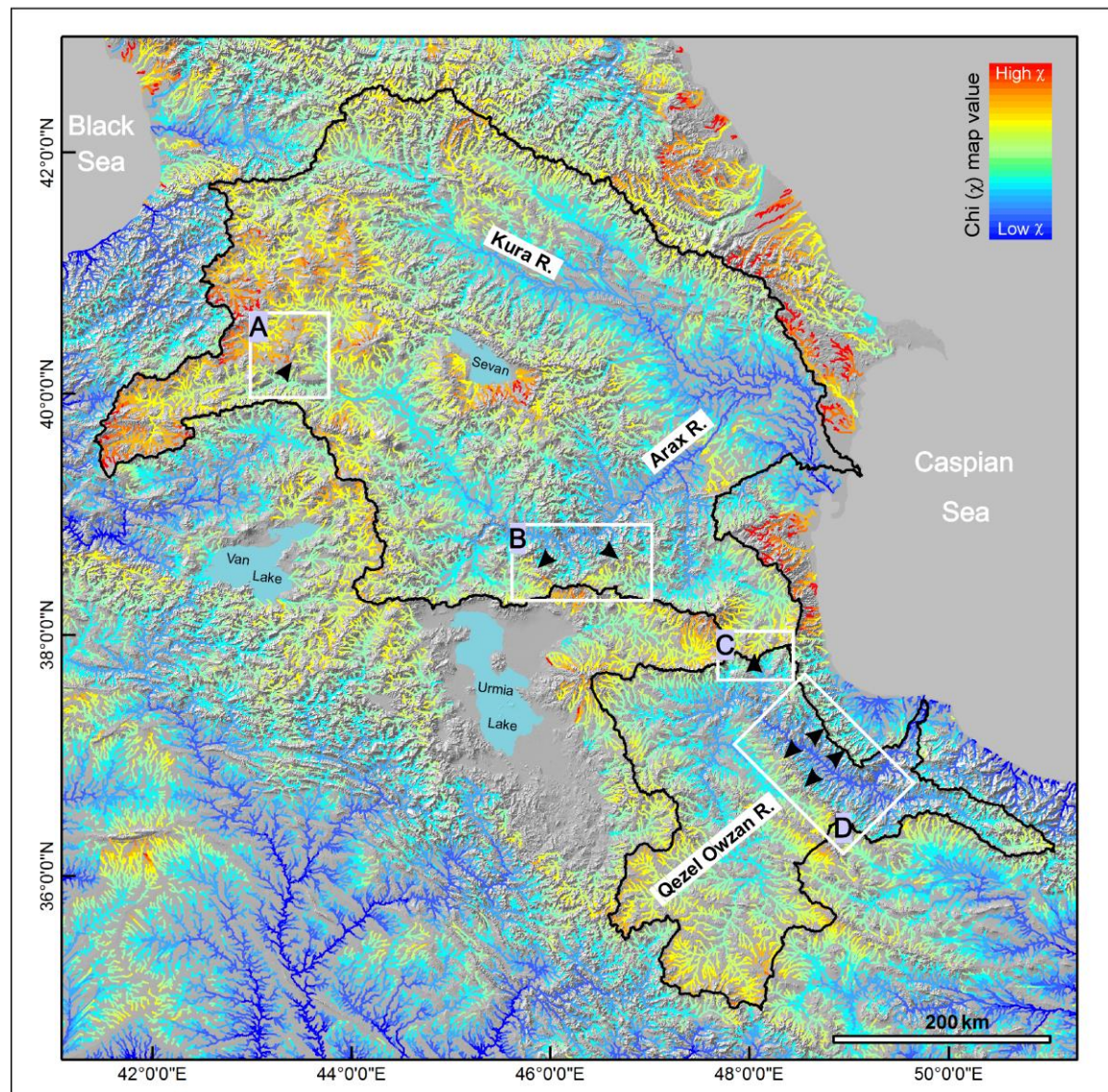


Fig. 2.8: Chi-map of the river catchments in study area, calculated from the 90 m SRTM DEM, using a threshold area for river channels initiation of 1 km^2 and a concavity $m/n = 0.45$. The rectangles on chi-map display location of chi-plot examples (A-D) thru the study area. These examples show disequilibrium along internal drainage divides and used for interpretation of divide motion. The inset figure is perspective view of the landscape (Landsat 7, Google Earth Image). Moreover, graphic of chi-plot response to area-loss victim (drainage area shifts plot to the right) or area-gain (drainage area shifts plot to the right) show in inset A (right corner). –Continued on next page.

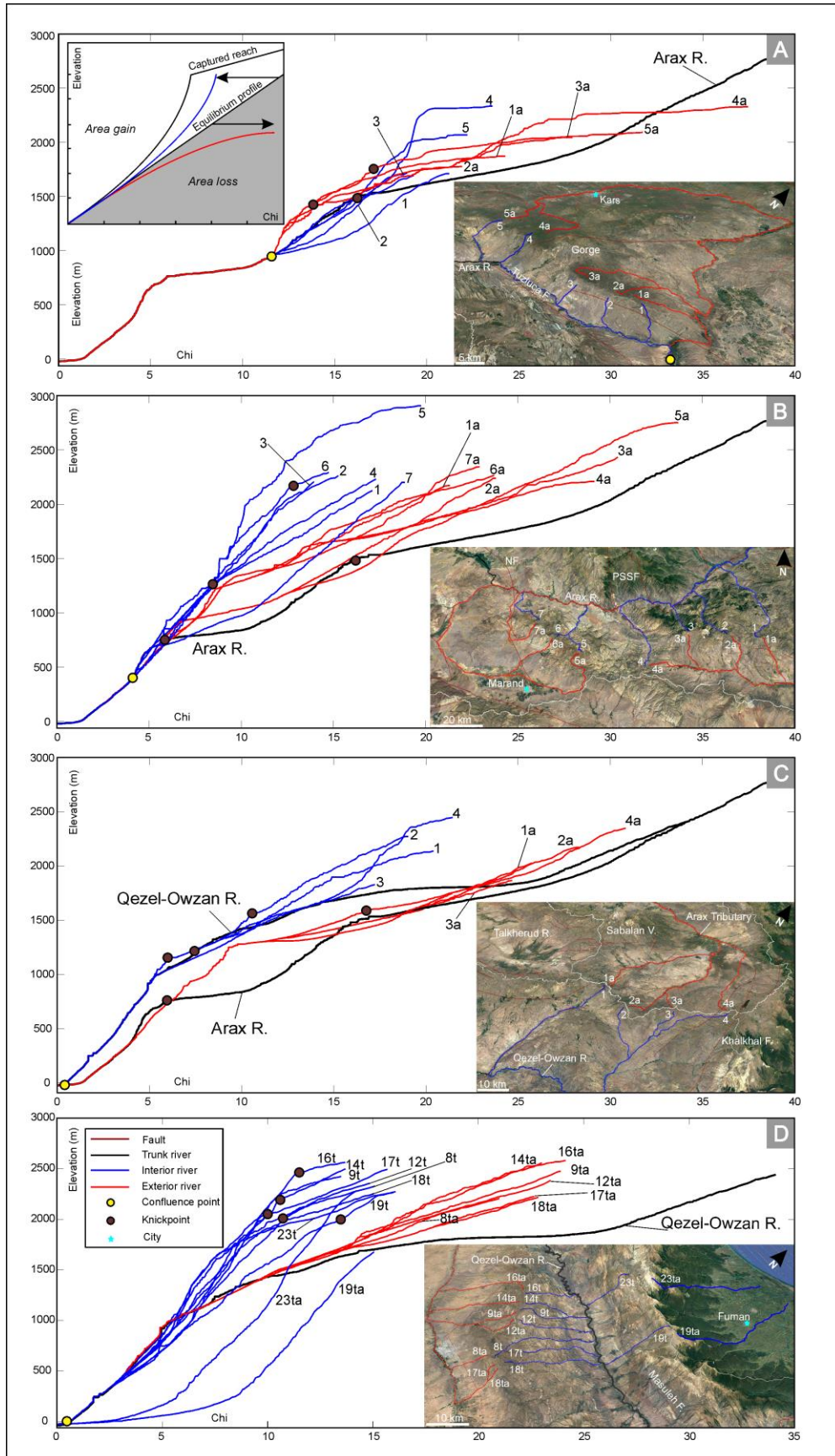


Fig. 2.8: -Continued from previous page.

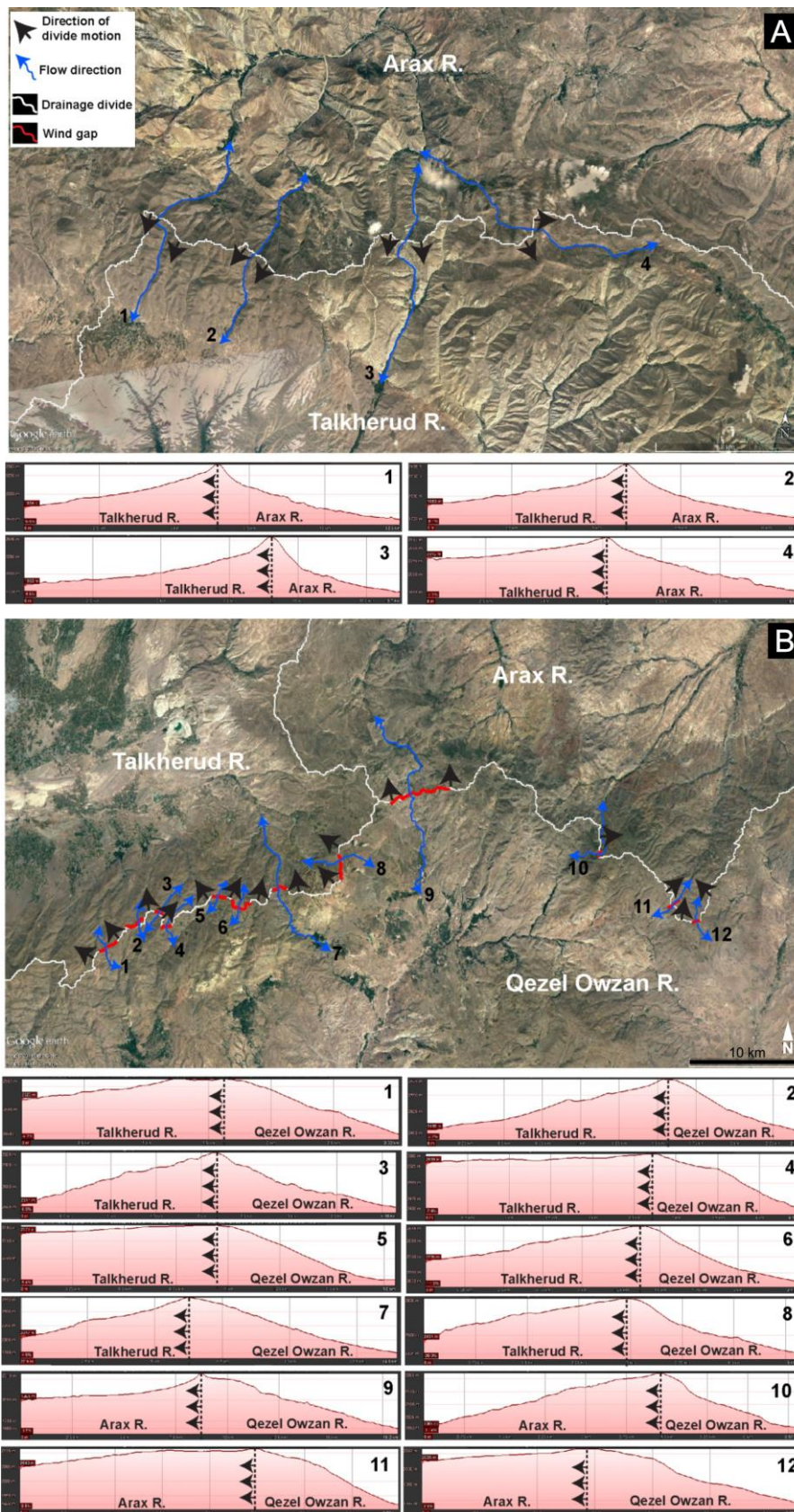


Fig. 2.9: Cross-divide asymmetry and direction of motion of the main drainage divide, from Google Earth topography in the regions A and C in the χ map of Fig. 2.8. (A): between the Talkherud and Arax Rivers. (B): between the Talkherud, Arax, and Qezel-Owzan Rivers.

2.5 Discussion

Our results describe a low-relief landscape in the upper watersheds of the Kura-Arax and Qezel-Owzan Rivers, indicating that the topography of the TIP interior is in a transient state in response to the plateau uplift (Morley et al., 2009). Little or no variations in local relief and low-gradient channels across the TIP interior, indicate that the topography of the plateau formed during uplift combined with low erosion and incision rates (Liu and Bird, 2008). Moreover, the low steepness of the channel reaches draining the upland surfaces are in equilibrium with an old base level. The high local relief on the flanks suggests that higher erosion rates are confined on the plateau margins, where orographic precipitation results in greater local erosion. Compared to the TIP, the relationship between local relief, mean elevations, and precipitation in the Lesser and Greater Caucasus regions suggests higher tectonic uplift (about 1 mm/yr; Avdeev and Niemi, 2011) and more efficient fluvial erosion.

Our analysis shows that most river profiles are out of equilibrium, and the downstream projection of the relict portion of the Kura-Arax and Qezel-Owzan Rivers implies incision of 700-1000 m in response to a base-level fall event (Figs. 2.5, 2.6). The knickpoints found in adjacent tributaries display various elevations and did not provide evidence for a common history of base-level change. Our results show that tributary knickpoints are controlled by local tectonic features and lithologic contrasts. In addition, the folded shape of Qezel-Owzan River profile is consistent with the geological structure in the middle part. Since the middle segment of the trunk channel (Fig. 2.6A) is not concordant with any mapped dip-slip fault, it is more likely that it is attributed to the Neogene folding, “Folded Miocene Belt” (Fig. 2.6A; Ballato et al., 2016). Moreover, the Quaternary fluctuations of the Caspian Sea level fall reached a minimum of ~-50 m below the present sea level (Forte and Cowgill, 2013), suggesting that the upstream migration of major knickpoints and the amount of river incision calculated from the paleo-profiles cannot be explained by eustatic-oscillations. Several lines of evidence indicate that the drainage systems of the Kura-Arax and Qezel-Owzan Rivers have integrated former internally drained areas above the plateau surface. The analysis of the χ maps and χ plots of the Kura, Arax, and Qezel-Owzan Rivers showed that most profile perturbations from the steady-state linear trend are consistent with drainage area capture from the plateau surface. The Arax River displays internal drainage reorganization in the middle and upper catchments (Figs. 2.8A, 2.8B). We found that the drainage divides of the Arax-Kura and Qezel-Owzan Rivers are asymmetric and move toward the plateau interior, confirming active drainage reorganization. Enhanced headward erosion by orographic precipitation on the plateau margins and rapid incision driven by large drainage area captures can also explain the formation of deep gorges (Fig. 2.10) and the amount of incision observed below

major knickpoints. Additional evidence for recent drainage capture comes from the sedimentary record of the Sefidrud River delta (Fig. 2.6A), which suggests a major drainage area capture in the Qezel-Owzan River basing during the Middle Pleistocene (Kazancı and Gulbabazadeh, 2013), when the paleo Qezel-Owzan River connected to the Sefidrud River through the Rudbar gorge and discharged to Caspian Sea (Fig. 2.6A).

The process of drainage reorganization was also affected by Quaternary volcanism, which created local high relief and directly affected the local base-levels in most of the western Caucasus Regions and western TIP (e.g. Lebedev et al., 2003; Lechmann et al., 2018) and NW part of the QORB (Lechmann et al., 2018). The basaltic-dacitic eruptions of the Aragats and Samsari, Ararat volcanoes in the Holocene (Karakhanian et al., 2002; Lebedev et al., 2003) changed base-level, generated steeper lower reaches along the flanks of the volcanic edifices, and formed knickpoints in the upper catchment of Kura-Arax River (Figs. 2.5, 2.6). The lava flows of the Ararat eruption occurred around 400 kyr (Allen et al., 2011b; Lechmann et al., 2018) filled the paleo-channels of Arax River tributaries. The rivers incised the gorges into the lava flows with an average incision rate of 0.015 mm/yr (Fig. 2.10C).

Coincidence of drainage divides and plateau margins with mountain ranges and structures indicates that tectonic deformation is the main driver of landscape evolution in the Caucasus regions and in the TIP. For example, the swath profiles show that the Alborz and Talesh Mountains are orographic barriers, reducing precipitation in the plateau interior and preventing efficient headward erosion of external drainages. The course of the Qezel-Owzan River in the eastern plateau margin follows the orientation of major structures. The Pambak-Sevan-Sunik Fault (PSSF) Zone is the main controller of the deformation pattern in the middle Arax catchment. This fault experienced a long-term slip-rate of about 1.3 mm/yr and 2.6/4 m vertical/oblique offset in PSSF5 (Fig. 2.8B; Karakhanian et al., 2004), which is in concordance with the major knickzone found in the middle Arax River (Fig. 2.6A). In the upper Arax, migration of the drainage divide of the Tuzluca escarpment toward the plateau interior in the northern Kars region (Fig. 2.8A) produced an internal capture, which is controlled by the Tuzluca fault (Dhont and Chorowicz, 2006). The drainage divides between the Arax, Talkehrud and Qezel-Owzan Rivers coincide with the SBF and NTF faults (Fig. 2.8C). We found several wind-gaps and observed topographic asymmetry across these drainage divides, revealing the strong impact of Quaternary deformation on the evolution of large-scale drainage patterns in the TIP (Fig. 2.9).



Fig. 2.10: Field photos of deep gorges examples in the study area. A,B: Deep gorges of Kura tributaries in Khrami (west of Kura Basin) and Ardahan Basin, respectively, C: Zang-e Mar (Arax tributary) deep gorge in Maku Region, D: Deep gorge in Qezel-Owzan River, Givi area, western Alborz.

Recent work suggested that a low-velocity anomaly under the Zagros Mountains reflects density differences in the upper mantle beneath the southwestern plateau (Copley and Jackson, 2006; Maggi and Priestley, 2005; Zor et al., 2003). This anomaly indicates that the plateau topography is dynamically supported (Copley and Jackson, 2006). Our swath profile analysis revealed a gently, eastward tilting of the plateau surface, which could be associated with upwelling of less-dense mantle in the southwestern TIP.

2.6 Conclusion

The results of our morphometric analysis show that the topography and large-scale drainage networks in the TIP and Caucasus regions are out of equilibrium. The relationship between topography, precipitation, fluvial incision, and the χ parameter indicates that the persistence of disequilibrium river networks and transient landscapes in the upper catchment of the Kura-Arax and Qezel-Owzan Rivers results from a combination of enhanced aridity in the internal plateau, rapid uplift of orographic barriers along the plateau margins, and exposure of resistant rocks

associated to the regional volcanic activity. The results of our profile analysis indicate that the river profiles are in disequilibrium and that perturbation from the steady-state trend are associated with drainage captures, regional tectonic features and contrasts in rock strength. The low values of channel steepness in the upper section of river profiles confirms that the presence of a relict landscape equilibrated with an old base-level. The incision of ~700-1000 deep river gorges below major knickpoints resulted from head-ward erosion and capture of former internally drained areas above the plateau in the studied rivers. The prominent perturbations in the χ plots of the Qezel-Owzan River and the development of the Sefidrud River Delta suggest that the capture of a large plateau area and subsequent river incision of the Amardos gorge occurred since the Middle Pleistocene. The χ map and drainage divide analysis shows that ongoing dynamics of drainage basins produce motion of water divides towards the internal plateau and persistent disequilibrium in the landscape of the TIP.

Table 2.3: Results of morphometric analysis of the Kura River Basin

Channel No.	Seg.	A_min (km ²)	A_Max (km ²)	K _{sn} (m ³ /s)	Theta	error (±2σ)	ks	R ²	Knickpoint elev. (m)	DFD ¹ (km)	DFM ² (km)	Upstream drainage area (km ²)
<u>1</u>	1-1	3.50E+05	1.30E+07	11.3	0.78	0.46	1.87E+03	0.79				
	1-2	3.80E+07	6.10E+08	6.3	1.4	0.69	6.31E+08	0.93	<u>2093.5</u>	11352.8	1149518.4	30863508
	1-3	1.40E+09	2.40E+09	37.9	1.5	2.2	2.92E+11	0.12	<u>1986.5</u>	50638.4	1110232.8	1423626456
	1-4	4.20E+09	1.00E+10	142	1	0.55	4.28E+07	0.22	<u>1735.6</u>	125658.8	1035212.4	2867895148
	1-5	1.10E+10	3.90E+10	86	0.62	0.32	4.71E+03	0.2	<u>901.6</u>	257575.6	903295.6	10562582608
	1-6	4.20E+10	2.00E+11	24.5	2.5	3.3	5.95E+24	0.19	105.3	645210	515661.2	41058110024
<u>2</u>	2-1	3.10E+05	1.30E+07	27.3	0.35	0.18	7.04	0.54				
	2-2	2.40E+07	7.60E+07	50.9	0.89	0.35	1.30E+05	0.58	2500.6	7589.2	1167405.2	15220968
	2-3	2.10E+08	1.40E+09	22.7	0.38	1.9	9.43E+00	0.05	<u>2103.3</u>	28547.6	1146446.8	203900324
	2-4	1.50E+09	2.80E+09	36.7	1.6	2.3	9.89E+11	0.12	1963.5	65799.6	1109194.8	1426488708
	2-5	4.50E+09	3.60E+10	100	0.8	0.16	4.02E+05	0.47	1739.7	139696	1035298.4	2867762020
<u>3</u>	3-1	6.00E+06	1.00E+07	82	1.1	0.51	5.50E+06	0.91				
	3-2	1.20E+07	3.20E+10	110	0.55	0.026	9.77E+02	0.89	2319.2	5012	987598.4	11071812
<u>4</u>	4-1	1.20E+06	1.00E+10	67.1	0.39	0.043	27.1	0.73				
	4-2	1.20E+10	3.70E+10	87.4	0.36	0.41	1.14E+01	0.06	<u>867.4</u>	111023.6	893817.2	10690281944
<u>5</u>	5-1	1.20E+05	3.50E+06	4.27	1.1	2.6	8.49E+04	0.97				
	5-2	9.10E+06	3.70E+10	132	0.59	0.025	2.48E+03	0.89	<u>3167.2</u>	3514.4	898268.4	3601852
<u>6</u>	6-1	1.10E+05	2.70E+05	59	0.83	0.21	5.86E+03	0.92				
	6-2	3.60E+05	4.20E+10	119	0.46	0.025	1.81E+02	0.84	2679	688	831973.2	303236
<u>7</u>	7-1	8.80E+05	5.60E+08	114	0.69	0.025	7.76E+03	0.95				
	7-2	6.00E+08	4.90E+09	65.9	0.79	0.15	9.46E+04	0.54	<u>1054.4</u>	59717.2	711156	576192776
<u>8</u>	8-1	3.50E+05	2.20E+06	109	0.78	0.21	8.50E+03	0.81				
	8-2	2.80E+06	4.00E+07	121	0.77	0.096	2.43E+04	0.79	<u>1535.6</u>	16296.4	747207.2	56719924
<u>9</u>	9-1	1.80E+06	1.90E+07	167	0.49	0.076	303	0.69				
	9-2	3.60E+07	1.10E+10	195	0.65	0.13	8.18E+03	0.4	1601.3	8206	563561.6	20080140
<u>10</u>	10-1	1.50E+06	7.60E+06	108	0.62	0.2	1.50E+03	0.74				
	10-2	1.20E+07	1.30E+08	189	0.51	0.066	544	0.72	<u>2379.1</u>	2734.4	608166.8	7714028
	10-3	1.50E+08	1.10E+10	32.6	0.56	0.21	342	0.59	<u>667.8</u>	24600.8	586300.4	137365908
<u>11</u>	11-1	8.00E+05	1.60E+07	191	0.52	0.081	514	0.71				
	11-2	2.90E+07	1.40E+08	216	0.9	0.075	7.23E+05	0.77	<u>2375.7</u>	5729.6	464941.6	22690928
<u>12</u>	12-1	1.70E+05	1.40E+06	114	0.3	0.089	16.6	0.52				
	12-2	3.10E+06	2.90E+07	184	0.84	0.069	1.10E+05	0.91	<u>3047.4</u>	2485.2	417768.4	2226196
	12-3	5.60E+07	1.50E+08	192	1.4	0.18	5.03E+09	0.64	1990.1	10104	410149.6	34591092
<u>13</u>	13-1	2.00E+05	1.00E+08	131	0.57	0.018	950	0.96				
	13-2	2.40E+08	6.20E+08	176	1.2	0.3	8.03E+08	0.43	<u>1318.4</u>	25012.4	373612.4	165137888
<u>14</u>	14-1	2.20E+05	2.50E+06	73.2	-0.11	0.096	0.0332	0.14				
	14-2	3.50E+06	3.50E+08	116	0.47	0.022	138	0.94	<u>1547.6</u>	3271.2	303705.6	3143300
15		1.80E+05	6.80E+08	40.4	0.54	0.024	202	0.96	-	-	-	-
16		1.40E+05	1.50E+09	114	0.42	0.024	65	0.85	-	-	-	-
<u>17</u>	17-1	7.00E+05	1.40E+07	16.6	0.69	0.46	1.19E+03	0.53				
	17-2	4.70E+07	8.70E+07	182	1.4	1.2	5.14E+09	0.13	<u>2904.9</u>	8060.8	555394	20849324
	17-3	1.90E+08	2.00E+09	148	0.46	0.14	247	0.28	<u>2116.7</u>	21456.8	541998	106206560
	17-4	2.20E+09	2.60E+09	166	6.8	3.7	4.18E+61	0.21	<u>699.3</u>	111626	451828.8	2165681928
<u>18</u>	18-1	1.40E+05	3.30E+06	51.8	0.089	0.075	0.405	0.19				
	18-2	4.90E+06	1.90E+07	155	0.58	0.25	1.40E+03	0.51	2523.7	3078.4	525246.8	3587060
	18-3	2.80E+07	4.80E+08	165	0.55	0.047	1.16E+03	0.78	2130.7	6364.4	521960.8	25257340

Table 2.3: -Continued from previous page

Channel No.	Seg.	A_min (km ²)	A_Max (km ²)	k _{sn} (m ^{0.5})	Theta	error (±2σ)	ks	R ²	Knickpoint elev. (m)	DFD ¹ (km)	DFM ² (km)	Upstream drainage area (km ²)
19	19-1	1.20E+07	5.70E+08	167	0.58	0.06	1.78E+03	0.76	1009	38402.8	568934	699484096
	19-2	8.70E+08	1.10E+09	176	3.1	0.95	2.56E+26	0.36				
20	20-1	1.10E+05	4.90E+07	122	0.12	0.046	0.651	0.19	1478.6	13867.6	612194.4	67917468
	20-2	7.10E+07	9.50E+08	135	0.25	0.051	2.6	0.43				
21	21-1	6.70E+05	9.60E+07	115	0.74	0.064	1.01E+04	0.86	1645.7	19244.4	710516.4	111716580
	21-2	1.20E+08	3.90E+10	133	0.57	0.049	1.54E+03	0.8				
22	22-1	1.40E+06	3.30E+08	40.5	0.79	0.087	1.27E+04	0.92	1584.6	22468	800759.6	394606184
	22-2	5.20E+08	9.70E+08	92.2	0.73	1.3	3.07E+04	0.07				
	22-3	1.30E+09	3.50E+10	126	0.83	0.16	5.84E+05	0.58				
23	23-1	7.50E+04	2.90E+06	24.5	0.35	0.11	6.86	0.65	2577.8	6058.8	766380.8	4970112
	23-2	6.00E+06	2.10E+08	152	0.43	0.058	99.2	0.62				
	23-3	5.80E+08	3.80E+10	77.1	0.57	0.071	1.31E+03	0.83				
	24-1	2.40E+05	2.90E+06	31.1	0.18	0.3	0.776	0.23				
24	24-2	3.70E+06	2.30E+07	44.7	2.9	0.54	8.92E+17	0.92	2203.7	2380.8	2283.6	839348.4
	24-3	4.00E+07	1.10E+08	14.5	4	1.5	7.64E+28	0.88				
	24-4	1.10E+08	1.50E+08	118	9	2	2.37E+71	0.77				
	24-5	2.60E+08	7.40E+08	24.1	1.3	0.95	3.03E+08	0.77				
	24-6	1.10E+09	1.90E+09	217	3.8	0.86	9.54E+32	0.56				
	24-7	2.30E+09	4.00E+10	67.2	0.47	0.11	119	0.78				
	25-1	1.50E+05	2.50E+08	66.6	0.39	0.03	27	0.88				
25	25-2	3.80E+08	3.80E+10	60	0.44	0.054	52.7	0.84	778	37747.6	714179.6	351435732
	26-1	8.80E+05	1.10E+08	75.6	0.3	0.089	6.85	0.41				
26	26-2	1.70E+08	3.90E+10	101	0.54	0.048	777	0.86	1249.8	24478.4	800898.8	124977608
	27	2.30E+05	4.10E+10	94.5	0.4	0.025	44.3	0.85				
28		1.60E+05	3.60E+10	94.9	0.45	0.019	99.4	0.93	-	-	-	-
29	29-1	3.40E+05	8.00E+07	57.4	0.53	0.039	195	0.93	1503.2	15602.4	904894	88152924
	29-2	1.20E+08	4.00E+10	98.1	0.53	0.042	572	0.85				
30	30-1	1.60E+05	2.80E+08	30.1	0.64	0.11	471	0.84	1963.3	35612.4	1024731.6	556837444
	30-2	2.20E+09	4.00E+10	99.6	1	0.11	1.11E+08	0.77				
31	31-1	3.20E+05	2.10E+08	69.8	0.19	0.099	1.11	0.15	1823.1	33248	1021775.2	317295796
	31-2	3.40E+08	3.80E+10	107	1.3	0.2	2.20E+10	0.54				
32	32-1	4.40E+05	3.00E+08	85.5	0.55	0.061	402	0.76	1728.4	45514.4	1034918.8	2867998692
	32-2	4.10E+09	3.90E+10	103	1	0.16	4.05E+07	0.53				
33	33-1	4.70E+05	8.20E+07	2.07	1	0.27	7.61E+04	0.98	2070.7	19090	1127549.6	83508236
	33-2	1.40E+09	2.80E+09	37.9	1.5	2.2	2.92E+11	0.12				
	33-3	4.20E+09	3.80E+10	103	1	0.16	4.05E+07	0.53				

¹ Distance From Divide (DFD)

² Distance From Mouth (DFM)

Values with underline show in the Figs. 2.5A, B as major knickpoints.

Table 2.4: Results of morphometric analysis of the Arax River Basin

Channel No.	Seg.	A_min (km ²)	A_Max (km ²)	k _{sn} (m ^{0.9})	Theta	error (±2σ)	ks	R ²	Knickpoint elev. (m)	DFD ¹ (km)	DFM ² (km)	Upstream drainage area (km ²)
1	1-1	9.10E+04	3.00E+08	12.6	0.62	0.066	196	0.98				
	1-2	3.20E+08	1.10E+09	26.3	2.9	13	1.74E+23	0.15	2059	12590.4	861765.7	302057100
	1-3	1.20E+09	2.50E+09	35	5.9	5.1	3.98E+51	0.64	1902	41735.3	832620.8	1162633500
	1-4	2.80E+09	7.10E+09	45	1.7	0.68	6.20E+13	0.65	1708	89012.6	785343.5	2736180000
	1-5	9.70E+09	4.10E+10	61.4	1.7	0.36	1.68E+14	0.76	1445	200512.5	673843.6	7372547100
	1-6	6.60E+10	9.30E+10	154	1.7	1	3.39E+15	0.28	625	650534	223822.1	63394585200
2 (SE)	2-1	1.40E+05	4.50E+05	19.7	0.32	2.9	4.41	0.67				
	2-2	8.30E+05	4.30E+09	34	0.77	0.053	9.09E+03	0.95	1852	779.2	325815.9	607500
	2-3	4.80E+09	6.70E+09	142	6.8	4.1	1.64E+64	0.46	1237	122436.4	246070.9	4689000900
	2-4	7.30E+09	9.40E+10	174	0.52	0.096	946	0.6	893	137349.7	189245.4	6870687300
3	3-1	8.10E+04	1.20E+06	39.6	0.049	0.097	0.0531	0.093				
	3-2	3.60E+06	1.00E+07	73.6	1.9	0.23	3.18E+11	0.96	2274	2166.5	335289.5	1976400
	3-3	1.10E+07	3.10E+07	74.5	-1.1	0.41	7.11E-10	0.5	2022	5584.1	331871.9	10675800
	3-4	4.80E+07	4.60E+09	22.5	0.66	0.18	2.07E+03	0.71	1608	14772.3	322683.7	31444200
	3-5	4.80E+09	7.00E+09	119	1.8	2.2	1.16E+15	0.1	1237	122436.4	246070.9	4689000900
	3-6	7.30E+09	9.80E+10	174	0.52	0.096	946	0.6	887	85436.9	187994.3	6948180000
4	4-1	3.50E+05	1.00E+07	20.3	0.62	0.28	276	0.67				
	4-2	1.30E+07	2.00E+07	92	1.5	0.62	3.50E+09	0.7	2435	5357.9	341156.6	12870900
	4-3	2.10E+07	1.30E+08	273	0.61	0.13	4.57E+03	0.63	2254	9142	337372.5	20679300
	4-4	1.30E+08	4.60E+09	24.1	0.65	0.22	1.98E+03	0.61	1618	17234.8	329279.7	130685400
	4-5	4.70E+09	6.70E+09	137	3.9	2.9	5.24E+35	0.31	1237	122436.4	246070.9	4689000900
	4-6	7.30E+09	9.40E+10	174	0.51	0.096	772	0.6	887	85436.9	187994.3	6948180000
5	5-1	6.80E+04	3.70E+07	12.9	0.48	0.058	21.6	0.97				
	5-2	4.40E+07	4.30E+09	43.3	0.66	0.077	2.28E+03	0.88	1735	7403.6	357524.6	37349100
	5-3	4.80E+09	7.00E+09	117	2.1	2.4	4.70E+18	0.13	1236	118475.4	246452.8	4666782600
	5-4	1.10E+10	9.40E+10	175	0.53	0.11	1.18E+03	0.57	887	178244.2	187994.3	6948180000
6	6-1	1.50E+05	4.20E+09	52.2	0.51	0.035	127	0.9				
	6-2	4.80E+09	6.80E+09	121	3.8	2.8	1.82E+35	0.31	1236	119441.1	246797.4	4612156200
	6-3	7.40E+09	9.40E+10	174	0.51	0.098	776	0.59	887	178244.2	187994.3	6948180000
7	7-1	6.20E+04	5.70E+07	45.1	0.31	0.062	5.49	0.67				
	7-2	6.00E+07	1.40E+08	63.2	0.94	2.7	7.31E+05	0.54	1955	11405	357102.3	57963600
	7-3	1.90E+08	4.20E+09	52.7	0.72	0.18	1.26E+04	0.67	1751	19519.7	348987.6	148011300
	7-4	4.80E+09	6.80E+09	121	3.8	2.8	1.82E+35	0.31	1237	122436.4	246070.9	4689000900
	7-5	7.30E+09	9.30E+10	176	0.52	0.14	987	0.43	887	85436.9	187994.3	6948180000
8	8-1	6.70E+04	4.10E+06	37.9	0.16	0.08	0.74	0.4				
	8-2	6.00E+06	1.60E+07	71.1	2.1	0.31	1.08E+13	0.92	2062	3740.3	269690.9	4932900
	8-3	2.10E+07	6.80E+09	77.1	0.29	0.041	4.24	0.74	1723	9293.6	264137.6	17431200
	8-4	7.30E+09	9.40E+10	174	0.51	0.096	772	0.6	887	85436.9	187994.3	6948180000

Table 2.4: -Continued from previous page

Channel No.	Seg.	A_min (km ²)	A_Max (km ²)	k _{sn} (m ^{0.19})	Theta	error (±2σ)	ks	R ²	Knickpoint elev. (m)	DFD ¹ (km)	DFM ² (km)	Upstream drainage area (km ²)
9	9-1	6.70E+04	6.80E+06	83.5	0.44	0.048	71.8	0.85				
	9-2	8.80E+06	2.20E+07	139	0.54	0.32	689	0.2	3454	4668.7	373665.7	7136100
	9-3	2.30E+07	5.70E+07	171	1.4	0.3	5.42E+09	0.69	2845	11550.1	366784.3	21910500
	9-4	7.60E+07	4.20E+09	72.8	0.87	0.064	3.10E+05	0.92	2157	21464.8	356869.6	61057800
	9-5	4.70E+09	6.70E+09	137	3.9	2.9	5.24E+35	0.31	1236	118475.4	246452.8	4666782600
	9-6	7.40E+09	9.40E+10	174	0.51	0.098	776	0.59	887	178244.2	187994.3	6948180000
10	10-1	2.90E+05	5.80E+08	89	0.61	0.041	1.08E+03	0.88	1598	44788.8	264853.5	720632700
	10-2	7.50E+08	2.10E+09	67.2	1.3	0.62	2.64E+09	0.43	1196	101583.5	208058.8	2179750500
	10-3	2.30E+09	9.40E+10	170	0.52	0.065	837	0.71				
11		1.10E+05	9.80E+10	114	0.43	0.012	85.8	0.96	-	-	-	-
12	12-1	2.70E+05	4.00E+08	101	0.43	0.02	75.6	0.95	1239	24616.5	167960.6	425209500
	12-2	4.60E+08	1.10E+09	206	0.92	0.41	3.32E+06	0.26	481	62043.1	130534	1135215000
	12-3	1.20E+09	9.40E+10	148	0.46	0.055	196	0.91				
13	13-1	8.30E+04	1.00E+07	83.1	0.5	0.047	160	0.9	2123	5127.6	189912	15908400
	13-2	2.00E+07	2.80E+08	191	0.48	0.061	364	0.71	797	32200.1	162839.5	311161500
	13-3	3.20E+08	9.40E+10	170	0.51	0.035	770	0.93				
14		5.70E+04	9.40E+10	159	0.41	0.01	81.8	0.97	-	-	-	-
15	15-1	9.60E+04	6.00E+07	69.6	0.39	0.03	28.9	0.89	1061	36517.7	223512.4	370931400
	15-2	6.60E+10	9.60E+10	152	1.3	0.74	4.52E+11	0.28				
16	16-1	8.50E+04	1.00E+07	75.7	0.23	0.057	3.32	0.45	1954	8468.2	256586.5	23238900
	16-2	6.70E+07	5.80E+08	122	0.42	0.14	7.78E+01	0.42	876	48166.7	216888	622622700
	16-3	1.10E+09	9.40E+10	197	0.5	0.048	652	0.85				
17	17-1	7.30E+04	7.70E+06	141	0.3	0.053	16.7	0.62	2020	4690.6	240212	22226400
	17-2	2.50E+07	1.30E+08	167	1.1	0.13	8.54E+06	0.73	859	27239.5	217663.1	141223500
	17-3	2.10E+08	9.40E+10	201	0.46	0.061	259	0.77				
18	18-1	7.00E+04	2.00E+07	53.3	0.17	0.068	1.16	0.3	2471	8288.2	260910.6	23765400
	18-2	2.80E+07	6.50E+07	182	1.3	0.39	2.76E+08	0.55	1995	15437.2	253761.6	66922200
	18-3	7.50E+07	9.40E+10	217	0.5	0.029	679	0.87				
19	19-1	7.20E+04	3.10E+06	117	0.4	0.042	60.6	0.86	2243	2989.5	269071.5	5694300
	19-2	7.00E+06	9.40E+10	141	0.4	0.016	67.2	0.93				
20	20-1	2.20E+05	3.00E+08	21.1	0.38	0.056	7.89	0.86	1305	28095.7	295612.9	319561200
	20-2	3.40E+08	9.60E+10	149	0.41	0.036	78.6	0.82				
	20-3	7.60E+04	3.40E+05	25.9	0.23	0.53	2.03	0.27				
21	21-1	5.60E+05	4.70E+06	140	0.71	0.05	6.38E+03	0.92	2105	779.2	296490.3	469800
	21-2	5.40E+06	9.40E+10	112	0.29	0.028	3.69	0.8	1196	5777.1	291492.4	5224500
	21-3	1.10E+05	7.20E+07	78.8	0.27	0.061	3.95	0.43				
22	22-1	1.30E+08	7.00E+09	59.2	0.69	0.086	8.08E+03	0.82	1652	31982.8	430805	108645300
	22-2	9.20E+09	9.40E+10	197	0.71	0.24	1.36E+05	0.33	891	153438.8	309349	9144689400
	22-3	8.00E+04	2.00E+07	115	0.27	0.036	9.08	0.74				
23	23-1	2.80E+07	6.90E+09	66.3	0.69	0.059	6.37E+03	0.88	1844	6639.8	401071.5	24389100
	23-2	9.20E+09	9.30E+10	201	0.61	0.2	1.19E+04	0.35	891	153438.8	309349	9144689400
	23-3	9.20E+09	9.30E+10	201	0.61	0.2	1.19E+04	0.35				

Table 2.4: -Continued from previous page

Channel No.	Seg.	A_min (km ²)	A_Max (km ²)	k _{sn} (m ^{0.9})	Theta	error (±σ)	ks	R ²	Knickpoint elev. (m)	DFD ¹ (km)	DFM ² (km)	Upstream drainage area (km ²)
24	24-1	1.70E+05	6.80E+09	91.3	0.48	0.027	139	0.89				
	24-2	9.20E+09	9.30E+10	201	0.61	0.2	1.19E+04	0.35	902	94861.9	311447.4	9137043000
25	25-1	8.00E+04	3.70E+07	22	0.17	0.063	0.38	0.57	1346	10184.7	401583.1	39819600
	25-2	4.90E+07	7.10E+09	36.7	0.31	0.078	2.94	0.68	898	100627.7	311140.1	9137229300
	25-3	9.20E+09	9.80E+10	196	0.63	0.19	1.76E+04	0.36				
26	26-1	8.30E+04	5.70E+07	32.9	0.51	0.047	86.8	0.95	2415	11277.7	481901.3	57145500
	26-2	7.10E+07	1.00E+09	58.3	0.2	0.15	0.452	0.15	1761	75823	417356	1364809500
	26-3	1.60E+09	7.00E+09	87.7	1.2	0.3	1.11E+09	0.65	898	100627.7	311140.1	9137229300
	26-4	9.20E+09	9.10E+10	204	0.6	0.2	8.25E+03	0.33				
27	27-1	9.30E+04	2.20E+08	36.6	0.42	0.062	24.3	0.8	2152	29316	431684.8	270207900
	27-2	5.80E+08	6.80E+09	110	0.95	0.16	3.52E+06	0.67	898	100627.7	311140.1	9137229300
	27-3	9.30E+09	9.40E+10	198	1.1	0.51	1.51E+09	0.21				
28	28-1	1.10E+05	8.80E+07	27.1	0.41	0.083	14.6	0.79	2176	24103.2	414329.9	134865000
	28-2	1.40E+08	9.40E+08	84.4	0.59	0.25	1.40E+03	0.47	1584	58812	379621.1	956107800
	28-3	1.20E+09	9.40E+09	110	0.072	0.12	0.0376	0.025	662	198714.9	239718.2	62666176500
	28-4	6.50E+10	9.40E+10	172	2.7	1.1	6.67E+26	0.36				
29	29-1	7.90E+04	6.80E+06	44.3	0.25	0.06	2.99	0.75	2122	3746.8	402522.8	9177300
	29-2	1.30E+07	8.00E+07	64	0.56	0.16	446	0.62	1569	25775.2	380494.4	173234700
	29-3	2.30E+08	5.00E+10	94.5	0.69	0.058	1.18E+04	0.9	687	153221.5	253048.1	61903909800
	29-4	6.60E+10	9.60E+10	152	1.3	0.74	4.52E+11	0.28				
30	30-1	5.40E+05	1.00E+08	21.2	0.37	0.094	6.84	0.75	1744, 1254	25336.5	405013.7	158136300
	30-2	1.70E+08	6.10E+10	71.4	0.45	0.081	101	0.73	633	204308.9	226041.3	62979857100
	30-3	6.50E+10	9.40E+10	162	2.2	0.92	9.74E+20	0.36				
31	31-1	6.70E+04	1.50E+08	34.9	0.2	0.049	0.719	0.52	1267	51992.2	420034.1	1560027600
	31-2	4.50E+09	6.20E+10	78.8	0.51	0.22	480	0.45	604	254505.9	217520.4	63479481300
	31-3	6.60E+10	9.40E+10	152	1.3	0.74	4.52E+11	0.28				
32	32-1	6.90E+04	1.20E+07	51.5	0.34	0.047	11.2	0.87	1138	55183.6	410066.7	1609834500
	32-2	4.50E+09	6.20E+10	78.8	0.51	0.22	4.80E+02	0.45	628	242297.4	222952.9	63432209700
	32-3	6.60E+10	9.60E+10	152	1.3	0.74	4.52E+11	0.28				
33	33-1	6.90E+04	7.70E+06	14.3	0.3	0.17	2.23	0.55	2452	7989.8	464688.4	11826000
	33-2	1.30E+07	5.50E+07	176	1.4	0.4	2.79E+09	0.85	2130	12254.7	460423.5	55914300
	33-3	5.70E+07	2.80E+08	57.5	1.5	0.57	1.69E+10	0.69	1834	26693	445985.2	320055300
	33-4	3.80E+08	4.80E+08	101	3.7	2.1	1.71E+30	0.45	1296	51452.2	421226	518918400
	33-5	1.70E+09	6.30E+10	83.8	0.47	0.17	197	0.47	628	242297.4	222952.9	63432209700
	33-6	6.50E+10	9.40E+10	166	2.5	1.1	6.05E+24	0.35				
34	34-1	3.60E+06	5.50E+07	50.3	0.43	0.079	36.9	0.8	1922	15474.5	520034.2	59535000
	34-2	6.60E+07	2.00E+09	57.6	0.38	0.29	17.3	0.19	1313	119087.6	416421.1	2520501300
	34-3	2.70E+09	5.00E+10	116	1	0.22	5.65E+07	0.71	635	309954.7	225554	62984166300
	34-4	6.60E+10	9.30E+10	154	1.7	1	3.39E+15	0.28				

Table 2.4: -Continued from previous page

Channel No.	Seg.	A_min (km ²)	A_Max (km ²)	k _{sn} (m ^{0.9})	Theta	error (±2σ)	ks	R ²	Knickpoint elev. (m)	DFD ¹ (km)	DFM ² (km)	Upstream drainage area (km ²)
35	35-1	1.10E+05	3.20E+06	14.3	-	0.077	0.0109	0.098				
	35-2	6.00E+06	1.20E+08	5.01	1.6	0.53	3.13E+09	0.97	2383	2772.2	565421.5	4090500
	35-3	1.50E+08	4.80E+08	92.7	3.7	0.5	1.09E+29	0.85	2204	17430.2	550763.5	123549300
	35-4	8.70E+08	2.00E+09	39.1	1.7	1.6	2.30E+13	0.31	1693	61044.2	507149.5	766835100
	35-5	2.50E+09	6.30E+10	102	0.65	0.15	1.41E+04	0.61	1290	153728.3	414465.4	2529751500
	35-6	6.50E+10	9.60E+10	171	2.6	1	2.31E+25	0.35	601	350763.3	217430.4	63479554200
36	36-1	8.10E+04	5.10E+10	49.7	0.47	0.04	79.4	0.84				
	36-2	6.50E+10	9.40E+10	159	2	0.94	3.41E+19	0.34	597	304584.8	216905.8	63481239000
37	37-1	7.40E+04	4.40E+06	87.2	-	0.066	0.0796	0.03				
	37-2	5.60E+06	4.60E+07	136	1.3	0.15	1.23E+08	0.8	2474	5588.2	538422.2	5329800
	37-3	9.40E+07	5.00E+10	35.2	0.85	0.1	2.62E+05	0.87	1529	17526.7	526483.7	75888900
	37-4	6.60E+10	9.40E+10	155	1.6	0.77	2.05E+14	0.32	640	312077.7	231932.7	62822976300
38	38-1	5.70E+04	1.20E+07	64.5	0.26	0.031	4.11	0.84				
	38-2	1.50E+07	4.10E+07	141	0.7	0.14	9.88E+03	0.58	2039	8797.4	558200.6	13154400
	38-3	1.90E+08	6.20E+10	16.2	0.39	0.15	11.4	0.48	1182	21611.6	545386.4	54553500
	38-4	6.50E+10	9.40E+10	159	2	0.94	3.41E+19	0.34	611	346810.8	220187.2	63465557400
39	39-1	1.20E+05	6.60E+06	13.3	-	0.095	0.00793	0.053				
	39-2	8.80E+06	6.40E+07	17.3	1.7	0.64	3.15E+10	0.85	2406	3402.2	597564.1	6941700
	39-3	9.10E+07	1.20E+08	60.4	7.7	3.9	6.20E+59	0.84	2169	13468.5	587497.8	72308700
	39-4	2.50E+08	4.90E+10	111	0.81	0.07	2.46E+05	0.89	1936	24078.9	576887.4	124448400
	39-5	6.60E+10	9.40E+10	148	0.85	0.74	3.29E+06	0.17	659	362297.3	238669	62668347300
40	40-1	7.50E+04	1.40E+07	40.7	0.44	0.065	37.4	0.9				
	40-2	2.20E+07	6.60E+07	80.7	3.5	0.89	7.18E+24	0.91	2198	6475.2	605395.8	20590200
	40-3	6.80E+07	1.20E+08	112	3.8	0.79	8.40E+28	0.91	1966	12978.8	598892.2	66492900
	40-4	1.30E+08	5.10E+10	119	0.8	0.058	2.94E+05	0.89	1751	19866.7	592004.3	131414400
	40-4	6.50E+10	9.40E+10	162	2.3	0.98	2.01E+22	0.37	636	383250.5	228620.5	62893891800
41	41-1	7.10E+04	1.40E+07	32.2	0.49	0.12	74.1	0.69				
	41-2	7.00E+07	5.00E+10	97.7	0.66	0.058	1.08E+04	0.88	1729	21787.5	609458.8	62216100
	41-3	6.50E+10	9.40E+10	162	2.2	0.92	9.74E+20	0.36	672	388845.9	242400.4	62592012900
42	42-1	5.50E+04	1.20E+06	17.7	-0.01	0.23	0.0661	0.0026				
	42-2	4.40E+06	5.00E+10	134	0.55	0.024	987	0.93	2633	2930.3	634512.3	3839400
	42-3	6.50E+10	9.40E+10	162	2.3	0.98	2.01E+22	0.37	669	396293.3	241149.3	62645424300
43	43-1	9.00E+04	1.10E+07	79.8	-	0.003	0.0698	6.20E-05				
	43-2	2.50E+07	5.30E+10	103	0.48	0.04	202	0.82	2274	7127.1	2274	13389300
	43-3	6.60E+10	9.40E+10	154	1.5	0.8	1.14E+14	0.31	646	454442.1	234285.7	62814730500
44	44-1	1.80E+05	7.00E+07	39	0.42	0.072	28.7	0.81				
	44-2	9.20E+07	7.10E+09	89	0.73	0.16	2.01E+04	0.66	2037	12050.4	742480.3	72657000
	44-3	7.60E+09	5.00E+10	90.3	1.4	0.21	8.86E+11	0.74	1474	66305.6	688225.1	7160521500
	44-4	6.60E+10	9.60E+10	152	1.3	0.74	4.52E+11	0.28	673	510497.3	244033.4	62470820700

Table 2.4: -Continued from previous page

Channel No.	Seg.	A_min (km ²)	A_Max (km ²)	k _{sn} (m ^{0.9})	Theta	error (±2σ)	ks	R ²	Knickpoint elev. (m)	DFD ¹ (km)	DFM ² (km)	Upstream drainage area (km ²)
45	45-1	8.40E+04	7.30E+07	36	0.63	0.063	463	0.89	2209	19474.2	798809.6	77371200
	45-2	1.10E+08	7.10E+09	62.7	0.75	0.092	2.60E+04	0.85	1476	129804.1	688479.7	7158520800
	45-3	7.60E+09	5.10E+10	84.3	1.2	0.26	1.98E+09	0.56	655	581548.6	236735.2	62774967600
	45-4	6.50E+10	9.40E+10	158	1.9	0.89	2.10E+18	0.34				
	46-1	7.00E+04	1.70E+08	39.9	0.59	0.072	397	0.82	2074	37097.4	815772.7	207821700
46	46-2	2.20E+08	7.10E+09	68.4	0.82	0.25	2.56E+05	0.54	1439	180743	672127.1	7375973400
	46-3	8.20E+09	5.00E+10	87.9	1.5	0.23	1.82E+12	0.75	673	608964	243906.1	62471063700
	46-4	6.60E+10	9.40E+10	157	1.8	0.84	2.90E+16	0.33				
47	47-1	2.00E+05	8.30E+06	5.52	0.31	2.4	1.2	0.13	2244	5296.3	837505.1	8764200
	47-2	1.20E+07	1.10E+08	27.4	1.4	0.32	2.98E+08	0.87	1916	28956	813845.4	283022100
	47-3	2.80E+09	6.90E+09	41.5	1.6	0.37	4.40E+12	0.89	1744	52038.4	790763	2686243500
	47-4	7.80E+09	5.00E+10	88.8	1.4	0.24	1.03E+12	0.73	655	606066.2	236735.2	62774967600
	47-5	6.50E+10	9.40E+10	160	2.2	0.99	3.21E+21	0.35				
48	48-1	8.40E+04	2.20E+09	64.9	0.59	0.037	588	0.91	1758	42659.6	792988.7	2658622500
	48-2	2.70E+09	7.10E+09	42.9	1.5	0.6	3.98E+11	0.62	1438	159181.7	676466.6	7365119400
	48-3	7.80E+09	5.30E+10	80.5	1.1	0.27	9.69E+08	0.54	627	611158.9	224489.4	63393208200
	48-4	6.50E+10	9.40E+10	159	2	0.94	3.415+19	0.34				
49	49-1	1.20E+05	9.50E+07	47.8	0.6	0.092	398	0.79	2008	16980.2	838099.5	134929800
	49-2	1.50E+08	2.00E+09	52	0.76	0.48	4.25E+04	0.53	1758	62091	792988.7	2658622500
	49-3	2.80E+09	7.00E+09	45	1.7	0.68	6.20E+13	0.65	1473	170917.6	684162.1	7180091100
	49-4	8.20E+09	5.20E+10	77	1.2	0.28	2.41E+09	0.56	646	620794	234285.7	62814730500
	49-5	6.50E+10	9.40E+10	166	2.5	1.1	6.05E+24	0.35				
50	50-1	9.70E+04	1.40E+07	37.4	0.24	0.12	1.81	0.33	2336	9532.8	873337.7	17390700
	50-2	1.80E+07	1.10E+09	49.4	0.77	0.1	1.85E+04	0.87	1901	50377	832493.5	1165152600
	50-3	1.20E+09	2.00E+09	35	5.9	5.1	3.98E+51	0.64	1757	90496.4	792374.1	2683351800
	50-4	2.80E+09	6.90E+09	40	1.5	0.41	9.60E+11	0.88	1475	196991.9	685878.6	7175530800
	50-5	7.70E+09	5.00E+10	86.5	1.4	0.22	5.22E+11	0.73	667	642155.8	240714.7	62645643000
	50-6	6.50E+10	9.40E+10	166	2.5	1.1	6.05E+24	0.35				
51	51-1	1.70E+05	1.40E+07	34.4	0.36	0.067	10.4	0.81	2481	10355.8	887115.9	17147700
	51-2	2.50E+07	3.00E+08	49	1.6	0.32	2.38E+10	0.78	2055	36103.3	861368.4	302275800
	51-3	3.10E+08	1.20E+09	33.4	2.7	1.1	7.73E+20	0.79	1901	50377	832493.5	1165152600
	51-4	1.20E+09	2.00E+09	35	5.9	5.1	3.98E+51	0.64	1751	105622.2	791849.5	2683594800
	51-5	2.80E+09	7.20E+09	43.1	1.1	0.71	4.43E+07	0.34	1445	221365.1	676106.6	7366156200
	51-5	7.60E+09	5.10E+10	84.3	1.2	0.26	1.98E+09	0.56	662	657536.2	239935.5	62649433800
52 (NW)	52-1	6.50E+10	9.40E+10	159	2	0.94	3.41E+19	0.34				
	52-1	7.60E+04	1.10E+09	79.9	0.31	0.051	8.01	0.58	1901	48855.9	832493.5	1165152600
	52-2	1.20E+09	2.00E+09	35	5.9	5.1	3.98E+51	0.64	1756	88233.4	793116	2658492900
	52-3	2.70E+09	6.80E+09	51.6	2.3	0.98	4.59E+19	0.59	1496	186671	694678.4	7132155300
	52-4	7.70E+09	5.10E+10	80.5	1.1	0.27	9.69E+08	0.54	642	648727.5	232621.9	62822239200
52-5	6.60E+10	9.40E+10	152	1.3	0.83	3.15E+11	0.25					

Table 2.4: -Continued from previous page

Channel No.	Seg.	A_min (km ²)	A_Max (km ²)	k _{sn} (m ^{0.19})	Theta	error (±2σ)	ks	R ²	Knickpoint elev. (m)	DFD ¹ (km)	DFM ² (km)	Upstream drainage area (km ²)
53	53-1	6.50E+04	6.60E+09	66	0.51	0.03	187	0.89				
	53-2	7.70E+09	5.00E+10	86.5	1.4	0.22	5.22E+11	0.73	1471	144896	685046.7	7178414400
	53-3	6.60E+10	9.40E+10	155	1.7	0.81	2.23E+15	0.33	659	591618.3	238324.4	62670032100
<u>54</u>	54-1	3.00E+05	2.10E+07	62.6	0.29	0.11	5.99	0.34	2155	9960.9	762415.1	31776300
	54-2	4.20E+07	6.80E+09	66.8	0.65	0.084	3.02E+03	0.83	1467	88881.2	683494.8	7213835700
	54-3	7.90E+09	5.00E+10	88.8	1.4	0.24	1.03E+12	0.73	687	522519.3	249856.7	61930615500
	54-4	6.60E+10	9.40E+10	157	1.9	0.89	3.93E+17	0.33				
55	55-1	1.00E+05	4.50E+07	44.8	0.53	0.068	133	0.83	2142	17957.2	754131	58279500
	55-2	6.20E+07	7.10E+09	72.8	0.61	0.17	2.40E+03	0.53	1479	89282.6	682805.6	7214491800
	55-3	7.70E+09	5.00E+10	86.5	1.4	0.22	5.22E+11	0.73	669	530811.6	241276.6	62645383800
	55-4	6.60E+10	9.40E+10	157	1.9	0.89	3.93E+17	0.33				
<u>56</u>	56-1	9.10E+04	8.80E+07	65.2	0.38	0.037	21.4	0.84	1804	19592.6	640300	125177400
	56-2	1.40E+08	6.00E+10	87.4	0.57	0.061	1.44E+03	0.81	646	425606.9	234285.7	62814730500
	56-3	6.50E+10	9.40E+10	166	2.5	1.1	6.05E+24	0.35				
<u>57</u>	57-1	8.70E+04	1.00E+08	57.4	0.23	0.07	1.92	0.42	2043	20990.5	812531.3	109674000
	57-2	1.80E+08	1.90E+09	32.8	0.41	0.41	18	0.26	1745	83948.3	749573.5	2231695800
	57-3	2.50E+09	7.80E+09	65.9	0.49	1.4	199	0.019	1262	241221.5	592300.3	8817724800
	57-4	9.50E+09	5.00E+10	76.9	2.5	0.28	2.96E+23	0.89	660	594365.5	239156.3	62667634500
	57-5	6.50E+10	9.40E+10	166	2.5	1.1	6.05E+24	0.35				
58	58-1	1.30E+05	2.10E+09	42.8	0.52	0.052	168	0.87	1753	80269.6	746388.6	2480973300
	58-2	3.00E+09	8.00E+09	65.9	0.83	2.2	4.56E+05	0.035	1416	195557.7	631100.5	8082431100
	58-3	9.40E+09	5.70E+10	70.1	2.1	0.38	2.22E+19	0.73	651	590776.8	235881.4	62782055100
	58-4	6.60E+10	9.40E+10	155	1.7	0.81	2.23E+15	0.33				
<u>59</u>	59-1	1.40E+05	1.20E+07	41.2	0.48	0.074	59.5	0.8	2108	7245.5	751252.7	12611700
	59-2	2.60E+07	1.30E+08	45.4	0.44	0.37	47.2	0.32	1914, 2100	19423.2	739075	135650700
	59-3	2.10E+08	7.70E+09	56.6	0.37	0.2	17.2	0.28	1225	174964.5	583533.7	8851752900
	59-4	9.40E+09	5.00E+10	76.9	2.5	0.28	2.96E+23	0.89	654	522272.2	236226	62777583900
	59-5	6.60E+10	9.60E+10	152	1.3	0.74	4.52E+11	0.28				
<u>60</u>	60-1	8.90E+04	8.20E+06	39.2	0.34	0.19	8.94	0.49	2552	5357.9	747267.4	17763300
	60-2	3.50E+07	4.70E+08	158	3.6	0.42	3.33E+26	0.93	1967	30875.1	721750.2	473598900
	60-3	4.90E+08	7.90E+08	165	5	1.4	3.38E+41	0.72	1649	53231	699394.3	848564100
	60-4	4.90E+09	8.10E+09	38.8	0.26	3.3	1.01	0.005	1391	170941.9	581683.4	8853713100
	60-5	9.50E+09	5.00E+10	76.9	2.5	0.28	2.96E+23	0.89	630	530774.3	221851	63436235400
	60-6	6.60E+10	9.40E+10	159	2.1	1	2.27E+20	0.34				
<u>61</u>	61-1	1.00E+05	4.70E+07	60.2	0.31	0.058	8.01	0.69	2191	11675	736733.3	49669200
	61-2	5.50E+07	7.20E+08	17.8	0.88	0.76	1.96E+05	0.48	1694	60980.9	687427.4	911517300
	61-3	9.60E+08	7.70E+09	22.5	0.54	0.42	190	0.85	1422, 1212	125767.1	622641.2	8307449100
	61-4	9.40E+09	5.00E+10	76.9	2.5	0.28	2.96E+23	0.89	642	515786.4	232621.9	62822239200
	61-5	6.50E+10	9.40E+10	162	2.3	0.98	2.01E+22	0.37				

Table 2.4: -Continued from previous page

Channel No.	Seg.	A_min (km ²)	A_Max (km ²)	k _{sn} (m ^{0.9})	Theta	error (±2σ)	ks	R ²	Knickpoint elev. (m)	DFD ¹ (km)	DFM ² (km)	Upstream drainage area (km ²)
62	62-1	7.30E+04	1.10E+07	74.4	0.38	0.047	27.6	0.87				
	62-2	2.30E+07	7.20E+08	44.3	0.56	0.12	346	0.74	2390	5349	733543.6	12482100
	62-3	9.30E+08	7.80E+09	67.4	2	0.93	7.89E+15	0.51	1701	51195.2	687697.4	911395800
	62-4	9.50E+09	5.00E+10	76.9	2.5	0.28	2.96E+23	0.89	1402	114115.7	624776.9	8298531000
	62-5	6.50E+10	9.40E+10	162	2.3	0.98	2.01E+22	0.37	673	494859.2	244033.4	62470820700
63	63-1	5.50E+05	2.60E+07	140	0.23	0.13	4.03	0.18				
	63-2	3.20E+07	8.10E+09	104	0.66	0.046	5.50E+03	0.89	2576	9368.2	706993.3	28422900
	63-3	9.40E+09	5.00E+10	76.9	2.5	0.28	2.96E+23	0.89	1391	94769.5	621592	8308332000
	63-4	6.50E+10	9.40E+10	164	2.5	1.1	1.09E+25	0.35	659	478037.1	238324.4	62670032100
64	64-1	1.10E+05	1.10E+06	17.9	0.39	0.31	8.09	0.62				
	64-2	1.30E+06	3.5E+06	57.8	0.13	0.38	5.78E+01	0.071	3138	2188.4	609570	1158300
	64-3	9.10E+06	4.10E+07	141	1	0.17	2.09E+06	0.64	2964	4565.7	607192.7	3766500
	64-4	4.90E+07	1.10E+08	60.1	0.73	0.8	9.45E+03	0.13	1828	19436.9	592321.5	44914500
	64-5	1.30E+08	3.10E+08	75.5	1.9	0.7	7.75E+13	0.65	1458	40095.8	571662.6	117409500
	64-6	4.10E+08	6.00E+08	96.7	3.1	8.4	1.68E+25	0.074	1165	58221.7	553536.7	324648000
	64-7	7.50E+08	6.30E+10	24.9	0.24	0.25	0.302	0.17	954	72212.4	539546	683785800
	64-8	6.50E+10	9.40E+10	166	2.5	1.1	6.05E+24	0.35	631	386909	224849.4	63392301000
65	65-1	7.20E+04	5.20E+06	81.5	0.22	0.063	3.32	0.51				
	65-2	8.40E+06	4.10E+07	121	0.85	0.15	1.27E+05	0.67	3094	3454.9	541114	5929200
	65-3	4.60E+07	5.00E+10	144	0.87	0.048	5.69E+05	0.92	2118	17243.7	527325.2	43359300
	65-4	6.50E+10	9.40E+10	165	2.4	1	2.38E+23	0.35	674	301771.2	242797.7	62591664600
66	66-1	1.10E+05	2.80E+08	15.7	0.39	0.096	7.4	0.75				
	66-2	3.40E+08	7.30E+08	58.2	0.85	1.3	2.50E+05	0.074	2038	27074.9	570790	288457200
	66-3	8.60E+08	1.00E+09	381	7.4	2.1	1.00E+65	0.49	1712	64036.1	533828.8	845226900
	66-4	1.40E+09	6.30E+10	32.2	0.41	0.21	27.8	0.39	1002	88393.9	509471	1059820200
	66-5	6.50E+10	9.40E+10	160	2.2	0.99	3.21E+21	0.35	611	377677.7	220187.2	63465557400
67	67-1	1.30E+05	4.10E+08	63.3	0.47	0.031	92.4	0.91				
	67-2	5.70E+09	5.30E+10	138	1.5	0.29	1.52E+13	0.61	1683	49577.6	555420.2	5630569200
	67-3	6.50E+10	9.40E+10	166	2.5	1.1	6.05E+24	0.35	662	365062.3	239935.5	62649433800
68	68-1	7.50E+04	2.90E+08	63	0.58	0.02	460	0.98				
	68-2	5.70E+09	6.20E+10	121	1.2	0.21	1.40E+10	0.61	1912	112576.8	581790.5	4880055600
	68-3	6.50E+10	9.40E+10	159	2.1	1	2.27E+20	0.34	598	478908	215459.3	63484859700
69	69-1	1.10E+05	1.20E+07	47.9	-0.044	0.08	0.0385	0.034				
	69-2	1.90E+07	5.20E+07	198	0.68	0.25	1.08E+04	0.32	2835	6369.8	520794.2	17074800
	69-3	6.60E+07	5.10E+10	103	0.65	0.077	6.74E+03	0.75	1876	17151.3	510012.7	53443800
	69-4	6.50E+10	9.40E+10	166	2.5	1.1	6.05E+24	0.35	633	298978.1	228185.9	62894507400
70	70-1	1.40E+05	6.50E+06	30.1	0.54	0.15	1.57E+02	0.65				
	70-2	1.40E+07	5.10E+10	129	0.67	0.044	9.37E+03	0.88	2460	6369.8	484573.9	7452000
	70-3	6.50E+10	9.40E+10	164	2.5	1.1	1.09E+25	0.35	637	261289.4	229654.3	62840844900

Table 2.4: -Continued from previous page

Channel No.	Seg.	A_min (km ²)	A_Max (km ²)	k _{sn} (m ^{0.9})	Theta	error (±2σ)	ks	R ²	Knickpoint elev. (m)	DFD ¹ (km)	DFM ² (km)	Upstream drainage area (km ²)
71	71-1	7.10E+04	5.10E+10	118	0.42	0.036	72.4	0.76				
	71-2	6.50E+10	9.40E+10	166	2.5	1.1	6.05E+24	0.35	639	212506.4	231265.4	62837912700
<u>72</u>	72-1	9.70E+04	9.50E+05	34.1	0.2	0.2	1.46	0.43				
	72-2	3.00E+06	1.00E+07	58.1	1.5	0.17	4.70E+08	0.95	3079	1828.4	495127.5	1935900
	72-3	4.00E+07	2.60E+08	122	0.92	0.55	1.03E+06	0.25	2704	8990.4	487965.5	14717700
	72-4	3.30E+08	9.50E+08	131	1.2	0.6	1.38E+09	0.31	<u>1915</u>	30406.6	466549.3	327701700
	72-5	1.80E+09	5.10E+10	64.4	0.68	0.35	1.67E+04	0.36	<u>1190</u>	59437.2	437518.7	1007931600
	72-6	6.60E+10	9.40E+10	159	2	0.94	3.41E+19	0.34	679	249414.9	247541	62439060600
	73-1	2.40E+05	3.10E+07	87.6	0.22	0.046	2.75	0.55				
73	73-2	5.30E+07	5.30E+10	116	0.56	0.06	1.07E+03	0.74	2087	10191.2	380139.2	32643000
	73-3	6.50E+10	9.40E+10	171	2.6	1	2.31E+25	0.35	685	137806.9	252523.5	61907895000
	74-1	7.10E+04	5.80E+10	133	0.43	0.014	100	0.94				
74	74-2	6.40E+10	9.30E+10	189	3.7	1.3	2.52E+37	0.4	673	94374.6	241621.2	62595682200
75	75-1	2.20E+05	5.90E+10	141	0.37	0.018	36.8	0.88				
	75-2	6.50E+10	9.40E+10	171	2.6	1	2.31E+25	0.35	637	74760.8	230920.8	62838317700
76	76-1	5.70E+04	2.90E+06	76.2	0.33	0.038	17	0.9				
	76-2	4.60E+06	9.10E+10	243	0.47	0.014	347	0.94	3123	2263	229544.8	3418200
<u>77</u>	77-1	2.30E+05	1.10E+07	83.6	0.4	0.069	43.5	0.68				
	77-2	2.20E+07	5.80E+08	208	0.64	0.054	6.71E+03	0.82	2620	7118.2	216708.7	19342800
	77-3	6.40E+08	9.40E+10	132	0.44	0.031	130	0.91	<u>1141</u>	36300.4	187526.5	606309300
78	78-1	8.30E+04	2.40E+06	16.1	0.54	0.15	55.9	0.88				
	78-2	6.60E+06	5.00E+08	109	0.62	0.091	2.46E+03	0.67	3061	3364.9	290559.9	5143500
	78-3	5.20E+08	8.20E+08	129	1.4	1.9	1.93E+10	0.089	2028	38325.9	255598.9	509676300
	78-4	1.90E+09	9.80E+10	140	0.54	0.071	1.30E+03	0.72	1313	84143.7	209781.1	1749203100
<u>79</u>	79-1	8.10E+04	5.70E+07	52.6	0.37	0.031	17.1	0.93				
	79-2	8.80E+07	3.10E+08	158	1.3	0.67	9.16E+08	0.28	2711	13817.2	247494.8	77241600
	79-3	3.30E+08	9.60E+10	160	0.66	0.059	1.68E+04	0.72	<u>2031</u>	28347.9	232964.1	316831500
80	80-1	1.10E+05	7.40E+07	68.5	0.32	0.039	8.54	0.83				
	80-2	1.80E+08	9.30E+10	137	0.46	0.038	199	0.84	1496	17675.9	221247.7	105308100
81		9.30E+04	9.60E+10	107	0.39	0.013	34.7	0.95	-	-	-	-
82	82-1	8.10E+04	5.90E+07	104	0.3	0.02	9.82	0.9				
	82-2	8.20E+07	9.00E+10	88.7	1.3	0.094	2.83E+09	0.9	1124	12671.5	93949.6	77784300
<u>83</u>	83-1	7.20E+04	1.50E+07	61.2	0.52	0.073	178	0.78				
	83-2	2.10E+07	1.10E+08	82.5	0.49	0.48	205	0.17	<u>1069</u>	8555.8	101311.1	19221300
	83-3	1.30E+08	9.60E+10	56.5	0.36	0.066	10.4	0.66	<u>790</u>	19374.6	90492.3	124424100

^{1,2} As explained in Table 2.3

Values with underline show in the Figs. 2.5A, C as major knickpoints.

Table 2.5: Results of morphometric analysis of the Qezel-Owzan River Basin

Channel No.	Seg.	A_min (km ²)	A_Max (km ²)	K _{sn} (m ^{0.9})	Theta	error (±2σ)	ks	R ²	Knickpoint elev. (m)	DFD ¹ (km)	DFM ² (km)	Upstream drainage area (km ²)
<u>1</u>	1-1	5.30E+05	6.40E+09	40.3	0.57	0.04	409	0.9				
	1-2	7.30E+09	2.40E+10	49.7	0.59	0.68	1.62E+03	0.23	1605	105675	663333	6504268770
	1-3	2.80E+10	4.50E+10	93.5	0.54	0.83	786	0.12	1308	279099	489909	23185905768
	1-4	4.80E+10	5.40E+10	222	3.50	2.20	3.76E+34	0.16	961.1	437154	331854	42100147989
	1-5	6.00E+10	6.20E+10	165	15.00	13.00	1.23E+158	0.23	250 (Dam)	676953	119307	56201202558
2	2-1	2.20E+05	1.80E+10	31	0.27	0.03	1.13	0.81				
	2-2	2.20E+10	4.20E+10	111	0.15	0.60	0.0898	0.01	1388.302	195840	540156	21973382244
	2-3	4.40E+10	5.00E+10	223	3.60	2.10	6.87E+35	0.17	924.0438	413991	322005	42205977747
	2-4	5.60E+10	5.80E+10	166	15.00	13.00	4.47E+157	0.23	250	616566	119430	56201142006
<u>3</u>	3-1	2.80E+05	7.50E+07	11.6	0.20	0.09	0.287	0.71				
	3-2	3.40E+08	1.80E+10	61.2	0.49	0.07	157	0.85	1930.052	17475	688923	137112435
	3-3	2.20E+10	4.20E+10	111	0.15	0.60	0.0898	0.01	1390.445	164019	542379	21956094648
	3-4	4.40E+10	5.00E+10	223	3.60	2.10	6.87E+35	0.17	944.0952	383517	322881	42203775168
	3-5	5.60E+10	5.80E+10	166	15.00	13.00	4.47E+157	0.23	214.9095	587460	118938	56203511103
4	4-1	1.70E+05	8.70E+08	12.3	0.26	0.03	0.595	0.93				
	4-2	1.10E+09	2.30E+10	82.8	0.50	0.12	265	0.73	1673.725	48708	596631	1019529162
	4-3	2.50E+10	4.20E+10	96	0.91	0.83	7.94E+06	0.23	1307.074	155220	490119	23185383507
	4-4	4.40E+10	5.00E+10	223	3.60	2.10	6.87E+35	0.17	953.8755	317526	327813	42170176377
	4-5	5.60E+10	5.80E+10	166	15.00	13.00	4.47E+157	0.23	250	525786	119553	56201020902
<u>5</u>	5-1	4.80E+04	3.00E+06	45.2	0.37	0.06	15.6	0.88				
	5-2	3.20E+06	6.20E+08	20.8	0.74	0.09	3.55E+03	0.93	2014.098	2586	567723	3073014
	5-3	1.00E+09	4.20E+10	93.7	0.30	0.05	3.34	0.63	1728.651	40698	529611	767322513
	5-4	4.40E+10	5.00E+10	223	5.00	2.50	8.70E+50	0.22	930.4586	248391	321918	42206333490
	5-5	5.60E+10	5.80E+10	166	15.00	13.00	4.47E+157	0.23	250	450879	119430	56201142006
<u>6</u>	6-1	5.00E+05	3.40E+06	69.3	1.10	0.18	3.73E+05	0.89				
	6-2	6.60E+06	2.60E+07	199	1.30	0.21	1.82E+08	0.74	3230.455	3027	347163	6138459
	6-3	3.10E+07	1.10E+09	102	0.35	0.09	16.3	0.38	2577.47	8859	341331	28285353
	6-4	1.20E+09	5.70E+09	137	1.00	0.18	3.22E+07	0.54	1454.181	85485	264705	1181097036
	6-5	5.60E+10	5.80E+10	166	15.00	13.00	4.47E+157	0.23	250	230760	119430	56201142006
<u>7</u>	7-1	9.20E+04	1.60E+06	48.5	0.19	0.18	1.83	0.3				
	7-2	2.10E+06	4.30E+06	70.9	2.10	0.56	2.44E+12	0.84	2554.87	1623	399621	1687887
	7-3	4.50E+06	4.00E+07	44.1	0.96	0.17	2.28E+05	0.89	2333.771	3969	397275	4359744
	7-4	4.10E+07	8.20E+07	131	1.30	0.52	9.93E+08	0.69	2096.961	14316	386928	40524426
	7-5	8.30E+07	2.60E+08	46.2	0.77	0.32	2.16E+04	0.69	1893.607	18879	382365	82320444
	7-6	2.90E+08	6.40E+08	101	0.27	0.79	3.25	0.03	1714.812	35340	365904	289817010
	7-7	6.50E+08	1.60E+09	121	0.98	0.98	1.23E+07	0.11	1458.932	51687	349557	645953598
	7-8	1.80E+09	4.50E+10	286	0.58	0.14	7.22E+03	0.81	1050.708	79131	322113	1802466522
	7-9	4.50E+10	5.00E+10	222	4.60	2.60	1.16E+47	0.21	772.4138	112440	288804	44626430412
	7-10	5.60E+10	5.80E+10	164	16.00	14.00	6.27E+170	0.23	250	281691	119553	56201020902

Table 2.5: -Continued from previous page

Channel No.	Seg.	A_min (km ²)	A_Max (km ²)	k _{sn} (m ^{0.9})	Theta	error (±2σ)	ks	R ²	Knickpoint elev. (m)	DFD ¹ (km)	DFM ² (km)	Upstream drainage area (km ²)
8	8-1	5.90E+05	8.50E+07	64.3	0.47	0.05	95.2	0.89	1728.486	14355	410730	87399243
	8-2	9.00E+07	1.20E+08	136	1.80	2.10	1.27E+13	0.36	1598.126	18534	406551	120437928
	8-3	1.20E+08	4.20E+10	92.9	0.39	0.06	30.8	0.72	922.9877	105339	319746	42217974612
	8-4	4.40E+10	5.00E+10	223	4.50	2.40	1.83E+45	0.19	245.2058	306024	119061	56203458120
	8-5	5.60E+10	5.80E+10	166	15.00	13.00	4.47E+157	0.23				
9	9-1	6.80E+04	3.50E+06	27.6	0.23	0.09	1.49	0.68	2099.547	2919	480039	5025816
	9-2	5.70E+06	1.60E+08	51.4	0.60	0.08	749	0.88	1720.052	22422	460536	169280685
	9-3	1.90E+08	1.00E+09	49.6	0.02	0.21	0.00949	0	1443.443	61836	421122	1029255327
	9-4	1.10E+09	4.20E+10	106	0.45	0.11	129	0.64	922.0444	161286	321672	42207695910
	9-5	4.40E+10	5.00E+10	223	3.60	2.10	6.87E+35	0.17	250	363774	119184	56203450551
	9-6	5.60E+10	5.80E+10	166	15.00	13.00	4.47E+157	0.23				
10	10-1	1.70E+05	2.30E+09	73.5	0.46	0.03	8.43E+01	0.88	1533.278	84774	443427	2329019145
	10-2	3.00E+09	4.20E+10	112	0.57	0.18	1.65E+03	0.49	973.4696	194928	333273	42096635973
	10-3	4.20E+10	5.00E+10	223	4.90	2.40	2.16E+49	0.21	202.4266	409980	118221	56206379754
	10-4	5.60E+10	5.80E+10	164	16.00	14.00	6.27E+170	0.23				
11	11-1	6.50E+05	9.90E+06	45	0.60	0.07	417	0.95	2376.43	4281	501066	11308086
	11-2	1.30E+07	1.30E+08	49.4	0.43	0.20	42.7	0.53	2127.1	15366	489981	131420547
	11-3	1.50E+08	2.00E+08	70.1	1.30	5.40	3.63E+08	0.07	1983.953	22239	483108	198133713
	11-4	2.00E+08	5.30E+08	89.8	1.30	0.63	1.86E+09	0.55	1797.106	36723	468624	530094915
	11-5	5.40E+08	1.60E+09	69.6	0.82	0.35	1.69E+05	0.32	1244.852	113403	391944	1653773517
	11-6	1.70E+09	4.30E+10	108	0.30	0.21	5.2	0.25	912.4451	191346	314001	878.24272
	11-7	4.40E+10	5.00E+10	223	3.50	2.20	3.04E+34	0.16	250	385917	119430	56201142006
	11-8	5.60E+10	5.80E+10	166	15.00	13.00	4.47E+157	0.23				
12	12-1	7.00E+04	4.10E+08	54.7	0.51	0.03	1.41E+02	0.93	1736.927	60357	600105	472381290
	12-2	8.10E+08	4.20E+10	77.5	0.34	0.07	7.53E+00	0.6	989.6229	323655	336807	41988527946
	12-3	4.40E+10	5.00E+10	223	5.00	2.50	8.70E+50	0.22	250	540048	120414	50184725562
	12-4	5.60E+10	5.80E+10	164	16.00	14.00	6.27E+170	0.23				
13	13-1	8.40E+04	4.30E+09	29.5	0.38	0.04	12.1	0.85	1584.983	106017	659655	4376191437
	13-2	4.50E+09	2.30E+10	46.4	0.24	0.30	0.445	0.13	1321.75	270144	495528	23019864615
	13-3	2.30E+10	4.20E+10	109	0.87	0.59	2.82E+06	0.23	955.5558	438105	327567	42171659901
	13-4	4.40E+10	5.00E+10	223	5.00	2.50	8.70E+50	0.22	250	646242	119430	56201142006
	13-5	5.60E+10	5.80E+10	166	15.00	13.00	4.47E+157	0.23				
14	14-1	1.10E+05	3.80E+09	33.1	0.45	0.03	35.7	0.92	1630.535	129036	668298	4278816252
	14-2	4.50E+09	2.30E+10	46.4	0.24	0.30	0.445	0.13	1302.204	308091	489243	23186617254
	14-3	2.50E+10	4.20E+10	95.1	0.66	0.81	1.68E+04	0.15	961.4406	463233	333027	42096885750
	14-4	4.40E+10	5.00E+10	223	3.60	2.10	6.87E+35	0.17	250	677781	119553	56201020902
	14-5	5.60E+10	5.80E+10	166	15.00	13.00	4.47E+157	0.23				
15	15-1	7.50E+05	4.50E+09	26.1	0.37	0.05	5.52	0.87	1614.642	105675	663333	6504268770
	15-2	6.80E+09	2.20E+10	51.8	0.58	0.56	1.22E+03	0.24	1307.896	279099	489909	23185905768
	15-3	2.50E+10	4.20E+10	94.4	0.93	0.78	1.19E+07	0.29	961.6993	437154	331854	42100147989
	15-4	4.40E+10	5.00E+10	223	3.60	2.10	6.87E+35	0.17	250	676953	119307	56201202558
	15-5	5.60E+10	5.80E+10	166	15.00	13.00	4.47E+157	0.23				

Table 2.5: -Continued from previous page

Channel No.	Seg.	A_min (km ²)	A_Max (km ²)	K _{sa} (m ^{0.9})	Theta	error (±2σ)	ks	R ²	Knickpoint elev. (m)	DFD ¹ (km)	DFM ² (km)	Upstream drainage area (km ²)
1t	1t-1	4.40E+07	5.10E+08	98.2	0.19	0.13	0.764	0.13				
	1t-2	5.30E+08	6.50E+08	212	0.86	3.40	8.70E+05	0.01	1196.12	41454	243732	525175065
	1t-3	6.80E+08	5.00E+10	206	0.60	0.06	8.35E+03	0.93	808.2892	59670	225516	673232274
2t	2t-1	3.80E+06	1.10E+07	109	1.00	0.33	1.14E+06	0.79				
	2t-2	1.20E+07	5.00E+07	160	0.98	0.26	1.27E+06	0.63	1857.826	5553	221877	11156706
	2t-3	5.10E+07	1.10E+08	171	0.85	0.58	2.09E+05	0.43	1444.598	10557	216873	49735899
	2t-4	1.30E+08	5.00E+10	169	0.47	0.04	330	0.93	1119.8	15657	211773	112884066
3t	3t-1	2.20E+06	1.40E+07	173	0.77	0.12	2.46E+04	0.83				
	3t-2	1.80E+07	2.90E+07	151	1.40	0.58	2.68E+09	0.6	1848.525	5880	203310	15372639
	3t-3	5.10E+07	5.00E+10	183	0.48	0.04	354	0.87	1478.861	10428	198762	38548917
4t	4t-1	1.10E+06	3.90E+06	115	0.78	0.15	1.43E+04	0.76				
	4t-2	4.70E+06	1.10E+07	181	0.29	0.22	16.7	0.26	1656.478	3810	165477	4223502
	4t-3	1.20E+07	1.60E+07	216	2.90	1.50	7.77E+19	0.63	1271.534	5982	163305	11890899
	4t-4	1.90E+07	4.90E+10	141	0.96	0.15	9.61E+05	0.72	1000.025	7611	161676	16818318
5t	5t-1	3.40E+06	1.70E+07	128	0.71	0.18	9.10E+03	0.78				
	5t-2	1.80E+07	4.70E+07	118	0.57	0.49	993	0.15	1185.542	4485	111153	17068095
	5t-3	6.40E+07	1.60E+08	90.1	2.80	0.60	9.83E+20	0.72	781.4043	12924	102714	54489231
6t	6t-1	7.60E+04	7.40E+06	56.6	0.19	0.07	1.57	0.46				
	6t-2	1.40E+07	2.20E+07	258	1.50	0.46	1.35E+10	0.56	1328.183	4938	103482	13276026
	6t-3	6.20E+07	5.80E+10	73.5	0.33	0.06	8.18	0.78	711.869	9096	99324	23229261
7t	7t-1	6.10E+05	1.10E+08	98.1	0.29	0.04	8.49	0.67				
	7t-2	1.30E+08	5.10E+10	223	0.49	0.07	537	0.74	1177.536	18558	168147	120468204
8t	8t-1	3.10E+06	3.00E+07	84	0.10	0.19	0.27	0.04	1971.858	6882	213549	29753739
	8t-2	3.20E+07	9.70E+07	148	0.44	0.65	1.33E+02	0.06	1571.598	15603	204828	97488720
	8t-3	9.90E+07	1.50E+08	287	0.27	1.00	1.00E+01	0.01	1034.456	24009	196422	148110192
	8t-4	1.50E+08	5.50E+10	216	0.50	0.05	685	0.86				
9t	9t-1	2.30E+06	1.10E+07	71.1	0.78	0.26	1.45E+04	0.72	2211.939	5445	218190	12821886
	9t-2	1.40E+07	5.60E+10	229	0.42	0.03	150	0.78				
10t	10t-1	4.30E+05	2.30E+06	61.2	0.45	0.11	206	0.81	1997.229	3114	210570	2717271
	10t-2	4.80E+06	1.50E+07	233	0.13	0.15	1.18	0.05	1175.975	8703	204981	15486174
	10t-3	1.70E+07	3.70E+07	131	1.80	35.00	1.29E+12	0.72				
11t	11t-1	2.00E+05	1.50E+06	66.8	0.29	0.10	8.02	0.68	2088.422	2280	211686	2467494
	11t-2	4.90E+06	1.50E+07	237	0.13	0.14	1.18	0.06	1175.975	8985	204981	15486174
	11t-3	1.70E+07	5.10E+10	118	0.41	0.02	69.6	0.95				
12t	12t-1	9.70E+05	7.50E+06	99	0.48	0.12	151	0.7	2168.124	4476	211929	8189658
	12t-2	1.30E+07	4.50E+07	215	0.40	0.16	99.3	0.25	1049.572	16341	200064	45694053
	12t-3	4.80E+07	5.10E+10	158	0.43	0.03	128	0.92				
13t	13t-1	5.20E+05	3.30E+06	89.2	0.52	0.09	250	0.84	2072.207	2940	214680	3678534
	13t-2	4.50E+06	7.10E+06	174	0.11	0.48	0.902	0.01	1513.344	6279	211341	8908713
	13t-3	9.60E+06	4.90E+10	197	0.45	0.02	227	0.93				
14t	14t-1	8.80E+05	5.30E+06	102	0.51	0.14	257	0.7	2186.626	3621	219057	6070338
	14t-2	6.40E+06	2.50E+07	186	0.88	0.32	2.31E+05	0.57	1695.872	7446	215232	27694971
	14t-3	2.90E+07	5.00E+10	217	0.49	0.03	507	0.91				
15t	15t-1	1.20E+06	6.70E+06	108	0.13	0.09	0.918	0.21	1946.852	6060	218517	8522694
	15t-2	1.00E+07	1.70E+07	262	2.20	0.33	5.93E+14	0.8	1125.871	11427	213150	19452330
	15t-3	2.40E+07	5.10E+10	157	0.42	0.03	90.3	0.95				

Table 2.5: -Continued from previous page

Channel No.	Seg.	A_min (km ²)	A_Max (km ²)	k _{sn} (m ^{0.9})	Theta	error (±2σ)	ks	R ²	Knickpoint elev. (m)	DFD ¹ (km)	DFM ² (km)	Upstream drainage area (km ²)
16t	16t-1	6.30E+05	6.50E+06	45.5	0.28	0.15	4.14	0.53				
	16t-2	8.10E+06	3.60E+07	213	0.65	0.08	5.53E+03	0.78	<u>2447.965</u>	3339	234336	6925635
	16t-3	4.60E+07	5.00E+10	228	0.46	0.03	303	0.9	1460.131	11934	225741	39661560
17t	17t-1	1.30E+06	8.70E+06	78.1	0.54	0.09	299	0.82				
	17t-2	1.10E+07	3.30E+07	197	0.36	0.22	44.1	0.64	<u>2046.746</u>	6147	195660	9688320
	17t-3	3.80E+07	5.20E+07	295	3.20	0.64	3.81E+23	0.77	1732.373	8646	193161	37216773
	17t-4	5.60E+07	4.90E+10	174	0.47	0.04	282	0.86	1166.173	13338	188469	56018169
18t	18t-1	8.80E+05	2.40E+07	71.5	0.57	0.07	472	0.89				
	18t-2	4.00E+07	5.60E+07	216	1.20	0.66	2.35E+08	0.26	<u>1913.385</u>	8949	194004	28315629
	18t-3	6.10E+07	5.00E+10	198	0.50	0.03	530	0.91	1222.168	18513	184440	56850759
19t	19t-1	5.70E+05	1.10E+06	42	0.63	0.59	494	0.6				
	19t-2	1.90E+07	6.70E+07	166	0.81	0.15	9.56E+04	0.69	<u>2019.064</u>	2592	195003	2497770
	19t-3	7.40E+07	5.00E+10	143	0.43	0.08	129	0.74	740.2012	19356	178239	74267028
20t	20t-1	1.30E+06	2.10E+07	130	0.76	0.07	1.70E+04	0.9				
	20t-2	4.40E+07	5.10E+10	147	0.41	0.04	82.7	0.88	1293.29	9909	191133	32705649
21t	21t-1	5.40E+05	1.00E+06	125	0.79	0.52	1.25E+04	0.46				
	21t-2	1.40E+06	2.90E+06	250	1.20	0.94	2.23E+07	0.34	1802.62	1674	203253	1233747
	21t-3	3.50E+06	5.10E+10	136	0.45	0.02	159	0.94	1394.421	3087	201840	3413619
22t	22t-1	1.20E+05	1.90E+06	83.4	0.39	0.06	37.6	0.87				
	22t-2	3.10E+06	5.10E+10	80.2	0.35	0.03	18.7	0.92	925.9615	1941	202143	2217717
23t	23t-1	6.10E+05	1.60E+06	53.8	0.91	0.84	3.05	0.78				
	23t-2	2.30E+06	3.50E+07	73.2	0.15	0.10	0.68	0.18	<u>2180.59</u>	2274	229368	1839267
	23t-3	5.60E+07	5.60E+10	208	0.42	0.05	171	0.7	1444.598	10557	216873	49735899
24t	24t-1	1.80E+05	1.50E+06	111	0.31	0.10	17.6	0.59				
	24t-2	1.80E+06	3.20E+06	247	0.61	0.29	2.78E+03	0.64	1923.83	1803	224379	1703025
	24t-3	3.60E+06	9.60E+06	207	1.50	0.16	1.82E+09	0.86	1706.391	2505	223677	3307653
	24t-4	1.10E+07	4.90E+10	123	0.39	0.02	42.2	0.96	1009.454	6561	219621	10626876

^{1,2} As explained in Table 2.3

Values with underline show in the Fig. 2.6 as major knickpoints.

3 Spatial variability of ^{10}Be erosion rates in the north Iranian Plateau and margin: Insight from landscape evolution across different tectono-stratigraphic zones

Amaneh Kaveh Firouz ^a, Jean-Pierre Burg ^a, Negar Haghypour ^a,
Sanjay Kumar Mandal ^b, Ramin Elyaszadeh ^c, Marcus Christl ^d

^a *Geological Institute, ETH Zurich, Sonneggstrasse 5, 8092 Zurich, Switzerland*

^b *Geochemistry of the Earth's surface, Helmholtz Centre Potsdam, 14473 Potsdam, Germany*

^c *Geological Survey of Iran (GSI), Northwestern Regional Office, 5167733551 Tabriz, Iran*

^d *Laboratory of Ion Beam Physics, ETH Zurich, Schafmattstrasse 20, 8093 Zurich, Switzerland*

This chapter is in preparation for submission to Earth and Planetary Science Letters

Abstract

To determine the main controls on present-day landscape evolution in the north Iranian Plateau and its margin, we studied the Qezel-Owzan River Basin, which cross-cuts three distinct tectono-stratigraphic zones with north-south lithological and topographic variability and seismicity. To test whether active tectonics and exhumation of the bedrock led to changes in the landscapes, we studied differences between temporal erosion rate changes. We measured ^{10}Be concentration in river sands and analyzed the topographic metrics using digital elevation models with 30 m and 1 km resolution precipitation data to explore the topographic/climatic relationship with the millennial-scale erosion rates. The high relief part of the lower catchment yields higher erosion rates than the low relief and high plateau in the upper and middle catchments. The local relief, hillslope, and channel steepness are in moderate-correlation with erosion rates in the Qezel Owzan catchment, suggesting that tectonics and local lithology continue to control the differences in topographic relief differences in the region during present day uniform climate conditions. Areas in the lower catchment that show increased seismicity are also associated with higher erosion rates and higher geomorphic indices. The earthquake focal mechanism solutions show that an active thrust faulting component is responsible for higher channel steepness and local relief in the lower catchment. The measured short-term erosion rates are consistent with long-term erosion rates derived from thermochronometry in the west Alborz. The results point to a near topographical steady state in the upper, middle and lower catchments and reflect the balance between tectonics and erosion rates in the northern part of Iranian Plateau.

3.1 Introduction

The north Iranian Plateau represents a thickened and low-relief morphotectonic province (e.g. Ballato and Strecker, 2014) with a mean elevation of about 1800 m. Uplift from ~1000 m elevation of the Iranian Plateau started after ~17 Ma (e.g. Morley et al., 2009). The northern margin of the plateau is the high and narrow Alborz Mountain Range (AMR, Fig. 3.1) that developed in the Late Cretaceous-Early Tertiary in the collision zone between Arabia and Eurasia (e.g. Berberian and Berberian, 1981; Şengör, 1990). The high AMR acted as an orographic barrier that influenced the climate conditions of the Iranian Plateau. Previous studies suggest that tectonic forcing in the Late Miocene (Madanipour et al., 2013) and the wetter climate in the Pliocene (Heidarzadeh et al., 2017; Rezaeian et al., 2012) were the main topographic controllers. Due to present-day semi-arid climate conditions and the high topography since the Late Miocene-Early Pliocene (Madanipour et al., 2013), we supposed that the steep river channels in the AMR northern margin of the Iranian Plateau are responses to tectonic forcing.

To better understand the evolution of high and low-relief landforms in the west of the AMR and in the studied part of the Iranian Plateau, we measured ^{10}Be cosmogenic nuclide concentration from river sand. The Qezel-Owzan River Basin (QORB) is the largest catchment in the studied region (Fig. 3.2a). We chose this basin to explore the erosion rates and their relationship with topographic metrics extracted from digital elevation models. Results allow testing the recent landscape evolution across tectonostratigraphically distinct zones under nearly uniform climatic conditions (Hijmans et al., 2005), from the upper to lower catchment the Sanandaj-Sirjan Zone (SSZ; Figs. 3.1 and 3.2b), Central Iran Zone (CIZ; Figs. 3.1 and 3.2c), and AMR (Fig. 3.1 and 3.2d; e.g. Alavi, 1991). The crustal thickness is about 40-45 km in the SSZ and CIZ and >50 km beneath the AMR (Jiménez-Munt et al., 2012).

Previous thermochronometry studies using Apatite Fission Track (AFT) and apatite (U-Th)/He dating (AHe) have produced cooling ages in the west AMR and Talesh Mountains (Madanipour et al., 2013; Rezaeian et al., 2012). There is no thermochronological information on the Iranian Plateau. According to Rezaeian et al. (2012), AHe data can be interpreted as high erosion rates in the west AMR during Late Miocene to Early Pliocene times. These authors suggest that these erosion rates are controlled by climate conditions due to the Caspian isolation and related base-level fall in the Pliocene at times of unchanging regional tectonics. However, Madanipour et al. (2013) suggested that exhumation (as erosion proxy) of the northern margin of the Iranian Plateau is due to the rigidity of the South Caspian block that hindered northward expansion of the Iranian Plateau. According to the U-Pb zircon ages of volcanic ashes intercalated in the Mianeh Basin

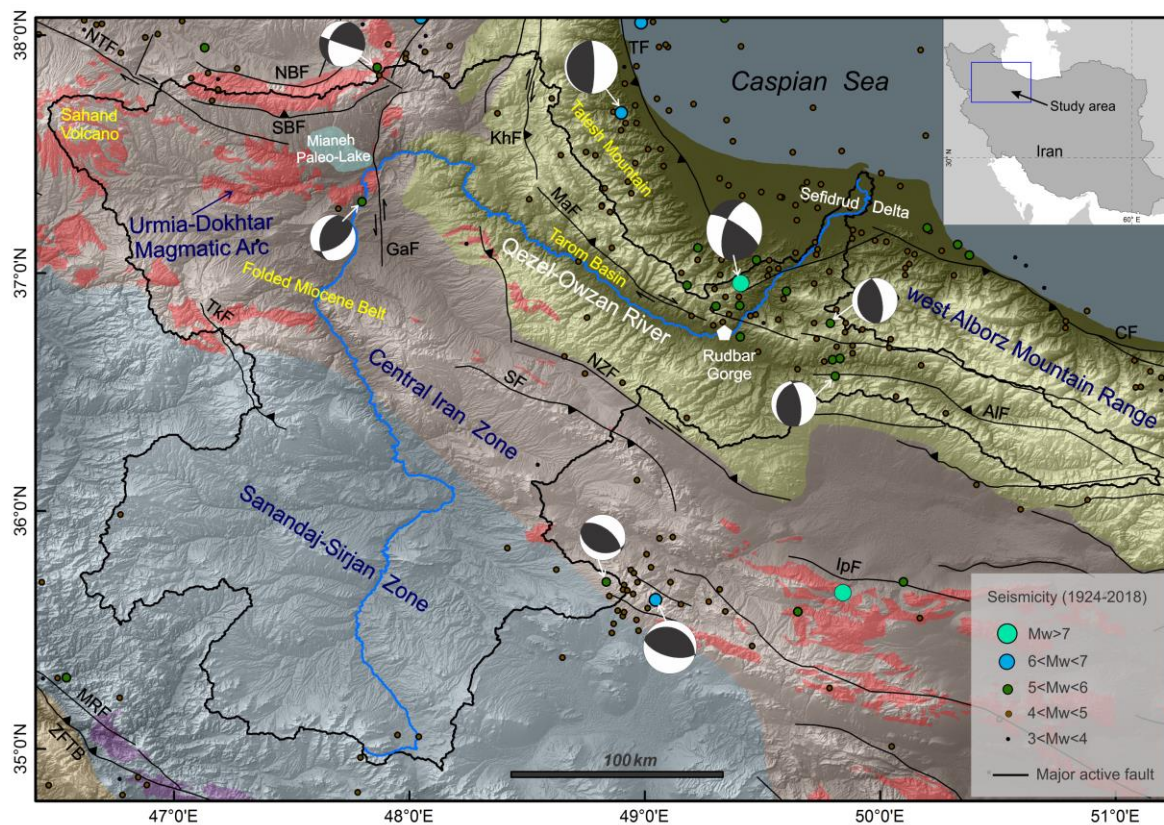


Fig. 3.1: Tectono-stratigraphic and topographic overview of the study area. Various tectono-stratigraphic zones (blue letters), major active faults and seismicity (USGS earthquake catalogue; <https://earthquake.usgs.gov/earthquakes/search/>), fault plane solutions (Harvard CMT catalog; <http://www.globalcmt.org/CMTsearch.html>) in the studied Qezel-Owzan Catchment (black polygon) in NW Iran. Explanation of the active faults name from active fault map of Iran (Hessami et al., 2003), NW Iran (Faridi et al., 2017): AIF=Alamutrud Fault; CF=Caspian Fault; GaF=Garmachay Fault; IpF=Ipak Fault; KhF=Khalkhal Fault; Maf=Masuleh Fault; MRF=Main Recent Fault; NBF=North Bozghush Fault; NTF=North Tabriz Fault; NZF=North Zanzan Fault; SBF=South Bozghush Fault; SF=Soltanieh Fault; TF=Talesh Fault; Tkf=Takhte Solayman Fault; ZFTB=Zagros Fold and Thrust Belt.

paleo-lake sedimentary sequence (Fig. 3.1), Heidarzadeh et al. (2017) suggested that the Qezel-Owzan River (QOR) drained the north Iranian Plateau until the Pliocene. They further suggested that due to wet climate conditions in the Early Pliocene, the QOR captured the Mianeh Paleo-lake (Fig. 3.1) and discharged to the Caspian Sea (Clifton et al., 2000; Heidarzadeh et al., 2017; Hinds et al., 2004). However, other studies suggested that the QOR connected to the Caspian Sea during Middle Pleistocene after the opening of the Rudbar gorge, QOR captured the Sefidrud River (Fig. 3.1), and consequently increasing the sedimentary budget in the Sefidrud delta (Fig. 3.1; Kazanci and Gulbabazadeh, 2013).

Low-temperature thermochronometer data with >1 Ma timescales is applied to study upper crustal deformation and exhumation histories (e.g. Kirby et al., 2002), but cannot resolve the short-term erosion rates. The lack of temporal and spatial evolution of short-term erosion rates and geomorphic processes in the study area, led us to calculate these rates by analyzing the cosmogenic nuclides (^{10}Be) measured in the north Iranian Plateau and margins from river

sediments along the trunk channel and major tributaries of the QORB (Fig. 3.3a). This study aims to answer the following questions: (1) What is the magnitude and distribution of millennial-scale erosion rates across the region? (2) How do millennial-scale erosion rates compare with long-term (> 1 Ma) exhumation rates? (3) Did the QOR reach a steady state or is it still in a transient state condition after capturing the Mianeh paleo-lake in Early Pliocene? (4) What are the main controls on landscape evolution in the internal plateau and the Alborz Mountain Range? (5) How and when does erosion adjust to tectonic uplift and base level changes in terms of space and time across the study area?

3.2 Study area

3.2.1 Geological, geomorphological and seismic setting

Collision between the Arabian and Eurasian Plates affected the north Iranian Plateau since at least the Late Eocene (e.g. Ricou, 1994; Şengör et al., 1988). The north Iranian Plateau includes parts of the SSZ and CIZ (Fig. 3.1). These continental fragments were separated from Gondwana during the Permian-Mesozoic, which correspond to the opening of the Neo-Tethys Sea (e.g. Stampfli, 2000). The northern margin of the Plateau is the steeply flanked AMR anticlinorium (Fig. 3.1; Berberian, 2014; Berberian and King, 1981; Stocklin, 1968). Compared to the southern flank of west AMR, the northern flank has no trace of Eocene volcanism and other Paleogene rocks whereas the intensity of folding decreases towards the Caspian Sea (Stocklin, 1968). The AMR has undergone oblique shortening related to northward motion of Iranian Plateau (Allen et al., 2002).

This study is focused on the QORB, which is divided into upper, middle and lower catchments (Fig. 3.3b) corresponding approximately to the SSZ, CIZ and AMR, respectively (Fig. 3.1). (1) The upper catchment has a low relief between ~100 and ~600 m elevation. The corresponding SSZ strikes NW-SE between the Zagros Fold and Thrust Belt (ZFTB) to the southwest and the CIZ to the northeast (Fig. 3.1). The SSZ mainly consists of Mesozoic metamorphic and plutonic rocks covered by Tertiary conglomerate, sandstone, mudstone, and limestone (Fig. 3.4a). (2) The middle catchment flows on the low relief CIZ between ~100 and ~1600 m elevation. The CIZ is composed of Precambrian metamorphic and plutonic rocks covered by Tertiary limestones and mudstones (Fig. 3.4a; e.g. Berberian and King, 1981). The Urmia-Dokhtar Magmatic Arc (UDMA, Fig. 3.1) formed on the CIZ and is attributed to the Neo-Tethys subduction below the SSZ and the CIZ (e.g. Alavi, 2007). UDMA and Neogene volcanism has built the high topography of the western CIZ.

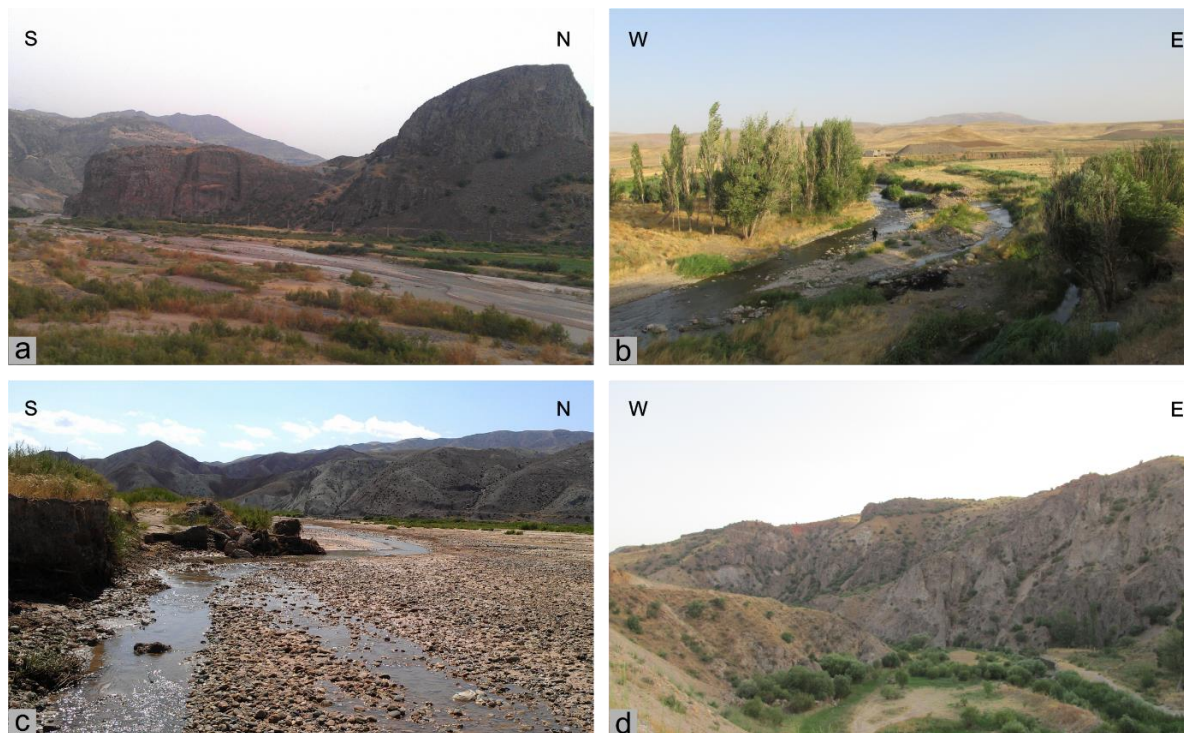


Fig. 3.2. Field photographs illustrating the different topographic overview of the Qezel-Owzan River Basin from trunk channel (a), upper catchment in the Sanandaj-Sirjan Zone (b), middle catchment in the Central Iran Zone (c), and lower catchment in the Alborz Mountain Range (d).

(3) The lower catchment crosses the W-E high relief AMR (between 600 and >3400 m) that achieved present-day altitude since the Late Miocene (Axen et al., 2001) with >50 km crustal thickness and absence of a deep crustal root (Jiménez-Munt et al., 2012). The AMR is composed of Paleozoic metamorphic rocks and Tertiary granitoids, which are overlain by Paleogene, mostly volcanoclastic sediments (Fig. 3.3a). The AMR separates the north Iranian Plateau to the south from the Caspian Sea to the north (Fig. 3.1).

From an active tectonic point of view (Fig. 3.1), the SSZ has a low seismic activity while the CIZ has been subjected to mostly moderate earthquakes ($M_w < 5$) with some large events along the Ipak Fault (Fig. 3.1; 1962, $M_w: 7.2$), which have a 3000-5000 yr recurrence time (Berberian and Yeats, 1999). The west AMR is a seismic zone with large-strong magnitude earthquakes (Fig. 3.1). The Rudbar earthquake (1990, $M_w: 7.4$; Fig. 3.1) is one of the largest earthquakes that occurred in the west Alborz, where recurrence times are also few thousand years (Berberian and Yeats, 1999). The active fault systems in the west AMR and Talesh Mountains, accommodated regional shortening into components of north-south thrust faulting (4-6 mm/yr) and dominantly dextral strike-slip faulting (1-2 mm/yr; e.g. Jackson et al., 2002).

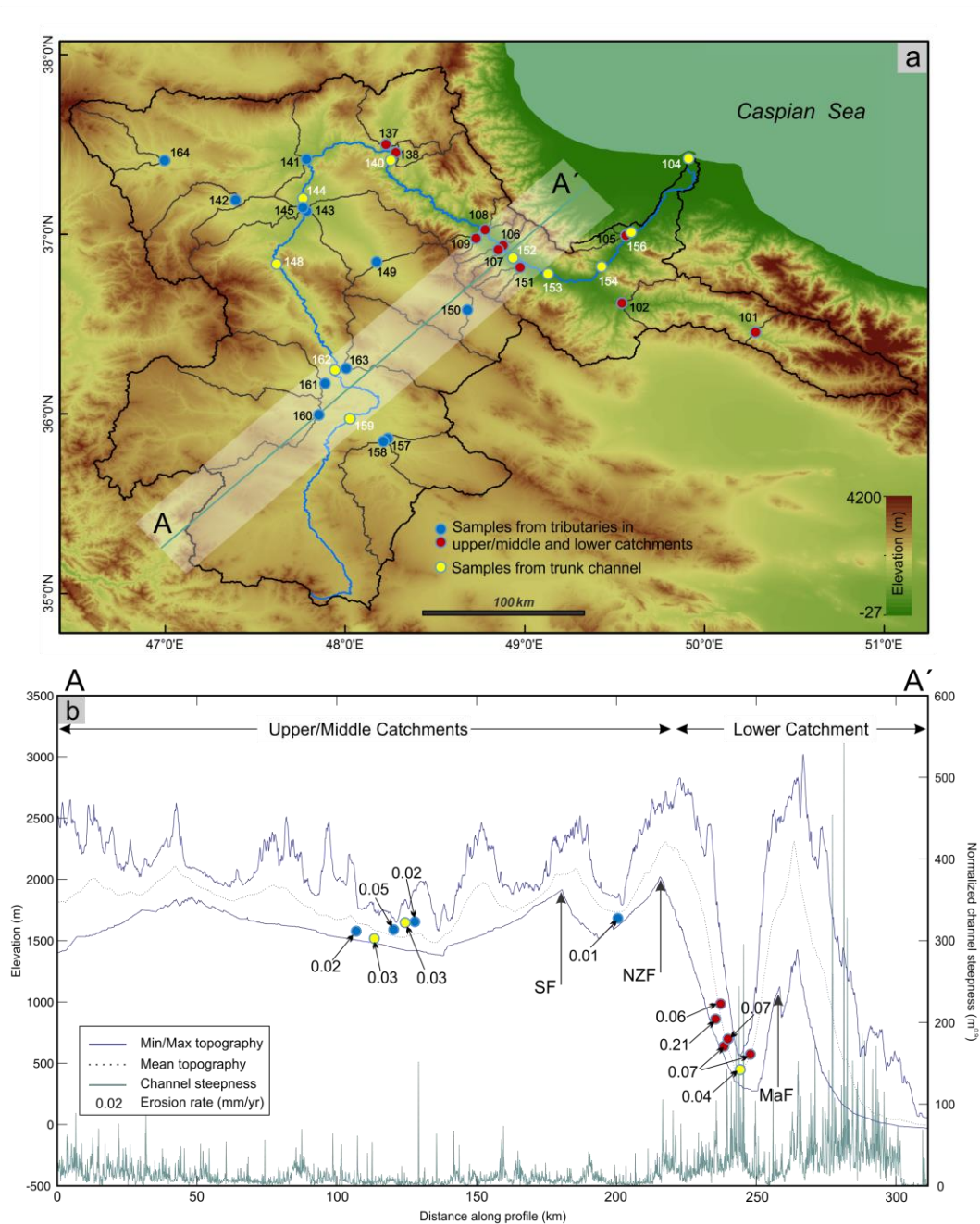


Fig. 3.3: (a) Topographic overview and river catchments of the Qezel-Owzan River Basin from a SRTM 90 m DEM (Jarvis et al., 2008b). Blue line: main river; Black polygons: sampled catchments; Sampling locations displayed with color-coded circles, white: from trunk channel; red: from tributaries. Numbers refer to sample ID used in the main text and Tables 3.1-3.3. (b) Topographic swath (50 km width) and channel steepness (green line) profiles (A–A′ located in Fig. 3.3a) with sampled points and erosion rates. Black lines = active faults (names as in Fig. 3.1).

3.2.2 Climatic and hydrologic setting

The north Iranian Plateau underwent climate changes from wet to semi-arid during the Early Pliocene (Clifton et al., 2000; Hinds et al., 2004). The upper and middle catchments have sparse

vegetation and experience rainfall of ~350 mm/yr, mostly during spring and summer. The mean temperature varies between ~-4°C in January and 26°C in July (Djamali et al., 2009; Sharifi and Safari Sinigani, 2012). The lower catchments, which has semi-Mediterranean climate (warm and humid) and dense vegetation, shows a strong gradient of annual precipitations from ~1500 mm/yr in the Caspian coastal plain to ~600 mm/yr on the AMR northern flank. The mean temperature varies from 1°C in February to 26°C in July in the coastal plain (e.g. Hijmans et al., 2005; Leroy et al., 2011).

The upper and middle parts of QORB include longer tributaries than the lower part. The tributaries of upper and middle catchments are mostly seasonal, developing shallow channels in W-E or E-W flow-directions, while the tributaries in the lower catchment are permanent with deeper channels than the upper and lower catchment and S-N or N-S flow-directions. The trunk channel “QOR” discharges into the Caspian Sea at an -27 m elevation. The Caspian Sea-level varied from -1500 m in the Early Pliocene to -50 m in the Late Pleistocene (Forte and Cowgill, 2013; Kakroodi et al., 2015), which could also have affected the erosion rates in the QORB.

3.3 Data and methods

3.3.1 ¹⁰Be-derived erosion rates

We measured catchment-wide erosion rates using in situ cosmogenic ¹⁰Be concentrations from river sands along the QOR trunk channel and major tributaries (locations in Fig. 3.3a).

3.3.1.1 *Sampling strategy*

The samples were taken at 32 points that collect sediments from catchment areas between ~90 and 58,623 km², respectively (Fig. 3.1). Sand was taken from active sandbars within or nearby the active channels of tributaries to have diverse grain sizes and to avoid sampling from junction points. The sampling locations along the trunk channel (samples 162, 140 and 156; Fig. 3.3a) are representative of total sediment flux for each tectono-stratigraphic zone (Fig. 3.3a).

3.3.1.2 *Analytical procedures for river sediments*

First, sands were sieved to 250–1000 μm. Quartz grains were purified from the sieved sands following standard procedures at ETH Zurich (Lupker et al., 2012). Then, ~300 μg of ⁹Be carrier solution was mixed with the purified quartz and the whole was dissolved in concentrated HF (40%). ¹⁰Be was extracted using ion-exchange chromatography and pH-sensitive precipitations. Isotopic measurements of the Be were performed on the 0.5 MV NEC Pelletron “TANDY” AMS (Accelerator Mass Spectrometer) at the ETH Zurich (Christl et al., 2013). All measured ¹⁰Be/⁹Be

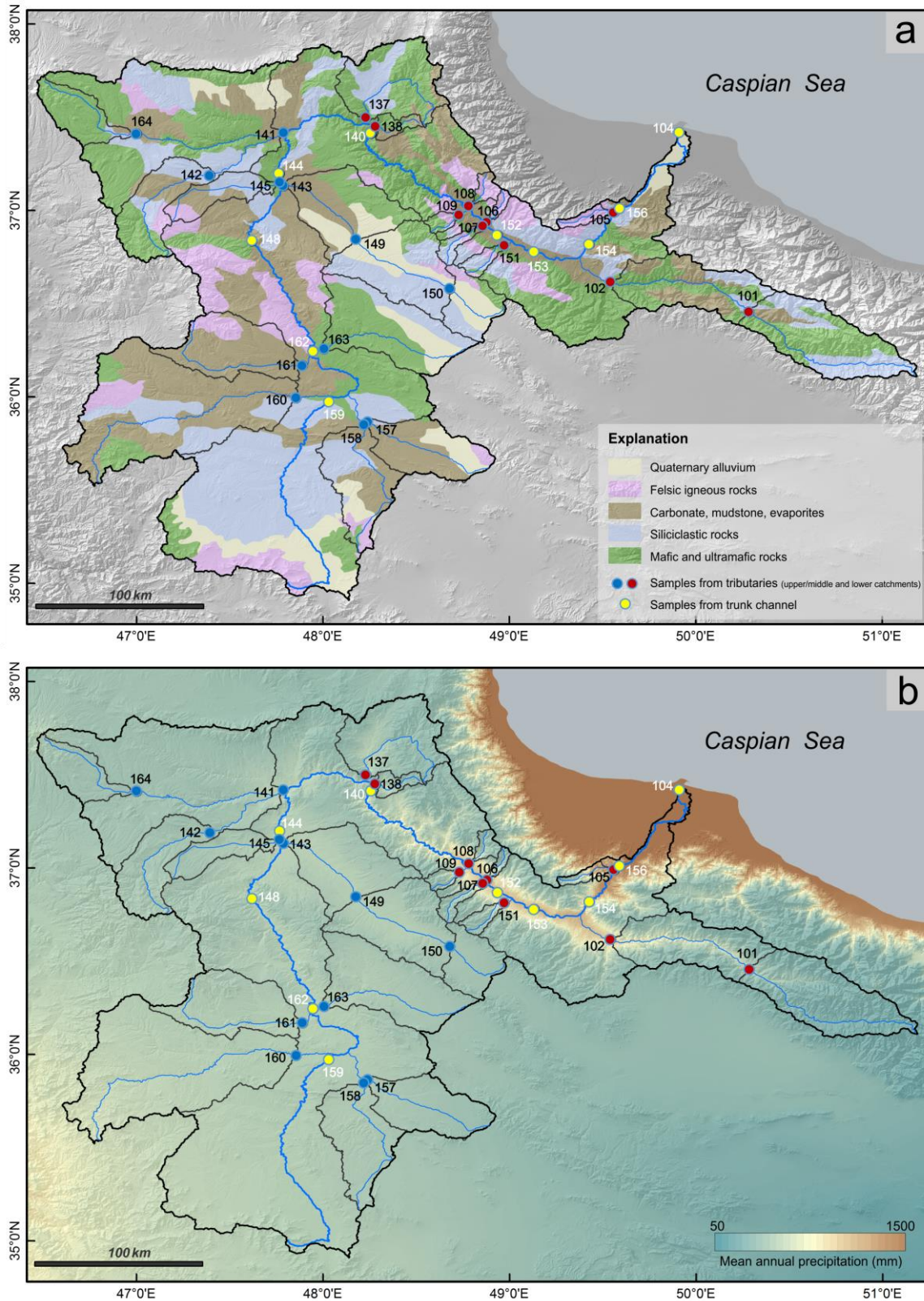


Fig. 3.4: Geologic and climatic overview of the Qezel-Owzan River Basin. (a) Simplified geological map of the area, based on Geological maps of NW Iran (scale: 1:250,000, Geological Survey of Iran, 1969-1994). (b) Annual precipitation data as a proxy for climatic variability, derived from 1 km resolution Worldclim (<http://worldclim.org/version2>) averaged over the 1950–2000 period. Lines, polygons, circles and numbers as in Fig. 3.3a.

ratios were normalized to the secondary standard of S2007N at the ETH Zurich (Christl et al., 2013). The subtracted procedural blank ratio ($^{10}\text{Be}/^9\text{Be}$) was $7.151 (\pm 0.62) \times 10^{-15}$ ($n = 9$) from the measurements. The blank error and analytical uncertainties were propagated into all the ^{10}Be concentrations (Table 3.1).

3.3.1.3 Calculation for erosion rates

The erosion rates were calculated using the CRONUS-Earth online calculator version 2.3 (Balco et al., 2008; <https://hess.ess.washington.edu/>). Lal/Stone scaling factors were used to convert the measured ^{10}Be concentrations to erosion rates. The reference nucleonic ^{10}Be production rate for this scaling scheme is 4.39 ± 0.37 atoms $\text{gqtz}^{-1}\text{a}^{-1}$ using the revised 07KNSTD standardization (Nishiizumi et al., 2007). The environmental parameters such as effective elevation, effective latitude, and effective longitude were extracted from SRTM DEM 90 m (Jarvis et al., 2008), allowing us to use the CRONUS calculator for determining drainage basin erosion rates (following the procedure of Portenga and Bierman, 2011). A topographic shielding factor of the catchment drainage area was determined from the 90 m SRTM DEM using the formulation of Codilean (2006), based on 5° intervals in both elevation angles and azimuth (Table 3.1).

3.3.2 Climatic and topographic analysis

Mean annual rainfall for each drainage catchment as a proxy of climate was calculated with 1 km resolution Worldclim precipitation data (<http://worldclim.org/version2>). This data covers a period from 1950 to 2000 (Hijmans et al., 2005; Fig. 3.4b, Tables 3.2, 3.3).

Local relief refers to the quantitative measure of vertical elevation variation in a landscape, which we measured within a moving circular window with radius of 250 m to 2 km (Fig. 3.8a) to account for potential scaling effects (DiBiase et al., 2010). Mean local relief is the average of all elevation values within a sampled catchment and is less dependent on the scale and quality of the sampled DEM than other topographic metrics. This analysis can measure the landscape steepness and correlates well with short-term erosion rates in a global scale (Montgomery and Brandon, 2002). The hillslope angle is a metric dependent on the DEM scale and quality (Fig. 3.8b).

The local channel steepness (k_{sn} ; Fig. 3.8c) is a normalized steepness index in the most graded river profiles (Whipple, 2004). The channel steepness index “ ks ” is related to the local slope “ S ” and the upstream area “ A ” based on the equation “ $S = ksA^{-\theta}$ ”, where $\theta = m/n$ is the channel concavity index (Flint, 1974). The k_{sn} is a practical metric to investigate the relationship between topography and spatial patterns of erosion (e.g. Scherler et al., 2014). Generally, k_{sn} index has two approaches: (1) slope-area and (2) precipitation. According to the semi-arid and homogenous climate conditions across the studied area, we followed the slope-area approach.

All the topographic metrics were extracted from ALOS World 3D-30m DEM (<http://www.eorc.jaxa.jp/ALOS/en/aw3d30/index.htm>) and reported in Table 3.3.

3.3.3 Exhumation rate

To better understand the regional geological records over a longer period than 1 Ma and derive erosion-driven exhumation histories that could change the topographic relief, we used 18 AFT and (AHe) ages previously published on the lower and a small part of the middle QOR catchment (Madanipour et al., 2013; Rezaeian et al., 2012; Fig. 3.5b). We converted these ages to exhumation rates by following standard procedures. The dependence of closure temperature on cooling rate and the advection of heat by rock motion towards the Earth's surface are included in the method (Willett and Brandon, 2013).

We considered two thermal models: (1) a steady state model valid for low erosion rates and (2) an eroding half-space model that captures the transient increase of geothermal gradient with erosion, but has no steady state. It is assumed for each case that the data consist of one or more thermochronometric ages, present-day surface geothermal gradient, and topographic information including the elevation at which the age was obtained. Analytical solutions for the steady case (explicit expression) and the transient case (root-finding problem) are provided to derive the erosion rate from these data.

3.4 Results

3.4.1 Catchment-averaged erosion rates

Millennial-timescale catchment-averaged erosion rates from ^{10}Be concentrations are shown in Fig. 3.5a, b and Table 3.1. They define two groups: The first group includes erosion rates measured from the QOR trunk channel. This group has erosion rates of 0.03 ± 0.004 to 0.09 ± 0.012 mm/yr from upper to lower catchment (Fig. 3.4b). The second group includes erosion rates from tributaries; these rates vary from 0.01 ± 0.001 to 0.22 ± 0.041 mm/yr.

The erosion rates are higher in the western tributaries than in the eastern ones in the upper and middle catchments. Erosion rates increase from the upper to middle catchment. Some tributaries in the western part of the middle catchment (samples 142, 145) have high erosion rates about 0.11 ± 0.01 mm/yr (Fig. 3.5a) which are attributed to the high erodability of the Sahand volcano silicic tuffs or Folded Miocene Belt activity (Figs. 3.1 and 3.4a). The average erosion rates in the sampled catchments of west AMR (samples 101, 102, 105) are higher than tributaries in the Tarom basin (Figs. 3.1 and 3.4a). Bedrock type does not affect the regional erosion rates in any of the three catchment parts (Fig. 3.6 and Table 3.2). However rock type can have a local effect (e.g.,

Sahand Volcano tuffs Fig. 3.4a). The lack of regional rock type effect suggests that a stronger tectonic effect drives the catchment averaged erosion rates, in consistency with more frequent earthquakes in the lower catchment and the potential growth of the Miocene fold belt (Fig. 3.1).

3.4.2 Erosion rates and climatic gradients

Plots of annual precipitation rates versus average erosion rates show a weak correlation ($R^2=0.017$ and $R^2=0.114$) in the upper/middle and lower catchments, respectively (Fig. 3.7a). However, the erosion rates in the lower catchment are more dependent on climate conditions because annual precipitation is two times higher (~550 mm/yr; Fig. 3.4b) than in the upper and middle catchments.

3.4.3 Erosion rates and topographic metrics

The topographic metric analysis was carried out to assess controls of topography on erosion rates (Tables 3.1 and 3.3).

There are two groups of correlation between average erosion rates and topographic metrics, which correspond to the upper/middle catchments and lower catchment, separately (Figs. 3.7b-7e). The results in the upper/middle catchment show: average erosion rates and mean local relief in a 2 km radius window ($R^2=0.288$, Fig. 3.7b), hillslope angle ($R^2=0.372$, Fig. 3.7c), and channel steepness index ($R^2=0.372$, Fig. 3.7d). Results in the lower catchment show: average erosion rates and mean local relief ($R^2=0.170$, Fig. 3.7b), hillslope angle ($R^2=0.151$, Fig. 3.7c), and channel steepness index ($R^2=0.091$, Fig. 3.7d). However, these correlations are at least 2 times stronger in the upper and middle catchments than the lower catchment (Figs. 3.7b-d).

The channel steepness profiles (Fig. 3.3b) indicate higher erosion rates in high topography of the AMR, which indicates that lower catchment is in a different state than upper and middle catchments.

In addition, average erosion rates and drainage area of sampled catchments in the upper/middle and lower catchments show scattered distributions $R^2=0.060$ and $R^2=0.385$, respectively (Fig. 3.7e).

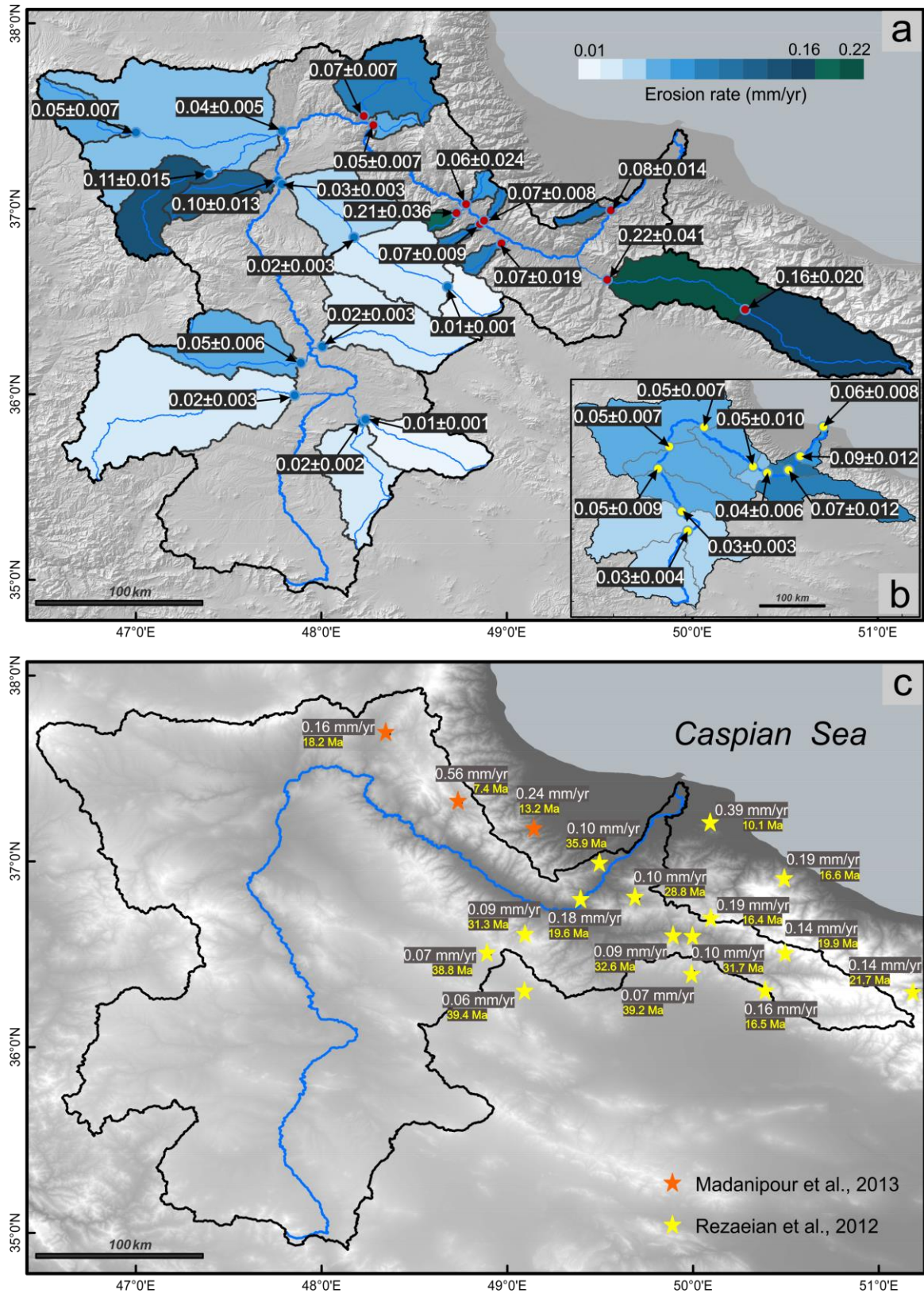


Fig. 3.5: Short-term erosion rates from ^{10}Be -measurements in the Qezel-Owzan River Basin. (a) Erosion rates for the sampled tributaries. (b) Erosion rates along the main river trunk channel. (c) Long-term exhumation and erosion age and rates Apatite Fission Track (AFT) data by (Rezaeian et al., 2012) and (Madanipour et al., 2013). Lines, polygons, circles and numbers as in Fig. 3.3a.

3.4.4 Correlation between short-term erosion rates and long-term exhumation rates

The calculated short-term erosion rates in the lower catchment are compatible with long-term exhumation rates (0.56 mm/yr; Madanipour et al., 2013; Fig. 3.5b). The high exhumation rates (0.56 and 0.16 mm/yr) in the western part of the lower catchment (Talesh Mountains, Fig. 3.1) are not in agreement with the slow short-term erosion rates there (Fig. 3.5). The eastern part of the lower catchment (west AMR), with long term exhumation rates of about 0.14 and 0.10 mm/yr, are in agreement with erosion rates derived from ^{10}Be (Fig. 3.5). Moreover, two long term exhumation rates (0.06 and 0.07 mm/yr) in the middle catchment are in good agreement with the short term erosion rates there (Fig. 3.5). These compliant correlations indicate that the landscape and topography in the middle and western part of the lower catchments of QOR is close to stable conditions and experiences slow erosion rates compared to the last 39.4 Ma (Late Eocene). In contrary, the eastern part of the lower catchment experiences almost constant erosion rates over the same period.

3.5 Discussion

In a region with limited effect of climate in the present-day, the river erosion can be used as a proxy for tectonic uplift, base-level change, or variations in sediment supply (Burbank et al., 1992). The Qezel-Owzan River Basin displays two groups of erosion rates: Low rates in the upper and middle catchments (SSZ and CIZ) and higher rates in the lower catchment (AMR; Figs. 3.1 and 3.5a, b).

The higher erosion rates in the lower catchment of QOR (south flank of AMR and Talesh Mountains), are dependent on present-day climate conditions but due to the weak correlation with erosion rates, climatic conditions are not the main regulators of landscape and topography (Figs. 3.4b and 3.7a). Apatite-He thermochronology in the AMR (Fig. 3.5c) indicates accelerated cooling in the Late Miocene-Early Pliocene. Considering constant convergence rate between Arabia and Eurasia since the Late Miocene, Rezaeian et al. (2012) attributed increased cooling to an increased exhumation rate as a response to changing climate conditions rather than tectonic influence. In the Late Miocene-Early Pliocene, the area experienced wet climate conditions and QOR merged with the Tarom Basin (Fig. 3.1) to discharge into the Caspian Sea (Heidarzadeh et al., 2017). In addition, sedimentation increased in the delta adjacent to Caspian Sea during the Middle Pleistocene, when Qezel-Owzan River connected to the Caspian Sea (Kazancı and Gulbabazadeh, 2013). All evidence from Late Miocene to Middle Pleistocene is attributed to climate influence as a main controller of landscape evolution.

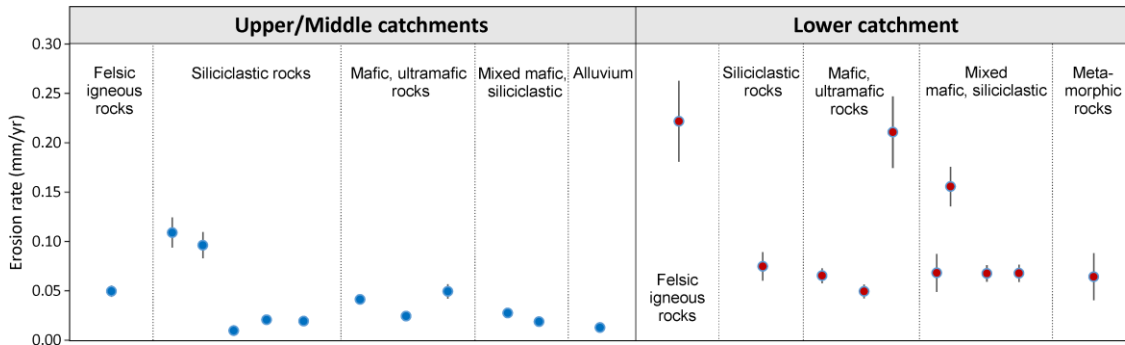


Fig. 3.6: Lithology-type plot versus erosion rates. Bedrock lithology for each sampled catchment extracted from geological maps (explained in Fig. 3.4a) shown with different symbol and color coded for upper/middle and lower parts of the catchment. Y-axis error bars (2σ): uncertainty in measured ^{10}Be content (Balco et al., 2008).

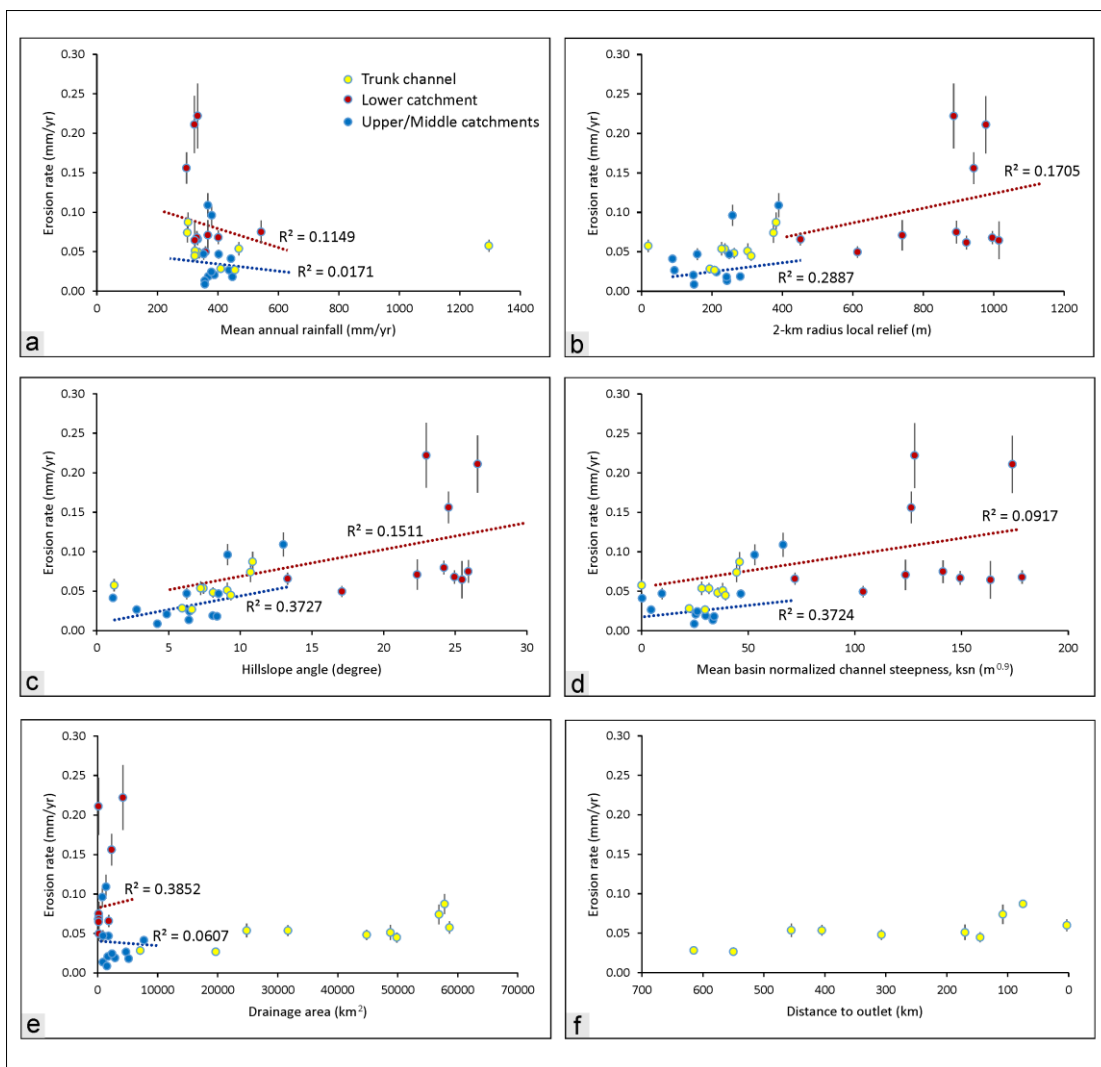


Fig. 3.7: Relationships between climatic/topographic parameters and ^{10}Be -derived catchment-averaged erosion rates in the upper, middle, and lower parts of the catchment and along trunk channel to find the role of tectonic, lithology and climate in modulating the landscape evolution: (a) Mean annual rainfall, (b) Local relief from a 2-km radius window, (c) Catchment-mean hillslope angle, (d) Catchment-mean normalized channel steepness index, ksn. (e) Catchments drainage area (f) Trunk channel samples distance to the outlet. Y-axis error bars (2σ) as in Fig. 3.6 and x-axis error bars are not shown but given in Table 3.3.

Our results show no significant relationship between the bedrock lithology and average erosion rates across the QORB, except in a local cases such as the tuffs of Sahand Volcano (Fig. 3.5a). In this case, higher erosion rates may be attributed to the Folded Miocene Belt activity (Fig. 3.1), which caused growth strata (~14.6 to 12.4 Ma) and have had an impact on local topography and subsidence pattern (Ballato et al., 2016). Generally, the siliciclastic rocks are dominant in the upper and middle catchments of QOR with lower erosion rates than the lower catchment with dominantly mafic rocks (Fig. 3.4a). Comparison of the three catchment parts show that the high erodible rocks in the upper-middle catchments did not control the erosion rates (Fig. 3.6). Therefore, the effect of lithology on the short-term erosion rate patterns and basin topography is insignificant and was excluded from the Qezel-Owzan catchment.

Topographic metrics and catchment-averaged erosion rates show a moderate correlation (Figs. 3.7a-f and 3.8). The topographic indices suggest a different state in the lower catchment of QOR. The lower catchment with low-erodible rocks (except for local cases) and moderate amount of precipitation (~550 mm/yr), displays higher channel steepness and incision rates than the upper/middle catchments (Figs. 3.1, 3.5a). Crustal shortening and thickening in the Middle-Late Miocene caused northward and vertical growth of the northern Iranian Plateau margin (Ballato et al., 2016). Integrating paleomagnetic data with stratigraphic, structural and GPS information shows that the present-day system of thrust (Caspian Fault; Fig. 3.1) and sinistral strike-slip faults (e.g. Guest et al., 2006) started in the Early Pliocene in the northern Iranian Plateau (Mattei et al., 2017). Short-term average erosion rates measured with ^{10}Be -derived methods correlate well with long-term erosion rates in the middle and lower catchments (Fig. 3.5). This reflects that for about 5 Ma ago the landscape in the north Iranian Plateau and its margin experienced slow erosion rates. Consequently, the topography of the lower catchment in Qezel-Owzan has reached a steady state for a period longer than 10^6 yr (Willett and Brandon, 2002). This can reflect topographic equilibrium relative to regional shortening (e.g. Pirouz et al., 2017) and limited contribution of mantle-flow processes that build up the north Iranian Plateau (Ballato et al., 2016). In the upper catchment, there is no thermochronometric data. The isostatic response of the thick (average 45 km; Jiménez-Munt et al., 2012) continental crust may be the main controlling factor of erosion in this part of the plateau (e.g. Stephenson and Lambeck, 1985).

Earthquake focal mechanisms (Fig. 3.1) in the AMR show dominant thrust components. Yet, nearly constant erosion rates supports the idea that faulting is predominantly strike-slip in the Tarom Basin.

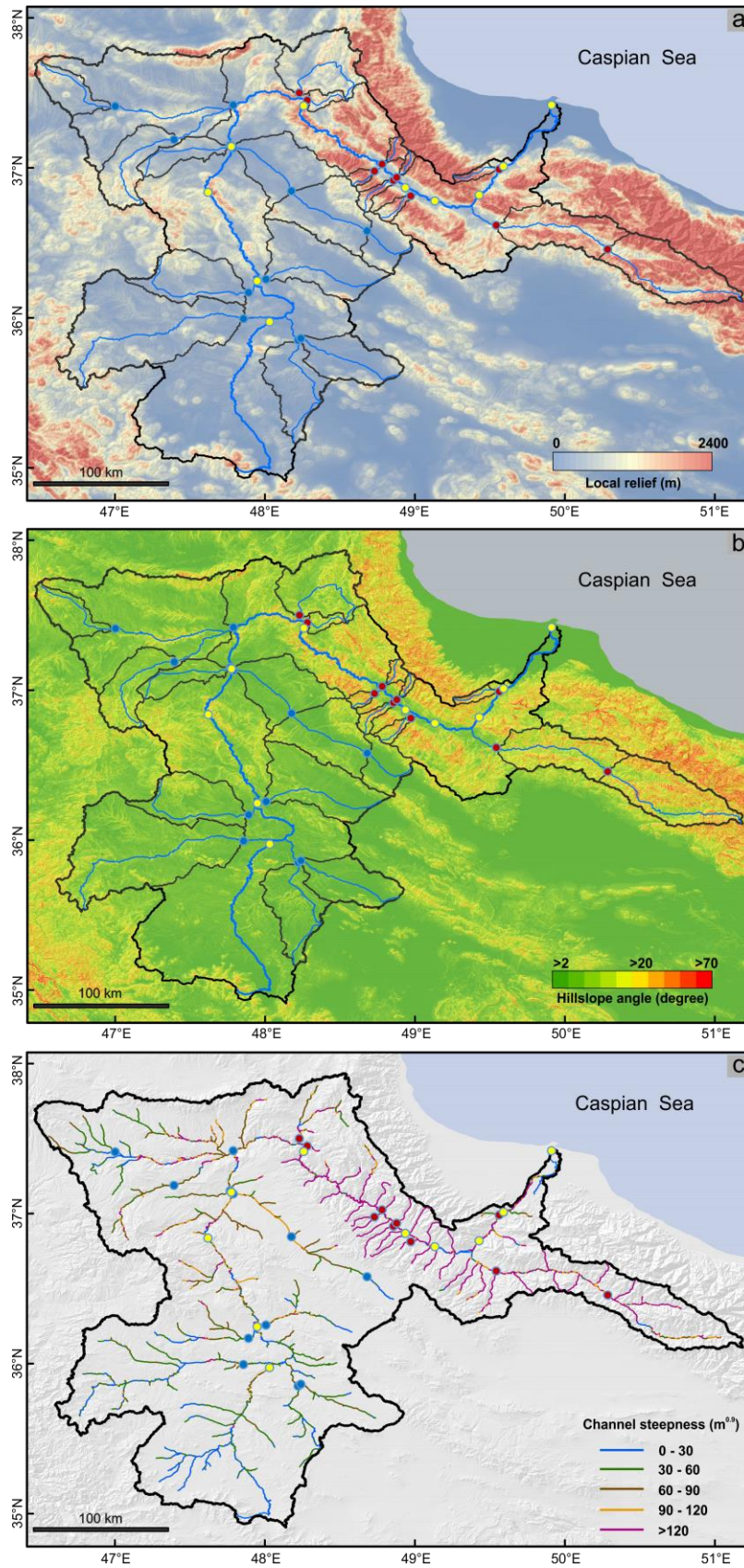


Fig. 3.8: Different topographic overview of the Qezel-Owzan River Basin, which shown in Fig. 3.7b, c, d. (a) Local relief map from a 2-km radius window, (b) Hillslope angle map, (c) Normalized channel steepness map. Coloured circles (sampling location) as in Fig. 3.7.

3.6 Conclusion

This study provides 32 catchment-averaged erosion rates derived from ^{10}Be content in the northern Iranian Plateau and margin.

Catchment-averaged erosion rates in the low relief upper catchment “Sanandaj-Sirjan Zone” range from 0.01 ± 0.001 to 0.05 ± 0.006 mm/yr, in the middle catchment “Central Iran Zones” they range from 0.01 ± 0.001 to 0.11 ± 0.015 mm/yr, and in the high relief lower catchment “Alborz Mountain Ranges” they range from 0.05 ± 0.007 and 0.22 ± 0.041 mm/yr. This suggests that a different state exists between the upper/middle and lower catchments of the Qezel-Owzan River. This difference coincides with differences in seismicity.

Present-day climatic conditions and rock types are not the main controllers of short-term erosion rates across the Qezel-Owzan River Basin.

In the upper/middle catchments, eastward-flowing tributaries have higher erosion rates than the westward-flowing ones. This difference is associated with low resistance rock (tuff) in the SE flank of Sahand Volcano or perhaps unknown active structures (e.g. Folded Miocene Belt). The low relief high plateau with regionally low short-term erosion rates is controlled by the isostatic response of the thick continental crust. This suggests that a balance exists between regional tectonics and erosion rates in the north Iranian Plateau.

In the lower catchment, the tributaries in the west Alborz Mountains, show higher erosion rates than tributaries in Tarom Basin. This indicates different states in the western and eastern parts of the lower catchment, which may reflect thrust- vs strike slip active faulting. Comparison between long-term exhumation rates with millennial-scale erosion rates suggests that the western part of lower catchment has experienced a slow erosion rate and steady condition since ~ 5 Ma, indicating a balance between erosion rate and regional shortening.

Table 3.1: Summary of measured ^{10}Be concentrations and calculated catchment-averaged erosion rates

Sample ID ^a	Sample Latitude (°N)	Sample Longitude (°E)	Mean basin latitude ^b (°N)	Mean basin longitude ^c (°E)	Effective basin elevation ^d (m)	Mean basin topographic shielding factor ^e	Blank corrected ^{10}Be concentration $\pm 1\sigma$ ^f ($\times 10^4$ atoms $\text{g}_{\text{quartz}}^{-1}$)	Erosion rate ^g (mm yr^{-1}) $\pm 2\sigma$
<u>Qezel-Owzan trunk channel</u>								
Az-Gh 159	35.9725	48.0315	35.4025	47.6919	1920.50	0.9994	35.31 \pm 1.78	0.03 \pm 0.004
Az-Gh-162	36.2451	47.9486	35.7394	47.7086	1913.10	0.9995	38.2 \pm 1.5	0.03 \pm 0.003
Az-Gh-148	36.8360	47.6207	35.8944	47.7690	1917.20	0.9996	18.94 \pm 1.22	0.05 \pm 0.009
Az-Gh 144	37.1442	47.7749	34.2041	45.2683	1874.10	0.9997	17.71 \pm 0.85	0.05 \pm 0.007
Az-Gh 140	37.4473	48.2757	36.4980	47.7444	1883.90	0.9988	20.83 \pm 1.08	0.05 \pm 0.007
Az-Gh-152	36.8679	48.9366	36.4146	47.8643	1784.83	0.9986	18.31 \pm 1.53	0.05 \pm 0.010
Az-Gh 153	36.7784	49.1330	36.4146	47.8643	1784.83	0.9986	20.71 \pm 1.27	0.07 \pm 0.012
Az-Gh 154	36.8184	49.4289	36.4146	47.8643	1784.83	0.9982	12.08 \pm 1.18	0.07 \pm 0.012
Az-Gh 156	37.0100	49.5907	36.4146	47.8643	1784.83	0.9982	10.39 \pm 0.69	0.09 \pm 0.012
Az-S-104	37.4157	49.9159	36.7022	48.3374	1850.90	0.9982	17.14 \pm 0.84	0.06 \pm 0.008
<u>Upper/middle catchments</u>								
Az-Gh 158	35.8498	48.2216	35.5511	48.1914	1869.00	1.0000	47.31 \pm 1.41	0.02 \pm 0.002
Az-Gh 157	35.8625	48.2399	35.7176	48.5644	1906.10	1.0000	114.1 \pm 2.5	0.01 \pm 0.001
Az-Gh 163	36.2559	48.0070	36.3715	48.3529	1898.90	0.9999	41.7 \pm 1.68	0.02 \pm 0.003
Az-Gh 150	36.5783	48.6815	36.4917	48.7962	1966.40	0.9997	79.17 \pm 2.05	0.01 \pm 0.001
Az-Gh-149	36.8452	48.1774	36.6383	48.5251	1935.60	0.9997	56.16 \pm 3.86	0.02 \pm 0.003
Az-Gh 143	37.1317	47.7895	36.7853	48.3673	1828.20	0.9998	36.86 \pm 1.17	0.03 \pm 0.003
Az-Gh 160	35.9934	47.8569	35.9347	47.1703	1982.80	1.0000	58.34 \pm 3.74	0.02 \pm 0.003
Az-Gh 161	36.1684	47.8907	36.2595	47.5236	1979.20	0.9997	22.62 \pm 0.9	0.05 \pm 0.006
Az-Gh 164	37.4109	47.0016	37.5181	46.6876	2037.60	0.9990	24.32 \pm 1.48	0.05 \pm 0.007
Az-Gh 142	37.1876	47.3946	37.0199	47.1067	2098.90	0.9993	10.16 \pm 0.62	0.11 \pm 0.015
Az-Gh 145	37.1517	47.7685	37.0868	47.4356	1641.60	1.0000	8.87 \pm 0.51	0.10 \pm 0.013
Az-Gh 141	37.4184	47.7887	37.399	47.1361	1906.50	0.9997	25.17 \pm 0.91	0.04 \pm 0.005
<u>Lower catchment</u>								
Az-Gh-109	36.9767	48.7305	36.9398	48.6374	2037.60	0.9919	5.05 \pm 0.53	0.21 \pm 0.036
Az-Gh-107	36.9300	48.8724	36.8182	48.7144	1926.30	0.9956	15.17 \pm 0.71	0.07 \pm 0.009
Az-Gh 151	36.8126	48.9728	36.7276	48.8479	1899.40	0.9964	14.14 \pm 3.04	0.07 \pm 0.019
Az-Gh 137	37.4991	48.2300	37.6889	48.3742	1869.70	0.9992	4.52 \pm 5.59	0.07 \pm 0.007
Az-Gh-138	37.4491	48.2819	37.4574	48.3867	1746.20	0.9993	19.15 \pm 1.07	0.05 \pm 0.007
Az-Gh-108	37.0242	48.7816	37.1187	48.8777	1943.00	0.9966	16.28 \pm 3.58	0.06 \pm 0.024
Az-Gh-106	36.9354	48.8791	37.0326	48.9511	1848.10	0.9969	14.58 \pm 0.64	0.07 \pm 0.008
Az-S-105	36.9900	49.5625	36.9634	49.4066	1079.00	0.9966	7.9 \pm 1.16	0.08 \pm 0.014
Az-Sh-101	36.4559	50.2860	36.3102	50.6841	2494.80	0.9963	4.63 \pm 2.33	0.16 \pm 0.020
Az-Sh-102	36.6167	49.5424	36.4362	50.3629	2160.30	0.9969	5.13 \pm 0.68	0.22 \pm 0.041

^a Catchment number shown in Figs. 3.3, 3.4 and 3.5.

^{b, c, d} Mean basin latitude, mean basin longitude, and effective basin elevation were calculated as per Portenga and Bierman (2011). These were the coordinates and elevations entered into the CRONUS-Earth online calculator version 2.3 (see text for details).

^e Catchment-averaged topographic shielding correction factor determined from the 90-m SRTM DEM using the algorithm of Codilean (2006) based on 5° intervals in both azimuth and elevation angles.

^f Measured ^{10}Be concentration corrected for the blank. Propagated errors (1σ) include the analytical uncertainties in the measured nuclide concentrations and the error of the blank.

^g Catchment-averaged erosion rate (with units L/T) based on the time-dependent production rate scaling model of Lal (1991)/Stone (2000). The reported uncertainty (external uncertainty) includes the measured errors from the counting statistics and the blank correction, as well as production rate and scaling uncertainties, see details in Balco et al. (2008).

Table 3.1: -Continued from previous page

Sample ID	Sample weight (g)	Carrier amount added (mg)	$^{10}\text{Be}/^9\text{Be}$ ($\times 10^{12}$)	Error (%)	Blank corrected ^{10}Be concentration (10^4 atoms/ g_{quz})	Uncertainty ($\times 10^4$ atoms/ g_{quz})	Uncertainty (%)
<u>Qezel-Owzan trunk channel</u>							
Az-Gh 159	12.0200	0.3066	0.2183	4.15%	35.31	1.78	5.04
Az-Gh-162	22.0500	0.3081	0.4223	3.63%	38.20	1.50	3.93
Az-Gh-148	23.5900	0.3088	0.2277	5.75%	18.94	1.22	6.44
Az-Gh 144	25.3500	0.3080	0.2293	3.95%	17.71	0.85	4.80
Az-Gh 140	21.3600	0.3069	0.2282	4.41%	20.83	1.08	5.18
Az-Gh-152	20.4400	0.4690	0.1265	7.44%	18.31	1.53	8.36
Az-Gh 153	14.3600	0.3058	0.1561	4.64%	20.71	1.27	6.13
Az-Gh 154	12.8500	0.3167	0.0829	6.07%	12.08	1.18	9.77
Az-Gh 156	24.8500	0.3058	0.1367	4.84%	10.39	0.69	6.64
Az-S-104	34.4930	0.3071	0.3001	4.41%	17.14	0.84	4.90
<u>Upper/middle catchments</u>							
Az-Gh 158	20.6800	0.3080	0.4892	2.71%	47.31	1.41	2.98
Az-Gh 157	17.2000	0.3061	0.9781	2.10%	114.10	2.50	2.19
Az-Gh 163	14.9000	0.3053	0.3168	3.52%	41.70	1.68	4.03
Az-Gh 150	36.3200	0.3078	1.4211	2.55%	79.17	2.05	2.59
Az-Gh-149	8.8400	0.3076	0.2530	6.29%	56.16	3.86	6.87
Az-Gh 143	27.1000	0.3106	0.4951	2.92%	36.86	1.17	3.17
Az-Gh 160	11.3200	0.3071	0.3341	6.03%	58.34	3.74	6.41
Az-Gh 161	32.9500	0.3063	0.3768	3.61%	22.62	0.90	3.98
Az-Gh 164	20.8400	0.3080	0.2578	5.49%	24.32	1.48	6.09
Az-Gh 142	30.3000	0.3078	0.1602	4.65%	10.16	0.62	6.10
Az-Gh 145	36.3300	0.3086	0.1669	4.44%	8.87	0.51	5.75
Az-Gh 141	33.7200	0.3070	0.4270	3.30%	25.17	0.91	3.62
<u>Lower catchment</u>							
Az-Gh-109	25.9920	0.3073	0.0736	5.75%	5.05	0.53	10.50
Az-Gh-107	29.6680	0.3063	0.2312	3.86%	15.17	0.71	4.68
Az-Gh 151	4.2400	0.3062	0.0387	8.88%	14.14	3.04	21.50
Az-Gh 137	2.0600	0.3111	0.0135	13.83%	4.52	5.59	23.67
Az-Gh-138	22.5800	0.3020	0.2257	4.79%	19.15	1.07	5.59
Az-Gh-108	4.9080	0.3075	0.0483	14.08%	16.28	3.58	21.99
Az-Gh-106	32.0500	0.2717	0.2702	3.57%	14.58	0.64	4.39
Az-S-105	10.7900	0.3080	0.0509	6.03%	7.90	1.16	14.68
Az-Sh-101	5.1840	0.4629	0.0139	12.46%	4.63	2.33	50.32
Az-Sh-102	18.8620	0.3072	0.0567	6.00%	5.13	0.68	13.26

Table 3.2: Catchment lithologies, characteristics and erosion rates

Sample ID	Catchment flow direction	Catchment area (km ²)	Mean elevation (m)	Rainfall (mm yr ⁻¹) ^a ± 1σ	Outcropping rock units ^b (% surface)						Erosion rate (mm yr ⁻¹) ± 2σ
					FI	SC	M	A	M-UM	L-E	
<u>Upper/middle catchments</u>											
Az-Gh 158	westward	1664.80	1862.85	388.15 ± 7.14	0.098	36.172	0.042	45.977	8.560	9.150	0.02 ± 0.002
Az-Gh 157	westward	1513.30	1893.81	356.96 ± 20.27	0.000	21.826	5.083	62.141	3.255	7.694	0.01 ± 0.001
Az-Gh 163	westward	2388.10	1883.35	378.32 ± 19.53	1.967	9.228	0.627	57.414	19.443	11.321	0.02 ± 0.003
Az-Gh 150	westward	845.90	2004.94	356.60 ± 12.66	5.982	5.409	0.212	65.831	17.504	5.061	0.01 ± 0.001
Az-Gh-149	westward	2879.40	1910.00	368.35 ± 31.12	4.461	21.553	0.344	53.237	17.166	3.239	0.02 ± 0.003
Az-Gh 143	westward	4701.20	1143.15	436.77 ± 3.48	4.614	13.524	0.212	49.235	19.636	12.779	0.03 ± 0.003
Az-Gh 160	eastward	5157.00	1966.37	447.79 ± 28.93	0.000	45.261	5.511	22.377	9.406	17.445	0.02 ± 0.003
Az-Gh 161	eastward	1785.30	1954.54	402.17 ± 11.39	4.409	27.757	4.835	27.435	1.291	34.273	0.05 ± 0.006
Az-Gh 164	eastward	867.10	1562.77	352.56 ± 1.08	3.037	5.568	0.000	10.841	76.839	3.715	0.05 ± 0.007
Az-Gh 142	eastward	1376.80	2062.16	366.72 ± 9.93	1.168	29.203	4.009	5.518	16.408	43.693	0.11 ± 0.015
Az-Gh 145	eastward	749.20	1612.36	379.30 ± 18.85	12.599	32.820	4.384	0.607	0.000	49.590	0.10 ± 0.013
Az-Gh 141	eastward	7683.00	1040.48	443.22 ± 0.69	7.006	18.322	0.719	18.004	34.277	21.673	0.04 ± 0.005
<u>Lower catchment</u>											
Az-Gh-109	northward	136.95	1954.68	322.18 ± 12.92	23.053	2.328	0.000	0.118	73.290	1.211	0.21 ± 0.036
Az-Gh-107	northward	195.71	426.67	401.62 ± 0.96	11.936	36.929	0.000	2.497	39.170	9.468	0.07 ± 0.009
Az-Gh 151	northward	192.33	1846.63	366.87 ± 70.31	16.989	30.971	0.000	1.022	49.790	1.228	0.07 ± 0.019
Az-Gh 137	southward	1843.60	1826.93	333.53 ± 35.86	12.342	9.906	0.040	20.651	46.861	10.199	0.07 ± 0.007
Az-Gh-138	southward	216.60	1701.77	359.23 ± 54.54	9.528	0.000	0.000	0.575	53.045	36.852	0.05 ± 0.007
Az-Gh-108	southward	162.92	1876.67	323.43 ± 23.41	3.469	10.070	56.138	4.115	13.121	13.086	0.06 ± 0.024
Az-Gh-106	southward	86.88	1748.89	330.43 ± 30.63	4.175	13.705	41.069	3.960	23.076	14.014	0.07 ± 0.008
Az-S-105	eastward	157.52	985.67	543.02 ± 153.24	0.000	60.311	19.551	0.566	6.473	13.099	0.08 ± 0.014
Az-Sh-101	westward	2321.10	2406.45	296.13 ± 35.52	19.974	27.450	0.000	9.680	31.515	11.381	0.16 ± 0.020
Az-Sh-102	westward	4202.20	2004.60	333.03 ± 67.32	17.967	23.320	0.000	7.611	34.053	17.048	0.22 ± 0.041

^a Mean annual rainfall obtained from 50 years daily gridded data averaged during the period of 1950-2000 (Hijmans et al., 2005).

^b Abbreviations of rock units: FI = Felsic Igneous rocks (e.g. granite, gneiss, rhyolite, latite, acidic tuff), SC = Silici Clastic rocks (e.g. conglomerate, sandstone, siltstone, quartzite), M = Metamorphic rocks (schist, slate, phyllite, amphibolite), A = Alluvium, M-UM = Mafic and Ultramafic rocks (e.g. gabbro, anorthosite, dolerite, monzonite, nepheline-syenite), L-E = Limestone and Evaporites rocks (e.g. mudstone, claystone, gypsiferous).

Table 3.3: Catchment climatic/topographic metrics

Sample ID	Rainfall (mm yr ⁻¹) ± 1σ	Mean elevation (m) ± 1σ	Local relief (m) ^a ± 1σ	Mean slope (°)	Catchment-averaged k_{sn} (m ^{0.9}) ^b	Catchment-averaged k_{sn} (m ^{0.9}) ^c
<u>Qezel-Owzan trunk channel</u>						
Az-Gh 159	388.15 ± 7.14	1936.79 ± 160.69	194.05 ± 55.02	5.94	22.34	15.30
Az-Gh-162	356.96 ± 20.27	1989.51 ± 223.97	207.14 ± 135.85	6.63	29.82	20.08
Az-Gh-148	378.32 ± 19.53	2004.27 ± 252.73	227.35 ± 156.65	7.23	28.19	19.08
Az-Gh 144	356.60 ± 12.66	1958.01 ± 275.95	236.66 ± 163.01	7.43	31.63	21.42
Az-Gh 140	368.35 ± 31.12	1620.18 ± 266.03	262.77 ± 173.30	8.10	35.68	24.41
Az-Gh-152	436.77 ± 3.48	1562.23 ± 414.36	301.36 ± 209.36	9.09	38.08	26.00
Az-Gh 153	447.79 ± 28.93	1542.97 ± 431.62	311.55 ± 240.94	9.35	39.34	26.86
Az-Gh 154	402.17 ± 11.39	1444.58 ± 391.61	374.57 ± 287.09	10.72	44.53	30.65
Az-Gh 156	352.56 ± 1.08	1418.05 ± 351.28	382.31 ± 291.44	10.86	45.94	31.56
Az-S-104	366.72 ± 9.93	1392.06 ± 297.46	399.81 ± 270.42	11.84	46.37	32.90
<u>Upper/middle catchments</u>						
Az-Gh 158	388.15 ± 7.14	1862.84 ± 144.15	147.30 ± 81.31	4.87	25.36	16.54
Az-Gh 157	356.96 ± 20.27	1893.80 ± 175.53	149.05 ± 109.37	4.22	24.72	15.53
Az-Gh 163	378.32 ± 19.53	1883.34 ± 173.90	212.88 ± 128.84	6.46	26.12	16.59
Az-Gh 150	356.60 ± 12.66	2004.93 ± 161.35	242.91 ± 136.83	6.42	33.43	21.10
Az-Gh-149	368.35 ± 31.12	1910.00 ± 253.23	280.51 ± 183.95	8.08	30.00	19.20
Az-Gh 143	436.77 ± 3.48	1143.14 ± 19.10	93.43 ± 5.98	2.77	4.48	3.10
Az-Gh 160	447.79 ± 28.93	1966.37 ± 192.55	241.69 ± 130.44	8.37	34.03	23.90
Az-Gh 161	402.17 ± 11.39	1954.54 ± 279.07	249.26 ± 131.27	8.49	46.54	31.00
Az-Gh 164	352.56 ± 1.08	1562.76 ± 32.54	158.39 ± 29.69	6.27	9.58	6.00
Az-Gh 142	366.72 ± 9.93	2062.15 ± 346.81	389.60 ± 147.06	13.00	66.34	42.14
Az-Gh 145	379.30 ± 18.85	1612.35 ± 310.61	258.23 ± 84.63	9.12	53.01	33.88
Az-Gh 141	443.22 ± 0.69	1040.47 ± 1.48	88.09 ± 10.00	1.12	0.29	0.20
<u>Lower catchment</u>						
Az-Gh-109	322.18 ± 12.92	1954.67 ± 58.87	977.98 ± 223.34	26.56	173.78	103.78
Az-Gh-107	401.62 ± 0.96	426.67 ± 16.67	222.09 ± 24.44	5.41	6.53	4.32
Az-Gh 151	366.87 ± 70.31	1846.63 ± 47.55	740.37 ± 196.16	22.34	123.70	77.20
Az-Gh 137	333.53 ± 35.86	1826.92 ± 253.72	451.43 ± 154.97	13.30	71.84	43.74
Az-Gh-138	359.23 ± 54.54	1701.77 ± 286.69	613.35 ± 121.44	17.09	103.83	64.71
Az-Gh-108	323.43 ± 23.41	1876.67 ± 310.65	1015.00 ± 221.21	25.47	163.50	97.98
Az-Gh-106	330.43 ± 30.63	1748.88 ± 417.52	996.45 ± 248.42	24.94	178.32	107.34
Az-S-105	543.02 ± 153.24	985.66 ± 132.35	894.34 ± 228.76	25.91	141.27	100.05
Az-Sh-101	296.13 ± 35.52	2406.45 ± 619.33	943.59 ± 281.34	24.53	126.41	70.18
Az-Sh-102	333.03 ± 67.32	2004.59 ± 538.95	886.54 ± 265.23	22.98	127.97	75.39

^a Local relief from a 2-km radius window from 30m DEM (see text for details).

^b Normalized channel steepness index, k_{sn} , calculated by slope-area method and using drainage area as a proxy for discharge (see text for details).

^c Normalized channel steepness index, k_{sn} calculated by integral method and replacing area with rainfall driven discharge.

4 Present-day crustal deformation of the Turkish-Iranian Plateau: insights from kinematic modelling

Amaneh Kaveh Firouz^a, Laurentiu Danciu^b, Alireza Khodaverdian^b, Jean-Pierre Burg^a

^a *Geological Institute, ETH Zurich, Sonneggstrasse 5, 8092 Zurich, Switzerland*

^b *Swiss Seismological Service (SED), ETH Zurich, 8092 Zurich, Switzerland*

This chapter will be submitted to an international journal of earth science after some modifications

Abstract

Convergence between the Arabian and Eurasian Plates causes crustal deformation that is partly accommodated within the Turkish-Iranian Plateau and Caucasus mountain belts. The Neotectonics of the region is a complex combination of active faults, tectonic uplift, Neogene-Quaternary volcanism, sea-level fluctuations and offset drainage networks. The dominant faults are the NW-SE striking eastern segment of the North Anatolian Fault (NAF) and North Tabriz Fault (NTF), both with shallow and diffuse seismicity and dextral strike slip component. Seismic activity is concentrated along these active faults and is often considered, together with fault properties (location, geometry and slip-rates), a proxy to the crustal deformation.

To quantitatively evaluate the spatial distribution of ongoing crustal deformation in the study region, we developed a regional kinematic model, built upon information and data on tectonic plate boundaries, geology (fault traces and slip-rates), geodetic measurements (GPS measurements) and principal stress directions. Hence, in this chapter, we discuss the development of a dynamic (kinematic) model as a proxy to assess the crustal deformation of the E-Turkish-NW Iranian Plateau and surrounding areas. Firstly, the slip rates for all mapped faults are estimated and secondly, the regional strain rate fields are evaluated. Inherent uncertainties are associated to both geodetic and geologic measurements and quantitatively accounted for in our kinematic model. The kinematic slip rates of the faults in the region indicate a high active shortening (~ 11 mm/yr) across the Alborz-Talesh, Bitlis and Greater Caucasus Mountain ranges. High strain rate fields ($\sim 10^{-14.4}$ to $10^{-15.4}$ s⁻¹) are concentrated in narrow zones along the eastern

segment of the NAF towards the NTF in the Turkish-Iranian Plateau, which is in relative agreement with morphotectonic measurements, active faulting and the observed seismicity in the region. Moreover, there are various regions of high strain fields that are not located along fault systems, which might indicate unknown or unmapped active faults. Low strain rate fields are observed in the north Iranian Plateau away from active features which are also indicated by low seismicity. Our previous work based on geomorphological analysis (river profile analysis) and erosion rates (cosmogenic ^{10}Be) suggests that tectonic movement is a significant controller of topography and landscape evolution in the investigated study region. However, geomorphological analysis might be suitable to understand the regional deformation as their results are consistent with high values of strain rates along the active faults as well as with the observed seismicity in this region.

4.1 Introduction

The region of interest is located at the core of the Turkish-Iranian plateau and extends into the northern part to the Caucasus (Fig. 4.1). This region is known for intense seismic activity due to collision of the Arabian and Eurasian plates (Fig. 4.1; Hempton, 1987; Reilinger et al., 2006a). Two thrust belts, the Zagros Mountains and the Caucasus Mountains bound the region to the south and to the north, respectively (Jackson and McKenzie, 1984).

The neo-tectonics of the region is complex, including shallow and diffuse seismicity and modification of topography by volcanoes and river drainage systems. Geodynamic models suggest that the Arabia-Eurasia convergence alone cannot explain the neo-tectonics of the region and that remnant subduction below the Caucasus or delamination below the Lesser Caucasus may be active (e.g. Vernant and Chery, 2006). A significant part of this deformation is accommodated by strike-slip faulting (Karakhanian et al., 2004; Masson et al., 2006; Vernant et al., 2004). Despite the fact that fault activity is important, fault slip rates and contribution of distributed seismic sources have remained partly unknown. Furthermore, the NW-SE striking eastern segment of the North Anatolian Fault (NAF) and North Tabriz Fault (NTF, Fig. 4.2), both with earthquakes and dextral strike slip fault plane solutions confined to shallow depth (10-42 km; Copley and Jackson, 2006) suggest possible linkage between these two faults at depth. Previous geological studies suggest that the associated Khoy-Mishu-Tabriz fault system in NW Iran (Fig. 4.2) may be reworked suture (e.g. Alavi, 2007).

To forecast tectonic deformation within a given region integrates, some key elements, such as the plate model, continental deformation and dynamic models might be considered. Two kinematic models are often used (Thatcher, 1995): (i) continental microplate tectonics where deformation is

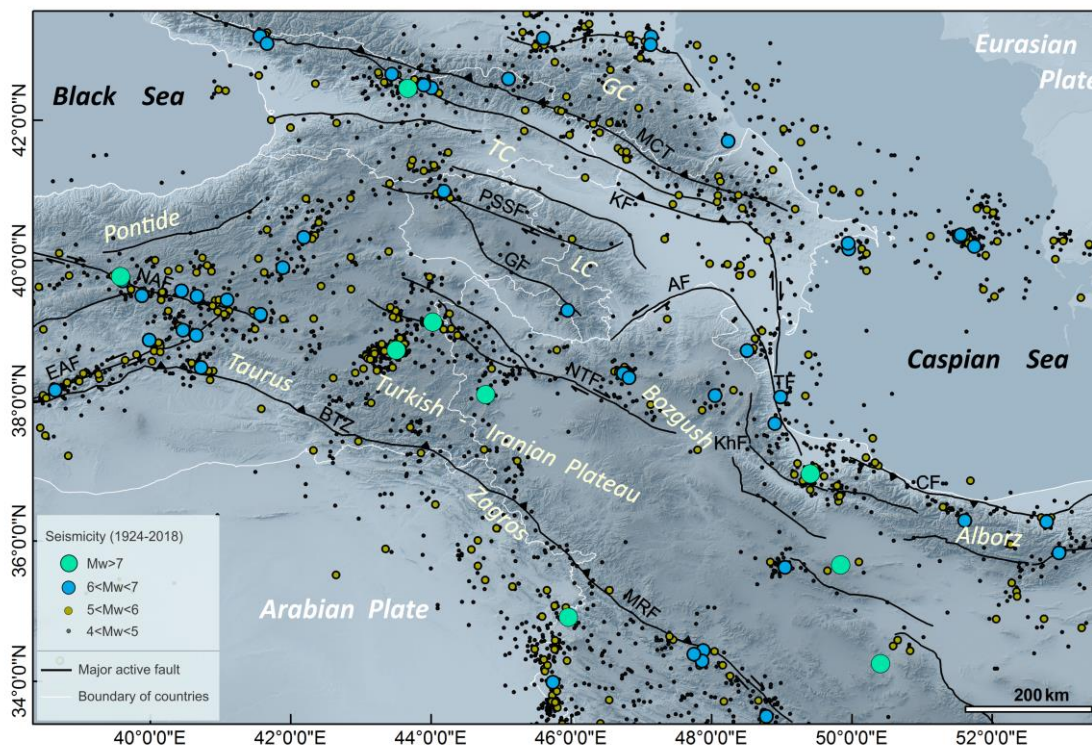


Fig. 4.1: Topography of the Turkish-Iranian Plateau and Caucasus Region from a SRTM 90m DEM (Jarvis et al., 2008). Colored circles: seismicity of the area based on USGS earthquake catalog. Yellow abbreviations: subdivision of Caucasus regions (GC: Greater Caucasus, TC: Trans-Caucasus and LC: Lesser Caucasus). Explanation of the active faults name from active fault map of Iran (Hessami et al., 2003), NW Iran (Faridi et al., 2017; Nazari et al., 2013), Turkey (Dhont and Chorowicz, 2006; Koçyiğit et al., 2001), Armenia (Karakhanian et al., 2004), Georgia (Forte et al., 2014; Gudjbidze and Gamkrelidze, 2003): AF=Arax Fault; BTZ=Bitilis Thrust Zone; CF=Caspian Fault; GF=Garni Fault; KF= Kura Fault; KhF=Khalkhal Fault; MCT=Main Caucasus Thrust; MRF=Main Recent Fault; NTF=North Tabriz Fault; PSSF=Pambak-Sevan-Sunik Fault; TF=Talesh Fault.

concentrated in major active faults; (ii) continental continuum tectonics where a strain rate field is distributed throughout the deforming region. The continental microplate model considers only the major boundary faults and neglects smaller faults within the blocks. For instance, by using geodetic measurements, some parts of the Turkish-Iranian Plateau and southern part of Caucasus are modeled with elastic blocks separated by a few boundary faults and neglect the minor faults within the blocks (e.g. Djamour et al., 2011; Karakhanyan et al., 2013; Reilinger et al., 2006a; Sokhadze et al., 2018). Therefore, it cannot resolve the detailed shape and small-scale variations of the strain pattern (Stein and Mazzotti, 2007). Discharging the small geological features may be a reasonable assumption, given that there are examples of non-tectonic lineaments, i.e. flood, erosion scarps, strandlines, alluvial terrace scarps, and escarpments that are not tectonic.

Historical and present-day seismicity indicate seismic patterns related to identify faults (Fig. 4.1). The correlation between seismicity and potentially active faults is important as seismicity does not cover enough observational time to describe the recurrence cycle of large magnitude

earthquakes. Hence, deformation patterns derived from seismicity may be incomplete (Fig. 4.1 for an overall view of the correlation between seismicity and active faults). To describe the continuous continental deformation, additional information is required. Today, the best practice is to combine geodesy, geologic data and global plate tectonic reconstructions to quantitatively characterize the deformation pattern of a given region (e.g. Djamour et al., 2011; Reilinger et al., 2006a).

In this study, we applied a continuous kinematic modelling technique aiming to understand the present-day crustal deformation of the east Turkish-NW Iranian Plateau and surrounding mountain belts. The continuous kinematic model (i.e. “kinematic finite-element model, Bird and Liu, 2007) combines active faults, principal stress directions with geodetic velocities to estimate velocity and strain rate fields, given a-prior boundary conditions. Boundaries conditions are constrained by the rates and direction of movement of the major neighboring tectonic plates. Note, that the tectonic regime and stresses can vary with time, thus the tectonic forces applied early in the plate movement may not be the same as today. Next, geodetic and regional stress directions, and geological slip rate of the active faults are other important keys.

Two goals are set: (i) estimate fault slip rates with less uncertainties; (ii) estimate the spatial distribution of crustal strain rates in the region by considering regionally compiled geodetic velocities, geological datasets (active faults) and regional stress orientations. Note, that the kinematic model considers a continental continuum tectonic models, hence, the best fit of the kinematic model yields an estimate of long-term deformation, fault slip rates, and distribution of strain rates between active faults.

In this chapter, first we aim to describe the active tectonic background of the study region, then describe the applied method and input datasets and finally discuss the results to estimate the long-term fault slip-rates and the strain rate field in the Turkish-Iranian Plateau and the Caucasus Regions.

4.2 Regional background: tectonics, geology and seismicity

The Turkish-Iranian Plateau and Caucasus regions (Fig. 4.1) belong to the Alpine-Himalayan orogenic belt (e.g. McKenzie, 1978; Stocklin, 1968). This region extends over ~1,500,000 km² and trends WNW-SSE, results from Arabia-Eurasia collision since the Late Eocene (e.g. Ricou, 1994; Şengör et al., 1988). The region is actively deforming due to the northward motion of the Arabian plate with respect to Eurasia (23-25 mm/yr, e.g. Reilinger et al., 2006a). A significant portion of the crustal movement is absorbed by shortening and is accommodated within active faults (Djamour et al., 2011; Karakhanian et al., 2004; Masson et al., 2006; Vernant et al., 2004).

The historical/instrumental seismic catalogues show that moderate to large-magnitude earthquakes occur in the region since at least 600 BC (e.g. Ambraseys, 1978; Berberian et al., 2001; Berberian and King, 1981). The majority of the plateau stands on a mean elevation of about 1800 m, except the high relief mountain ranges in the north and south. GPS measurements indicate that the current northward crustal motion of the Turkish-Iranian Plateau is 13–15 mm/yr with respect to a fixed Eurasia (Reilinger et al., 2006a; Zarifi et al., 2014). East Turkey (Anatolia) and NW Iran are located between the Caucasus Thrust to the north and the Bitlis-Zagros Thrust Belt/suture zone to the south (Fig. 4.1). The earthquake fault plane solutions mostly display strike-slip components (Copley and Jackson, 2006) with a variety of kinematic roles including strain partitioning (Talebian and Jackson, 2002). The active faults are NW-SE dextral, NE-SW sinistral strike slips that can generate large-magnitude earthquakes (e.g. Ambraseys and Melville, 2005; Karakhanian and Abgaryan, 2004). These fault directions are conjugate and separate the wedge-like Anatolian Plate from the Eurasian and Arabian Plates, respectively (Arpat and Saroglu, 1972; Arpat and Saroglu, 1975). The Caucasus is a WNW-ESE trending mountain range between the Black Sea to the west and the Caspian Sea to the east (Pirouz et al., 2017). It is sub-divided into three main domains from north to south (Fig. 4.1): Greater Caucasus (GC), Trans-Caucasus (TC), and Lesser Caucasus (LC). GPS measurements indicate that the convergence rate across the mountains is increasing eastward from ~ 2 mm/yr near the Black Sea to ~ 15 mm/yr near the Caspian Sea (Kadirov et al., 2012; Reilinger et al., 2006a). Seismic data display mostly moderate to large events (USGS catalogue from 1924-2018; Fig. 4.1). Fold systems contribute to N-S crustal shortening (Copley and Jackson, 2006; Philip et al., 2001). According to focal mechanisms, the current regime is dominated by thrusting (Jackson, 1992b). Active examples in the GC are the Main Caucasus Thrust (MCT), Kura Fold and Thrust Belt (KFTB), and Adjara-Trialeti Fault Zone (Figs. 4.1, 4.2). The frequency of strong earthquakes in the east Turkish Plateau are higher than the NW Iranian Plateau (Fig. 4.1). The number of seismic events in the Lesser Caucasus is greater than the number of events occurring in the Greater Caucasus (Fig. 4.1; e.g. Karakhanian et al., 2004).

4.3 Kinematic model: method, assumptions and input data

4.3.1 Method and assumptions

The continuous kinematic model, adopted in this study was implemented in the finite-element program - Neokinema (Bird and Liu, 2007). The input datasets used to develop the model are GPS measurements, geological slip rates and stress directions.

Anelastic (or permanent) strain rates and probable fault slip-rates probabilistically estimated over long observational time intervals (10^4 - 10^6 yr) are the main result of the kinematic model.

The key assumptions of the model are: (i) self-consistently balanced geodetic velocities for temporary effects of shallow fault locking before being used to estimate long-term tectonic flow; (ii) principal ‘stress directions’ to constrain orientations and senses of strain-rate in the continuum between faults; (iii) a bootstrap method to obtain the median level of scalar anelastic strain-rate in these continuum elements. Sensitivity analyses are mandatory to find a best-fit to all data sets (Liu and Bird, 2008).

The model is dimensionless (Bird, 2009) due to the objective function of model which is a function of both dimensional model predictions (p) and corresponding dimensional data values (r) divided by a dimensional covariance matrix (C) or by individual datum standard deviations (σ), and

$$\Pi = -(\bar{P} - \bar{r})^T [\tilde{C}_{GPS}^{-1}] (\bar{P} - \bar{r}) - \frac{1}{L_0} \sum_{m=1}^M \int_{\text{length}} \frac{(p_m - r_m)^2}{\sigma_m^2} dl - \frac{1}{A_0} \sum_{n=1}^3 \iint_{\text{area}} \frac{(p_n - r_n)^2}{\sigma_n^2} da \quad (1)$$

Where the \bar{P} is the vector of target velocities derived from geodetic benchmark, C_{GPS} is covariance matrix, r is vector of the predicted velocities at benchmark; the second term involves: M is long-term fault offset rates r_m with their uncertainty σ_m and the predicted offset rates (p_m), and the third term related to orientations and size of distributed permanent deformation rate tensors between modeled faults. $n=1$ is related to uncertainty of continuum deformation rate, $\sigma_n = 1$ is parameter mu (μ : scalar measure of typical anelastic strain rates in a continuum) and one of the three tuning parameters (more explanation in the next paragraph), $n = 2$ and $n = 3$, are related to principal stress directions (Liu and Bird, 2008). Three tuning parameters (A_0 , L_0 , and μ) are applied to find the best-fitted model. A_0 is the area of a continuum with its stress directions and limited stiffness, which is as important as one geodetic benchmark in the solution. L_0 shows the length of fault with the prescribed geological slip-rate.

The relative quality of the fits between the geologic-geodetic data and the continuum constraints are controlled by adjusting A_0 and L_0 . Three dimensionless misfit measures are used to explore the quality of any particular model. Each measure is a root-mean-square norm (N_2) of a vector of non-dimensionalized misfit to data:

$$N_2^{\text{geodetic}} = \sqrt{\frac{1}{2B} \sum_{b=1}^B (\bar{P}_b - \bar{r}_b)^T [\tilde{C}_b^{-1}] (\bar{P}_b - \bar{r}_b)} \quad (2)$$

Where B is the number of GPS benchmarks; this misfit at each benchmark involves only the local (2×2) covariance of its two horizontal components C_b , and

$$N_2^{\text{stress}} = \sqrt{\frac{1}{\sum a_i} \sum_{i=1}^{\text{elements}} a_i \left(\frac{p_i - r_i}{\sigma_i} \right)^2} \quad (3)$$

Where a_i are the area of the finite-elements and the predictions (p_i) and data (r_i) are both transformed versions of the azimuth of the most compressive principal horizontal strain rate, and

$$N_2^{\text{potency}} = \sqrt{\frac{1}{\sum \sum l_{im} w_m h_{im}^{\text{sup}}} \sum_{i=1}^{\text{elements}} \sum_{m=1}^M l_{im} w_m h_{im}^{\text{sup}} \left(\frac{p_{im} - r_m}{\sigma_m} \right)^2} \quad (4)$$

Where l_{im} is the trace length of fault m in element i , w_m is the down-dip width of the seismogenic portion of fault m , and h_{im}^{sup} is the greater one of the model heave rate or datum heave rate.

The above N-factors are required to set-up the suitable kinematic model and the main objective is to obtain values ≤ 2 and as close as possible to 1. Models with values below 1 are considered to be over conservative whereas models above 2 are considered too simplistic. Thus, sensitivity analysis is conducted to choose the best fitted model with focus on N-factors range of values between 1 and 2. Such sensitivity analysis is given in Section 4.4.

In the next sections we discuss the main input datasets used in the development of the kinematic model for our region of interest.

4.3.2 Input data

To assess the regional deformation flow, the spatial distribution of strain rate is evaluated by using four datasets: the geological fault slip rates (Fig. 4.2, Table S1), collected and homogenized for the entire region, maps of regional stress directions (Fig. 4.3, Table S2), geodetic velocities data (Fig. 4.4, Table S3) and velocity boundary conditions (Fig. 4.2).

4.3.2.1 Active Faults

The dataset has been compiled from available reports and publications. (1) seismotectonic maps of Iran (Hessami et al., 2003) and NW Iran (Nazari et al., 2013), (2) active fault maps of NE Turkey (scale: 1:250,000; Emre et al., 2012), (3) dataset from Danciu et al. (2017) and Giardini et al. (2013) and (4) different articles providing detail information on active faults in the given region (e.g. Azad et al., 2011; Berberian and Yeats, 1999; Dhont and Chorowicz, 2006; Forte et al., 2014; Karakhanian et al., 2004). Moreover, the active faults were revised (189 entries) using the satellite images (Landsat, Google Earth) and the ~90m resolution Shuttle Radar Topography Mission (SRTM) DEM (Jarvis et al., 2008). The active faults were primarily selected using the following criteria from Danciu et al. (2017):

- Identified Holocene active faults - capable of earthquakes during the last 10 000 years with high values of slip-rates (i.e. Northern Anatolian Faults, Zagros Transform Faults)
- Active in Quaternary period (2 million years) with a slip-rate of about 0.1mm/year
- Faults with a slip rate ≥ 0.1 mm/yr corresponding to 1m in Holocene (~10 000 years)

- Faults responsible for earthquakes with moment magnitude ($M_w > 6$)
- Fully parameterized geometry and geological slip rates.

In the present investigation, the resulting dataset consists of 189 entries, where each fault dataset entry describes the fault location, geometrical properties, and seismogenic characteristics. The fault location is described by the location of map trace, but most of the dataset entries are sub-surface traces, hence have some degree of uncertainty. The geological slip rate of a given fault covers a long period of time and does not represent a constant motion along this fault, even though the motions of tectonic plates are regular.

In fact, fault slip rates are measured from offset of geological and geomorphological features, paleoseismological investigations, remote sensing, and geodetic information with respect to age. Heave rates and uncertainties on the faults contribute to the target strain rates of all elements. The throw rate of dip-slip faults and their uncertainties can be converted into the heave rate and its uncertainty by using assumed fault dips in the kinematic model. This is also done by iterating the solution for nonlinearities equations (typically 20 times; Bird and Kagan, 2004). Dip-slip faults are permitted to slip obliquely (with strike-slip no more than a specified fraction of dip-slip) to allow a more flexible fault network.

The uncertainties on the slip-rates depend on uncertainties in geology and geodetic velocity, which is about 1 standard deviation of the geological and geodetic data (Fig. 4.4). However, the uncertainty decreases to ~ 0.6 mm/yr in NW Iran and the central part of the Alborz range thanks to dense and precise GPS network. Conversely, the southern part of the Iranian Plateau (e.g., Zagros belt) suffers from disperse geodetic data with high uncertainties, and thus uncertainties on slip rates increase to 1.7–2 mm/yr. The highest uncertainty occurs for the Bitlis-Zagros zone and the lowest uncertainty for the Lesser Caucasus and north Iranian Plateau (Fig. 4.4 and Tables S1, S3).

All reported slip rate sources are independent from seismicity because our aim is to produce a map of estimated long-term deformation rates. Thus, given the importance of slip-rates in our attempt to understand the regional tectonic deformation, we investigate the impact of the slip-rates in the kinematic model. As such, we consider first the impact of the overall dynamics of a system described by GPS measurements, stress direction, boundary conditions to the slip-rates estimates, via the kinematic modeling of the region. The impact is quantified by measures of uncertainties on the existing/reported slip-rates values of the active faults. Secondly, the impact is quantified by new estimates of the slip-rates for the faults dataset. Details of the two alternative kinematic model are given in section 4.5.

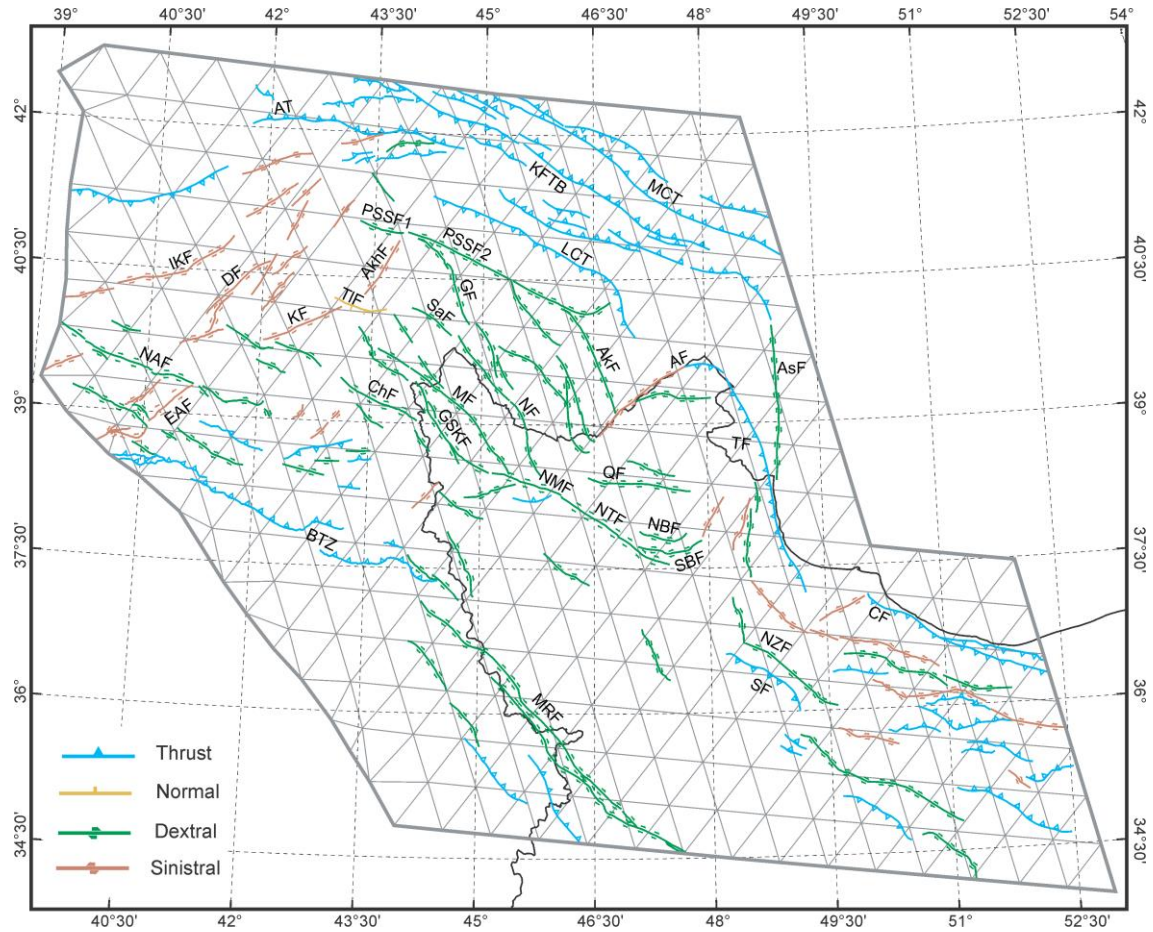


Fig. 4.2: Traces of active/potentially active faults in the Turkish-Iranian Plateau and Caucasus Regions. Given colors to the traces are according to their sense of movements. The background is finite-element grid used in the kinematic modelling. Heavy grey outline displays boundaries. Black polyline is border of NW Iran.

4.3.2.2 Stress Directions

This dataset is obtained from the World Stress Map (WSM; Heidbach et al., 2016). WSM describes the crustal stress patterns at a global scale using stress inversion of earthquake focal mechanisms. A total of 1621 nodes within the greater frame (29°E – $62^{\circ}\text{E} \times 24^{\circ}\text{N}$ – 52°N , Fig. 4.1) was retained and used to interpolate the principal stress direction at the center of each finite element of the model (Bird and Li, 1996).

The domain of the kinematic model is considered as elastic medium and the stress directions are responsible for the regional strain rate directions. Thus, different stress regimes, derived from observed seismicity, including strike-slip (SS), normal faulting (NF), thrust faulting (TF), and combinations of NF with SS (trans-tension, NS) and TF with SS (trans-pressure; TS) are considered. The stress regime in NW Iran changes from oblique to strike slip faulting (Afra et al., 2017; Fig. 4.3). In eastern Anatolia and Lesser Caucasus, the direction of maximum horizontal

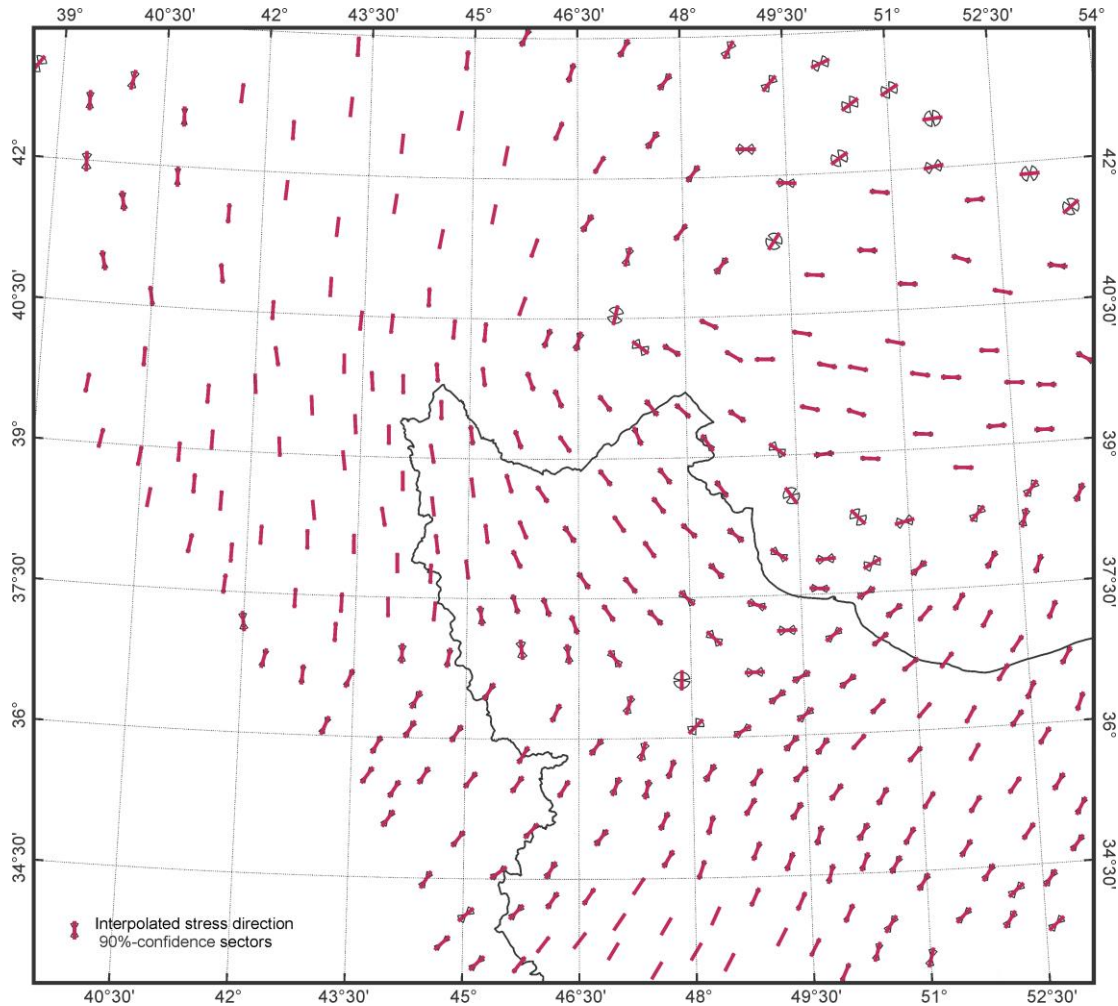


Fig. 4.3: Interpolation of horizontal principal stress directions from World Stress Map (WSM; Heidbach et al., 2016), shown in one third of interpolated directions. The stress regime changes from NW Iran to eastern Anatolia and Lesser Caucasus.

stress is nearly north-south (Karakhanyan et al., 2013). The direction turns to east-west in the Talesh region (Fig. 4.3). The results substantiate the strike-slip and thrust faulting stress regimes in northwest Iran. Note, that the overall stress directions are estimated from seismicity, thus they may not represent the long-term stress profile of the region, unless the earthquake catalogue is complete for several seismic cycles.

4.3.2.3 Geodetic Velocity

Fig. 4.4 shows the GPS measurements (horizontal velocities) in the region of interest. Holding GPS stations, as a reference, preferably away from any active fault, "fixed" (e.g. located in the Eurasia plate) allows determining the relative motion of other stations with respect to that reference station. Therefore, an array of instruments across the region shows (with uncertainties) ongoing surface displacements, which might help to estimate the slip rate of major faults

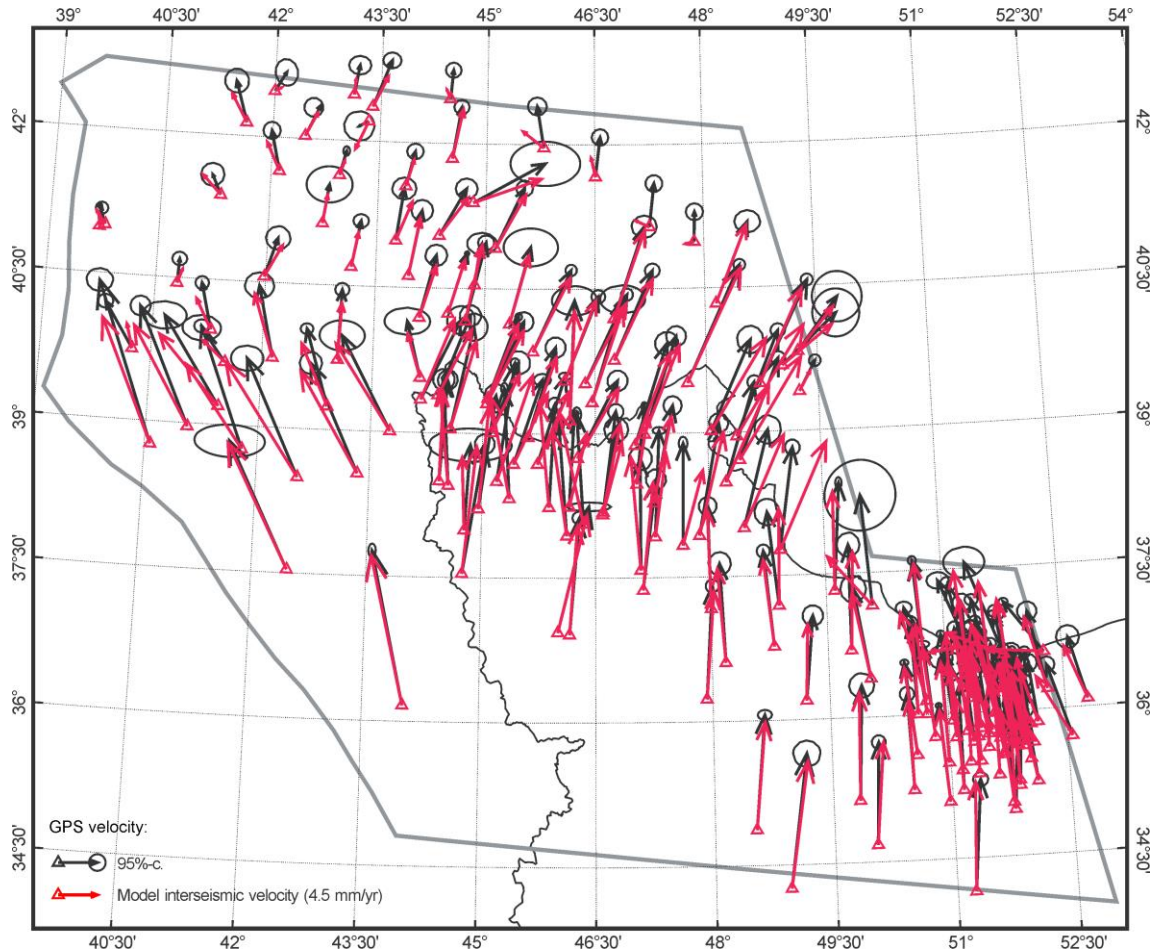


Fig. 4.4: Velocities at geodetic benchmarks (red arrows) relative to measured ones (black arrows) with interseismic velocity about 4.5 mm/yr as a scale. Uncertainty on measurements are given by the size of the circle. All GPS data transformed to a unified frame “ITRF2008” relative to Eurasia (Palano et al., 2017) and used in this study to constrain the kinematic model of the region.

(e.g. Reilinger et al., 2006). GPS measurements were compiled from Kadirov et al. (2012), Karakhanyan et al. (2013), Sokhadze et al. (2018), and Palano et al. (2017). The dataset consists of GPS velocities measured within 10 years campaign, between 2006 and 2016, by 208 stations and homogenized as a unified frame “ITRF2008” relative to Eurasia fixed (Palano et al., 2017). In addition, GPS benchmarks were considered as internal point constraints on the velocity field. Before being used in the model, the GPS data were corrected by analytical solutions for rectangular dislocations in a homogeneous half-space media.

The GPS measurements show a divergence of velocity vectors between East Turkey (SE-NW), NW Iran (almost N-S), and the Caucasus (SW-NE; Fig. 4.4) thus indicating that this region is tectonically complex with heterogeneous stress regimes.

4.3.2.4 *Velocity Boundary Conditions*

Velocity boundary conditions may be imposed around the margins of a kinematic simulation, and this is highly required as a way of enforcing both (approximate) rigidity of the surrounding plates and correct net relative velocity across the model domain (Bird, 2009). The western boundary of our model is a boundary of the Arabian and Anatolian plates, according to the model PB2002 (Bird, 2003). For the east, south and northern boundaries, the velocity on the boundary nodes are extracted from the kinematic model of the whole Iranian Plateau presented by Khodaverdian et al. (2015; Fig. 4.2).

4.4 **Kinematic model: model details and tuning parameters**

In our investigation the kinematic model comprises regionally compiled GPS measurements, stress directions and all the active faults. A first step in the development of the model is to evaluate the impact of the errors in the assigned slip-rates.

As such, we alternate the use of faults, with and without the slip-rates. When the former was considered will contribute to estimate the regional strain rate whereas the later will provide the basis for comparison with assigned slip-rates of the active faults dataset. Note, that the inputs of the kinematic model are the same (GPS measurements, stress directions, fault location) for the two cases, but the tuning parameters are evaluated separately in the next section.

A comparison was conducted with existing peer-reviewed literature and discussed in section 4.5. Moreover, to evaluate the impact of every input dataset on the regional strain values an extensive sensitivity analysis was conducted. Alternative pairs of input data were considering either faults with slip-rates or GPS measurements and stress direction. The boundary condition representation and the stress directions within the region are constant input to the kinematic model. The differences observed for the two cases, indicate dominant inputs when deriving the regional strain rate map.

In the next section the evaluation of the tuning parameters to setup a suitable kinematic model of the region is provided. The domain of our geo-spatial model is divided into 2-dimensional triangular elements, generating a gridded mesh of finite elements, where every grid point has 2 degrees of freedoms (i. e. the south and east components of the long-term mean velocity (Kong and Bird, 1995). Differentiation of the velocity on grid points reveals a 2- dimensional permanent strain rate tensor.

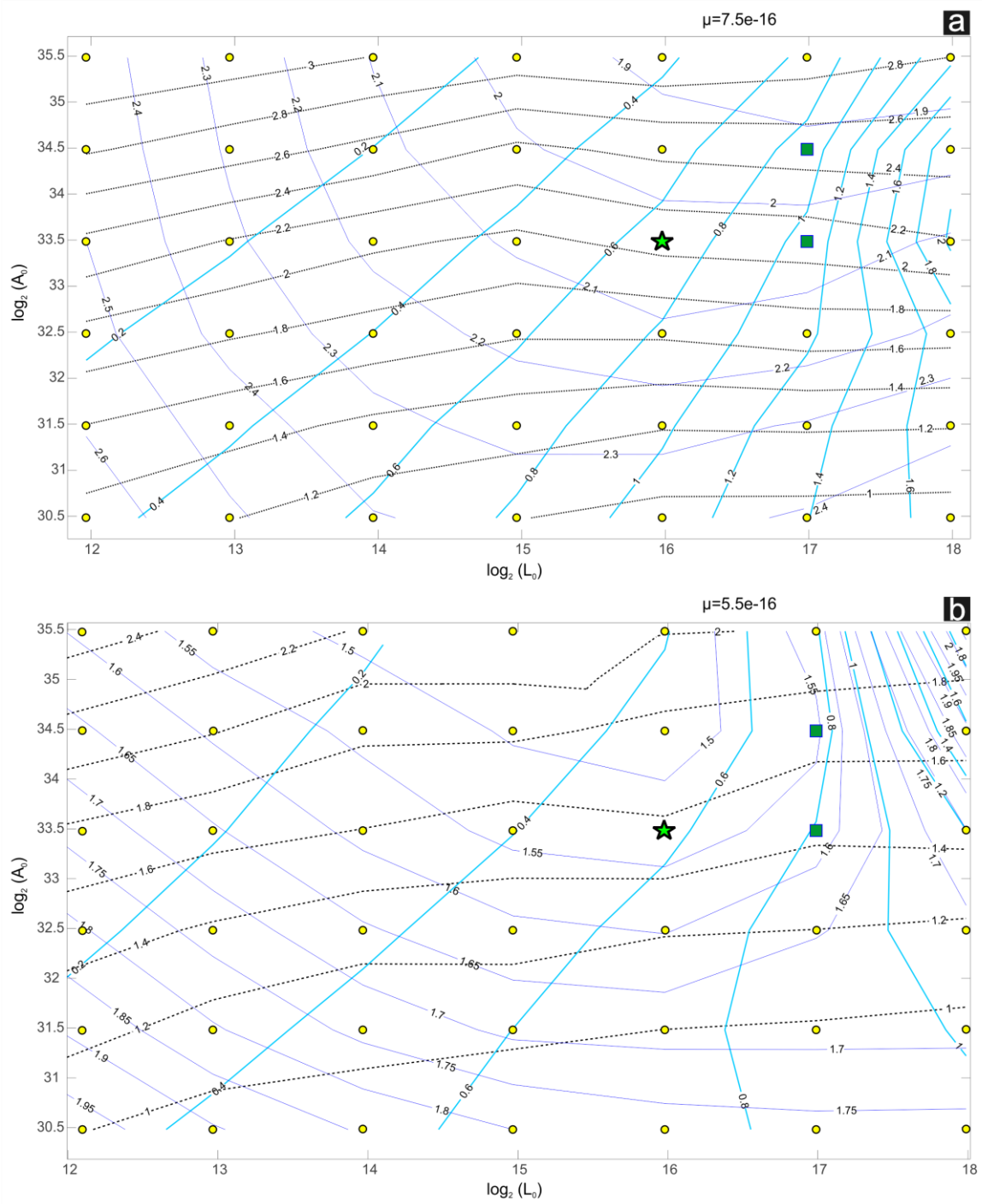


Fig. 4.5: Three misfit measures “potency, geodetic, stress” are shown by thick, thin, and dotted lines and their values as a function of tuning parameters L_0 and A_0 , for $\mu = 7.5 \times 10^{16}$ and $5.5 \times 10^{16} \text{ s}^{-1}$ for models a (comprehensive model with all given input dataset) and b (kinematic model without fault slip-rate input dataset), respectively. Each model is shown by solid circle. Model with the optimum values of (L_0, A_0) shown by green star which is concordance with the best-fit of our kinematic model and the green squares are acceptable models.

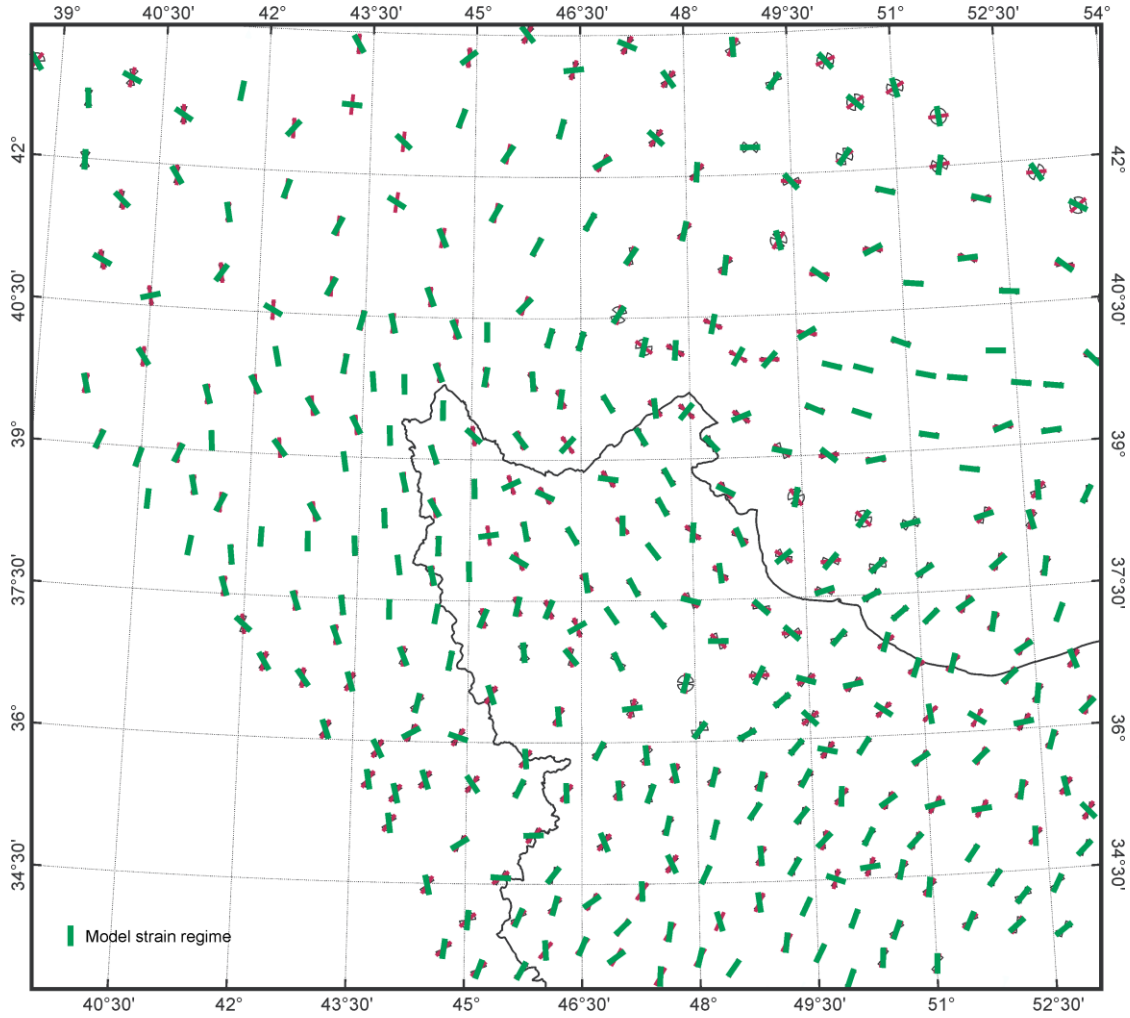


Fig. 4.6: calculated strain direction (green) relative to interpolated stress direction (red).

To support the model building process and find the best-fitted kinematic model, we performed a sensitivity analysis of three primary adjustable parameters (tuning parameters described in section 4.4) for two analyzed kinematic models with different input datasets (with all given dataset and excluding fault slip-rates). A two-dimensional finite element grid of triangles are used to cover the study area (Fig. 4.2). The triangles have same size to be homogenous and to improve the accuracy of results. The grid of this study is composed of 779 nodes and 495 triangles with 50-63 km long sides (Fig. 4.2). Parameter μ (μ) is a prior/input uncertainty of continuum deformation rate and to find the best suitable value.

Considering all given datasets, we tested four μ values from 6.0×10^{-16} , 6.5×10^{-16} , 7.0×10^{-16} , $7.5 \times 10^{-16} \text{ s}^{-1}$ which was reached fit for $7.5 \times 10^{-16} \text{ s}^{-1}$. Then we tried, 42 models fixed at $1.2 \times 10 \text{ m}^2$ (A_0) and $6.4 \times 10^4 \text{ m}$ (L_0) with fixed μ at $7.5 \times 10^{-16} \text{ s}^{-1}$ to find the best values of A_0 and L_0 (Fig. 4.5). To find the best fitted model between the 42 models, the level of misfit errors from N_2 geodetic, N_2 potency and N_2 stress is restricted to values < 2 due to uncertainties of our input dataset. The

mean uncertainty on relative velocity for the geodetic data is about 1.6, due to uncertainty on GPS data of 0.1 – 2.43 mm/yr. Given the insufficient information on slip-rates of the active faults, we assumed an average of 1.8 mm/yr with uncertainty of 0.15-10 mm/yr for potency slip-rate uncertainty. Furthermore, we limited the stress direction uncertainty to 2, considering geodetic data and potency slip-rates (Fig. 4.3). In addition, the uncertainty of μ , allows more flexibility of the kinematic model. Consequently, large μ values reduce misfit errors of geologic, geodetic, and stress direction data. GPS velocity vectors and interpolated stress directions in our best-fitted model have more than 85% confidence between the calculated and measured (Figs. 4.4, 4.6). For an assumed A_0 , increasing L_0 places less weight on fault slip rates and more on geodetic data, stress directions, and continuum boundary conditions. Conversely, for an assumed L_0 , increasing A_0 reduces the relative weight of continuum conditions and stress directions and increases the weight of GPS data and fault slip rates.

When the kinematic model without fault slip-rates is considered three μ values are tested: 5.5×10^{-16} , 6.5×10^{-16} , 7.0×10^{-16} , s^{-1} and the stable value was $\mu = 5.5 \times 10^{-16} s^{-1}$. Next, 42 models with fixed $A_0 = 1.2 \times 10^2 m^2$ and $L_0 = 6.4 \times 10^4 m$ were calibrated to find the best values of A_0 and L_0 (Fig. 4.5b). In this try, the misfits of potency slip-rates, geodetic and stress directions were limited to about 2 due to uncertainties about 2, 1.2 and 1.7 mm/yr for potency, geodetic and stress, respectively. The discrepancy between the two tried kinematic models is mu parameter.

4.5 Results and discussion

In the next two sections we provide an overview of the main results of the kinematic model with first estimated fault slip-rates and then strain field.

4.5.1 Estimation of fault slip rates

In this section, we illustrate and compare our results with published ones as summarized in Table 4.1. The kinematic model with constant GPS, stress and boundary conditions provides the basis to estimate the slip-rates given the fault location. The estimated slip-rates or the probable values are summarized in and given in Fig. 4.7. The range of slip-rates values is about 0.02 to 25 mm/yr. Furthermore, a comparison is conducted with respect to peer-reviewed literature. According to such peer-reviewed literature, 20 active faults have reported activity rates due to geodetic, paleoseismology and geological investigations and were retained for comparison.

Probable slip rates of all active faults, the effect of uncertainties of the slip-rates indicate a good agreement of the mean slip-rate values. Moreover, the dispersion around the mean slip-rates is lower due to use of additional datasets (GPS and stress direction) and calibration of tuning

parameters in the kinematic model. The agreement between the slip-rates values are given in Fig. 4.8a, b.

Figure 4.7 indicates the estimated slip-rates on the basis of active fault location and the basic kinematic model. Comparison between the probable fault slip-rates and EMM dataset indicates that the scattered distribution and weak correlation (Fig. 4.8c). This model has more consistency with published slip-rates for some major active faults (e.g. TF, EAF, PSSF) compared to the minor faults (Figs. 4.7a and 4.7b).

Probable slip-rates evaluated with the kinematic model for the major active faults in the Northern part of Iranian Plateau, varying between ~ 1 and 4 mm/yr (Fig. 4.7). The Soltanieh Fault (SF) with SW-dipping thrust (Berberian and Arshadi, 1976) and a dextral component, reported as one of the least active faults in the literature (e.g. Allen et al., 2011a). The historical and instrumental earthquakes ($M > 5$) along SF with the lack of geomorphic evidence were used to infer that the slip-rate of SF should be 0 (Berberian and Arshadi, 1976). The only evidence of SF strike-slip activity is the 10-15 km right-lateral displacement of the so-called Abhar syncline which indicates that the strike-slip motion should be dominant component (Allen et al., 2011), while our kinematic model gives precedence to the thrust component (Fig. 4.7) and estimated a heave rate of about 1.6 mm/yr for SF (Fig. 4.7). To the north of SF, the North Zanzan Fault (NZF) is characterized by 15-20 m high scarp in the Late Quaternary which suggests a dominant dip-slip faulting (Allen et al., 2011a; Azad et al., 2011). Trying a thrust component with zero value input for the NZF, the model output shows minor amount of thrusting while dextral slip fits observations much better. There is no estimated slip rate along the NZF in the available works. Using purely elastic block model from geodetic data, cannot estimate the slip rates of the SF and NZF due to their location within the block, but probable slip-rate estimated about 1.2 - 1.5 mm/yr right lateral for NZF (Fig. 4.7).

In the northwestern part of the Iranian Plateau, the estimated fault slip rates vary between ~ 1 and ~ 6 mm/yr. On the western margin of the South Caspian Basin and across the Talesh Mountain, the Talesh Fault (TF) has a thrust component accommodating about 6 mm/yr of regional shortening (Fig. 4.7), which was estimated at ~ 8 mm/yr in block model (Reilinger et al., 2006a). To the east of TF, the kinematic-based slip-rates are ~ 1 mm/yr slip rate for Astara Fault (AsF) as given in Figs. 4.2, 4.7, which is close to the geodetic estimation of $\sim 1.23 \pm 0.03$ mm/yr (Barzegari et al., 2016). The highest slip rate value (about 6 mm/yr) is estimated along the North Tabriz Fault (NTF, Fig. 4.7). Again, this is in good agreement with paleoseismological investigations ascribing an average slip rate along the NTF of ~ 6.5 mm/yr, (Faridi et al., 2017), which is further supported

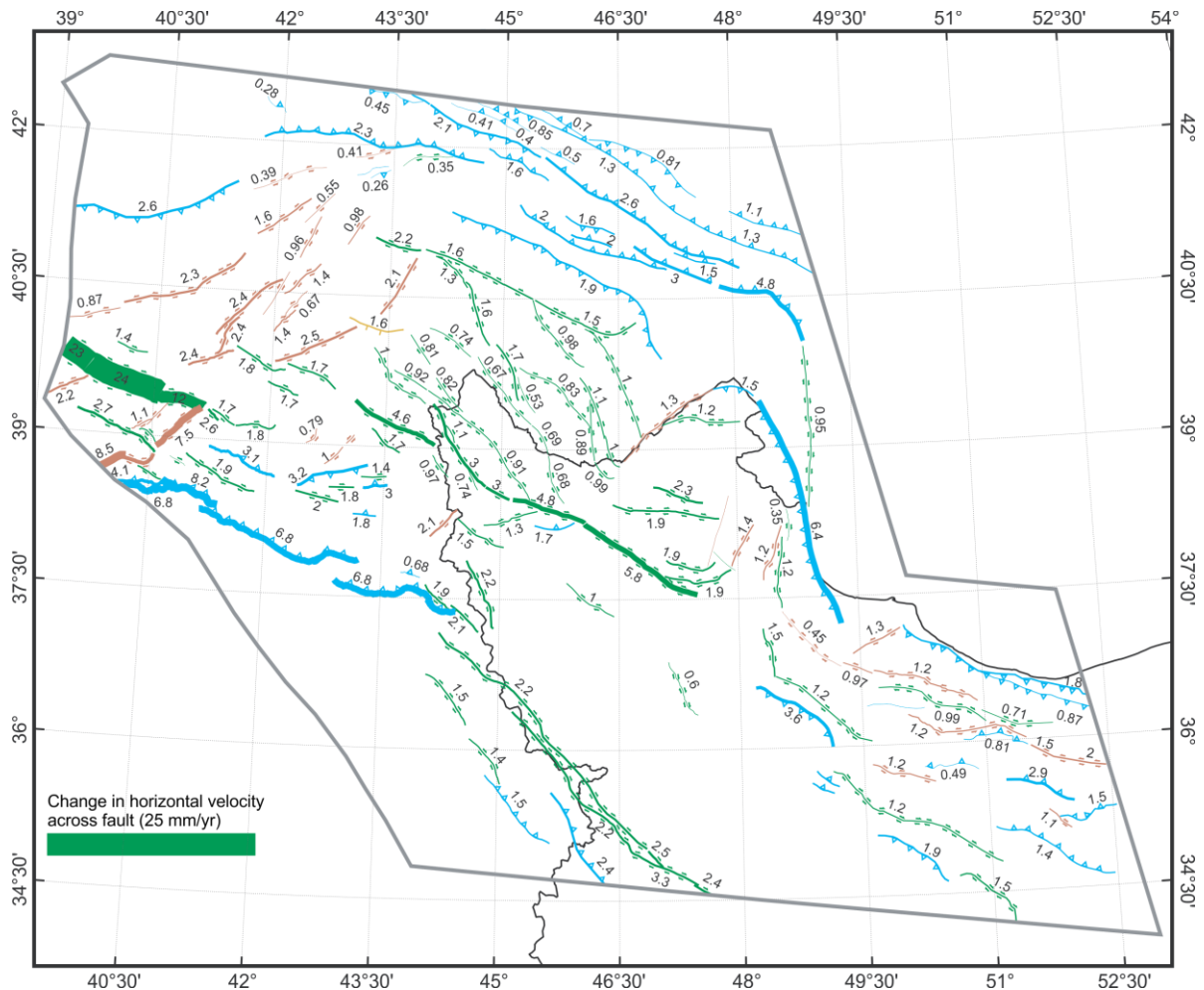


Fig. 4.7: (a) The slip and shortening-rates estimated from best-fitted complete kinematic model. The thickness of each line is related to the long-term slip rate. –Continued on next page.

by 6 to 10 mm/yr from InSAR analysis (Su et al., 2017; Table 4.1). To the northwest of NTF, the probable slip-rates of Gailatu-Siahcheshmeh-Khoy Fault (GSKF) is consistent with a slip rate of 2 mm/yr from paleoseismological studies (Faridi 2018). Due to the weakness of the block model and low density of GPS network, there is limited testing for the GSKF by the block model (Djamour et al., 2011), however, (Karakhanian et al., 2004) estimated less than 2 mm/yr slip rates for the GSKF according to long recurrence time interval (>1500 yr). The present investigation indicates a slip rate of ~1-3 mm/yr for GSKF (Fig. 4.7a) which is in good agreement with previous studies. The North Mishu Fault (NMF) is another active fault located between GSKF and NTF and geodetic data estimated slip-rate about 2.62 mm/yr (Su et al., 2017). Estimated a 4.8 mm/yr dextral slip rate for it (Fig. 4.7a). Another more recent active fault is the Qoshadagh Fault (QF, Fig. 4.2), which experienced a seismic event in 2012 (Faridi et al., 2017). The model yields ~1.9 mm/yr average slip rate for it, in good agreement with results of paleoseismological analysis (~1.9 mm/yr, Faridi, 2018).

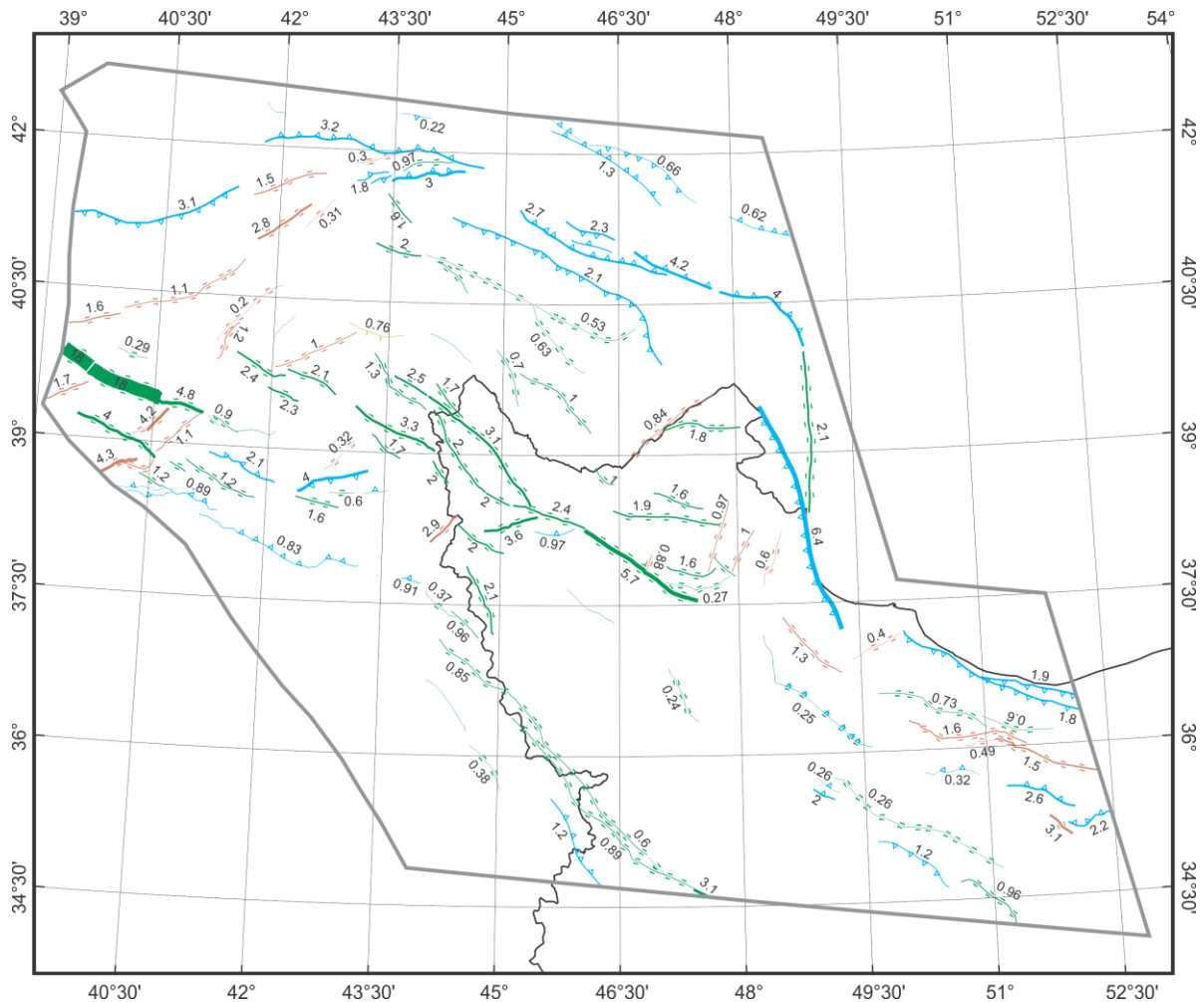


Fig. 4.7: -Continued from previous page- **(b)** The slip-rates estimated from best-fitted kinematic model excluding input slip-rates.

The Arax Fault (AF) is segmented into two parts with an important thrust component to the east and a dominant sinistral strike slip component to the west (Fig. 4.2). The estimated slip-rate suggests 1.5 and 1.3 mm/yr for the AF components, respectively (Fig. 4.7a). Part of the eastward movement of Azerbaijan Region relative to the Caspian Sea is parallel to the inferred sinistral faults (e.g. AF; Jackson, 1992b).

The north and south Bozgush Faults (NBF and SBF; Fig. 4.1) are minor active faults within the NW Iran block and our model predicted a slip rate of ~ 1.9 mm/yr along it (Fig. 4.7a). Drainage displacements along these faults show dextral movement and recent geological studies in the Bozgush Mountain shows range-parallel right lateral faults (Faridi et al., 2017). According to the upper bound measurement in block model, the slip-rates could yield less than 1-2 mm/yr for NBF and SBF (Djamour et al., 2011). For the similar case, kinematic model estimated slip rate of ~ 1 mm/yr (Fig. 4.7a) along the Maku Fault (MF, Fig. 4.2) and this in good agreement with upper bound measurement in block model, about 1 mm/yr for MF (Djamour et al., 2011). This indicates

that the minor active faults within the blocks, can be effective to active deformation of area, not necessarily the major faults located in the block boundary.

The predicted slip rates from the kinematic model vary between 1.4 and ~ 3.3 mm/yr along the strike slip faults and between 1.5 and 2.4 mm/yr for the thrust faults (Fig. 4.7a) in the west Iranian Plateau. The Main Recent Fault (MRF) of Zagros is a main geological structure in this region. The geomorphological analysis indicates a 1.6-3.2 mm/yr slip rate for MRF (Alipour et al., 2012), while in situ cosmogenic dating (^{36}Cl) indicates 3.5-12.5 mm/yr slip rates (Authemayou et al., 2009). Due to lack of GPS networks close to the MRF, Palano et al. (2017) estimated the slip rate in an indirect way by vector decomposition and suggested ~ 8 to 11 mm/yr right lateral slip rate. This implies large differences between our result, which is varying between 1.9 and 3.3 mm/yr from NW to SE along the fault (Fig. 4.7a) with those by Authemayou et al. (2009) and Palano et al. (2017). The applied method by Authemayou et al. (2009) and Palano et al. (2017) have high uncertainties compared to our results and their approaches are probably not appropriate to measure slip rate of the faults. To achieve the precise slip rate value along the MRF, the region needs more studies and denser GPS networks. .

To the south of the Turkish Plateau, the Bitlis Thrust Zone (BTZ, Fig. 4.1), the predicted fault heave rate with the kinematic model is ~ 7 to 9 mm/yr from east to west (Fig. 4.7a). A block model using GPS data estimated a slip rate of only $1.2\text{-}3.7\pm 0.4$ mm/yr (Reilinger et al., 2006a). This discrepancy may reflect the differences in modelling assumptions. Moreover, geological and geomorphological studies are lacking to estimate the slip rate of BTZ.

The dextral North Anatolian Fault (NAF) is the major active fault system in eastern Turkey, separating the Anatolian and Eurasian Plates (Fig. 4.1). This fault controls the neotectonic evolution of Turkey and the eastern Mediterranean region and is characterized by a strong and large seismicity ($M_w > 6$). The measured GPS velocities depict an average of right lateral slip rate $\sim 25.3\pm 0.2$ mm/yr in the eastern segments of NAF (Reilinger et al., 2006a). Probable slip rates are estimated to be between 12-24 mm/yr along the eastern segments of the NAF (Fig. 4.7a) and is in good agreement with previous studies. The sinistral East Anatolian Fault (EAF) is the second major fault system in Turkey, between the Anatolian and Arabian Plates (Fig. 4.1). This fault, considered as a conjugate to the NTF terminates at the Karliova triple junction where it meets with the NTF. Present investigation estimated slip rates between 6.6-8.5 mm/yr in the NE segments of EAF (Fig. 4.7a) and GPS measured slip rate $\sim 6.3\pm 1.0$ mm/yr (Aktug et al., 2016), which is closer to our estimation rather than $\sim 9.9\pm 0.2$ mm/yr by Reilinger et al. (2006a).

The Chalderan Fault (ChF) is one of the main active faults in eastern Turkey with a recorded large earthquake ($M=7.3$, 1976; Fig. 4.1). Probable slip-rate estimated 4.6 mm/yr along ChF for the

Region	Fault Name	Estimated Slip Rate (mm/yr)	Slip Rates From Other Studies		
			Slip Rate (mm/yr)	Method	Reference
NW Iran	North Tabriz Fault (NTF)-Amand segment	~6 (RL)	6.5	Paleoseismology	Faridi, 2018
	Gailatu-Siahcheshmeh-Khoy Fault (GSKF)	~1-3 (RL)	2	Paleoseismology	Faridi, 2018
	North Mishu Fault (NMF)	4.8 (RL)	2.62	Geodetic	Zhe Su et al., 2017
	Qoshadagh Fault (QF)	1.9 (RL)	1.9	Paleoseismology	Faridi et al., 2018 unpublished
	Talesh Fault (TF)	6.4 (Sh)	~8	Geodetic	Reilinger et al., 2006
	Astara Fault (AsF)	~1 (RL)	1.23	Geodetic	Barzegari et al., 2016
	Main Recent Fault (MRF)	1.9-3.5 (RL)	1.6-3.2	Geomorphic indices	Alipoor et al., 2012
East Turkey	NAF (in the eastern segments)	12-24 (RL)	25±0.2	Geodetic	Reilinger et al., 2006
	EAF (in the eastern segments)	6.6-8.5 (LL)	6.3±1.0; 9.9±0.2	Geodetic	Aktug et al., 2016; Reilinger et al., 2006
	Chalderan Fault (ChF)	4.6 (RL)	3.27±0.17	Geology	Selçuk et al., 2016
LC	Pambak-Sevan-Sunik Fault (PSSF)	~1-2.2 (RL)	2±1	Geodetic	Karakhian et al., 2013
	PSSF1	~2.2 (RL)	~2	Paleoseismology	Ritz et al., 2016
	Akery Fault (AkF)	1 (RL)	1.5	Geodetic	Karakhian et al., 2013
	Akhourian Fault (AkhF)	2.1 (LL)	0.1-0.7	Geodetic	Karakhian et al., 2013
	Garni Fault (GF)	0.53-1.6 (RL)	0.6	Geodetic	Karakhian et al., 2013
	Nakhchivan Fault (NF)	0.68-0.74 (RL)	0.5-1	Geodetic	Karakhian et al., 2013
	Sardarapat Fault (SaF)	0.81 (RL)	0.2	Geodetic	Karakhian et al., 2013
	Lesser Caucasus Fault (LCF)	1.9 (Sh)	3-5	Geodetic	Sokhadze et al., 2018
TC-GC	Kura Fold and Thrust Belt (KFTB)	~8-10 (Sh)	7-12	Geodetic	Reilinger et al., 2006
	Main Caucasus Thrust (MCT)	4-5 (Sh)	3-5	Geodetic	Sokhadze et al., 2018

LC: Lesser Caucasus, TC: Trans-Caucasus, GC: Greater Caucasus, RL: Right-Lateral, LL: Left Lateral, Sh: Shortening

Table 4.1: Comparison of estimated horizontal slip rates (mm/yr) of selected faults with some recent studies according to geological, geomorphological, paleoseismological and geodetic measurements.

dextral component, which is nearly in agreement with the geological slip rate of about 3.27 ± 0.17 mm/yr over ~290 ka. (Selçuk, 2016; Table 4.1). The eastern Turkey is a location of several active faults, which are mostly unknown in terms of slip rates. Along the western Arax River, two active faults “Kagizman and Tuzluca Faults (KF, TIF; Fig. 4.2)” are located with sinistral and normal components, respectively. Many landslides in this area are attributed to the normal TIF (Person, 1987; Sevindi et al., 2004). Satellite images display a scarp along the TIF, which is adjacent to

the uplifted flat area in Kars Plateau (Dhont and Chorowicz, 2006). Probable slip-rates are estimated to be about 2.5 and 1.6 mm/yr along the KF and TIF, respectively (Fig. 4.7a). The Horasan and Dumlu Fault systems (Fig. 4.2) are active faults with only recorded seismic events ($M_w < 6$, Fig. 4.1; Dhont and Chorowicz, 2006), where kinematic model estimated sinistral slip rates about 1.4 and 2.4 mm/yr (Fig. 4.7a). The active faults within and to the east of Van Lake displays many instrumental moderate earthquakes and one large earthquake (Fig. 4.1); our model predicted heave rates ~ 1.8 -3.2 mm/yr and dextral slip rates ~ 1.4 -2 mm/yr (Fig. 4.7a).

Probable slip rates are estimated to be between 1 and ~ 2.2 mm/yr for the faults in the Lesser Caucasus Region (Fig. 4.7a). The Pambak-Sevan-Sunik Fault (PSSF, Fig. 4.1) is one of the main active faults in this region. The geomorphological analysis along the PSSF (PSSF2; Fig. 4.2) suggests a slip rate of 2.24 ± 0.96 mm/yr by using river displacement along the segment (Philip et al., 2001). Moreover, geological measurements from the displacement of volcanic cones along the segment PSSF4, estimated a slip rate of $\sim 0.53 \pm 0.04$ mm/yr (Philip et al., 2001). Ritz et al. (2016) estimated right lateral movement ~ 2 mm/yr along the PSSF1 (Fig. 4.2) by using paleoseismological analysis. Slip rates from GPS velocity vectors are about 2 ± 1 mm/yr along PSSF and the highest values belong to PSSF1 with ~ 1.7 -2.2 mm/yr (Karakhanyan et al., 2013). Present investigation estimated slip-rates ~ 1 and 2.2 mm/yr changing along the segments of PSSF (Fig. 4.7a), which is in good agreement with the above-mentioned studies (i.e. geological and geodetic estimations). All evidence indicates that the segment PSSF1 localized most of the recent deformation in this region. Moreover, estimated slip rates of the other active faults in Lesser Caucasus are increasing from 1 mm/yr (Akrey Fault “AkF”) in the east to 2 mm/yr (Akhourian Fault “AkhF”) in the west (Fig. 4.7a). The Garni Fault (GF) and Nakhchevan Fault (NF) are located between these faults and display slip rates 0.53-1.6 and 0.68-0.74 mm/yr, respectively (Fig. 4.7a). According to Karakhanyan et al. (2013), deduced slip rates from the block model for these faults are different from our estimations except the NF with 0.5-1 mm/yr, which is nearly consistent with our result. Conversely, they estimated slip rates of about 1.5 mm/yr for the AkF, 0.6 mm/yr for the northern segment of GF, and about 0.1-0.7 mm/yr for the AkhF (Table 4.1). The Lesser Caucasus Thrust (LCT) is one of the major structures in the region and we estimated slip rate ~ 1.9 mm/yr (Fig. 4.7a) for it whereas GPS data measured 3-5 mm/yr (Sokhadze et al., 2018).

The active thrust fault systems of the Trans and Greater Caucasus have heave rates varying between 1 and ~ 5 mm/yr (Fig. 4.7a). There is no geological slip rates for the active faults to verify and compare with our model estimation. Kura Fold and Thrust Belt (KFTB) is one of the main structure in the Transcaucasus, and the prior studies by GPS measurements

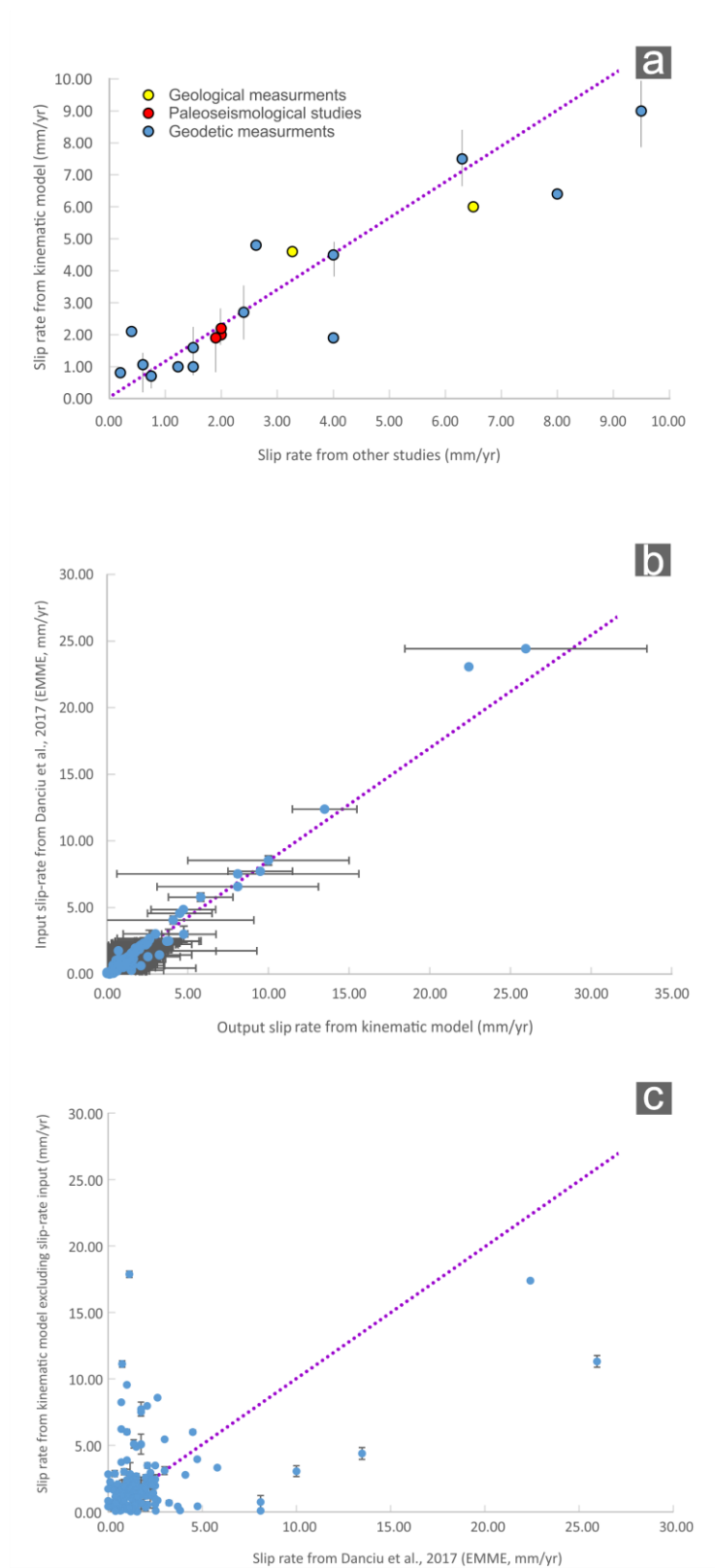


Fig. 4.8: Plots of estimated fault slip rates from kinematic model versus published slip-rates in the literatures. Y-axis uncertainties (2σ) reflecting the range of estimated slip rates (from the kinematic model) along different segments of faults as in Table 4.1 for Fig a. The circles with different colors indicated that the different methods to measure the slip-rates in Fig. a. Figs b and c indicates correlation between estimated slip-rates from comprehensive kinematic model and EMME dataset (b) and kinematic model without fault slip-rates input and EMME (c).

(Forte et al., 2014; Kadirov et al., 2012; Reilinger et al., 2006a), estimated slip rate ~ 7 and ~ 12 mm/yr. This is consistent with the present investigation, which shows about 8-10 mm/yr regional shortening in the KFTB (Fig. 4.7). Main Caucasus Thrust (MCT) is a major active fault in the Greater Caucasus with shortening rate ~ 4 -5 mm/yr (Fig. 4.7a), which is fairly in agreement with previous studies based on GPS data ~ 2 -3 mm/yr (e.g. Forte et al., 2014; Reilinger et al., 2006a) and 3-5 mm/yr (Sokhadze et al., 2018).

4.5.2 Tectonic strain field

The spatial distribution of ongoing crustal deformation estimated by the dynamic model is given in Fig. 4.9 as the logarithmic value of the greatest magnitude of the principal strain rate. To find the dominant input to the regional kinematic model, two cases are considered with either faults and slip-rates or GPS measurements and stress direction (as explained in section 4.3). Furthermore, geomorphological analysis are suitable to extract some evidence of regional deformation from the drainage system (i.e. knickpoints, higher erosion rates) and/or topography (lithology changes and base-level fluctuations). Therefore, the results of the geomorphological investigations for the given region as summarized in Chapter 2 and 3 are used hereinafter to support our understanding of the regional variability of the strain rate.

The regional strain rates evaluated by the kinematic model (see section 4.2 for model details), indicate that a large part of the deformation in the northern margin of the Iranian Plateau is localized within a mean strain rate of $\sim 10^{-14.5} \text{ s}^{-1}$ by the Alborz Mountain Range (Fig. 4.1). The internal part of the north Iranian Plateau displays a moderate mean strain rate $\sim 10^{-15.7} \text{ s}^{-1}$ (Fig. 4.9). The deformation rate differs between the internal plateau and its margin, is consistent with the strain rate model given the dominant fault input (Fig. 4.10b), which shows the effect of active faults to accommodate the strain. In addition, this implies that most of the major active faults in the north Iranian Plateau and its margin are properly mapped. The prior weakness of some tectonic structures (i.e. Caspian Fault) and reactivation of them during Late Miocene until now is the reason for deformation in the northern part of Iran (e.g. Berberian and King, 1981; Zanchi et al., 2006). The geomorphological indicators given in Chapter 2, based on river profile analysis and erosion rates show evidence of active tectonics (mostly active fault systems) from the rivers in the Alborz Mountain Range compared to the north Iranian Plateau. This is consistent with the frequency of earthquakes ($M_w > 4$ and a large event of moment magnitude (M_w) ~ 7.2 in 1990; Fig. 4.1) in the Alborz Mountain Range and high strain rates. The slow deformation in the internal plateau can be approximated as a relatively rigid block that is bounded by seismically active ranges.

A zone of high strain rate about $10^{-14.2}$ to $10^{-14.4} \text{ s}^{-1}$ is located in the Talesh Mountains (Fig. 4.9). Our FBM highlights the role of Talesh Fault to accommodate the strain in the mountains (Fig. 4.10b) while in the absence of faults with GBM, the strain rate is decreasing (Fig. 4.10a). Talesh Mountains are influenced by regional compressional stress and accommodated about 6 mm/yr of shortening (Fig. 4.7a), which can be attributed to the Talesh thrust with westward-dip. The GPS velocity vectors with about 11-12 mm/yr displayed and confirmed the eastward movement of this region toward the Caspian Basin (Djamour et al., 2010; Djamour et al., 2011). Seismicity shows that deformation is accommodated by strike-slip faults (e.g. Sangavar and Khalkhal Faults; Figs. 4.1, 4.2 and 4.9). Effect of active faults provided by the geomorphological analysis indicate high erosion rates in the rivers close to Khalkhal and Talesh Faults (Fig. 4.1), also indicating by their location in the region with high strain rates (i.e. Talesh Mountains) also seen in Fig. 4.9. This area experienced strong earthquakes (e.g. 1978, 1980, 1998; $M_w > 6$; Fig. 4.1) at shallow depth between 30-60 km.

The Bitlis-Zagros suture is a zone with mean strain rates of about $10^{-14.7}$ and 10^{-15} s^{-1} (Figs. 4.1 and 4.9). Due to lack of dense GPS network and data in this region, there is less possibility to compare the effect of fault and other geological features to accommodate the strain, but FBM displays the high effect of thrust and dextral strike slip faults on deformation rates (Fig. 4.10b). The N-S shortening and E-W extension of the Turkish Plateau are consistent with westward motion of the plateau relative to fixed Eurasia (Reilinger et al., 2006a). The uplift of the Turkish-Iranian Plateau since Middle/Late Miocene (e.g. Celâl and Yilmaz, 1981; Pirouz et al., 2017), the dominant strike-slip faulting, the absence of major dip-slip faults, do not support a model of ongoing crustal thickening (Dhont and Chorowicz, 2006). However, our estimated slip rate for Bitlis Thrust zone shows regional shortening which was absorbed within the Bitlis suture (Fig. 4.9). The fault plane solutions show that the strike-slip mechanism is the most dominant mechanism in the Bitlis-Zagros suture, usually with a reverse component (Abdulnaby et al., 2014). This region recorded several earthquakes mostly $< 5 M_w$ (Fig. 4.1) at shallow depth between 15-60 km.

Along the eastern segment of NAF to North Tabriz Fault (NTF), our kinematic model displays high strain rates about $10^{-14.4}$ to 10^{-15} s^{-1} (Fig. 4.9). The resulting strain rate of the two particular cases when only faults and only GPS are considered in addition to the basic kinematic model, indicate similar regions of high values as given in Figs. 4.10a, b. The small differences might be due to completeness of data in the region. Both GPS measurements and fault location are well calibrated in the region. The results of our geomorphological analysis on the Arax River show that the perturbation from the steady-state trend is associated with active faulting in the NW Iran

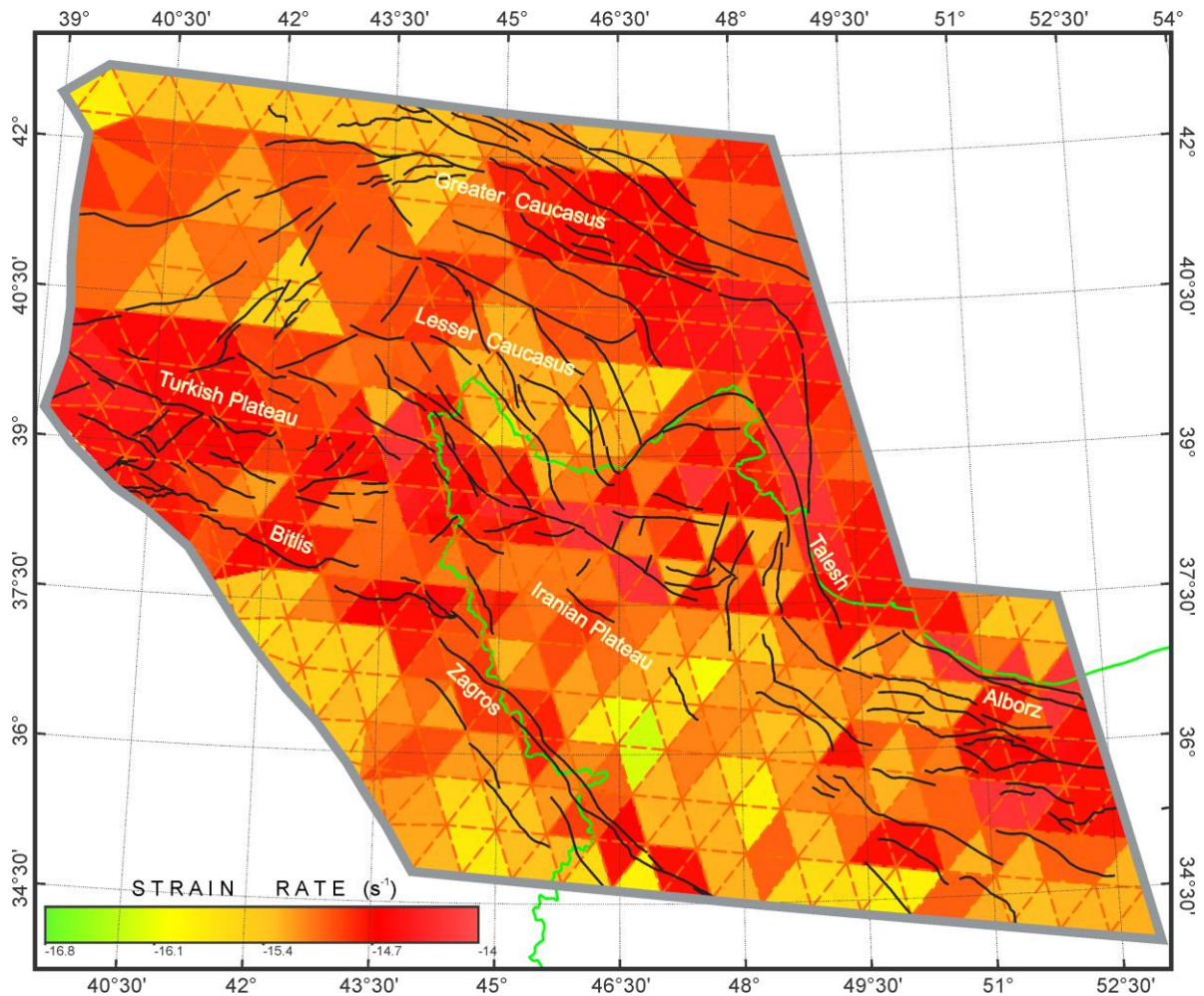


Fig. 4.9: The spatial distribution of current crustal deformation from comprehensive kinematic model including all dataset (fault trace and displacement, geodetic velocities and stress directions) in the studied part of Turkish-Iranian Plateau and Caucasus Regions. The colored pattern is the logarithm of the greatest magnitude of the strain rate (s^{-1}), including grid (grey lines), faulting (black lines) and geographical border of Iran (green line).

and east Turkey, as observed by the seismicity (Fig. 4.1) and high strain rate values. According to right-lateral motion of NAF, the northern block is moving to the east and transfers the stress to the Iranian Plateau by accommodating within the dextral strike-slip faults (e.g. ChF, GSKF, NMF, NTF; Fig. 4.1). Most of the earthquakes after 1999 migrated from the eastern segment of NAF to the NTF (Fig. 4.1), while they mostly triggered to the west Anatolia between 1939 and 1999 (e.g. Barka, 1996). In addition, the NW Iranian Plateau has extrusion to the east which is indicated by right-lateral strike-slip faults and folded structures from horsetail features (Su et al., 2017). Many moderate magnitude earthquakes occurred in the surface linkage gap between NAF and ChF, which are all shallow depth (<15 km) like most of the seismic events along the same strike to the NAF and ChF-GSKF (Fig. 4.1). This may indicate the linkage of NAF and ChF at depth and continuation into the NTF. The SE termination of NTF is associated with low strain rates of about $10^{-16} s^{-1}$ to the east and internal Plateau which is the site of some N-S striking active fault

(e.g. Garmachay, Faridi et al., 2017). The local Iranian network recorded some small earthquakes (<2.5 magnitude) along the same strike (NW-SE) which are mostly migrating to the SE (2009 to 2016, Fig. 4.1). Previous geological studies explained that the GSKF-NMF-NTF are overprinted a suture zone (Alavi, 1991; Alavi, 2007; Mesbahi et al., 2016). Our study shows almost constant high strain rate along this fault system. Strain rates for the area located south of overprinted suture zone (Central Iran), the GSKF-NMF-NTF, is lower than the northern part (Azerbaijan region). The seismicity pattern in terms of frequency and depth does not show large distinction in the south and north of the GSKF-NMF-NTF (Figs. 4.1 and 4.2). However some differences are observed (e.g. more seismic events in the north). According to teleseismic tomography, the Moho depth along the GSKF-NMF-NTF is about 40 km while in the south and north it is about 30 and 50 km, respectively (Shad Manaman et al., 2011). Therefore, most of the mentioned evidence could reflect the lithosphere differences.

The Trans and Greater Caucasus with basins and young mountain ranges are located in the regions with strain rates about 10^{-15} s^{-1} (Fig. 4.9). The Greater Caucasus is the region of active shortening and the north and south dipping sub-parallel thrust fault systems are mostly accommodating the present-day shortening ($\sim 10 \text{ mm/yr}$) within the folds and mountain ranges (e.g. Forte et al., 2015a; Sokhadze et al., 2018). When the strain rates are compared with the erosion rates from the geomorphological analysis (Chapter 3 and work in preparation), a good agreement is observed along the Main Caucasus Thrust (MCT), and is also consistent with the evidence from Kura River attributed to the active fault system. Destructive strong and large earthquakes ($M_w > 6$; Fig. 4.1; e.g. Racha-1991) occurred in the central part of the orogen at mostly shallow depth (<15 km). All the geodetic, geologic and seismic events agree with the location of high strain within the Trans and Greater Caucasus region (Fig. 4.9). Our estimated shortening rate ($\sim 10 \text{ mm/yr}$, Fig. 4.7a) for the central part of Greater Caucasus supporting the active tectonic of region with more than 1 mm/yr uplift (Avdeev and Niemi, 2011), exhumation (e.g. Allen et al., 2002) and possible post-collisional subduction of relict ocean in the Kura Basin to the east (Cowgill et al., 2016).

The Lesser Caucasus displays a strain rate about 10^{-15} s^{-1} along the PSSF in the segment 1 and 2 (Figs. 4.2 and 4.9), while to the south, the strain rate is decreasing to 10^{-16} and 10^{-17} s^{-1} . The fault based strain-rates do not show the higher effect of active faults on strain accommodation (Fig. 4.10b), where GPS based strain rates can still show high strain rates (Fig. 4.10a). Based on geomorphological analysis (chi analysis, Chapter 2) on the Arax River tributaries, the region with low strain rate is close to steady state. The analysis of the river profiles show evidence of active faults (e.g. PSSF4, PSSF5, GF) which is in relative agreement with the lower occurrence rate of earthquakes (Fig. 4.1). The PSSF segments (1 and 2) with higher strain rates than the other

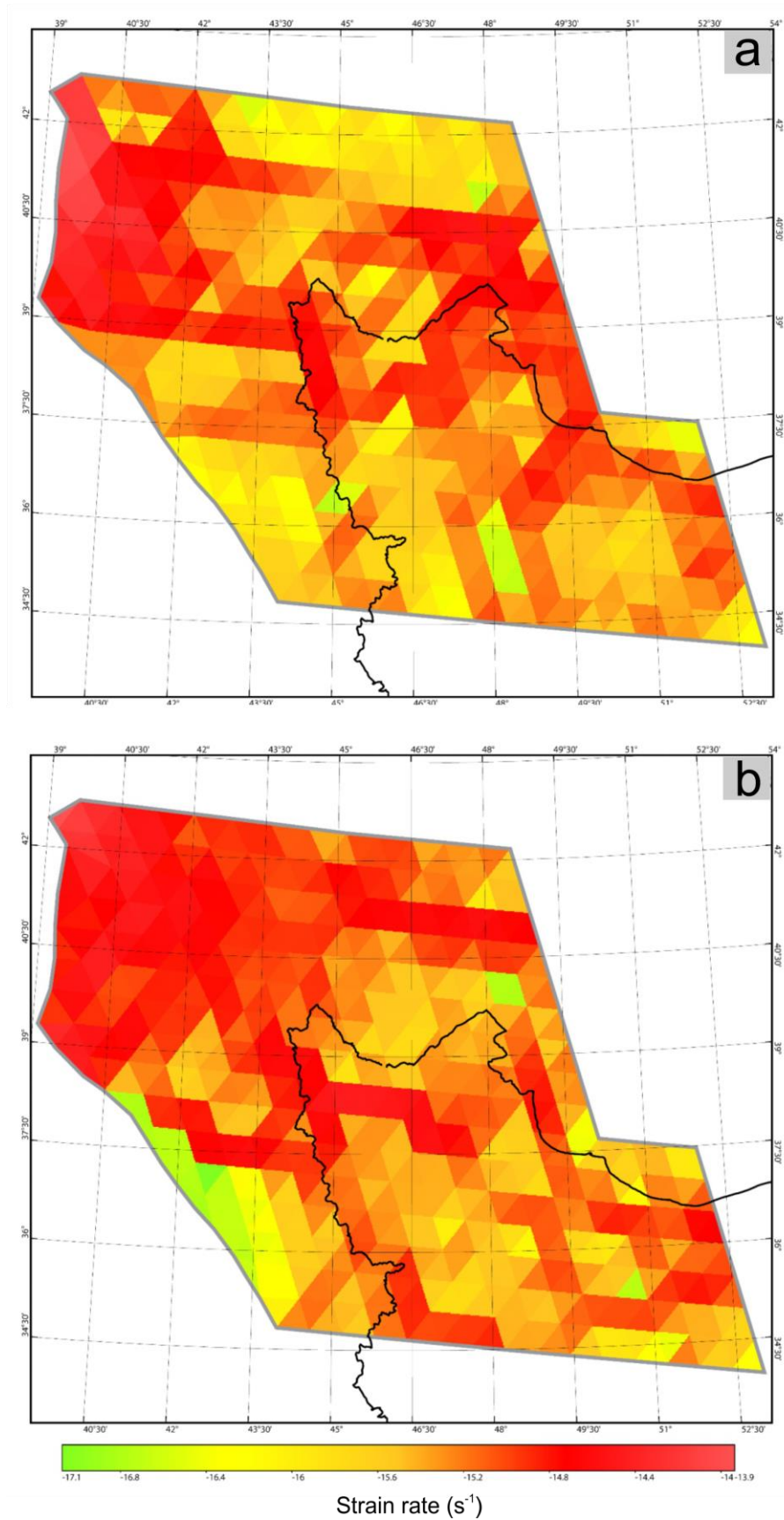


Fig. 4.10: Tried two more strain rate models to find the dominant input driving crustal deformation from our dataset: (a) in absence of faults, and (b) excluding GPS.

segments, are located along the Sevan–Akeru suture zone (Cavazza et al., 2017) on which the strong earthquake of 1988 ($M_w > 6$; Fig. 4.1) occurred. In addition, our results clearly show that the strain pattern is not the same in the Trans-Greater and Lesser Caucasus (Fig. 4.9), which corroborates that there are two independent tectonic blocks for these regions (Karakhanyan et al., 2013).

4.6 Conclusion

We applied a continuous kinematic modelling to quantify the tectonic flow, ongoing distributed deformation and fault slip rates in the Turkish-Iranian Plateau and the Caucasus Region.

The fault slip-rates estimated by the kinematic model for a newly developed dataset of active faults, indicate that deformation is essentially taken up by active faults. The estimated slip rate values represent the averaged kinematics over a period of 10^7 years. Thus, they can be seen as long term geological observations.

The estimated slip-rates from our kinematic model display lower uncertainties compared to previous studies.

These uncertainties may indicate, that the geomorphic expression for faulting is variable across the region, perhaps because: (i) recurrence times vary across the region; (ii) displacement varies and location of seismic activity is variable over time, too. Overall, the probable slip-rates for the major faults are mostly consistent with the assigned slip-rates in previous studies (EMME14, Iran).

The regional permanent strain field obtained from kinematic model indicates active crustal deformation with higher strain rates localized within the Alborz, Talesh, Bitlis-Zagros and Greater Caucasus Mountain Ranges, respectively. The kinematic model of the region suggests that the high strain rates are accommodated by active thrust faults.

Prior geomorphological analysis given in Chapter 2 and 3, indicate that active tectonics (especially active fault systems) is a significant controller of topography in our study area as described by erosion rates along the main drainage networks (e.g. Kura-Arax and Qezel-Owzan Rivers) of the region. These results are in good agreement with the results of the regional kinematic model, which is consistent with high strain rates along the active faults as well as the observed seismicity in this region.

5 Conclusion, outlook and work in preparation

5.1 Conclusion

The chapters of this thesis presented studies of the landscape evolution and ongoing crustal deformation across the western part of the Turkish-Iranian Plateau and Caucasus Regions. On a regional scale, we produced quantitative information on erosion rates and drainage networks and investigated the effect of strain accumulation to determine how deformation is accommodated using a regional strain model. Comparison with previous morphotectonic studies clarified where and how high relief was developed and whether the relief is in a transient or steady state.

The relationship between topography, precipitation and fluvial incision indicate that the Qezel-Owzan drainage network in the western part of the Turkish-Iranian Plateau and south Caucasus regions is not in equilibrium. This is documented in the upper catchment of the Kura-Arax and Qezel-Owzan Rivers where the landscape results from a combination of higher aridity in the internal plateau, rapid uplift of orographic barriers (Alborz, Talesh and Caucasus mountain ranges) along the plateau margins. In addition, disequilibrium and perturbation from the steady-state are associated with drainage captures, which show ongoing dynamics of the drainage basins where water divides migrate towards the internal plateau.

Tracing spatial and temporal variability of short-term erosion rates is also important when assessing landscape evolution and topography. Our current study, provides new millennial-scale erosion rates derived from river sand ^{10}Be content across three distinct tectono-stratigraphic zones from the upper to lower catchments in the north Iranian Plateau and west Alborz Mountain Range. The lower catchment “Alborz Mountain Ranges” has a higher erosion rate with higher topographic metrics and annual precipitation and increased seismicity compared to the upper/middle catchments in the plateau. This suggests that a different state exists between the upper/middle and lower catchments of the Qezel-Owzan River. Relationships between long-term exhumation rates (AFT/He data) and short-term erosion rates in the lower catchment suggest that

the region has experienced a steady erosion rate since ~5 Ma, indicating a balance between erosion rate and regional shortening. (Samples from the Arax-Kura River are currently being processed and show a similar balance between erosion rate and regional shortening).

As hypothesized, the main driver on the landscape evolution is tectonic. To assess the tectonic flow and overall kinematics of active faults and ongoing crustal deformation in the Turkish-Iranian Plateau down to the south Caucasus Regions, we applied a regional strain rate model. This model includes geodetic, geologic data and stress direction inputs that are confined by plate boundary conditions, tectonic forces and rheological properties. One of the critical results quantified by the model is the slip-rate of active faults, which shows that deformation is localized along the seismically active faults. The slip-rates are determined for a period of 10^7 years, which depict the average long-term kinematics in the region. Results show that crustal deformation is mostly accommodated by the active fault systems, mostly right-lateral strike slip faults. However, the study revealed that part of the deformation and a high degree of shortening is due to active thrust faults within Talesh and Bitlis regions, with additional shortening accommodated by the fold and thrust system in the Alborz and Greater Caucasus mountain belts.

5.2 Outlook

This study shows the importance of the active fault system on strain accommodation in the studied region. The lack of geological and paleoseismological studies along the fault in the east Turkish Plateau and Greater Caucasus would extend these geodetic results.

The region is affected by shortening and uplift due to convergence between Arabian and Eurasian Plates. However, further studies on uplift rate are necessary to compare deformation in terms of slip-rate and regional uplift.

Since a large part of the region is covered and affected by Neogene-Quaternary Volcanism (i.e. quartz-poor rocks unfavourable for ^{10}Be cosmogenic nuclide dating), applying and comparing other Quaternary dating methods would complement the erosion rates provided in this study.

The application of thermochronometry is currently limited to the Alborz and Talesh Mountains and is lacking in the north Iranian Plateau, where it would provide insight on past regional tectonics (> 1 Ma).

5.3 Work in preparation

Spatial variability of ^{10}Be erosion rates and landscape evolution in segment of Turkish-Iranian Plateau and west Caucasus Region: the Kura-Arax River Basin

This work will be divided into the Kura and Arax River Basins for subsequent publications with:

Kura: Amaneh Kaveh Firouz ^a, Jean-Pierre Burg ^a, Negar Haghypour ^a, Lasha Sukhishvili ^b, Marcus Christl ^c, Whitney Behr ^a

^a *Geological Institute, ETH Zurich, Sonneggstrasse 5, 8092 Zurich, Switzerland*

^b *Institute of Earth Sciences & National Seismic Monitoring Centre, Ilia State University, Tbilisi, Georgia*

^c *Laboratory of Ion Beam Physics, ETH Zurich, Schafmattstrasse 20, 8093 Zurich, Switzerland*

Arax: Amaneh Kaveh Firouz ^a, Jean-Pierre Burg ^a, Negar Haghypour ^a, Emrah Ozpolat ^b, Ramin Elyaszadeh ^c, Marcus Christl ^d, Whitney Behr ^a

^a *Geological Institute, ETH Zurich, Sonneggstrasse 5, 8092 Zurich, Switzerland*

^b *Eurasia Institute of Earth Sciences, Istanbul Technical University, Saryyer-Istanbul, 34469, Turkey*

^c *Geological Survey of Iran (GSI), Northwestern Regional Office, 5167733551 Tabriz, Iran*

^d *Laboratory of Ion Beam Physics, ETH Zurich, Schafmattstrasse 20, 8093 Zurich, Switzerland*

5.3.1 Introduction

The Turkish-Iranian Plateau (TIP) and Caucasus region is a good example of a plateau with young mountain ranges, which is characterized by high topographic relief (1600-3400 m). This region is geologically complex due to different tectonic processes, including post-collisional volcanism and active faulting. This area is characterized by significant spatial variation in uplift rates (e.g. Cavazza et al., 2017; Karakhanian et al., 2004), which may be explained by potential coupling between rock uplift rates, erosion rates, regional topographic/climate variability, and Caspian Sea level fluctuations. This connection, however, receives considerably less attention in literature in the Turkish-Iranian Plateau and Caucasus region than in west Turkish and east Iranian Plateau. The Kura-Arax River Basin is the largest catchment in the studied region, which discharges into the Caspian Sea. This catchment cross-cuts distinct tectono-stratigraphic zones with west-east variations in lithology, topography, seismicity, and uplift rate.

According to our geomorphological analysis, the landscape is in a transient state in the upper catchment of Kura-Arax and middle Arax. This is a combination of enhanced aridity in the internal plateau, rapid uplift of orographic barriers along the plateau margins, and exposure of resistant rocks associated to the regional volcanic activity. The results of our river profile analysis show that the perturbation from the steady-state trend is associated with active faulting in the

middle Arax. This is characterized by high channel steepness, large concentration of knickpoints (mostly controlled by local tectonic features) along the trunk channel, and tributaries. The drainage basin indicates some evidence of drainage capture and migration to the Iranian plateau (as Karakhanian et al., 2004 mentioned: Arax River migration to the south due to fault activity), same as the upper Arax migration to the Kars Plateau (east Turkey). The upper segment of Kura-Arax is mostly affected by lithological changes and Neogene-Quaternary volcanism. The climate and annual precipitation along the Arax River from upper to lower catchment is almost uniform and semi-arid (Hijmans et al., 2005). Coincidence of drainage divides and plateau margins with mountain ranges and structures indicates that tectonic deformation is the main driver of landscape evolution in the Caucasus regions and in the TIP. Furthermore, the northern part of Kura River is affected by Main Caucasus Thrust (MCT, which is the main controller of active shortening across the Greater Caucasus Mountain Ranges), and the activity of this fault diminishes to the east (Forte et al., 2016). Our river profile analysis shows that knickpoints related to faults are concentrated in the west Kura, and the chi analysis indicates river capturing to the east Kura. The results of geomorphological analysis are in good agreement with applied kinematic modelling, which is consistent with high strain rates along the active faults as well as the observed seismicity in this region. This suggests that active tectonics is a significant controller of topography, but spatial-temporal resolution of these results is limited based on the techniques used.

Due to the area size and relatively limited thermochronological data (e.g. Apatite fission-track data), the long-term deformation process and controlling factors in the TIP and Caucasus are poorly characterized. Some previous low-temperature thermochronology, namely Apatite fission-track data, shows three effects of tectonics on long-term deformation: (1) the exhumation in the NW Iran (Misho complex) is diachronous along strike and affected by faults since 21-22 Ma (Early Miocene; Behyari et al., 2017); (2) Central Lesser Caucasus shows that a portion of this orogen underwent a discrete phase of cooling/exhumation at 18–12 Ma (Early Miocene) as a result of the structural reactivation in a segment of the Sevan–Akeru suture zone (Cavazza et al., 2017), and (3) rapid exhumation of the central Greater Caucasus in the Pliocene results from the collision of the Lesser Caucasus with Eurasia and complete subduction of the oceanic lithosphere across this segment of the Arabia-Eurasia plate boundary (Avdeev and Niemi, 2011).

Previous thermochronology results (Avdeev and Niemi, 2011; Behyari et al., 2017; Cavazza et al., 2017), geomorphologic analyses and kinematic modelling (chapters 2, 3, 4) showed that the main driver of the long-term landscape evolution (during the Miocene to Pliocene) in this area is the tectonics. Although we have comprehensive information on the long-term landscape evolution of the study region, there is no study that focused on the recent landscape evolution (Quaternary).

To improve our understanding of the Quaternary evolution of this region, we aim to determine the main controls on present-day landscape evolution and the topographic expression of active tectonics in the study area (Kura-Arax River Basin). Since erosion is the effective surface process on the landscape evolution, we plan to address the following questions:

- (1) Do the erosion rates show significant differences and transient state across the Kura-Arax River Basin?
- (2) What is the main controller of recent landscape evolution in different segments of the catchment?
- (3) Are there any changes in short-term erosion rates consistent with variations in MCT activity from west to east Kura?
- (4) What is the relationship between short-term erosion rates and long-term exhumation rates?

5.3.2 Methodology

To constrain the short-term erosion rates for the interested area, we are using cosmogenically produced isotopes ^{10}Be in river sands. Tracing spatial and temporal variability of short-term erosion rates is important when assessing landscape evolution and topography. Our short-term erosion data will help to better understand recent deformation patterns and controlling factors in the western part of TIP and Caucasus region. In addition, our data (erosion rates) from eastern TIP (Qezel-Owzan River Basin) will help to compare recent deformation patterns and controlling factors across the TIP.

The specific objectives of the work (landscape evolution analysis) have three components: First, quantify the relationship between ^{10}Be -derived catchment-wide erosion rates and commonly used topographic metrics derived from a 90 m digital elevation model. Second, compare the spatial variation in catchment-wide erosion rates with our previous work, fault displacement rates, and other published work on long-term exhumation rates. And third, test the effect of various lithology (mostly sandstone, granite, volcanoclastic, and tuff in the interested area) on the millennial scale erosion rates. These data sets will allow to determine the controlling factors and their relative importance to the long term topographic evolution in the study area.

5.3.3 Prior results and ongoing work

During PhD project, the geomorphological analysis of the Kura-Arax River Basin has been done. Furthermore, we applied regional kinematic modelling to quantitatively evaluate the spatial distribution of ongoing crustal deformation in the study region. To calculate the erosion rates of the Kura-Arax catchment, sampling and field observation has been done. The results of 26

samples have already been analyzed (yellow circles in Fig. 5.1). We expect higher erosion rates in the lower catchment of the Arax as a result of increasing area, but the trend of erosion rates along the main Arax trunk channel shows no systematic gradient from upper to lower Arax. Segments with higher erosion rates correspond to knickpoints/knickzones in the upper and middle Arax caused by active faulting. Our results from Arax tributaries show higher erosion rates in the middle part where many active faults cross the region, and we extracted their signal on our geomorphological analysis. In addition, our kinematic modelling shows high strain rates attributed to active faults in the middle Arax. The upper catchment of the Arax shows high erosion rate in the Kars Plateau (eastern Turkey), while we expected low erosion rates based on prior work, therefore additional 10-12 analyses are required for verification (Fig. 5.1). In the lower catchment of Arax, river capturing/migration may affect erosion rate, and we need more analysis to determine whether river migration from the Qezel-Owzan catchment to the Arax significantly affects erosion rates or not (Fig. 5.1). Two samples from two tributaries of upper Kura, from west to east show decreasing erosion rates, which is in agreement with diminishing MCT activity to the east. However in order understand the MCT activity with respect to erosion rate, additional 10-12 analyses should be conducted (Fig. 5.1).

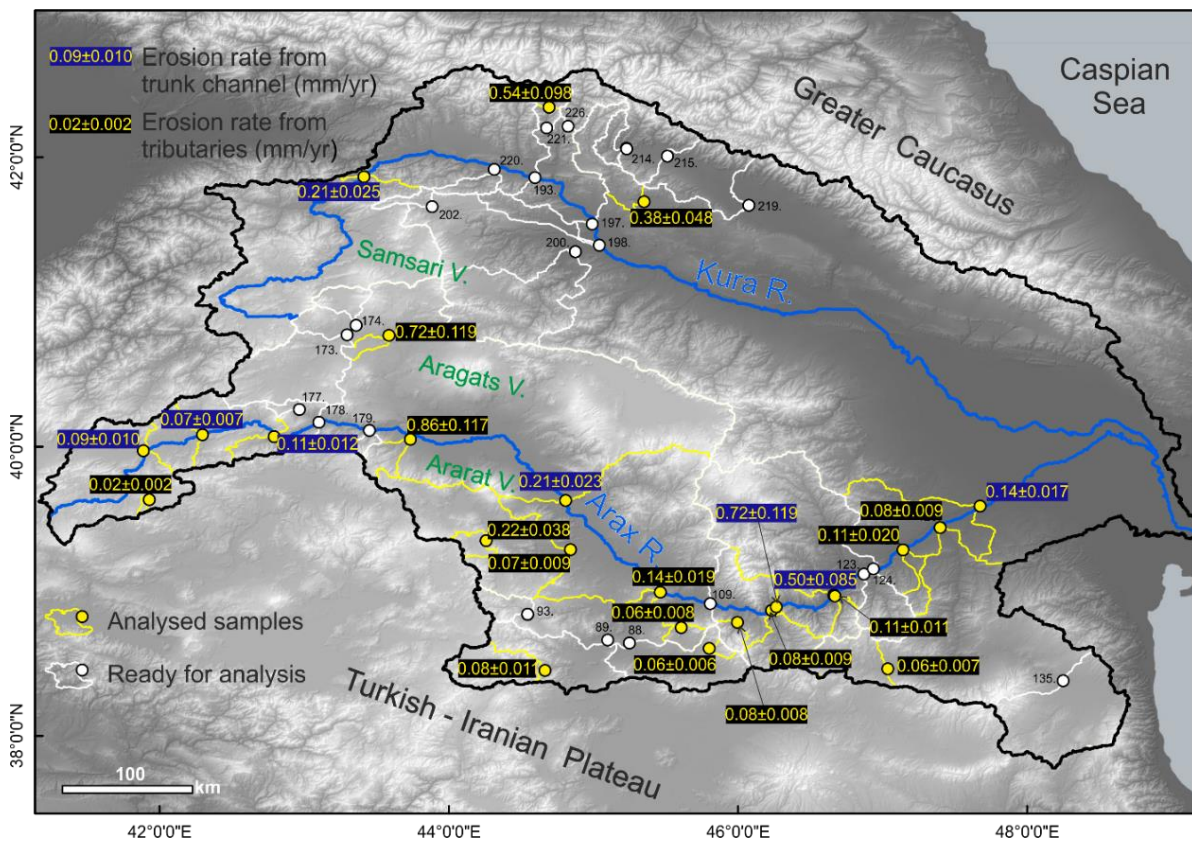


Fig. 5.1: The location of samples (yellow circles: done, white circles: ready for analysis) across the Kura-Arax River Basin.

Bibliography

- Abdulnaby, W., Mahdi, H., Numan, N.M., Al-Shukri, H., 2014. Seismotectonics of the Bitlis–Zagros fold and thrust belt in northern Iraq and surrounding regions from moment tensor analysis. *Pure and Applied Geophysics*, 171(7): 1237-1250.
- Adamia, S.A. et al., 1981. Tectonics of the Caucasus and adjoining regions: implications for the evolution of the Tethys ocean. *Journal of Structural Geology*, 3(4): 437-447.
- Adamia, S.A., Lordkipanidze, M., Zakariadze, G., 1977. Evolution of an active continental margin as exemplified by the Alpine history of the Caucasus. *Tectonophysics*, 40(3-4): 183-199.
- Aktug, B. et al., 2016. Slip rates and seismic potential on the East Anatolian Fault System using an improved GPS velocity field. *Journal of Geodynamics*, 94: 1-12.
- Alavi, M., 1991. Tectonic map of the Middle East: Tehran, Geological Survey of Iran, scale 1: 5,000,000. Google Scholar.
- Alavi, M., 2007. Structures of the Zagros fold-thrust belt in Iran. *American Journal of science*, 307(9): 1064-1095.
- Alipoor, R., Zaré, M., Ghassemi, M.R., 2012. Inception of activity and slip rate on the Main Recent Fault of Zagros Mountains, Iran. *Geomorphology*, 175: 86-97.
- Allen, M.B., Jones, S., Ismail-Zadeh, A., Simmons, M., Anderson, L., 2002. Onset of subduction as the cause of rapid Pliocene-Quaternary subsidence in the South Caspian basin. *Geology*, 30(9): 775-778.
- Allen, M.B., Kheirkhah, M., Emami, M.H., Jones, S.J., 2011a. Right-lateral shear across Iran and kinematic change in the Arabia—Eurasia collision zone. *Geophysical Journal International*, 184(2): 555-574.
- Allen, M.B. et al., 2011b. ⁴⁰Ar/³⁹Ar dating of Quaternary lavas in northwest Iran: constraints on the landscape evolution and incision rates of the Turkish-Iranian plateau. *Geophysical Journal International*, 185(3): 1175-1188.
- Ambraseys, N., 1978. The relocation of epicentres in Iran. *Geophysical Journal International*, 53(1): 117-121.
- Ambraseys, N.N., Melville, C.P., 2005. A history of Persian earthquakes. Cambridge university press.
- Arpat, E., Saroglu, F., 1972. The East Anatolian fault system: thoughts on its development. *Bulletin of the Mineral Research and Exploration Institute of Turkey*, 78: 33-39.
- Arpat, E., Saroglu, F., 1975. Some recent tectonic events in Turkey. *Bull. Geol. Soc. Turkey*, 18(1): 91-101.
- Authemayou, C. et al., 2009. Quaternary slip-rates of the Kazerun and the Main Recent Faults: active strike-slip partitioning in the Zagros fold-and-thrust belt. *Geophysical Journal International*, 178(1): 524-540.
- Avdeev, B., Niemi, N., 2009. Spatial and temporal patterns of exhumation in the Greater Caucasus from low-temperature thermochronometry, AGU Fall Meeting Abstracts.
- Avdeev, B., Niemi, N.A., 2011. Rapid Pliocene exhumation of the Central Greater Caucasus constrained by low-temperature thermochronometry. *Tectonics*, 30(2).
- Axen, G.J., Lam, P.S., Grove, M., Stockli, D.F., Hassanzadeh, J., 2001. Exhumation of the west-central Alborz Mountains, Iran, Caspian subsidence, and collision-related tectonics. *Geology*, 29(6): 559-562.
- Azad, S.S. et al., 2011. The Zandjan fault system: Morphological and tectonic evidences of a new active fault network in the NW of Iran. *Tectonophysics*, 506(1-4): 73-85.
- Balco, G., Stone, J.O., Lifton, N.A., Dunai, T.J., 2008. A complete and easily accessible means of calculating surface exposure ages or erosion rates from ¹⁰Be and ²⁶Al measurements. *Quaternary geochronology*, 3(3): 174-195.
- Ballato, P., 2009. Tectonic and climatic forcing in orogenic processes: the foreland basin point of view, Alborz mountains, N Iran. *Niedersächsische Staats-und Universitätsbibliothek*.
- Ballato, P. et al., 2016. Tectono-sedimentary evolution of the northern Iranian Plateau: insights from middle-late Miocene foreland-basin deposits. *Basin Research*.
- Ballato, P. et al., 2015. The growth of a mountain belt forced by base-level fall: Tectonics and surface processes during the evolution of the Alborz Mountains, N Iran. *Earth and Planetary Science Letters*, 425: 204-218.
- Ballato, P. et al., 2010. Middle to late Miocene Middle Eastern climate from stable oxygen and carbon isotope data, southern Alborz mountains, N Iran. *Earth and Planetary Science Letters*, 300(1-2): 125-138.
- Ballato, P., Strecker, M.R., 2014. Assessing tectonic and climatic causal mechanisms in foreland-basin stratal architecture: insights from the Alborz Mountains, northern Iran. *Earth Surface Processes and Landforms*, 39(1): 110-125.
- Barka, A., 1996. Slip distribution along the North Anatolian fault associated with the large earthquakes of the period 1939 to 1967. *Bulletin of the Seismological Society of America*, 86(5): 1238-1254.

- Barzegari, A. et al., 2016. Evaluation of slip rate on Astara fault system, North Iran. *Journal of Earth Science*, 27(6): 971-980.
- Beeson, H.W., McCoy, S.W., Keen-Zebert, A., 2017. Geometric disequilibrium of river basins produces long-lived transient landscapes. *Earth and Planetary Science Letters*, 475: 34-43.
- Behyari, M. et al., 2017. Analysis of exhumation history in Misho Mountains, NW Iran: Insights from structural and apatite fission track data. *Neues Jahrbuch für Geologie und Paläontologie-Abhandlungen*, 283(3): 291-308.
- Berberian, F., Berberian, M., 1981. Tectono-plutonic episodes in Iran. *Zagros Hindu Kush Himalaya Geodynamic Evolution*: 5-32.
- Berberian, M., 2014. Earthquakes and coseismic surface faulting on the Iranian Plateau, 17. Elsevier.
- Berberian, M., Arshadi, S., 1976. On the evidence of the youngest activity of the North Tabriz Fault and the seismicity of Tabriz city. *Geol. Surv. Iran Rep*, 39: 397-418.
- Berberian, M. et al., 2001. The 1998 March 14 Fandoqa earthquake (Mw 6.6) in Kerman province, southeast Iran: re-rupture of the 1981 Sirch earthquake fault, triggering of slip on adjacent thrusts and the active tectonics of the Gowk fault zone. *Geophysical Journal International*, 146(2): 371-398.
- Berberian, M., King, G., 1981. Towards a paleogeography and tectonic evolution of Iran. *Canadian journal of earth sciences*, 18(2): 210-265.
- Berberian, M., Yeats, R.S., 1999. Patterns of historical earthquake rupture in the Iranian Plateau. *Bulletin of the Seismological society of America*, 89(1): 120-139.
- Berg, L.S., 1950. *Natural Regions of the USSR*. Natural regions of the USSR.
- Bird, P., 2003. An updated digital model of plate boundaries. *Geochemistry, Geophysics, Geosystems*, 4(3).
- Bird, P., 2009. Long-term fault slip rates, distributed deformation rates, and forecast of seismicity in the western United States from joint fitting of community geologic, geodetic, and stress direction data sets. *Journal of Geophysical Research: Solid Earth*, 114(B11).
- Bird, P., Kagan, Y.Y., 2004. Plate-tectonic analysis of shallow seismicity: Apparent boundary width, beta, corner magnitude, coupled lithosphere thickness, and coupling in seven tectonic settings. *Bulletin of the Seismological Society of America*, 94(6): 2380-2399.
- Bird, P., Li, Y., 1996. Interpolation of principal stress directions by nonparametric statistics: Global maps with confidence limits. *Journal of Geophysical Research: Solid Earth*, 101(B3): 5435-5443.
- Bird, P., Liu, Z., 2007. Seismic hazard inferred from tectonics: California. *Seismological Research Letters*, 78(1): 37-48.
- Borisov, A.A., Halstead, C.A., 1965. *Climates of the USSR*.
- Burbank, D.W., Anderson, R.S., 2011. *Tectonic geomorphology*. John Wiley & Sons.
- Burbank, D.W., Vergés, J., MUNOZ, J.A., Bentham, P., 1992. Coeval hindward-and forward-imbricating thrusting in the south-central Pyrenees, Spain: Timing and rates of shortening and deposition. *Geological Society of America Bulletin*, 104(1): 3-17.
- Cavazza, W. et al., 2017. Thermochronometric evidence for Miocene tectonic reactivation of the Sevan–Akera suture zone (Lesser Caucasus): a far-field tectonic effect of the Arabia–Eurasia collision? *Geological Society, London, Special Publications*, 428(1): 187-198.
- Celâl, A., Yilmaz, Y., 1981. Tethyan evolution of Turkey: a plate tectonic approach. *Tectonophysics*, 75(3-4): 181-241.
- Christl, M. et al., 2013. The ETH Zurich AMS facilities: Performance parameters and reference materials. *Nuclear Instruments and Methods in Physics Research Section B: Beam Interactions with Materials and Atoms*, 294: 29-38.
- Çiner, A., 2004. Turkish glaciers and glacial deposits. *Developments in Quaternary Sciences*, 2: 419-429.
- Clifton, H. et al., 2000. Climatic and other controls on the deposition of the lower and middle Productive Series, Azerbaijan, 1st AAPG's Inaugural Regional International Conference, July 9–12, 2000, Istanbul, Turkey, pp. 78.
- Codilean, A.T., 2006. Calculation of the cosmogenic nuclide production topographic shielding scaling factor for large areas using DEMs. *Earth Surface Processes and Landforms*, 31(6): 785-794.
- Copley, A., Jackson, J., 2006. Active tectonics of the Turkish-Iranian plateau. *Tectonics*, 25(6).
- Cowgill, E. et al., 2016. Relict basin closure and crustal shortening budgets during continental collision: An example from Caucasus sediment provenance. *Tectonics*, 35(12): 2918-2947.
- Danciu, L. et al., 2017. The 2014 earthquake model of the Middle East: seismogenic sources. *Bulletin of Earthquake Engineering*: 1-32.
- Delunel, R. et al., 2010. Surface exposure dating and geophysical prospecting of the Holocene Lauvitel rock slide (French Alps). *Landslides*, 7(4): 393-400.

- Dettman, D.L., Fang, X., Garzzone, C.N., Li, J., 2003. Uplift-driven climate change at 12 Ma: a long δ 18 O record from the NE margin of the Tibetan plateau. *Earth and Planetary Science Letters*, 214(1): 267-277.
- Dhont, D., Chorowicz, J., 2006. Review of the neotectonics of the Eastern Turkish–Armenian Plateau by geomorphic analysis of digital elevation model imagery. *International Journal of Earth Sciences*, 95(1): 34-49.
- DiBiase, R.A., Whipple, K.X., Heimsath, A.M., Ouimet, W.B., 2010. Landscape form and millennial erosion rates in the San Gabriel Mountains, CA. *Earth and Planetary Science Letters*, 289(1-2): 134-144.
- Dilek, Y., Altunkaynak, Ş., 2010. Geochemistry of Neogene–Quaternary alkaline volcanism in western Anatolia, Turkey, and implications for the Aegean mantle. *International Geology Review*, 52(4-6): 631-655.
- Dilek, Y., Imamverdiyev, N., Altunkaynak, Ş., 2010. Geochemistry and tectonics of Cenozoic volcanism in the Lesser Caucasus (Azerbaijan) and the peri-Arabian region: collision-induced mantle dynamics and its magmatic fingerprint. *International Geology Review*, 52(4-6): 536-578.
- Djamali, M. et al., 2009. Vegetation history of the SE section of the Zagros Mountains during the last five millennia; a pollen record from the Maharlou Lake, Fars Province, Iran. *Vegetation History and Archaeobotany*, 18(2): 123-136.
- Djamour, Y. et al., 2010. GPS and gravity constraints on continental deformation in the Alborz mountain range, Iran. *Geophysical Journal International*, 183(3): 1287-1301.
- Djamour, Y., Vernant, P., Nankali, H.R., Tavakoli, F., 2011. NW Iran-eastern Turkey present-day kinematics: results from the Iranian permanent GPS network. *Earth and Planetary Science Letters*, 307(1-2): 27-34.
- Donner, S. et al., 2015. The Ahar-Varzeghan Earthquake Doublet (Mw 6.4 and 6.2) of 11 August 2012: Regional Seismic Moment Tensors and a Seismotectonic Interpretation. *Bulletin of the Seismological Society of America*.
- Faridi, M., Burg, J.-P., Nazari, H., Talebian, M., Ghorashi, M., 2017. Active faults pattern and interplay in the Azerbaijan region (NW Iran). *Geotectonics*, 51(4): 428-437.
- Flint, J., 1974. Stream gradient as a function of order, magnitude, and discharge. *Water Resources Research*, 10(5): 969-973.
- Forte, A.M., Cowgill, E., 2013. Late Cenozoic base-level variations of the Caspian Sea: a review of its history and proposed driving mechanisms. *Palaeogeography, Palaeoclimatology, Palaeoecology*, 386: 392-407.
- Forte, A.M., Cowgill, E., Whipple, K.X., 2014. Transition from a singly vergent to doubly vergent wedge in a young orogen: The Greater Caucasus. *Tectonics*, 33(11): 2077-2101.
- Forte, A.M. et al., 2015a. Late Miocene to Pliocene stratigraphy of the Kura Basin, a subbasin of the South Caspian Basin: implications for the diachroneity of stage boundaries. *Basin Research*, 27(3): 247-271.
- Forte, A.M., Whipple, K.X., Bookhagen, B., Rossi, M.W., 2016. Decoupling of modern shortening rates, climate, and topography in the Caucasus. *Earth and Planetary Science Letters*, 449: 282-294.
- Forte, A.M., Whipple, K.X., Cowgill, E., 2015b. Drainage network reveals patterns and history of active deformation in the eastern Greater Caucasus. *Geosphere*, 11(5): 1343-1364.
- Gamkrelidze, I., 1986. Geodynamic evolution of the Caucasus and adjacent areas in Alpine time. *Tectonophysics*, 127(3-4): 261-277.
- Garzzone, C.N. et al., 2008. Rise of the Andes. *science*, 320(5881): 1304-1307.
- Giachetta, E., Willett, S.D., 2018. A global dataset of river network geometry. *Scientific data*, 5: 180127.
- Giardini, D. et al., 2013. Seismic Hazard Harmonization in Europe (SHARE): Online Data Resource, doi: 10.12686/SED-00000001-SHARE.
- Gobejishvili, R., Lomidze, N., Tielidze, L., 2011. Late Pleistocene (Wurmian) glaciations of the Caucasus. *Quaternary Glaciations: Extent and Chronology*, edited by: Ehlers, J., Gibbard, PL, and Hughes, PD, Elsevier, Amsterdam: 141-147.
- Golonka, J., 2004. Plate tectonic evolution of the southern margin of Eurasia in the Mesozoic and Cenozoic. *Tectonophysics*, 381(1-4): 235-273.
- Golonka, J., 2007. Geodynamic evolution of the south Caspian Basin.
- Goren, L., 2016. A theoretical model for fluvial channel response time during time-dependent climatic and tectonic forcing and its inverse applications. *Geophysical Research Letters*, 43(20).
- Gudjabidze, G., Gamkrelidze, I., 2003. Geological map of Georgia. Georgian State Department of Geology.
- Guest, B. et al., 2006. Thermal histories from the central Alborz Mountains, northern Iran: Implications for the spatial and temporal distribution of deformation in northern Iran. *Geological Society of America Bulletin*, 118(11-12): 1507-1521.
- Hack, J.T., 1960. Interpretation of erosional topography in humid temperate regions. *Bobbs-Merrill*.

- Hayakawa, Y., Matsukura, Y., 2003. Recession rates of waterfalls in Boso Peninsula, Japan, and a predictive equation. *Earth Surface Processes and Landforms*, 28(6): 675-684.
- Heidarzadeh, G., Ballato, P., Hassanzadeh, J., Ghassemi, M.R., Strecker, M.R., 2017. Lake overspill and onset of fluvial incision in the Iranian Plateau: Insights from the Mianeh Basin. *Earth and Planetary Science Letters*, 469: 135-147.
- Heidbach, O., Rajabi, M., Reiter, K., Ziegler, M., 2016. World stress map 2016. *Science*, 277: 1956-1962.
- Hempton, M.R., 1987. Constraints on Arabian plate motion and extensional history of the Red Sea. *Tectonics*, 6(6): 687-705.
- Hessami, K. et al., 2003. Paleoearthquakes and slip rates of the North Tabriz Fault, NW Iran: preliminary results. *Annals of Geophysics*.
- Hijmans, R.J., Cameron, S.E., Parra, J.L., Jones, P.G., Jarvis, A., 2005. Very high resolution interpolated climate surfaces for global land areas. *International journal of climatology*, 25(15): 1965-1978.
- Hinds, D. et al., 2004. Sedimentation in a discharge dominated fluvial-lacustrine system: the Neogene Productive Series of the South Caspian Basin, Azerbaijan. *Marine and Petroleum Geology*, 21(5): 613-638.
- Houseman, G., England, P., 1993. Crustal thickening versus lateral expulsion in the Indian-Asian continental collision. *Journal of Geophysical Research: Solid Earth*, 98(B7): 12233-12249.
- Howard, A.D., 1994. A detachment-limited model of drainage basin evolution. *Water Resources Research*, 30(7): 2261-2285.
- Howard, A.D., Kerby, G., 1983. Channel changes in badlands. *Geological Society of America Bulletin*, 94(6): 739-752.
- Howe, T.M., Bird, P., 2010. Exploratory models of long-term crustal flow and resulting seismicity across the Alpine-Aegean orogen. *Tectonics*, 29(4).
- Ivy-Ochs, S., Kober, F., 2008. Surface exposure dating with cosmogenic nuclides. *Eiszeitalter und Gegenwart*, 57(1/2): 179-209.
- Jackson, J., 1992a. Partitioning of strike-slip and convergent motion between Eurasia and Arabia in eastern Turkey and the Caucasus. *Journal of Geophysical Research: Solid Earth (1978–2012)*, 97(B9): 12471-12479.
- Jackson, J., 1992b. Partitioning of strike-slip and convergent motion between Eurasia and Arabia in eastern Turkey and the Caucasus. *Journal of Geophysical Research: Solid Earth*, 97(B9): 12471-12479.
- Jackson, J., McKenzie, D., 1984. Active tectonics of the Alpine—Himalayan Belt between western Turkey and Pakistan. *Geophysical Journal International*, 77(1): 185-264.
- Jackson, J., Priestley, K., Allen, M., Berberian, M., 2002. Active tectonics of the south Caspian basin. *Geophysical Journal International*, 148(2): 214-245.
- Jarvis, A., Reuter, H.I., Nelson, A., Guevara, E., 2008. Hole-filled SRTM for the globe Version 4. available from the CGIAR-CSI SRTM 90m Database (<http://srtm.csi.cgiar.org>).
- Jiménez-Munt, I., Fernández, M., Saura, E., Vergés, J., Garcia-Castellanos, D., 2012. 3-D lithospheric structure and regional/residual Bouguer anomalies in the Arabia—Eurasia collision (Iran). *Geophysical Journal International*, 190(3): 1311-1324.
- Joannin, S. et al., 2014. Vegetation, fire and climate history of the Lesser Caucasus: a new Holocene record from Zarishat fen (Armenia). *Journal of Quaternary Science*, 29(1): 70-82.
- Kadirov, F. et al., 2012. Kinematics of the eastern Caucasus near Baku, Azerbaijan. *Natural Hazards*, 63(2): 997-1006.
- Kakroodi, A. et al., 2015. Late Pleistocene and Holocene sea-level change and coastal paleoenvironment evolution along the Iranian Caspian shore. *Marine Geology*, 361: 111-125.
- Karakhanian, A., Abgaryan, Y., 2004. Evidence of historical seismicity and volcanism in the Armenian Highland (from Armenian and other sources). *Annals of Geophysics*.
- Karakhanian, A. et al., 2002. Holocene-historical volcanism and active faults as natural risk factors for Armenia and adjacent countries. *Journal of Volcanology and Geothermal Research*, 113(1): 319-344.
- Karakhanian, A.S. et al., 2004. Active faulting and natural hazards in Armenia, eastern Turkey and northwestern Iran. *Tectonophysics*, 380(3-4): 189-219.
- Karakhanyan, A. et al., 2013. GPS constraints on continental deformation in the Armenian region and Lesser Caucasus. *Tectonophysics*, 592: 39-45.
- Kazancı, N., Gulbabazadeh, T., 2013. Sefidrud delta and quaternary evolution of the southern Caspian Lowland, Iran. *Marine and Petroleum Geology*, 44: 120-139.
- Kehl, M., 2009. Quaternary climate change in Iran—the state of knowledge. *Erdkunde*: 1-17.
- Kehl, M., Frechen, M., Skowronek, A., 2005. Paleosols derived from loess and loess-like sediments in the Basin of Persepolis, Southern Iran. *Quaternary International*, 140: 135-149.

- Keskin, M., 2005. Domal uplift and volcanism in a collision zone without a mantle plume: Evidence from Eastern Anatolia. *MantlePlume*. Org.
- Khain, V., Koronousky, N., 1997. Caucasus, *Encyclopedia of European and Asian regional geology*. Springer, pp. 127-136.
- Khodaverdian, A., Zafarani, H., Rahimian, M., 2015. Long term fault slip rates, distributed deformation rates and forecast of seismicity in the Iranian Plateau. *Tectonics*, 34(10): 2190-2220.
- Kirby, E. et al., 2002. Late Cenozoic evolution of the eastern margin of the Tibetan Plateau: Inferences from $^{40}\text{Ar}/^{39}\text{Ar}$ and (U-Th)/He thermochronology. *Tectonics*, 21(1): 1-1-1-20.
- Kirby, E., Whipple, K.X., 2012. Expression of active tectonics in erosional landscapes. *Journal of Structural Geology*, 44: 54-75.
- Knipper, A., 1975. Oceanic Crust in the Structure of the Alpine Fold Region. *Geol. Inst. Trudy*.
- Koçyiğit, A., Yilmaz, A., Adamia, S., Kuloshvili, S., 2001. Neotectonics of East Anatolian Plateau (Turkey) and Lesser Caucasus: implication for transition from thrusting to strike-slip faulting. *Geodinamica Acta*, 14(1-3): 177-195.
- Kong, X., Bird, P., 1995. SHELLS: A thin-shell program for modeling neotectonics of regional or global lithosphere with faults. *Journal of Geophysical Research: Solid Earth*, 100(B11): 22129-22131.
- Kühni, A., Pfiffner, O.-A., 2001. The relief of the Swiss Alps and adjacent areas and its relation to lithology and structure: topographic analysis from a 250-m DEM. *Geomorphology*, 41(4): 285-307.
- Kurter, A., Sungur, K., 1980. Present glaciation in Turkey. *International Association of Hydrological Sciences*, 126: 155-160.
- Lal, D., 1991. Cosmic ray labeling of erosion surfaces: in situ nuclide production rates and erosion models. *Earth and Planetary Science Letters*, 104(2): 424-439.
- Lebedev, V. et al., 2003. The Samsari volcanic center as an example of recent volcanism in the Lesser Caucasus: K-Ar geochronological and Sr-Nd isotopic data, *DOKLADY EARTH SCIENCES C/C OF DOKLADY-AKADEMIIA NAUK. INTERPERIODICA PUBLISHING*, pp. 1323-1328.
- Lechmann, A., Burg, J.-P., Ulmer, P., Guillong, M., Faridi, M., 2018. Metasomatized mantle as the source of Mid-Miocene-Quaternary volcanism in NW-Iranian Azerbaijan: Geochronological and geochemical evidence. *Lithos*, 304: 311-328.
- Lemcke, G., Sturm, M., 1997. $\delta^{18}\text{O}$ and trace element measurements as proxy for the reconstruction of climate changes at Lake Van (Turkey): Preliminary results, Third millennium BC climate change and Old World collapse. Springer, pp. 653-678.
- Leroy, S. et al., 2011. Late Little Ice Age palaeoenvironmental records from the Anzali and Amirkola Lagoons (south Caspian Sea): Vegetation and sea level changes. *Palaeogeography, Palaeoclimatology, Palaeoecology*, 302(3-4): 415-434.
- Liu, Z., Bird, P., 2008. Kinematic modelling of neotectonics in the Persia-Tibet-Burma Orogen. *Geophysical Journal International*, 172(2): 779-797.
- Lordkipanidze, M., 1980. Alpine volcanism and geodynamics of the central segment of the Mediterranean fold belt. *Metsniereba*, Tbilisi, 162.
- Lupker, M. et al., 2012. ^{10}Be -derived Himalayan denudation rates and sediment budgets in the Ganga basin. *Earth and Planetary Science Letters*, 333: 146-156.
- Lydolph, P.E., Landsberg, H.E., 1977. *Climates of the soviet union*, 7. Elsevier Scientific Publishing Company.
- Madanipour, S., Ehlers, T.A., Yassaghi, A., Enkelmann, E., 2017. Accelerated middle Miocene exhumation of the Talesh Mountains constrained by U-Th/He thermochronometry: evidence for the Arabia-Eurasia collision in the NW Iranian Plateau. *Tectonics*.
- Madanipour, S. et al., 2013. Synchronous deformation on orogenic plateau margins: Insights from the Arabia-Eurasia collision. *Tectonophysics*, 608: 440-451.
- Maggi, A., Priestley, K., 2005. Surface waveform tomography of the Turkish-Iranian plateau. *Geophysical Journal International*, 160(3): 1068-1080.
- Masson, F. et al., 2006. Extension in NW Iran driven by the motion of the South Caspian Basin. *Earth and Planetary Science Letters*, 252(1-2): 180-188.
- Mattei, M. et al., 2017. Oroclinal bending in the Alborz Mountains (Northern Iran): New constraints on the age of South Caspian subduction and extrusion tectonics. *Gondwana Research*, 42: 13-28.
- McKenzie, D., 1978. Active tectonics of the Alpine-Himalayan belt: the Aegean Sea and surrounding regions. *Geophysical Journal International*, 55(1): 217-254.
- Mesbahi, F., Mohajjel, M., Faridi, M., 2016. Neogene oblique convergence and strain partitioning along the North Tabriz Fault, NW Iran. *Journal of Asian Earth Sciences*, 129: 191-205.
- Messenger, E. et al., 2013. Late Quaternary record of the vegetation and catchment-related changes from Lake Paravani (Javakheti, South Caucasus). *Quaternary Science Reviews*, 77: 125-140.

- Miller, K.G. et al., 2005. The Phanerozoic record of global sea-level change. *science*, 310(5752): 1293-1298.
- Montgomery, D.R., Brandon, M.T., 2002. Topographic controls on erosion rates in tectonically active mountain ranges. *Earth and Planetary Science Letters*, 201(3-4): 481-489.
- Montgomery, D.R., Foufoula-Georgiou, E., 1993. Channel network source representation using digital elevation models. *Water Resources Research*, 29(12): 3925-3934.
- Morley, C.K. et al., 2009. Structural development of a major late Cenozoic basin and transpressional belt in central Iran: The Central Basin in the Qom-Saveh area. *Geosphere*, 5(4): 325-362.
- Mulch, A., Uba, C.E., Strecker, M.R., Schoenberg, R., Chamberlain, C.P., 2010. Late Miocene climate variability and surface elevation in the central Andes. *Earth and Planetary Science Letters*, 290(1): 173-182.
- Niemann, J.D., Gasparini, N.M., Tucker, G.E., Bras, R.L., 2001. A quantitative evaluation of Playfair's law and its use in testing long-term stream erosion models. *Earth Surface Processes and Landforms*, 26(12): 1317-1332.
- Nishiizumi, K. et al., 2007. Absolute calibration of ¹⁰Be AMS standards. *Nuclear Instruments and Methods in Physics Research Section B: Beam Interactions with Materials and Atoms*, 258(2): 403-413.
- Okay, A.I., Zattin, M., Cavazza, W., 2010. Apatite fission-track data for the Miocene Arabia-Eurasia collision. *Geology*, 38(1): 35-38.
- Olivetti, V., Cyr, A.J., Molin, P., Faccenna, C., Granger, D.E., 2012. Uplift history of the Sila Massif, southern Italy, deciphered from cosmogenic ¹⁰Be erosion rates and river longitudinal profile analysis. *Tectonics*, 31(3).
- Oveisi, B. et al., 2009. Thick-and thin-skinned deformation rates in the central Zagros simple folded zone (Iran) indicated by displacement of geomorphic surfaces. *Geophysical Journal International*, 176(2): 627-654.
- Palano, M., Imprescia, P., Agnon, A., Gresta, S., 2017. An improved evaluation of the seismic/geodetic deformation-rate ratio for the Zagros Fold-and-Thrust collisional belt. *Geophysical Journal International*.
- Perron, J.T., Royden, L., 2013. An integral approach to bedrock river profile analysis. *Earth Surface Processes and Landforms*, 38(6): 570-576.
- Person, W.J., 1987. Seismological Notes—March-April 1986. *Bulletin of the Seismological Society of America*, 77(1): 314-318.
- Philip, H., Avagyan, A., Karakhanian, A., Ritz, J.-F., Rebai, S., 2001. Estimating slip rates and recurrence intervals for strong earthquakes along an intracontinental fault: example of the Pambak–Sevan–Sunik fault (Armenia). *Tectonophysics*, 343(3-4): 205-232.
- Philip, H., Cisternas, A., Gvishiani, A., Gorshkov, A., 1989. The Caucasus: an actual example of the initial stages of continental collision. *Tectonophysics*, 161(1): 1-21.
- Pirouz, M., Avouac, J.-P., Hassanzadeh, J., Kirschvink, J.L., Bahroudi, A., 2017. Early Neogene foreland of the Zagros, implications for the initial closure of the Neo-Tethys and kinematics of crustal shortening. *Earth and Planetary Science Letters*, 477: 168-182.
- Portenga, E.W., Bierman, P.R., 2011. Understanding Earth's eroding surface with ¹⁰Be. *GSA today*, 21(8): 4-10.
- Portenga, E.W. et al., 2015. Erosion rates of the Bhutanese Himalaya determined using in situ-produced ¹⁰Be. *Geomorphology*, 233: 112-126.
- Pritchard, D., Roberts, G., White, N., Richardson, C., 2009. Uplift histories from river profiles. *Geophysical Research Letters*, 36(24).
- Reichenbacher, B. et al., 2011. Late miocene stratigraphy, palaeoecology and palaeogeography of the Tabriz basin (NW Iran, Eastern Paratethys). *Palaeogeography, Palaeoclimatology, Palaeoecology*, 311(1-2): 1-18.
- Reilinger, R. et al., 2006a. GPS constraints on continental deformation in the Africa-Arabia-Eurasia continental collision zone and implications for the dynamics of plate interactions. *Journal of Geophysical Research: Solid Earth*, 111(B5).
- Reilinger, R. et al., 2006b. GPS constraints on continental deformation in the Africa-Arabia-Eurasia continental collision zone and implications for the dynamics of plate interactions. *Journal of Geophysical Research: Solid Earth (1978–2012)*, 111(B5).
- Rezaeian, M., Carter, A., Hovius, N., Allen, M., 2012. Cenozoic exhumation history of the Alborz Mountains, Iran: New constraints from low-temperature chronometry. *Tectonics*, 31(2).
- Ricou, L.-E., 1994. Tethys reconstructed: plates, continental fragments and their Boundaries since 260 Ma from Central America to South-eastern Asia. *Geodinamica acta*, 7(4): 169-218.
- Ritz, J.-F. et al., 2016. Active tectonics within the NW and SE extensions of the Pambak-Sevan-Syunik fault: Implications for the present geodynamics of Armenia. *Quaternary International*, 395: 61-78.

- Rizza, M. et al., 2013. Morphotectonic and geodetic evidence for a constant slip-rate over the last 45 kyr along the Tabriz fault (Iran). *Geophysical Journal International*: ggt041.
- Robinson, A., Banks, C., Rutherford, M., Hirst, J., 1995. Stratigraphic and structural development of the Eastern Pontides, Turkey. *Journal of the Geological Society*, 152(5): 861-872.
- Rosenbloom, N.A., Anderson, R.S., 1994. Hillslope and channel evolution in a marine terraced landscape, Santa Cruz, California. *Journal of Geophysical Research: Solid Earth* (1978–2012), 99(B7): 14013-14029.
- Scherler, D., Bookhagen, B., Strecker, M.R., 2014. Tectonic control on ¹⁰Be-derived erosion rates in the Garhwal Himalaya, India. *Journal of Geophysical Research: Earth Surface*, 119(2): 83-105.
- Schwanghart, W., Kuhn, N.J., 2010. TopoToolbox: A set of Matlab functions for topographic analysis. *Environmental Modelling & Software*, 25(6): 770-781.
- Schwanghart, W., Scherler, D., 2014. Short Communication: TopoToolbox 2-MATLAB-based software for topographic analysis and modeling in Earth surface sciences. *Earth Surface Dynamics*, 2(1): 1.
- Selçuk, A.S., 2016. Evaluation of the relative tectonic activity in the eastern Lake Van basin, East Turkey. *Geomorphology*, 270: 9-21.
- Şengör, A., 1990. A new model for the late Palaeozoic—Mesozoic tectonic evolution of Iran and implications for Oman. *Geological Society, London, Special Publications*, 49(1): 797-831.
- Şengör, A., Altıner, D., Cin, A., Ustaömer, T., Hsü, K., 1988. Origin and assembly of the Tethyside orogenic collage at the expense of Gondwana Land. *Geological Society, London, Special Publications*, 37(1): 119-181.
- Şengör, A., Kidd, W., 1979. Post-collisional tectonics of the Turkish-Iranian plateau and a comparison with Tibet. *Tectonophysics*, 55(3-4): 361-376.
- Sevindi, C., Kopar, İ., Kaya, G., 2004. AKDAM (KAĞIZMAN-KARS) HEYELANI/Akdam (Kağızman-Kars) Landslide. *Doğu Coğrafya Dergisi*, 9(11).
- Shad Manaman, N., Shomali, H., Koyi, H., 2011. New constraints on upper-mantle S-velocity structure and crustal thickness of the Iranian plateau using partitioned waveform inversion. *Geophysical Journal International*, 184(1): 247-267.
- Sharifi, A. et al., 2015. Abrupt climate variability since the last deglaciation based on a high-resolution, multi-proxy peat record from NW Iran: The hand that rocked the Cradle of Civilization? *Quaternary Science Reviews*, 123: 215-230.
- Sharifi, Z., Safari Sinigani, A., 2012. Arsenic and other irrigation water quality indicators of groundwater in an agricultural area of Qorveh Plain, Kurdistan, Iran. *Am Eurasian J Agric Environ Sci*, 12(4): 548-555.
- Sokhadze, G. et al., 2018. Active convergence between the Lesser and Greater Caucasus in Georgia: Constraints on the tectonic evolution of the Lesser–Greater Caucasus continental collision. *Earth and Planetary Science Letters*, 481: 154-161.
- Sosson, M. et al., 2010. Subductions, obduction and collision in the Lesser Caucasus (Armenia, Azerbaijan, Georgia), new insights. *Geological Society, London, Special Publications*, 340(1): 329-352.
- Stein, R.S., Barka, A.A., Dieterich, J.H., 1997. Progressive failure on the North Anatolian fault since 1939 by earthquake stress triggering. *Geophysical Journal International*, 128(3): 594-604.
- Stein, S., Mazzotti, S., 2007. Continental intraplate earthquakes: science, hazard, and policy issues, 425. *Geological Society of America*.
- Stephenson, R., Lambeck, K., 1985. Isostatic response of the lithosphere with in-plane stress: Application to central Australia. *Journal of Geophysical Research: Solid Earth*, 90(B10): 8581-8588.
- Stocklin, J., 1968. Structural history and tectonics of Iran: a review. *AAPG Bulletin*, 52(7): 1229-1258.
- Stone, J.O., 2000. Air pressure and cosmogenic isotope production. *Journal of Geophysical Research: Solid Earth*, 105(B10): 23753-23759.
- Su, Z., Wang, E.-C., Hu, J.-C., Talebian, M., Karimzadeh, S., 2017. Quantifying the Termination Mechanism Along the North Tabriz-North Mishu Fault Zone of Northwestern Iran via Small Baseline PS-InSAR and GPS Decomposition. *IEEE Journal of Selected Topics in Applied Earth Observations and Remote Sensing*, 10(1): 130-144.
- Talebian, M., Jackson, J., 2002. Offset on the Main Recent Fault of NW Iran and implications for the late Cenozoic tectonics of the Arabia–Eurasia collision zone. *Geophysical Journal International*, 150(2): 422-439.
- Tarboton, D.G., Bras, R.L., Rodriguez-Iturbe, I., 1989. Scaling and elevation in river networks. *Water Resources Research*, 25(9): 2037-2051.
- Telbisz, T., Kovács, G., Székely, B., Szabó, J., 2013. Topographic swath profile analysis: a generalization and sensitivity evaluation of a digital terrain analysis tool. *Zeitschrift für Geomorphologie*, 57(4): 485-513.
- Thatcher, W., 1995. Microplate versus continuum descriptions of active tectonic deformation. *Journal of Geophysical Research: Solid Earth*, 100(B3): 3885-3894.

- Vernant, P., Chery, J., 2006. Low fault friction in Iran implies localized deformation for the Arabia–Eurasia collision zone. *Earth and Planetary Science Letters*, 246(3): 197-206.
- Vernant, P. et al., 2004. Present-day crustal deformation and plate kinematics in the Middle East constrained by GPS measurements in Iran and northern Oman. *Geophysical Journal International*, 157(1): 381-398.
- Vezzoli, G. et al., 2014. Tracking sediment provenance and erosional evolution of the western Greater Caucasus. *Earth Surface Processes and Landforms*, 39(8): 1101-1114.
- Vita-Finzi, C., 1969. Mediterranean valleys.
- von Blanckenburg, F., Willenbring, J.K., 2014. Cosmogenic nuclides: Dates and rates of Earth-surface change. *Elements*, 10(5): 341-346.
- Wang, Y. et al., 2017. How a stationary knickpoint is sustained: New insights into the formation of the deep Yarlung Tsangpo Gorge. *Geomorphology*, 285: 28-43.
- Whipple, K.X., 2004. Bedrock rivers and the geomorphology of active orogens. *Annu. Rev. Earth Planet. Sci.*, 32: 151-185.
- Whipple, K.X., 2009. The influence of climate on the tectonic evolution of mountain belts. *Nature geoscience*, 2(2): 97.
- Whipple, K.X., Tucker, G.E., 1999. Dynamics of the stream-power river incision model: Implications for height limits of mountain ranges, landscape response timescales, and research needs. *Journal of Geophysical Research: Solid Earth*, 104(B8): 17661-17674.
- Whipple, K.X., Tucker, G.E., 2002. Implications of sediment-flux-dependent river incision models for landscape evolution. *Journal of Geophysical Research: Solid Earth*, 107(B2).
- Whittaker, A.C., 2012. How do landscapes record tectonics and climate? *Lithosphere*, 4(2): 160-164.
- Willet, S.D., 2006. Tectonics, climate, and landscape evolution, 398. Geological Society of America.
- Willet, S.D., Brandon, M.T., 2002. On steady states in mountain belts. *Geology*, 30(2): 175-178.
- Willet, S.D., Brandon, M.T., 2013. Some analytical methods for converting thermochronometric age to erosion rate. *Geochemistry, Geophysics, Geosystems*, 14(1): 209-222.
- Willet, S.D., McCoy, S.W., Perron, J.T., Goren, L., Chen, C.-Y., 2014. Dynamic reorganization of river basins. *Science*, 343(6175): 1248765.
- Wobus, C. et al., 2006a. Tectonics from topography: Procedures, promise, and pitfalls. *Geological Society of America Special Papers*, 398: 55-74.
- Wobus, C. et al., 2006b. Tectonics from topography: Procedures, promise, and pitfalls. *Special papers-geological society of america*, 398: 55.
- Yang, R., Willet, S.D., Goren, L., 2015. In situ low-relief landscape formation as a result of river network disruption. *Nature*, 520(7548): 526.
- Yildirim, C., Schildgen, T.F., Echtler, H., Melnick, D., Strecker, M.R., 2011. Late Neogene and active orogenic uplift in the Central Pontides associated with the North Anatolian Fault: Implications for the northern margin of the Central Anatolian Plateau, Turkey. *Tectonics*, 30(5).
- Yilmaz, E., Haupt, K., Mosbach, K., 2000. The use of immobilized templates—A new approach in molecular imprinting. *Angewandte Chemie International Edition*, 39(12): 2115-2118.
- Zakariadze, G. et al., 1983. The ophiolite volcanic series of the Lesser Caucasus. *Ofioliti*, 8(3): 439-465.
- Zanchi, A., Berra, F., Mattei, M., Ghassemi, M.R., Sabouri, J., 2006. Inversion tectonics in central Alborz, Iran. *Journal of Structural Geology*, 28(11): 2023-2037.
- Zarifi, Z., Nilfouroushan, F., Raeesi, M., 2014. Crustal stress map of Iran: insight from seismic and geodetic computations. *Pure and Applied Geophysics*, 171(7): 1219-1236.
- Zonenshain, L.P., Pichon, X., 1986. Deep basins of the Black Sea and Caspian Sea as remnants of Mesozoic back-arc basins. *Tectonophysics*, 123(1-4): 181-211.
- Zor, E. et al., 2003. The crustal structure of the East Anatolian plateau (Turkey) from receiver functions. *Geophysical Research Letters*, 30(24).

Acknowledgements

This research was financed by Structural Geology and Tectonics Group (SGT, PA2330-022) under the guidance of Prof. Jean-Pierre Burg at ETH Zurich, Switzerland from October 2014 to September 2018. I would like to express my special gratitude to my supervisor, *Jean-Pierre Burg*, for granting me the opportunity to do this doctorate. I appreciate all your scientific and financial supports, the liberty you gave me during my work to learn many new methods in active tectonics. Moreover, special thanks to my co-supervisor, *Laurentiu Danciu*, for his continuous scientific support during my doctorate, positive energy, teaching me self-confidence, training me the true way to think and how to enjoy with my work. *Merci beaucoup and mulțumesc mult* to both of you dears, I learned a lot from you during my doctorate.

Dear *Regula Schaelchli*, *Ingrid Okanta* and *Sigrid Trindler* thank you for all your administrative support and *Thomas Löffler* for the informatics support.

Administrative and logistical support by the Geological Survey of Iran (GSI), Istanbul Technical University (ITU), and Ilia State University of Tbilisi (Georgia) is sincerely acknowledged. Thanks to *Mohammad-Taghi Korehie*, *Razieh Lak*, *Manouchehr Ghorashi*, *Mohammad Faridi*, *Abdolhamid Sartipi*, *Cengiz Yildirim*, *Gültekin Topuz*, *Morteza Talebian*, *Mikheil Elashvili*, and *Lasha Sukhishvili* for their roles in setting up my field trip in NW Iran, NE Turkey and Georgia. This work would not have been possible without your assistants “*Ramin Elyaszadeh and the hospitality of his family*, *Taher Khoshzare*, *Emrah Özpolat and his friends*, *Giorgi Merebashvili*” and my patient drivers “*Hossein Asdaghi and Levan Kvashali*” in the field. Special acknowledgment to *my dear father and brothers* who attended and helped me in the field and with the shipment of the samples to the ETH.

I would like to thank *Sanjay Kumar Mandal*, *Emanuele Giachetta*, and *Sean Francis Gallen* for teaching me remote sensing methods and helpful discussions. Thanks to *Alireza Khodaverdian* for training Kinematic modelling and discussions. The successful result of this thesis would not have been possible without the great support of the cosmogenic lab, sedimentary and mineral separation labs, Ion Beam Physics Group at ETH Höggerberg. I have enjoyed working with them and special acknowledge goes to: *Negar Haghipour*, *Maria Giuditta Fellin* and *Marcus Christl*. Thanks *Negar* and *Giuditta* for discussions. The useful discussions with *Vincenzo Picotti*, *Maarten Lupker*, *Oguz Gogus*, *Saleh Hamed*, and *Adam Forte* are acknowledged.

I am very grateful to *Ali Mohammadi* “my officemate, colleague, neighbor and friend” for all his company during good and bad times of my doctorate. I was able to survive my doctorate with his moral support and helpful discussions. Special thanks to my nice friends *Quinn Wenning* and *Ozge Karakas* for patiently checking my written English, and all the nice moments. Also special thanks to my dear friends *Anna Lechmann*, *Neda Meshk-Sar*, *Mahmoud Hefny* and *Stéphane Beaussier* for all kindness and memorable times.

I shared so many good memories and lunch time with colleagues in SGT “*Wen*, *Sanjay*, *Shankar*, *Rita*, *Sebastian*, *Friedrich*, *Stefania*, *Marcel*, *Neil*, *Claudio*, *Alba*, *Richard*, *Marine*, *Saima*, *Xiaoyu*, and *Gisel Peri*”. Thanks a lot to our Iranian Mafia “*Neda*, *Mohammadreza*, *Morteza*, *Mehrdad*, *Alireza*, *Meysam-Samaneh*, *Ahoura*, *Mohsen*, *Vahid*, *Mohammadjavad*, *Atefeh* and *Neda*” for all the happy times and parties. Furthermore, many thanks go to *Lechmann sisters (Sarah and Julia) and their parents*, *Asim Sengör*, *Ada Gençoğlu*, *Sara Gerber*, *Aditi Chatterjee*, *Patrizia Will*, *Daniela Bolrão*, *Jessica Munch*, *Benedetta Dini*, *Larissa de Palézieux*, *Jochem Braakhekke*, *Pilar Sanchez*, *Daniela Hunziker*, *Jonas Ruh*, *Letícia Luz*, *Tessa van der Voort*, *Giuliano Krättli*, *Thamy Lara*, *Lucie Tajcmanová*, *Judith McKenzie*, *Chris and Gisele Vasconcelos*, and *Philippe Roth* for the nice moments shared over these last four years.

Thanks to my external examiner, *Sébastien Castelltort*, and chair, *Lucie Tajcmanová*, for assisting with the defense proceedings.

I would like to acknowledge *Whimney Behr* for financial support the rest part of this project “*work in preparation*”.

My special thanks to *Hamid Nazari* and *Khalil Baharfirouzi* for showing me a new world of Earth science after my master thesis and work in GSI.

Thanks my dearest friends “*Roja*, *Marjan*, *Mina* and *Fariba*”, even while away from Iran they never forgot me, and always being a source of stability and encouragement with their friendships.

My deepest appreciation and love to my bests, *my dear parents*, *great brothers and family*, for all successes during my doctorate and before, unlimited support, love and encouragement that yield the source of inspiration for my educations.

Finally, I wish you dears all the best in life and the same to those whom I might have forgotten to acknowledge here.

Amaneh, 24.08.2018

Curriculum Vitae

Amaneh Kaveh Firouz

Date of Birth: 09.02.1981
Nationality: Iranian
E-mail: amaneh.kaveh@gmail.com

Education

2014 – 2018: **ETH Zurich, Switzerland**
PhD in Structural Geology and Tectonics, ETH, Zurich, Switzerland.
Ph.D. Thesis: *Active collision zones: morphotectonic analysis, cosmogenic nuclide evidence and kinematic modelling of the Turkish-Iranian Plateau and Caucasus Regions*
Supervisor: *Prof. Dr. Jean-Pierre Burg*

2006 – 2009: **Master of Structural geology and Tectonics, Azad University, branch of science and research, Tehran, Iran**
Master's Thesis: *Paleoseismological investigation along the North Tehran Fault zone (Branch of Chitgar Fault).*
Supervisor: *Dr. Hamid Nazari*

2001 – 2005: **Bachelor of Geology, Payam Noor University, Tehran, Iran**

Practical experience

2017 - 2018: Assistant of sediment lab, ETH Zurich
2016 - 2018: Work in quaternary dating labs (cosmogenic nuclide and carbon), ETH Zurich
2016 - 2017: Assistant of Quaternary molasse course, ETH Zurich
2012 - 2015: Co-advisor of 2 theses in Caspian Project (Research Institute of Earth Science)
2009 - 2014: Geologist (active tectonic) in Geological survey of Iran, Tehran
2009 - 2010: Cooperation with Central Zagros project, NIOC, Iran

Computer skills

Microsoft Office: good
Adobe Illustrator and Photoshop: very good
ArcGIS: very good
Matlab: good

Language skills

Persian: very good (native)
English: good

Publications

Iranian Journals: 10 papers (first-author/co-author)

International Journals: 1 published paper (co-author), 1 under-revision paper (co-author), 3 manuscripts ready to submit (from my PhD, first-author)

International Conferences: 7 abstracts

Geological survey of Iran: 2 maps (morphotectonic/seismotectonic) and the reports

Appendix

Appendix A) Table S1A-Fault slip-rates (input) for comprehensive kinematic model:

F0000X	Descriptive text	Offset-rate	Sigma(mm/a)	ULxKm	LLxKm
F0001R	NAF_1939,1992eqks	22.420	7.538	-1	-1
F0002R	Akdogan_Golu_F.	1.750	2.000	-1	-1
F0003R	Kazbel_F	1.750	2.000	-1	-1
F0004R	Balik_Golu_F	1.000	2.000	-1	-1
F0005R	Sudugnu_F_2003eqk_Bingol	1.250	2.000	-1	-1
F0006R	Yenisu_F	0.625	2.003	-1	-1
F0007R	Caldiran_F	4.500	2.000	-1	-1
F0008L	Palandoken_F	2.500	2.000	-1	-1
F0009R	Hasantimur_Golu_F	0.850	2.000	-1	-1
F0010L	Baskale_F	2.090	2.000	-1	-1
F0011R	Igdir_F1	0.850	2.000	-1	-1
F0012R	Igdir_F2	0.850	2.000	-1	-1
F0013L	Olur_F	1.000	2.000	-1	-1
F0014R	NAF-1949 Elmali Earthquake	13.480	7.500	-1	-1
F0015R	NAF-1784 Elmali Earthquake	25.960	7.500	-1	-1
F0016L	EAF-1866 Earhtquake(Karlioiva)	8.100	5.000	-1	-1
F0017L	EAF-1971 Earthquake(Bingol)	8.100	5.000	-1	-1
F0018L	EAF-Genc	4.100	2.000	-1	-1
F0019L	EAF-2010 Basyurt Elazig Earthquake	9.490	5.000	-1	-1
F0020L	EAF-Palu	10.000	5.000	-1	-1
F0021R	Tutak1	1.750	2.000	-1	-1
F0022R	Karayazi	1.750	2.000	-1	-1
F0023L	Horasan	0.750	2.000	-1	-1
F0024L	Kagizman	2.500	2.000	-1	-1
F0025L	Malazgirt_1903 Earthquake	0.750	2.000	-1	-1
F0026L	Cobandede_1983 EarthquakeZone	1.500	2.000	-1	-1
F0027L	Dumlu	2.500	2.000	-1	-1
F0028L	Narman_zone	0.625	2.003	-1	-1
F0029R	Bulanik	1.750	2.000	-1	-1
F0030R	Ercis	1.750	2.000	-1	-1
F0031L	Suphan_Zone	1.000	2.000	-1	-1
F0032L	SuphanZone-Suphan_North	1.000	2.000	-1	-1
F0033R	Yukekova_Semdinli_Zone-Semdinli	2.000	2.000	-1	-1
F0034R	Yukekova_Semdinli_Zone-Yuksekoa	2.000	2.000	-1	-1
F0035T	Yukekova_Semdinli_Zone-Hakkari_North	0.625	2.003	-1	-1
F0036R	Van_Lake_Southern-Boundary	2.055	2.003	-1	-1
F0037R	Van_Lake_Southern-Boundary1	1.785	2.003	-1	-1
F0038T	Van_Lake_Southern-Boundary2	1.250	2.000	-1	-1
F0039T	Kalecik-Van	1.500	2.000	-1	-1
F0040R	Alabayir	1.500	2.000	-1	-1
F0041T	Mus_Thrust_Zone	1.625	2.003	-1	-1
F0042L	Senkaya	1.500	2.000	-1	-1
F0043L	Erzurum	2.500	2.000	-1	-1
F0044R	Tercan-Askale	1.500	2.000	-1	-1
F0045L	Posof-Savsat-South	0.550	2.000	-1	-1
F0046L	Kelkit-Coruh_Zone	1.500	2.000	-1	-1
F0047L	Ispir-Kelkit	2.300	2.000	-1	-1
F0048L	Kelkit	0.750	2.000	-1	-1
F0049L	Cildir	1.000	2.000	-1	-1
F0050R	1966-Varto-Earthquake	1.750	2.000	-1	-1
F0051R	1946-Ustukran-Earthquake	2.625	2.003	-1	-1

F0000X	Descriptive text	Offset-rate	Sigma(mm/a)	ULxKm	LLxKm
F0052T	Bitlis-Thrust-Zone-Siirt	3.700	2.000	-1	-1
F0053T	BitlisThrustZone_1866Kulp-Earthquake	4.750	2.000	-1	-1
F0054T	BitlisThrustZone_1975Lice-Earthquake	3.820	2.000	-1	-1
F0055T	BitlisThrustZone_Ergani-Cungus	2.530	2.000	-1	-1
F0056R	Kavakbasi	2.000	2.000	-1	-1
F0057T	GurpinarThrust	1.560	2.000	-1	-1
F0058R	Yayla	1.625	2.003	-1	-1
F0059L	Sancak-Uzunpinar1	1.000	2.000	-1	-1
F0060L	Sancak-Uzunpinar2	1.250	2.000	-1	-1
F0061L	MOF-Ovacik1	2.080	2.000	-1	-1
F0062T	SE-BlackSea_Margin	1.000	2.000	-1	-1
F0063R	Dagyolu-Caglayan_Zone	1.130	2.000	-1	-1
F0064L	Patnos	0.750	2.000	-1	-1
F0065N	Tuzluca	2.500	2.000	-1	-1
F0066T	Bitlis-Thrust-Zone_Hakkari	3.700	2.000	-1	-1
F0067R	Bingol-Karakocan1	2.625	2.003	-1	-1
F0068R	Dashte-Moghan	1.175	2.000	-1	-1
F0069R	Kushke-Nosrat	1.250	2.000	-1	-1
F0070R	Morvarid_MRF	2.500	2.000	-1	-1
F0071L	Pishva	1.000	2.000	-1	-1
F0072R	Piranshahr_MRF	2.250	2.000	-1	-1
F0073L	Sangavar	1.250	2.000	-1	-1
F0074R	Sartakht_MRF	2.250	2.000	-1	-1
F0075T	Talesh	2.250	2.000	-1	-1
F0076R	Zanjan	1.175	2.000	-1	-1
F0077L	Bozgush	1.500	2.000	-1	-1
F0078L	Ipak	1.200	2.000	-1	-1
F0079T	Mosha1	1.500	2.000	-1	-1
F0080T	North_Tehran	0.300	2.000	-1	-1
F0081T	HZF	1.500	2.000	-1	-1
F0082R	North_Tabriz	5.800	1.400	-1	-1
F0083T	Eshtehard	0.360	2.000	-1	-1
F0084T	Kahrizak	1.500	2.000	-1	-1
F0085R	Kandovan	0.700	2.000	-1	-1
F0086T	Khazar	3.238	5.000	-1	-1
F0087L	Masuleh	0.500	2.000	-1	-1
F0088T	North_Qazvin	0.148	2.000	-1	-1
F0089T	Garmsar	1.000	2.000	-1	-1
F0090R	Alamutrud	1.000	2.000	-1	-1
F0091T	Indes	0.360	2.000	-1	-1
F0092T	North_Alborz	0.360	2.000	-1	-1
F0093T	Soltanieh	1.450	1.975	-1	-1
F0094T	Tafresh	0.000	2.000	-1	-1
F0095L	Taleghan	1.250	0.225	-1	-1
F0096T	Sufian	2.100	3.000	-1	-1
F0097R	SNF	2.250	0.375	-1	-1
F0098R	GSKF	3.000	0.500	-1	-1
F0099R	Tasuj	1.365	2.000	-1	-1
F0100R	Ahar-Arasbaran	2.000	2.000	-1	-1
F0101R	GSKF2	3.000	0.500	-1	-1
F0102T	MRF1	1.500	2.000	-1	-1
F0103R	MRF2	1.500	2.000	-1	-1
F0104R	MRF3	1.500	2.000	-1	-1

F0000X	Descriptive text	Offset-rate	Sigma(mm/a)	ULxKm	LLxKm
F0105R	MRF4_Sahneh	2.500	2.000	-1	-1
F0106R	TakhteSolay	0.650	2.000	-1	-1
F0107R	MaraghehF.	1.000	2.000	-1	-1
F0108R	NZF2.	1.550	2.000	-1	-1
F0109R	Khalkhal_F.	1.295	2.003	-1	-1
F0110L	Lahijan_F.	1.425	2.003	-1	-1
F0111L	Kashachal_Bonan	1.250	2.000	-1	-1
F0112T	Eyvanekey_F.	0.550	2.000	-1	-1
F0113T	Avaj_F1	1.500	2.000	-1	-1
F0114T	Avaj_F2	1.500	2.000	-1	-1
F0115R	Qom_F	1.500	2.000	-1	-1
F0116T	Siahkuh_F	1.000	2.000	-1	-1
F0117L	Mosha2	1.500	2.000	-1	-1
F0118R	N.Khalkhal_F	0.350	2.000	-1	-1
F0119R	Astara_F	0.700	2.000	-1	-1
F0120T	Arax_F1	0.550	2.000	-1	-1
F0121L	Arax_F2	1.250	2.000	-1	-1
F0122R	Salmas_F	1.500	2.000	-1	-1
F0123R	N.Bozgush_F	2.000	2.000	-1	-1
F0124R	S.Bozgush_F	2.000	2.000	-1	-1
F0125R	N.Mishu_F	4.730	2.000	-1	-1
F0126R	Badalan_F	0.750	2.000	-1	-1
F0127R	Kamar-kasan_F	1.250	2.000	-1	-1
F0128R	Maku_F	0.850	2.000	-1	-1
F0129R	Ahar_F	2.350	2.000	-1	-1
F0130L	Rudbar_F	1.100	2.000	-1	-1
F0131R	Nakh1	0.750	2.000	-1	-1
F0132R	Nakh2	0.750	2.000	-1	-1
F0133R	Nakh3	0.750	2.000	-1	-1
F0134R	GamiF1	1.325	2.003	-1	-1
F0135R	GamiF2	1.750	2.000	-1	-1
F0136R	GamiF3	1.750	2.000	-1	-1
F0137R	GamiF4	0.625	2.003	-1	-1
F0138R	GamiF5	0.900	2.000	-1	-1
F0139R	PSSF1	2.400	2.000	-1	-1
F0140R	PSSF2	1.550	2.000	-1	-1
F0141R	PSSF3	1.550	2.000	-1	-1
F0142R	PSSF4	1.000	2.000	-1	-1
F0143R	PSSF5A	1.100	2.000	-1	-1
F0144R	PSSF5B	1.100	2.000	-1	-1
F0145R	PSSF5C	1.100	2.000	-1	-1
F0146R	PSSF5D	1.100	2.000	-1	-1
F0147L	Akhourian_F	2.000	2.000	-1	-1
F0148R	Akery_F	1.050	2.000	-1	-1
F0149T	LC_F	0.550	2.000	-1	-1
F0150T	Kura_F1	0.700	2.000	-1	-1
F0151T	Kura_F2	0.750	2.000	-1	-1
F0152T	Achara_Trialet	1.000	2.000	-1	-1
F0153T	Kura_FT1	0.850	2.000	-1	-1
F0154T	Kura_FT2	0.700	2.000	-1	-1
F0155T	Kura_FT3	0.720	2.000	-1	-1
F0156T	Kura_FT4	0.700	2.000	-1	-1
F0157T	Kura_FT5	0.720	2.000	-1	-1

F0000X	Descriptive text	Offset-rate	Sigma(mm/a)	ULxKm	LLxKm
F0158T	Kura_FT6	1.125	2.003	-1	-1
F0159T	Kura_FT7	1.100	2.000	-1	-1
F0160T	Kura_FT8	0.855	2.003	-1	-1
F0161T	MCT1	0.550	2.000	-1	-1
F0162T	MCT2	0.550	2.000	-1	-1
F0163T	MCT3	0.500	2.000	-1	-1
F0164T	MCT4	0.430	2.000	-1	-1
F0165T	MCT5	0.400	2.000	-1	-1
F0166T	MCT6	0.465	2.003	-1	-1
F0167T	Alasani_F	0.375	2.000	-1	-1
F0168T	MCT7	0.170	2.000	-1	-1
F0169T	MCT8	0.170	2.000	-1	-1
F0170T	Rioni_F	0.100	2.000	-1	-1
F0171T	Samsari1	0.150	2.000	-1	-1
F0172T	Samsari2	0.210	2.000	-1	-1
F0173T	Samsari3	0.210	2.000	-1	-1
F0174R	Samsari4	0.105	2.003	-1	-1
F0175L	S.Rioni	0.360	2.000	-1	-1
F0176L	Dzirula1	0.360	2.000	-1	-1
F0177R	Dzirula2	0.300	2.000	-1	-1
F0178T	MCT9	0.430	2.000	-1	-1
F0179T	MCT10	0.360	2.000	-1	-1
F0180T	MCT11	0.390	2.000	-1	-1
F0181L	DKHF	0.000	2.000	-1	-1
F0182L	PYF	0.000	2.000	-1	-1
F0183L	BAF	0.000	2.000	-1	-1
F0184L	Garmachay_F	0.000	2.000	-1	-1
F0185L	Aghmion_F	0.000	2.000	-1	-1
F0186L	GBF	0.000	2.000	-1	-1
F0187R	SSF	0.000	2.000	-1	-1
F0188R	S.Ararat	0.850	2.025	-1	-1
F0189R	Aragate	0.750	2.025	-1	-1
F0330T	Zanjan	0.000	5.000	-1	-1
F0190T	MCT12	0.390	2.000	-1	-1
F0191T	TerekF1	0.390	2.000	-1	-1
F0192T	TerekF2	0.390	2.000	-1	-1
F0193T	TerekF3	0.390	2.000	-1	-1

Appendix A) Table S1B-Fault slip-rates excluded (input) and given classified uncertainties:

F0000X	Descriptive text	Offset-rate	Sigma(mm/a)	ULxKm	LLxKm
F0001R	NAF_1939,1992eqks	0.000	20.000	-1	-1
F0002R	Akdogan_Golu_F.	0.000	5.000	-1	-1
F0003R	Kazbel_F	0.000	5.000	-1	-1
F0004R	Balik_Golu_F	0.000	5.000	-1	-1
F0005R	Sudugnu_F_2003eqk_Bingol	0.000	5.000	-1	-1
F0006R	Yenisu_F	0.000	5.000	-1	-1
F0007R	Caldiran_F	3.270	0.085	-1	-1
F0008L	Palandoken_F	0.000	5.000	-1	-1
F0009R	Hasantimur_Golu_F	0.000	5.000	-1	-1
F0010L	Baskale_F	0.000	5.000	-1	-1
F0011R	Igdir_F1	0.000	5.000	-1	-1
F0012R	Igdir_F2	0.000	5.000	-1	-1
F0013L	Olur_F	0.000	5.000	-1	-1
F0014R	NAF-1949 Elmali Earthquake	0.000	10.000	-1	-1
F0015R	NAF-1784 Elmali Earthquake	0.000	20.000	-1	-1
F0016L	EAF-1866 Earhtquake(Karlioiva)	0.000	10.000	-1	-1
F0017L	EAF-1971 Earthquake(Bingol)	0.000	10.000	-1	-1
F0018L	EAF-Genc	0.000	5.000	-1	-1
F0019L	EAF-2010 Basyurt Elazig Earthquake	0.000	10.000	-1	-1
F0020L	EAF-Palu	0.000	10.000	-1	-1
F0021R	Tutak1	0.000	5.000	-1	-1
F0022R	Karayazi	0.000	5.000	-1	-1
F0023L	Horasan	0.000	5.000	-1	-1
F0024L	Kagizman	0.000	5.000	-1	-1
F0025L	Malazgirt_1903 Earthquake	0.000	5.000	-1	-1
F0026L	Cobandede_1983 EarthquakeZone	0.000	5.000	-1	-1
F0027L	Dumlu	0.000	5.000	-1	-1
F0028L	Narman_zone	0.000	5.000	-1	-1
F0029R	Bulanik	0.000	5.000	-1	-1
F0030R	Ercis	0.000	5.000	-1	-1
F0031L	Suphan_Zone	0.000	5.000	-1	-1
F0032L	SuphanZone-Suphan_North	0.000	5.000	-1	-1
F0033R	Yukekova_Semdinli_Zone-Semdinli	0.000	5.000	-1	-1
F0034R	Yukekova_Semdinli_Zone-Yuksekov	0.000	5.000	-1	-1
F0035T	Yukekova_Semdinli_Zone-Hakkari_North	0.000	5.000	-1	-1
F0036R	Van_Lake_Southern-Boundary	0.000	5.000	-1	-1
F0037R	Van_Lake_Southern-Boundary1	0.000	5.000	-1	-1
F0038T	Van_Lake_Southern-Boundary2	0.000	5.000	-1	-1
F0039T	Kalecik-Van	0.000	5.000	-1	-1
F0040R	Alabayir	0.000	5.000	-1	-1
F0041T	Mus_Thrust_Zone	0.000	5.000	-1	-1
F0042L	Senkaya	0.000	5.000	-1	-1
F0043L	Erzurum	0.000	5.000	-1	-1
F0044R	Tercan-Askale	0.000	5.000	-1	-1
F0045L	Posof-Savsat-South	0.000	5.000	-1	-1
F0046L	Kelkit-Coruh_Zone	0.000	5.000	-1	-1
F0047L	Ispir-Kelkit	0.000	5.000	-1	-1
F0048L	Kelkit	0.000	5.000	-1	-1
F0049L	Cildir	0.000	5.000	-1	-1
F0050R	1966-Varto-Earthquake	0.000	5.000	-1	-1
F0051R	1946-Ustukran-Earthquake	0.000	5.000	-1	-1

F0000X	Descriptive text	Offset-rate	Sigma(mm/a)	ULxKm	LLxKm
F0052T	Bitlis-Thrust-Zone-Siirt	0.000	5.000	-1	-1
F0053T	BitlisThrustZone_1866Kulp-Earthquake	0.000	5.000	-1	-1
F0054T	BitlisThrustZone_1975Lice-Earthquake	0.000	5.000	-1	-1
F0055T	BitlisThrustZone_Ergani-Cungus	0.000	5.000	-1	-1
F0056R	Kavakbasi	0.000	5.000	-1	-1
F0057T	GurpinarThrust	0.000	5.000	-1	-1
F0058R	Yayla	0.000	5.000	-1	-1
F0059L	Sancak-Uzunpinar1	0.000	5.000	-1	-1
F0060L	Sancak-Uzunpinar2	0.000	5.000	-1	-1
F0061L	MOF-Ovacik1	0.000	5.000	-1	-1
F0062T	SE-BlackSea_Margin	0.000	5.000	-1	-1
F0063R	Dagyolu-Caglayan_Zone	0.000	5.000	-1	-1
F0064L	Patnos	0.000	5.000	-1	-1
F0065N	Tuzluca	0.000	5.000	-1	-1
F0066T	Bitlis-Thrust-Zone_Hakkari	0.000	5.000	-1	-1
F0067R	Bingol-Karakocan1	0.000	5.000	-1	-1
F0068R	Dashte-Moghan	0.000	5.000	-1	-1
F0069R	Kushke-Nosrat	0.000	5.000	-1	-1
F0070R	Morvarid_MRF	0.000	5.000	-1	-1
F0071L	Pishva	0.000	5.000	-1	-1
F0072R	Piranshahr_MRF	0.000	5.000	-1	-1
F0073L	Sangavar	0.000	5.000	-1	-1
F0074R	Sartakht_MRF	0.000	5.000	-1	-1
F0075T	Talesh	0.000	5.000	-1	-1
F0076R	Zanjan	0.000	5.000	-1	-1
F0077L	Bozgush	0.000	5.000	-1	-1
F0078L	Ipak	0.000	5.000	-1	-1
F0079T	Moshal	0.000	5.000	-1	-1
F0080T	North_Tehran	0.000	5.000	-1	-1
F0081T	HZF	0.000	5.000	-1	-1
F0082R	North_Tabriz	5.800	1.400	-1	-1
F0083T	Eshtehard	0.000	5.000	-1	-1
F0084T	Kahrizak	0.000	5.000	-1	-1
F0085R	Kandovan	0.000	5.000	-1	-1
F0086T	Khazar	0.000	5.000	-1	-1
F0087L	Masuleh	0.000	5.000	-1	-1
F0088T	North_Qazvin	0.000	5.000	-1	-1
F0089T	Garmsar	0.000	5.000	-1	-1
F0090R	Alamutrud	0.000	5.000	-1	-1
F0091T	Indes	0.000	5.000	-1	-1
F0092T	North_Alborz	0.000	5.000	-1	-1
F0093T	Soltanieh	0.000	5.000	-1	-1
F0094T	Tafresh	0.000	5.000	-1	-1
F0095L	Taleghan	0.000	5.000	-1	-1
F0096T	Sufian	0.000	5.000	-1	-1
F0097R	SNF	0.000	5.000	-1	-1
F0098R	GSKF	2.000	0.250	-1	-1
F0099R	Tasuj	0.000	5.000	-1	-1
F0100R	Ahar-Arasbaran	1.900	0.250	-1	-1
F0101R	GSKF2	2.000	0.250	-1	-1
F0102T	MRF1	0.000	5.000	-1	-1
F0103R	MRF2	0.000	5.000	-1	-1
F0104R	MRF3	0.000	5.000	-1	-1

F0000X	Descriptive text	Offset-rate	Sigma(mm/a)	ULxKm	LLxKm
F0105R	MRF4_Sahneh	0.000	5.000	-1	-1
F0106R	TakhteSolay	0.000	5.000	-1	-1
F0107R	MaraghehF.	0.000	5.000	-1	-1
F0108R	NZF2.	0.000	5.000	-1	-1
F0109R	Khalkhal_F.	0.000	5.000	-1	-1
F0110L	Lahijan_F.	0.000	5.000	-1	-1
F0111L	Kashachal_Bonan	0.000	5.000	-1	-1
F0112T	Eyvanekey_F.	0.000	5.000	-1	-1
F0113T	Avaj_F1	0.000	5.000	-1	-1
F0114T	Avaj_F2	0.000	5.000	-1	-1
F0115R	Qom_F	0.000	5.000	-1	-1
F0116T	Siahkuh_F	0.000	5.000	-1	-1
F0117L	Mosha2	0.000	5.000	-1	-1
F0118R	N.Khalkhal_F	0.000	5.000	-1	-1
F0119R	Astara_F	0.000	5.000	-1	-1
F0120T	Arax_F1	0.000	5.000	-1	-1
F0121L	Arax_F2	0.000	5.000	-1	-1
F0122R	Salmas_F	0.000	5.000	-1	-1
F0123R	N.Bozgush_F	0.000	5.000	-1	-1
F0124R	S.Bozgush_F	0.000	5.000	-1	-1
F0125R	N.Mishu_F	0.000	5.000	-1	-1
F0126R	Badalan_F	0.000	5.000	-1	-1
F0127R	Kamar-kasan_F	0.000	5.000	-1	-1
F0128R	Maku_F	0.000	5.000	-1	-1
F0129R	Ahar_F	0.000	5.000	-1	-1
F0130L	Rudbar_F	0.000	5.000	-1	-1
F0131R	Nakh1	0.000	5.000	-1	-1
F0132R	Nakh2	0.000	5.000	-1	-1
F0133R	Nakh3	0.000	5.000	-1	-1
F0134R	GarniF1	0.000	5.000	-1	-1
F0135R	GarniF2	0.000	5.000	-1	-1
F0136R	GarniF3	0.000	5.000	-1	-1
F0137R	GarniF4	0.000	5.000	-1	-1
F0138R	GarniF5	0.000	5.000	-1	-1
F0139R	PSSF1	2.000	0.250	-1	-1
F0140R	PSSF2	0.000	5.000	-1	-1
F0141R	PSSF3	0.000	5.000	-1	-1
F0142R	PSSF4	0.000	5.000	-1	-1
F0143R	PSSF5A	0.000	5.000	-1	-1
F0144R	PSSF5B	0.000	5.000	-1	-1
F0145R	PSSF5C	0.000	5.000	-1	-1
F0146R	PSSF5D	0.000	5.000	-1	-1
F0147L	Akhourian_F	0.000	5.000	-1	-1
F0148R	Akery_F	0.000	5.000	-1	-1
F0149T	LC_F	0.000	5.000	-1	-1
F0150T	Kura_F1	0.000	5.000	-1	-1
F0151T	Kura_F2	0.000	5.000	-1	-1
F0152T	Achara_Trialet	0.000	5.000	-1	-1
F0153T	Kura_FT1	0.000	5.000	-1	-1
F0154T	Kura_FT2	0.000	5.000	-1	-1
F0155T	Kura_FT3	0.000	5.000	-1	-1
F0156T	Kura_FT4	0.000	5.000	-1	-1
F0157T	Kura_FT5	0.000	5.000	-1	-1

F0000X	Descriptive text	Offset-rate	Sigma(mm/a)	ULxKm	LLxKm
F0158T	Kura_FT6	0.000	5.000	-1	-1
F0159T	Kura_FT7	0.000	5.000	-1	-1
F0160T	Kura_FT8	0.000	5.000	-1	-1
F0161T	MCT1	0.000	5.000	-1	-1
F0162T	MCT2	0.000	5.000	-1	-1
F0163T	MCT3	0.000	5.000	-1	-1
F0164T	MCT4	0.000	5.000	-1	-1
F0165T	MCT5	0.000	5.000	-1	-1
F0166T	MCT6	0.000	5.000	-1	-1
F0167T	Alasani_F	0.000	5.000	-1	-1
F0168T	MCT7	0.000	5.000	-1	-1
F0169T	MCT8	0.000	5.000	-1	-1
F0170T	Rioni_F	0.000	5.000	-1	-1
F0171T	Samsari1	0.000	5.000	-1	-1
F0172T	Samsari2	0.000	5.000	-1	-1
F0173T	Samsari3	0.000	5.000	-1	-1
F0174R	Samsari4	0.000	5.000	-1	-1
F0175L	S.Rioni	0.000	5.000	-1	-1
F0176L	Dzirula1	0.000	5.000	-1	-1
F0177R	Dzirula2	0.000	5.000	-1	-1
F0178T	MCT9	0.000	5.000	-1	-1
F0179T	MCT10	0.000	5.000	-1	-1
F0180T	MCT11	0.000	5.000	-1	-1
F0181L	DKHF	0.000	5.000	-1	-1
F0182L	PYF	0.000	5.000	-1	-1
F0183L	BAF	0.000	5.000	-1	-1
F0184L	Garmachay_F	0.000	5.000	-1	-1
F0185L	Aghmion_F	0.000	5.000	-1	-1
F0186L	GBF	0.000	5.000	-1	-1
F0187R	SSF	0.000	5.000	-1	-1
F0188R	S.Ararat	0.000	5.000	-1	-1
F0189R	Aragate	0.000	5.000	-1	-1
F0330T	Zanjan	0.000	5.000	-1	-1
F0190T	MCT12	0.000	5.000	-1	-1
F0191T	TerekF1	0.000	5.000	-1	-1
F0192T	TerekF2	0.000	5.000	-1	-1
F0193T	TerekF3	0.000	5.000	-1	-1

Appendix A) Table S2-Stress directions (input):

Names	E_long.	N_lat.	azi	quality	Names	E_long.	N_lat.	azi	quality	Names	E_long.	N_lat.	azi	quality	Names	E_long.	N_lat.	azi	quality
FMF	45.60	34.30	0	E	FMA	46.70	41.60	92	D	FMS	43.40	42.50	33	C	FMS	30.77	40.67	139	C
OC	30.67	36.88	0	C	FMS	33.95	27.57	93	C	DIF	30.01	31.73	34	D	FMS	33.82	27.62	140	C
FMS	55.40	39.30	0	D	FMS	32.74	28.92	93	C	BO	31.98	31.94	34	D	FMS	34.51	28.04	140	C
OC	29.10	40.18	0	B	BO	32.17	31.84	93	B	FMS	46.98	32.55	34	C	BO	50.63	29.91	140	E
OC	33.69	41.80	0	C	FMS	42.82	36.49	93	C	FMS	44.77	36.26	34	C	FMS	35.34	31.19	140	C
FMS	44.30	41.90	0	C	FMS	30.02	40.73	93	C	FMS	36.10	36.76	34	C	BO	32.25	31.54	140	B
FMS	50.47	31.77	1	C	FMS	31.74	30.54	94	C	FMS	44.60	42.50	34	C	HF	46.53	38.87	140	D
HFM	35.48	32.80	1	E	FMS	32.09	34.50	94	C	FMS	43.45	42.65	34	C	BO	51.31	40.07	140	D
FMS	58.19	35.46	1	C	FMS	29.22	40.69	94	C	FMS	47.19	43.45	34	C	FMS	34.83	40.60	140	C
FMS	41.60	43.20	1	C	FMS	34.03	27.58	95	C	FMS	57.67	26.52	35	C	FMA	48.20	40.60	140	D
FMS	53.95	26.75	2	C	BO	33.70	27.58	95	B	FMS	57.77	26.68	35	C	FMS	30.69	40.67	140	C
FMS	34.29	27.68	2	C	DIF	32.31	31.83	95	D	FMS	57.76	26.72	35	C	FMS	32.98	40.70	140	C
FMS	53.86	28.39	2	C	FMS	31.34	34.58	95	C	FMS	51.67	28.20	35	C	FMS	32.70	40.75	140	C
FMS	34.57	28.64	2	E	FMS	49.06	36.75	95	C	FMS	50.88	29.58	35	C	FMS	29.11	40.76	140	C
BO	31.85	31.92	2	B	FMS	43.88	37.77	95	C	FMS	51.61	29.96	35	C	FMS	34.25	41.13	140	C
FMS	45.71	34.14	2	C	FMS	31.10	29.66	96	C	FMS	47.05	32.58	35	C	FMS	37.74	25.29	141	C
FMS	50.65	34.59	2	C	FMS	31.12	29.68	96	C	FMS	47.60	32.76	35	C	FMS	33.87	27.49	141	C
FMS	61.50	35.91	2	C	FMS	29.68	32.28	96	C	FMS	44.82	36.04	35	C	FMS	33.18	28.78	141	C
FMS	35.71	37.23	2	C	FMS	43.89	37.80	96	C	FMS	52.78	36.34	35	C	FMS	48.86	37.57	141	C
FMS	43.58	38.67	2	C	FMS	29.05	38.03	96	C	FMS	58.33	36.56	35	C	FMS	55.80	26.99	142	C
FMS	46.25	43.37	2	C	FMA	48.40	40.60	96	D	GFI	58.52	36.72	35	B	HF	49.66	32.93	142	D
FMS	56.66	27.30	3	C	FMS	44.70	42.40	96	C	FMS	49.24	36.93	35	C	FMS	29.61	36.10	142	C
FMS	56.47	30.95	3	C	FMS	58.99	28.32	97	C	GFI	57.30	37.41	35	A	FMS	34.43	36.23	142	C
FMS	47.83	32.60	3	C	GFS	35.17	30.12	97	C	BO	51.22	40.11	35	B	FMS	54.32	37.37	142	C
FMS	48.46	32.73	3	C	FMA	35.30	32.60	97	D	FMS	53.14	40.47	35	C	FMS	33.19	39.40	142	C
FMS	50.59	34.50	3	C	FMS	40.85	36.27	97	C	FMS	51.06	28.49	36	C	FMS	40.75	39.48	142	C
FMS	47.66	34.54	3	C	FMS	40.87	36.36	97	C	FMS	57.79	30.01	36	C	FMS	50.09	40.31	142	C
FMF	57.50	35.70	3	E	FMS	29.41	36.96	97	C	BO	32.83	31.70	36	C	FMS	34.48	40.42	142	C
FMS	51.92	35.80	3	C	FMS	33.97	27.53	98	C	FMS	46.86	32.42	36	C	FMS	33.00	41.10	142	C
FMS	42.55	37.35	3	C	FMS	33.77	27.63	98	C	FMS	46.91	32.50	36	C	FMS	46.40	41.80	142	C
FMS	30.87	37.96	3	C	DIF	31.00	31.10	98	B	FMS	57.35	35.65	36	C	FMS	57.03	25.45	143	C
FMS	40.06	38.63	3	C	FMS	35.28	32.46	98	C	FMS	37.46	38.65	36	C	FMS	33.82	27.55	143	C
FMS	35.52	38.84	3	C	FMS	29.34	36.83	98	C	BO	51.48	40.00	36	A	FMS	39.73	39.59	143	C
FMS	33.21	39.45	3	C	FMS	29.06	39.17	98	C	FMS	34.13	40.56	36	C	FMS	34.48	40.42	143	C
FMS	32.95	39.50	3	C	FMS	29.42	39.19	98	C	FMS	58.24	29.10	37	C	FMS	36.90	40.54	143	C
FMS	33.05	39.55	3	C	FMS	30.16	40.40	98	C	FMS	60.10	32.35	37	C	FMS	34.83	40.56	143	C
FMS	55.60	27.43	4	C	FMS	29.13	40.56	98	C	FMS	47.83	32.73	37	C	FMS	34.78	40.59	143	C
FMS	57.05	27.74	4	C	FMS	32.01	30.18	99	E	FMS	47.85	32.73	37	C	FMS	43.60	41.30	143	C
FMF	34.66	28.84	4	C	BO	32.80	31.88	99	B	FMS	49.87	35.63	37	C	FMS	37.77	25.21	144	C
FMS	57.23	30.52	4	C	FMS	29.46	39.30	99	C	FMS	29.53	37.40	37	C	FMS	33.83	27.61	144	D
FMS	48.40	32.60	4	C	FMS	48.75	36.55	100	C	FMS	36.08	39.16	37	C	FMS	33.11	28.84	144	C
GVA	36.45	35.63	4	C	FMS	29.76	39.03	100	C	FMS	57.76	26.72	38	C	FMS	34.37	29.03	144	C
FMS	29.76	35.72	4	C	FMS	29.20	39.11	100	C	FMS	57.64	26.85	38	C	FMS	31.11	29.68	144	C
GFI	59.51	35.89	4	C	BO	51.35	40.04	100	D	FMS	33.97	27.48	38	C	FMS	31.57	29.90	144	C
FMS	39.67	39.41	4	C	FMA	46.10	40.30	100	D	FMS	51.75	28.27	38	C	FMF	35.39	31.04	144	B
FMF	30.59	40.66	4	A	FMS	46.20	40.30	100	C	FMS	47.86	32.66	38	C	FMA	35.35	31.15	144	D
FMS	44.90	41.60	4	C	FMS	33.80	27.67	101	C	FMS	52.78	36.33	38	C	FMS	36.37	37.35	144	C
FMS	43.50	42.40	4	C	FMS	32.22	30.46	101	C	FMS	57.81	37.11	38	E	FMS	30.16	38.10	144	C
FMS	42.92	42.71	4	C	FMS	32.63	34.89	101	C	FMS	57.90	37.13	38	C	FMS	34.14	39.76	144	C
FMS	41.49	43.34	4	C	FMS	29.30	37.80	101	C	GFI	58.10	37.69	38	B	FMS	40.70	40.05	144	C
FMS	55.83	26.72	5	C	FMS	29.11	38.81	101	C	FMS	41.60	39.10	38	C	FMF	35.00	40.10	144	E
FMS	54.10	28.35	5	C	FMS	29.11	38.81	101	C	FMS	29.57	39.20	38	C	FMF	34.26	40.35	144	E
FMS	56.20	28.95	5	C	FMS	29.17	39.13	101	C	FMS	43.90	42.40	38	C	FMS	31.00	40.50	144	C
GFS	35.75	33.33	5	C	FMS	30.05	40.46	101	C	FMS	47.14	43.56	38	C	FMS	33.14	40.57	144	C
FMS	32.34	34.89	5	C	FMS	33.95	27.50	102	C	BO	32.31	31.83	39	C	FMS	35.80	40.57	144	C
FMS	29.24	36.13	5	C	FMS	33.98	27.55	102	C	FMS	59.90	33.47	39	C	FMS	34.82	40.59	144	C
FMS	52.92	36.74	5	C	BO	33.49	27.89	102	B	FMS	59.73	33.96	39	C	FMS	43.80	42.40	144	C
FMS	30.18	37.17	5	C	BO	33.50	27.90	102	B	FMS	50.38	37.08	39	C	FMS	34.00	27.53	145	C
FMS	39.04	38.08	5	C	FMS	35.27	32.16	102	C	FMS	36.14	37.22	39	C	BO	33.70	27.72	145	C
FMS	40.05	38.82	5	C	FMS	29.27	36.99	102	D	FMS	30.70	37.73	39	C	FMF	34.66	28.84	145	A
FMS	33.11	39.42	5	C	FMS	29.08	39.12	102	C	DIF	52.00	27.00	40	E	FMS	34.90	29.13	145	C
FMS	30.63	40.60	5	C	BO	51.31	40.07	102	C	FMF	33.75	27.60	40	B	FMS	31.77	30.06	145	E
FMS	30.63	40.60	5	C	FMS	29.09	40.65	102	C	FMS	53.27	27.97	40	C	BO	31.52	32.27	145	B
FMS	30.63	40.60	5	C	FMS	29.97	40.74	102	C	FMS	51.86	28.48	40	C	FMS	35.30	33.30	145	C
FMS	42.80	41.00	5	C	FMS	30.77	40.75	102	D	FMS	51.58	30.16	40	C	HF	46.37	38.90	145	D
FMS	46.19	43.34	5	C	FMS	31.59	40.84	102	C	BO	49.77	30.34	40	E	FMS	43.56	38.92	145	C
FMS	33.85	27.71	6	C	FMS	33.46	41.03	102	C	BO	49.78	30.43	40	E	FMS	40.71	39.42	145	C
FMS	54.88	27.79	6	C	FMS	34.29	27.60	103	C	BO	34.63	31.62	40	D	FMS	34.47	40.42	145	C
FMS	30.01	37.17	6	C	BO	31.20	31.90	103	C	BO	34.63	31.62	40	D	FMS	36.40	40.66	145	C

Names	E_long.	N_lat.	azi	quality	Names	E_long.	N_lat.	azi	quality	Names	E_long.	N_lat.	azi	quality	Names	E_long.	N_lat.	azi	quality
FMS	37.96	37.93	6	C	DIF	31.20	31.90	103	C	FMS	46.96	32.38	40	C	FMS	31.13	29.67	146	E
FMS	40.22	38.82	6	C	FMS	49.43	38.20	103	C	FMS	51.92	35.80	40	C	FMF	42.30	36.30	146	E
FMS	39.99	38.87	6	C	FMS	29.05	40.59	103	C	GFI	56.83	37.36	40	C	FMS	48.80	37.40	146	C
FMS	43.40	42.50	6	C	FMS	32.60	40.90	103	C	FMS	31.11	38.94	40	C	FMS	48.80	37.40	146	C
FMS	55.65	27.14	7	C	FMS	32.50	41.50	103	D	FMS	53.89	39.83	40	C	FMF	35.50	40.25	146	E
FMS	55.68	27.48	7	C	FMS	31.12	29.62	104	C	FMS	43.50	41.80	40	C	FMS	33.15	40.27	146	C
FMS	52.03	29.34	7	C	FMS	32.25	30.31	104	C	BO	49.66	30.51	41	D	FMS	29.77	40.71	146	C
BO	34.64	31.65	7	D	FMS	35.48	31.91	104	D	BO	30.01	31.73	41	D	FMS	37.70	25.25	147	C
FMS	32.03	34.55	7	C	FMS	32.03	34.75	104	C	FMS	59.64	33.54	41	C	FMS	33.81	27.63	147	C
FMS	43.44	36.67	7	C	FMS	57.50	38.20	104	D	FMS	44.97	35.27	41	C	FMS	33.28	40.23	147	C
FMS	57.70	37.21	7	C	FMS	30.84	40.78	104	D	FMS	54.54	37.00	41	C	FMF	33.15	40.30	147	E
FMS	40.05	38.71	7	C	FMS	33.48	28.21	105	C	FMS	50.20	37.19	41	C	FMS	34.46	40.42	147	C
FMS	43.32	38.71	7	C	FMS	29.12	39.11	105	C	FMS	31.66	38.44	41	C	FMS	34.83	40.59	147	C
FMS	43.60	42.50	7	C	FMS	29.24	39.90	105	C	FMS	48.20	41.70	41	C	FMS	30.62	40.69	147	C
FMS	55.58	26.81	8	C	FMS	32.99	40.63	105	C	FMS	43.50	41.80	41	C	FMS	45.80	42.00	147	C
FMS	34.48	28.32	8	C	FMS	33.00	40.67	105	C	FMS	57.34	27.60	42	C	FMS	34.53	25.25	148	C
BO	50.67	30.02	8	E	FMS	33.83	41.14	105	C	FMS	58.95	31.11	42	C	FMS	56.20	27.46	148	C
BO	50.42	30.02	8	E	BO	33.75	27.55	106	B	BO	32.19	31.82	42	D	FMS	33.84	27.92	148	C
FMS	56.84	30.72	8	C	BO	33.71	27.57	106	C	FMS	49.10	32.04	42	C	FMS	33.66	28.00	148	C
FMS	35.95	36.27	8	C	BO	33.71	27.57	106	C	FMS	59.92	32.20	42	C	PC	35.17	30.57	148	C
FMS	35.58	36.87	8	C	FMS	52.98	28.37	106	C	FMS	46.29	32.78	42	C	FMS	35.50	32.05	148	C
FMS	37.16	37.27	8	C	FMS	31.15	29.72	106	C	FMS	57.53	37.32	42	C	FMS	29.30	35.68	148	C
FMS	43.34	38.71	8	C	BO	31.20	31.75	106	D	FMS	43.84	37.62	42	C	FMS	40.90	39.20	148	C
FMS	40.52	38.83	8	C	BO	32.16	31.83	106	D	GFI	30.24	37.70	42	E	FMS	40.90	39.40	148	C
FMA	47.80	40.90	8	D	BO	31.19	31.92	106	D	BO	51.44	40.03	42	B	FMS	34.80	40.59	148	C
FMS	55.36	27.44	9	C	FMS	35.48	31.93	106	D	FMA	47.80	40.60	42	D	FMS	34.80	40.59	148	C
FMS	56.40	27.61	9	C	FMS	49.33	38.06	106	C	FMS	47.40	41.00	42	C	FMS	56.15	27.09	149	C
BO	32.03	31.91	9	D	FMS	29.56	39.15	106	C	FMS	46.90	41.10	42	C	FMS	33.83	27.62	149	C
BO	30.09	31.96	9	D	FMS	31.09	30.28	107	C	FMS	46.50	41.70	42	C	FMF	35.27	30.70	149	D
FMS	32.68	34.42	9	C	FMS	29.09	39.10	107	C	FMS	33.80	27.70	43	C	BO	32.68	31.74	149	D
FMF	36.25	36.03	9	C	BO	48.97	40.18	107	D	FMS	51.48	29.36	43	C	FMS	54.05	39.47	149	C
FMS	30.91	37.92	9	C	FMS	30.67	40.71	107	D	FMS	51.50	29.85	43	C	BO	51.35	40.04	149	C
FMS	44.30	39.20	9	C	BO	33.36	28.00	108	D	FMS	57.59	30.09	43	C	FMS	34.81	40.58	149	C
FMS	44.00	41.30	9	C	BO	33.34	28.04	108	D	FMS	46.85	32.52	43	C	FMS	34.77	40.59	149	C
FMS	46.50	41.80	9	C	BO	50.75	29.92	108	E	FMS	56.50	32.76	43	C	FMS	44.40	41.70	149	C
FMS	45.90	42.10	9	C	FMS	30.62	29.95	108	C	GFI	59.17	36.12	43	E	FMS	43.90	42.40	149	C
FMS	55.59	26.70	10	C	FMS	31.70	30.50	108	E	FMS	51.58	36.55	43	C	BO	29.65	44.48	149	D
FMS	55.12	27.48	10	C	BO	31.00	31.10	108	B	FMS	38.01	39.52	43	C	FMS	34.03	27.54	150	C
FMS	56.50	27.59	10	C	FMA	35.47	32.46	108	D	FMS	44.10	42.30	43	C	FMS	33.99	27.79	150	C
FMS	56.87	27.86	10	C	FMA	35.16	32.70	108	D	FMS	55.04	27.55	44	C	GVA	37.00	33.37	150	B
FMS	56.34	28.04	10	C	FMS	47.00	40.60	108	C	FMS	51.64	28.45	44	C	GVA	37.67	33.83	150	C
FMS	57.53	30.26	10	C	FMS	29.56	42.16	108	C	FMS	51.52	29.95	44	C	FMS	33.01	40.33	150	C
FMS	50.91	31.77	10	C	FMS	34.35	26.88	109	C	FMS	51.13	30.04	44	C	FMF	36.75	40.51	150	E
FMS	50.95	31.83	10	C	FMS	32.84	28.93	109	C	DIF	32.85	31.91	44	C	FMS	29.13	40.76	150	C
FMS	47.80	32.58	10	C	FMS	31.16	29.66	109	C	FMS	47.56	32.71	44	C	FMS	33.63	40.87	150	C
FMS	47.79	32.68	10	C	BO	32.81	31.29	109	C	FMS	57.19	33.49	44	C	FMS	55.65	27.64	151	C
FMS	49.21	33.22	10	C	DIF	31.90	31.92	109	C	GFI	58.51	36.82	44	C	FMS	34.82	28.60	151	C
FMS	46.85	34.88	10	C	BO	31.83	32.10	109	B	GFI	30.09	37.57	44	E	GFI	58.84	36.31	151	B
GFI	58.52	36.87	10	B	FMS	29.21	36.89	109	C	FMS	30.19	37.64	44	C	FMS	55.92	37.85	151	C
FMS	30.63	39.89	10	C	FMS	29.77	39.05	109	C	BO	48.86	40.22	44	C	FMS	55.92	37.85	151	C
FMS	47.80	41.00	10	C	FMS	41.80	42.00	109	C	FMS	48.40	41.30	44	C	FMS	35.03	40.51	151	C
FMS	54.99	26.53	11	C	BO	33.73	27.43	110	B	BO	50.57	29.91	45	E	FMS	35.18	40.86	151	C
BO	33.68	27.81	11	C	FMS	29.80	27.80	110	C	BO	49.73	30.40	45	E	FMS	35.16	41.06	151	C
FMS	58.66	35.56	11	C	FMS	33.50	27.92	110	C	BO	49.79	30.40	45	E	FMS	55.81	26.77	152	C
FMS	32.41	36.02	11	C	FMS	31.11	29.61	110	C	FMS	59.43	34.04	45	C	FMS	34.04	27.42	152	C
FMS	41.17	39.28	11	C	FMS	32.44	35.02	110	C	FMS	44.00	41.40	45	C	FMS	34.65	28.70	152	C
FMS	43.80	41.40	11	C	FMS	29.74	39.03	110	C	FMS	43.40	42.50	45	C	FMS	32.78	28.94	152	C
FMS	43.80	41.50	11	C	FMS	30.00	39.03	110	C	FMS	60.26	26.98	46	C	FMS	34.73	29.07	152	C
FMS	44.80	42.40	11	C	FMS	29.26	39.34	110	C	FMS	49.93	30.90	46	C	PC	35.10	30.60	152	C
FMS	55.66	27.41	12	C	FMS	29.32	39.34	110	C	BO	32.19	32.05	46	B	GFS	35.48	32.07	152	D
FMS	56.77	27.48	12	C	BO	51.31	40.07	110	B	FMS	57.43	33.39	46	C	FMS	30.95	38.01	152	C
DIF	30.04	31.64	12	B	FMS	48.90	40.30	110	C	GFI	59.19	36.44	46	D	FMS	43.45	38.47	152	C
FMS	48.57	32.76	12	C	FMS	29.17	40.50	110	C	GFI	58.58	37.12	46	B	FMS	55.82	26.60	153	C
FMS	57.50	37.82	12	C	FMS	29.06	40.60	110	C	FMF	30.21	37.73	46	A	FMS	33.87	27.62	153	C
FMS	46.40	41.30	12	C	BO	33.70	27.80	111	C	FMS	38.99	38.78	46	C	FMS	33.79	27.65	153	E
FMS	43.80	41.40	12	C	BO	33.70	27.83	111	B	FMS	45.40	41.30	46	C	FMS	34.61	28.61	153	C
FMS	53.88	26.94	13	C	BO	33.70	27.83	111	B	FMS	45.00	41.70	46	C	FMS	32.16	28.67	153	C
FMS	56.19	27.46	13	C	FMA	35.46	32.48	111	D	FMS	33.80	27.65	47	C	FMS	33.16	28.67	153	C
FMS	55.62	27.53	13	C	FMS	29.04	39.11	111	C	FMS	50.71	29.78	47	C	FMS	34.48	29.31	153	C
FMS	33.72	27.72	13	C	FMS	51.81	40.23	111	C	FMS	51.25	29.93	47	C	BO	50.72	29.90	153	E
FMS	50.72	32.01	13	C	FMS	34.72	40.83	111	C	GFI	59.17	36.12	47	D	BO	32.16	31.83	153	D
FMS	55.96	32.16	13	C	BO	33.47	27.85	112	B	FMS	30.26	37.71	47	C	FMS	42.55	37.32	153	C
FMS	47.62	32.70	13	C	FMS	31.08	29.70	112	C	FMS	57.71	26.54	48	C	FMS	40.78	39.18	153	C

Names	E_long.	N_lat.	azi	quality	Names	E_long.	N_lat.	azi	quality	Names	E_long.	N_lat.	azi	quality	Names	E_long.	N_lat.	azi	quality
FMS	47.22	33.23	13	C	FMS	32.26	30.28	112	C	FMS	59.70	28.88	48	C	FMS	35.33	40.76	153	C
BO	32.73	34.07	13	D	GFI	58.84	36.31	112	D	BO	29.62	31.54	48	D	FMS	30.72	40.79	153	D
FMS	38.31	34.30	13	C	FMS	44.68	37.54	112	C	BO	30.04	31.58	48	D	FMS	43.50	41.50	153	C
FMS	38.83	38.40	13	C	FMS	31.35	38.35	112	C	FMS	52.27	35.74	48	C	FMS	45.70	41.90	153	C
FMS	42.02	40.52	13	C	FMA	48.40	40.50	112	D	FMS	29.89	37.74	48	C	FMS	43.60	42.30	153	C
FMS	30.30	40.71	13	C	FMA	48.80	40.50	112	D	GFI	56.93	37.95	48	E	FMS	55.83	26.74	154	C
FMS	54.29	27.54	14	C	FMS	29.97	40.75	112	C	FMS	38.15	39.52	48	C	FMS	56.56	27.41	154	C
FMS	56.18	31.83	14	C	FMS	33.90	27.50	113	C	BO	49.01	39.98	48	C	PC	35.12	30.68	154	C
GFS	35.55	32.18	14	D	FMS	34.83	28.78	113	C	BO	32.85	31.91	49	B	FMS	35.46	31.11	154	C
FMS	47.72	32.67	14	C	FMS	31.15	29.66	113	C	FMS	47.05	32.41	49	C	FMS	45.23	37.14	154	C
FMS	36.04	36.05	14	C	FMS	31.10	29.72	113	C	FMS	45.81	33.76	49	C	FMS	46.59	38.56	154	C
FMS	51.62	36.43	14	C	FMS	34.80	40.59	113	C	FMS	56.87	35.15	49	C	FMS	42.17	40.29	154	C
FMF	35.97	37.11	14	B	FMS	34.07	27.35	114	C	FMS	30.54	40.57	49	C	FMS	34.79	40.58	154	C
FMS	35.90	37.36	14	C	BO	33.52	27.93	114	B	BO	52.00	27.00	50	E	FMS	30.15	40.71	154	D
FMS	37.96	37.92	14	C	FMS	31.13	29.68	114	C	DIF	52.00	27.00	50	E	FMS	29.09	40.75	154	C
FMS	43.17	38.74	14	C	FMS	31.08	29.70	114	C	FMS	51.65	28.44	50	C	FMS	33.78	27.67	155	C
FMS	38.74	39.76	14	C	BO	32.52	31.58	114	D	FMS	51.78	30.14	50	C	FMS	32.80	30.65	155	E
FMS	43.30	41.70	14	C	DIF	32.52	31.58	114	D	BO	49.86	30.35	50	E	BO	32.54	31.58	155	D
FMS	53.57	26.42	15	C	FMS	34.29	32.04	114	C	BO	49.84	30.35	50	E	FMS	35.56	31.68	155	C
FMS	53.05	27.88	15	C	BO	31.32	32.12	114	D	FMS	49.29	36.85	50	C	GFS	35.58	32.37	155	C
FMS	51.83	28.35	15	C	FMS	51.72	40.39	114	C	GFI	57.58	37.04	50	B	FMS	34.80	40.59	155	C
BO	50.40	30.05	15	E	FMS	34.79	40.59	114	C	BO	51.30	40.06	50	A	FMS	29.11	40.75	155	C
BO	31.92	31.91	15	A	FMS	30.35	40.70	114	C	FMA	47.70	40.60	50	D	FMS	41.80	42.70	155	C
FMS	45.17	33.74	15	C	FMS	48.44	40.75	114	C	FMS	51.76	28.54	51	C	FMS	34.70	28.77	156	E
GFI	39.81	35.58	15	D	FMS	47.40	41.10	114	C	FMS	51.71	30.18	51	C	FMS	34.82	28.86	156	C
GFI	57.01	37.57	15	B	FMA	48.10	41.40	114	D	FMS	45.69	33.40	51	C	FMS	34.73	28.89	156	C
FMS	32.44	37.94	15	C	BO	33.45	27.74	115	B	BO	32.71	33.92	51	D	FMF	35.21	30.53	156	D
FMS	43.70	41.40	15	C	BO	33.49	27.87	115	B	FMS	30.87	38.43	51	C	FMS	33.59	40.84	156	C
FMS	46.82	41.60	15	C	FMS	34.62	28.23	115	C	FMS	53.91	28.34	52	C	FMS	53.66	28.19	157	C
BO	32.11	31.86	16	D	FMS	31.14	29.65	115	C	FMS	51.49	28.59	52	C	FMS	32.23	29.70	157	C
FMS	29.20	36.10	16	C	FMF	31.06	29.67	115	A	FMS	52.26	35.95	52	C	BO	31.44	32.34	157	C
FMS	54.73	36.53	16	C	FMS	31.12	29.73	115	C	FMF	44.20	36.00	52	E	GFS	35.58	33.22	157	C
FMS	60.13	36.74	16	C	FMS	35.31	33.33	115	C	FMS	51.92	36.41	52	C	FMS	35.60	35.82	157	C
FMS	59.60	37.32	16	C	FMS	42.86	36.98	115	C	FMS	43.79	37.62	52	C	FMS	29.39	37.78	157	C
FMS	40.14	38.78	16	C	FMS	52.05	39.72	115	C	GFI	30.13	37.72	52	D	FMS	43.30	38.46	157	C
FMS	30.42	40.69	16	D	FMS	30.49	39.89	115	C	FMS	30.51	37.77	52	C	FMS	35.91	39.95	157	C
FMS	44.29	40.94	16	C	FMS	35.55	40.51	115	C	DIF	52.00	27.00	53	E	FMS	35.38	40.72	157	C
FMA	46.20	41.20	16	D	FMS	34.79	40.60	115	C	FMS	35.50	31.08	53	C	FMS	29.11	40.76	157	C
FMS	43.60	41.80	16	C	FMS	30.72	40.68	115	C	FMS	49.65	32.14	53	C	FMS	35.95	40.88	157	C
FMS	47.62	32.73	17	C	FMS	48.70	40.70	115	C	FMS	31.74	34.09	53	C	FMS	43.80	41.20	157	C
FMS	43.35	35.89	17	C	FMS	43.60	42.40	115	C	FMS	43.96	37.42	53	C	FMS	43.70	42.00	157	C
FMF	60.00	36.80	17	E	FMS	33.62	27.53	116	C	FMS	57.58	37.84	53	C	FMS	30.92	45.36	157	C
GFI	58.49	37.18	17	B	FMS	33.66	27.65	116	C	FMS	30.70	37.85	53	C	FMS	31.69	30.72	158	E
FMS	36.34	37.39	17	C	FMS	31.09	29.69	116	C	FMS	36.99	37.87	53	C	FMS	53.24	35.90	158	C
FMS	54.87	39.60	17	C	FMS	30.63	29.74	116	C	FMS	59.97	32.19	54	C	FMS	51.56	36.30	158	C
FMS	45.00	42.50	17	C	BO	32.74	31.76	116	D	FMS	52.62	36.42	54	C	FMS	54.45	37.01	158	C
FMS	33.40	27.74	18	C	FMF	35.67	33.62	116	B	FMS	44.82	41.75	54	C	FMS	57.70	37.40	158	D
FMS	53.12	27.74	18	C	FMS	30.52	39.81	116	C	FMS	55.77	24.82	55	C	FMS	55.83	37.60	158	C
FMS	53.11	28.44	18	C	FMS	30.49	39.86	116	C	FMS	51.77	28.39	55	C	FMS	45.79	38.72	158	C
FMS	56.07	31.85	18	C	BO	51.36	40.05	116	B	FMF	45.80	35.30	55	E	FMS	33.18	39.39	158	C
FMS	32.95	34.61	18	C	FMS	52.70	40.60	116	D	FMS	45.15	36.84	55	C	FMS	33.08	39.42	158	C
FMS	43.34	35.76	18	C	FMS	29.10	40.68	116	C	FMS	29.60	37.60	55	C	FMS	33.11	39.47	158	C
FMS	48.97	35.82	18	C	FMS	46.81	41.59	116	C	FMS	30.71	37.86	55	C	FMS	55.12	39.56	158	C
FMS	43.72	36.99	18	C	BO	33.68	27.43	117	C	BO	51.04	40.07	55	D	FMS	32.94	40.55	158	C
FMS	42.47	37.18	18	C	BO	33.68	27.43	117	C	FMS	33.02	40.71	55	C	FMS	29.12	40.76	158	C
FMS	29.30	38.10	18	C	FMS	33.82	27.61	117	C	FMS	45.60	42.10	55	C	FMS	31.87	40.81	158	C
FMS	40.06	38.76	18	C	FMS	31.12	29.67	117	C	BO	49.75	30.36	56	E	FMF	34.75	28.93	159	B
FMS	39.96	38.83	18	C	FMS	31.12	29.88	117	C	FMS	52.41	35.68	56	C	GFS	35.55	32.00	159	C
FMS	39.66	39.58	18	C	BO	32.81	31.32	117	D	FMS	30.25	37.61	56	C	FMS	30.68	40.73	159	C
FMS	44.00	41.40	18	C	FMS	29.26	37.82	117	C	BO	49.07	39.96	56	D	FMS	29.04	41.17	159	C
FMS	44.90	41.60	18	C	FMS	43.90	41.40	117	C	FMS	31.00	41.09	56	C	FMS	43.60	41.50	159	C
FMS	44.20	41.70	18	C	BO	33.50	27.70	118	B	FMS	44.00	42.40	56	C	FMS	32.51	41.64	159	C
FMS	46.50	41.90	18	C	BO	33.49	27.74	118	B	FMS	34.00	27.52	57	C	GFS	35.52	31.82	160	C
FMS	55.77	27.78	19	C	BO	33.30	27.79	118	B	FMS	53.18	28.14	57	C	FMS	29.81	35.93	160	C
FMS	55.90	27.93	19	C	FMS	31.09	29.72	118	C	FMS	51.73	28.69	57	C	FMS	54.10	36.34	160	C
GFI	59.40	36.29	19	C	FMS	32.25	30.50	118	E	BO	30.16	31.98	57	C	FMS	54.10	36.34	160	C
GFI	58.01	37.49	19	A	FMS	31.74	30.54	118	C	FMS	58.24	33.99	57	C	HF	46.50	38.87	160	D
FMS	43.22	38.64	19	C	FMF	35.43	32.20	118	B	FMS	45.70	34.10	57	C	FMS	33.80	39.35	160	C
FMS	43.20	38.68	19	C	FMA	35.61	33.16	118	D	FMS	59.31	35.22	57	C	FMS	42.07	39.94	160	C
FMS	43.50	41.00	19	C	FMS	44.31	37.40	118	C	FMS	51.61	28.55	58	C	FMF	30.99	40.77	160	A
DIF	29.84	31.61	20	D	BO	51.35	40.05	118	C	FMS	59.69	28.94	58	C	FMS	31.03	40.89	160	C
FMS	48.92	32.66	20	C	FMS	52.10	40.31	118	C	BOT	47.78	31.03	58	A	FMS	43.80	42.40	160	C
FMS	48.03	34.38	20	C	FMS	47.62	40.58	118	C	DIF	32.70	33.80	58	D	FMS	41.80	42.70	160	C

Names	E_long.	N_lat.	azi	quality	Names	E_long.	N_lat.	azi	quality	Names	E_long.	N_lat.	azi	quality	Names	E_long.	N_lat.	azi	quality
FMS	44.67	36.01	20	C	FMS	30.93	40.78	118	C	FMS	45.61	34.41	58	C	FMS	31.11	29.67	161	C
GFI	59.07	36.11	20	C	FMS	33.80	28.03	119	C	FMS	45.55	34.96	58	C	FMS	37.12	37.32	161	C
FMS	51.61	36.40	20	C	FMS	31.16	29.74	119	C	FMS	44.10	35.04	58	C	FMS	31.99	38.31	161	C
FMS	51.56	36.42	20	C	FMS	35.51	32.19	119	C	FMA	46.30	41.70	58	D	FMS	44.03	39.12	161	C
FMS	36.31	36.92	20	C	FMS	42.62	37.00	119	C	FMS	58.03	33.06	59	C	FMS	35.34	40.33	161	C
FMF	43.40	37.20	20	E	FMS	29.16	40.61	119	C	FMS	31.41	34.56	59	C	FMS	34.79	40.59	161	C
FMS	39.09	38.50	20	C	FMS	29.14	40.90	119	C	FMS	44.10	35.09	59	C	FMS	33.01	40.61	161	C
FMS	43.22	38.64	20	C	FMF	34.00	41.05	119	E	FMS	31.05	37.92	59	C	FMS	43.50	41.50	161	C
FMS	37.33	40.10	20	C	FMS	31.13	29.72	120	C	DIF	52.00	27.00	60	E	FMS	43.80	42.40	161	C
FMS	47.90	40.70	20	C	FMS	32.35	29.82	120	C	FMS	59.69	29.20	60	C	FMS	57.01	27.88	162	C
FMS	48.30	40.70	20	C	FMF	32.08	30.13	120	A	GFI	30.17	37.66	60	E	GFI	34.92	29.53	162	A
FMS	53.86	27.02	21	C	BO	31.90	31.92	120	D	FMS	40.40	39.50	60	C	FMS	31.05	35.73	162	C
FMS	54.97	27.19	21	C	FMS	29.89	39.03	120	C	FMS	30.40	40.76	60	D	FMS	43.67	38.73	162	C
FMS	44.95	36.01	21	C	FMA	48.80	40.50	120	D	FMS	30.58	40.81	60	C	FMS	35.29	40.70	162	C
FMF	57.20	37.50	21	E	FMS	30.69	40.88	120	C	FMS	43.70	41.40	60	C	FMS	29.04	40.79	162	C
FMS	44.00	42.00	21	C	FMS	29.20	40.90	120	C	FMS	35.11	27.19	61	C	FMS	44.00	41.20	162	C
BO	30.55	44.41	21	C	FMS	33.50	41.00	120	C	FMS	51.36	29.29	61	C	FMS	43.50	42.40	162	C
FMS	53.38	27.52	22	C	FMS	33.53	41.02	120	C	FMF	35.03	30.25	61	D	FMS	56.08	27.36	163	C
FMS	54.05	28.26	22	C	FMS	33.57	41.02	120	C	BO	34.64	31.65	61	D	FMS	33.66	28.00	163	C
BO	50.50	30.12	22	E	FMS	34.05	27.46	121	C	FMS	45.70	34.31	61	C	BO	32.80	31.88	163	C
BO	30.04	31.64	22	C	FMS	31.11	29.62	121	C	GFI	30.38	37.77	61	E	GVA	35.48	33.05	163	B
FMS	47.35	32.31	22	C	FMS	31.13	29.69	121	C	FMS	31.22	38.52	61	C	GVA	35.78	33.10	163	B
FMS	48.29	32.51	22	C	FMS	31.10	29.72	121	C	BO	30.04	31.52	62	C	GVA	37.17	33.37	163	A
FMS	48.09	32.64	22	C	FMS	31.15	29.72	121	C	FMS	29.70	37.57	62	C	FMS	44.01	38.92	163	C
FMS	36.05	36.74	22	C	GFI	35.35	30.63	121	A	FMS	39.26	38.46	62	C	FMS	36.31	25.06	164	C
FMS	36.28	37.29	22	C	FMS	51.57	40.35	121	C	FMS	30.42	40.90	62	D	FMS	55.68	26.80	164	C
FMF	58.40	37.30	22	E	FMS	33.62	40.39	121	C	FMA	46.50	41.70	62	D	FMS	33.76	27.66	164	C
GFI	58.54	37.38	22	A	FMS	30.14	40.49	121	D	FMS	33.75	27.65	63	C	FMS	35.22	30.50	164	C
FMS	35.97	37.51	22	C	FMS	29.16	40.69	121	C	FMS	57.40	27.77	63	C	FMS	43.62	37.75	164	C
FMS	32.48	37.95	22	C	FMF	29.83	40.73	121	A	FMS	33.96	34.94	63	C	FMS	45.44	38.40	164	C
FMS	39.31	38.16	22	C	FMS	33.57	40.99	121	C	FMS	44.09	35.04	63	C	FMS	43.68	38.72	164	C
FMS	37.70	38.25	22	C	FMS	34.63	28.36	122	C	FMS	58.50	37.60	63	C	FMS	33.80	39.40	164	C
FMS	39.61	38.74	22	C	FMS	31.13	29.65	122	C	FMS	35.22	41.20	63	C	FMS	40.17	40.04	164	C
FMS	34.58	41.16	22	C	HF	46.52	38.87	122	D	FMS	60.01	34.50	64	C	FMS	34.40	40.08	164	C
FMS	53.49	27.53	23	C	FMS	50.37	40.39	122	C	FMS	55.74	36.62	64	C	FMS	35.02	40.52	164	C
FMS	51.68	28.00	23	C	FMS	50.27	40.41	122	C	GFI	30.04	37.53	64	C	FMS	30.57	40.57	164	C
FMS	54.40	28.13	23	C	FMS	29.10	40.60	122	C	BO	51.38	40.05	64	C	FMS	44.00	41.30	164	C
FMS	47.58	32.81	23	C	FMS	29.15	40.64	122	C	FMS	45.90	41.20	64	C	FMS	44.60	41.70	164	C
FMS	47.80	33.18	23	C	FMS	30.27	40.76	122	C	FMS	31.13	29.67	65	C	FMS	44.00	41.80	164	C
FMS	47.82	33.21	23	C	FMA	48.10	41.10	122	D	FMS	45.78	34.27	66	C	FMS	43.70	42.40	164	C
FMS	48.73	33.23	23	C	BO	29.68	44.52	122	D	FMS	29.51	37.04	66	C	FMS	43.80	42.40	164	C
FMS	60.02	33.58	23	C	BO	33.25	28.15	123	C	FMS	30.54	40.69	66	D	BO	33.75	27.69	165	D
FMS	57.92	35.45	23	C	FMS	32.78	28.94	123	C	FMS	30.67	40.70	66	D	FMS	52.85	28.40	165	C
FMS	35.98	36.04	23	C	FMF	31.50	29.70	123	A	FMS	43.80	41.80	66	C	OC	35.00	29.75	165	D
GFI	58.44	37.58	23	D	FMS	46.00	33.50	123	C	FMS	34.02	27.75	67	E	GFS	35.27	30.37	165	C
FMS	39.04	38.39	23	C	FMS	54.50	35.00	123	D	FMS	30.62	40.66	67	C	BO	48.10	32.13	165	D
FMS	30.87	38.60	23	C	FMS	30.50	40.64	123	C	BOT	48.12	31.26	68	B	GVA	36.15	33.17	165	C
FMS	43.22	38.72	23	C	FMS	34.83	40.73	123	C	BO	32.27	31.71	68	B	FMS	43.78	37.54	165	C
FMS	45.90	42.39	23	C	FMS	33.70	27.20	124	C	FMS	29.37	36.95	68	C	FMS	43.72	37.72	165	C
FMS	57.93	26.60	24	C	FMS	33.84	27.61	124	C	FMS	39.22	38.42	68	C	FMS	55.71	38.53	165	C
FMS	55.02	27.28	24	C	BO	33.65	27.74	124	B	FMS	30.39	40.76	68	D	FMS	33.06	39.41	165	C
FMS	52.17	27.54	24	C	FMS	34.00	29.45	124	C	FMS	49.44	31.59	69	C	FMS	42.10	40.40	165	D
FMS	52.52	29.35	24	C	FMS	30.87	29.56	124	C	FMS	35.47	31.90	69	D	FMS	44.90	41.60	165	C
FMS	47.35	32.48	24	C	FMS	31.13	29.70	124	C	FMS	29.89	37.60	69	C	FMS	56.07	27.40	166	C
FMS	47.77	32.76	24	C	FMS	35.47	32.35	124	C	BO	51.25	40.09	69	C	GVA	37.15	33.23	166	C
FMS	47.75	33.23	24	C	BO	51.35	40.04	124	C	FMS	29.18	40.62	69	C	FMS	54.47	35.49	166	C
FMS	49.80	35.70	24	C	BO	51.35	40.05	124	C	FMS	48.92	41.42	69	C	FMS	42.45	37.19	166	C
FMS	52.03	36.39	24	C	FMS	34.43	40.62	124	C	DIF	52.00	27.00	70	E	FMS	44.75	37.42	166	C
GFI	58.02	37.56	24	D	FMS	30.65	40.69	124	D	BO	32.81	31.18	70	D	FMS	43.30	38.73	166	C
GFI	30.13	37.61	24	E	FMS	30.27	40.75	124	D	HFG	33.10	34.90	70	A	FMS	31.36	40.57	166	C
FMS	38.54	38.08	24	C	BO	33.73	27.65	125	C	FMS	36.28	35.87	70	C	FMS	34.80	40.60	166	C
FMS	48.00	40.80	24	C	FMS	33.60	28.25	125	C	FMS	43.88	37.69	70	C	FMS	35.35	40.61	166	C
FMS	41.55	42.67	24	C	FMS	29.04	39.12	125	C	FMS	40.91	42.55	71	C	FMS	35.42	40.64	166	C
FMS	53.55	26.42	25	C	FMS	34.47	40.43	125	C	FMS	35.69	42.99	71	C	FMS	57.01	27.64	167	C
FMS	57.85	26.96	25	C	FMS	34.89	40.68	125	C	FMS	35.43	31.97	72	D	FMS	33.80	27.68	167	C
FMS	53.91	27.00	25	C	FMS	32.90	40.90	125	C	FMS	48.97	37.71	72	C	FMS	34.40	28.62	167	C
FMS	57.69	27.26	25	C	FMS	32.57	40.95	125	C	FMS	51.83	50.63	72	C	FMS	34.73	29.38	167	C
FMS	33.90	27.50	25	C	FMS	34.01	27.52	126	C	FMS	42.93	37.44	73	C	FMS	31.67	30.34	167	C
FMS	52.57	28.08	25	C	BO	33.65	27.71	126	C	FMS	29.70	37.60	73	C	FMS	42.44	37.20	167	C
FMS	52.98	28.57	25	C	FMA	35.64	32.83	126	D	FMS	30.39	40.76	73	D	FMS	43.51	38.42	167	C
FMS	34.80	28.69	25	C	FMF	44.50	37.40	126	E	FMS	57.36	26.75	74	C	FMS	42.57	39.16	167	C
FMS	50.86	29.63	25	C	FMS	34.47	40.42	126	C	FMS	31.21	38.62	74	C	FMS	33.10	39.43	167	C
FMS	56.87	31.34	25	C	FMS	34.79	40.59	126	C	FMS	29.16	39.14	74	C	FMS	42.72	39.60	167	C

Names	E_long.	N_lat.	azi	quality	Names	E_long.	N_lat.	azi	quality	Names	E_long.	N_lat.	azi	quality	Names	E_long.	N_lat.	azi	quality
BO	29.84	31.61	25	B	FMS	33.55	40.85	126	C	BO	51.25	40.10	74	C	FMS	32.18	30.36	168	E
BO	29.90	31.73	25	D	BO	33.76	27.71	127	C	BO	51.13	40.20	74	D	GVA	36.88	32.55	168	A
BO	29.87	31.85	25	D	FMS	31.09	29.68	127	C	FMS	30.01	40.72	74	C	FMF	39.45	33.25	168	B
DIF	31.85	31.92	25	D	FMS	31.14	29.72	127	C	BO	33.52	27.82	75	B	GFI	39.91	35.45	168	D
FMS	59.20	33.30	25	C	FMS	30.21	35.36	127	C	BO	33.49	27.87	75	B	FMS	30.93	38.00	168	D
FMS	51.43	36.45	25	C	FMS	46.81	38.46	127	C	FMS	34.10	34.28	75	C	FMS	39.03	39.55	168	C
GFI	57.83	36.90	25	B	BO	51.35	40.04	127	E	FMS	49.33	36.96	75	C	FMS	34.75	40.37	168	C
FMS	30.24	37.30	25	C	FMS	32.39	41.81	127	C	GFI	30.29	37.71	75	E	FMS	29.07	40.77	168	C
FMS	38.58	38.15	25	C	FMF	33.00	29.00	128	A	BO	51.32	40.08	75	B	FMA	47.60	41.00	168	D
FMS	39.23	38.45	25	C	FMS	47.77	37.36	128	C	FMS	51.09	28.92	76	C	FMS	55.85	26.92	169	C
FMS	35.89	38.80	25	C	FMS	30.48	40.52	128	D	FMS	34.58	33.05	76	D	FMS	56.81	30.76	169	C
FMS	48.00	40.70	25	C	FMS	29.16	40.60	128	C	GFI	30.38	37.76	76	E	DIF	32.80	31.88	169	C
FMS	55.79	26.77	26	C	FMS	30.08	40.75	128	C	FMS	31.17	38.66	76	C	FMS	50.68	31.98	169	C
FMS	51.67	30.20	26	C	FMS	34.66	40.82	128	C	FMS	29.74	39.06	76	C	FMS	47.55	34.39	169	C
FMS	47.73	32.65	26	C	FMA	47.50	40.90	128	D	FMS	29.95	40.25	76	C	FMS	55.54	38.50	169	C
FMS	52.07	36.38	26	C	FMS	43.80	41.20	128	C	FMS	33.30	40.97	76	C	FMS	33.10	39.46	169	C
FMS	59.47	36.99	26	C	FMS	33.67	27.48	129	C	FMS	58.22	34.04	77	C	FMS	32.98	40.61	169	C
FMS	56.62	37.63	26	C	FMS	33.93	27.49	129	C	FMS	43.29	37.78	77	C	FMS	56.81	28.04	170	C
FMS	30.87	38.15	26	C	FMS	33.76	27.87	129	C	FMS	30.41	37.79	77	C	GFS	35.25	30.23	170	C
FMS	39.00	38.19	26	C	FMS	35.54	31.76	129	D	FMS	33.05	38.83	77	D	GFS	34.65	30.97	170	D
FMS	36.98	39.34	26	C	FMS	35.59	31.78	129	D	FMS	40.98	42.59	77	C	FMS	45.78	34.14	170	C
FMS	33.68	40.84	26	C	HFM	35.65	32.70	129	E	FMS	33.95	27.56	78	C	FMS	54.84	36.79	170	C
FMS	44.00	41.20	26	C	FMS	29.68	38.06	129	C	BO	34.64	31.65	78	D	FMS	56.92	38.40	170	D
FMA	48.30	41.20	26	D	FMS	46.89	38.39	129	C	FMS	44.63	35.61	78	C	FMS	46.50	39.30	170	C
FMS	43.80	41.30	26	C	FMS	46.69	38.44	129	C	FMS	48.05	41.28	78	C	FMS	33.05	39.46	170	C
FMS	45.60	41.40	26	C	FMS	44.85	38.49	129	C	FMS	47.70	41.60	78	C	FMS	48.10	40.60	170	C
FMS	46.60	41.70	26	C	FMS	29.51	39.21	129	C	FMA	46.30	41.70	78	D	FMS	45.90	41.60	170	C
FMS	46.58	41.89	26	C	FMF	34.26	40.35	129	E	BO	33.53	27.80	79	B	FMS	45.00	42.50	170	C
BO	33.76	27.71	27	C	FMS	34.79	40.60	129	C	BO	32.35	31.69	79	C	FMS	33.62	27.61	171	C
BO	29.90	31.67	27	C	FMS	34.35	40.99	129	C	FMS	34.74	33.11	79	D	FMS	56.39	27.61	171	C
DIF	29.90	31.67	27	C	FMS	34.60	28.45	130	C	FMF	43.60	37.80	79	E	FMS	56.81	29.70	171	C
FMS	47.55	32.69	27	C	FMS	32.53	29.50	130	C	BO	48.97	40.08	79	E	FMS	56.93	30.64	171	C
FMS	53.22	35.96	27	C	FMS	31.13	29.72	130	C	FMS	29.13	40.60	79	C	FMS	43.67	38.82	171	C
GFI	59.19	36.44	27	D	FMS	42.57	37.18	130	C	FMS	30.37	40.76	79	C	FMS	43.83	39.65	171	C
FMS	36.01	36.58	27	C	FMS	37.31	40.47	130	C	GFI	30.31	37.74	80	E	FMS	55.80	26.66	172	C
FMS	35.77	37.44	27	C	FMS	34.82	40.55	130	C	FMS	45.50	42.40	80	C	FMS	48.21	34.05	172	C
GFI	57.44	37.50	27	E	FMS	49.30	40.70	130	C	FMS	59.17	28.40	81	C	FMS	54.47	35.49	172	C
GFI	58.06	37.50	27	B	FMS	35.91	40.79	130	C	BO	49.72	30.45	81	D	FMS	37.28	37.63	172	C
FMS	38.90	38.16	27	C	FMS	30.51	40.85	130	C	BO	31.24	31.66	81	C	FMS	34.80	40.60	172	C
FMS	30.24	38.28	27	C	FMA	47.90	40.90	130	D	FMS	35.73	33.85	81	C	FMS	30.77	40.66	172	C
FMS	55.04	39.40	27	C	FMS	46.70	41.60	130	C	BO	51.23	40.11	81	B	FMS	44.00	41.30	172	C
FMS	57.94	26.53	28	C	FMS	37.74	25.24	131	C	BO	51.25	40.12	81	D	FMS	45.70	41.60	172	C
FMS	54.43	27.16	28	C	FMS	33.94	27.48	131	C	FMS	30.41	40.77	81	D	FMS	43.30	41.70	172	C
FMS	52.95	27.34	28	C	FMS	34.02	27.49	131	C	FMS	35.91	42.65	81	C	FMS	55.89	26.65	173	C
FMS	33.81	27.53	28	C	FMS	34.00	27.52	131	C	FMS	45.47	42.93	81	D	FMS	55.38	28.24	173	C
FMS	48.37	32.54	28	C	FMS	34.00	27.61	131	C	BO	29.74	44.46	81	E	GFS	35.05	29.75	173	C
FMS	48.55	32.58	28	C	FMS	43.26	38.45	131	C	FMS	51.82	28.72	82	C	BO	50.23	30.24	173	E
FMS	47.64	32.70	28	C	FMS	35.67	40.37	131	C	BO	31.15	31.95	82	D	FMS	29.39	36.35	173	C
GFI	59.54	35.86	28	C	FMS	34.79	40.59	131	C	FMS	43.23	36.75	82	C	FMS	37.10	37.31	173	C
FMS	52.07	36.39	28	C	FMS	33.89	27.48	132	C	FMS	29.38	40.13	82	C	FMS	41.60	39.20	173	C
FMS	36.18	36.93	28	C	FMS	33.76	27.64	132	C	BO	51.12	40.18	82	B	FMS	36.70	40.70	173	C
GFI	57.65	36.94	28	B	FMS	33.28	27.69	132	C	FMS	50.60	40.50	82	D	FMS	34.08	28.36	174	C
FMS	57.45	37.47	28	C	FMA	35.48	31.70	132	D	FMA	46.30	41.80	82	D	BO	31.20	32.09	174	D
FMS	39.86	38.47	28	C	FMS	29.97	40.76	132	C	FMS	44.10	42.30	82	C	FMS	46.04	35.69	174	C
FMS	43.50	41.80	28	C	FMA	46.60	40.90	132	D	BO	33.64	27.62	83	B	FMS	54.53	37.46	174	C
FMS	41.64	43.22	28	C	FMA	48.70	41.00	132	D	BO	31.18	31.99	83	C	FMS	54.52	37.47	174	C
FMS	57.77	26.68	29	C	FMS	31.13	29.66	133	C	FMS	33.90	27.50	84	C	FMS	42.86	38.14	174	C
FMS	54.02	27.19	29	C	FMS	46.91	38.45	133	C	FMS	58.91	28.17	84	C	FMS	41.46	39.20	174	C
FMS	52.52	28.90	29	C	FMS	40.74	40.07	133	C	FMS	34.74	29.31	84	C	FMS	43.80	42.40	174	C
FMS	58.24	29.11	29	C	FMS	37.38	40.42	133	C	FMS	35.19	32.74	84	C	FMS	45.60	43.17	174	C
BO	50.46	30.00	29	E	FMS	30.89	40.66	133	C	FMS	57.75	34.73	84	C	FMS	41.60	43.20	174	C
FMS	48.95	35.65	29	C	FMS	34.89	40.67	133	C	GFI	39.91	35.45	84	D	FMS	34.94	29.34	175	C
GFI	58.65	37.02	29	E	FMS	31.00	40.67	133	C	FMS	49.74	36.67	84	C	GFS	35.67	33.22	175	C
FMS	34.76	40.37	29	C	FMS	30.63	40.70	133	D	BO	51.31	40.07	84	D	FMS	45.49	34.44	175	C
FMS	44.20	42.50	29	C	FMS	31.62	40.74	133	C	FMS	30.38	40.76	84	C	FMS	38.50	37.51	175	C
FMS	57.76	26.91	30	C	FMS	31.16	40.76	133	C	FMS	47.50	41.00	84	C	FMS	58.41	37.74	175	C
FMS	51.74	28.23	30	C	FMS	31.76	41.18	133	C	BO	33.84	27.73	85	B	FMS	57.44	38.08	175	C
FMS	34.65	28.72	30	C	FMS	33.82	27.62	134	C	FMS	33.13	28.55	85	C	FMS	43.51	38.67	175	C
BO	49.88	30.30	30	E	FMS	32.88	28.51	134	C	BO	32.66	31.98	85	B	FMS	48.70	39.60	175	D
BO	29.90	31.73	30	D	FMS	30.65	29.75	134	C	FMS	41.22	36.43	85	C	FMS	36.89	40.60	175	C
FMS	47.57	32.70	30	C	FMS	31.10	29.81	134	C	FMF	30.93	38.01	85	C	FMS	56.20	27.33	176	C
FMS	47.65	32.78	30	C	FMS	35.48	31.73	134	D	BO	51.12	40.18	85	C	FMS	54.30	27.90	176	C
FMS	50.79	34.47	30	C	FMS	33.28	37.31	134	C	BO	51.16	40.18	85	D	FMS	34.21	29.30	176	C

Names	E_long.	N_lat.	azi	quality	Names	E_long.	N_lat.	azi	quality	Names	E_long.	N_lat.	azi	quality	Names	E_long.	N_lat.	azi	quality
GFI	58.63	36.38	30	B	BO	51.31	40.07	134	D	FMS	35.49	32.09	86	D	FMS	50.90	31.53	176	C
FMS	35.42	36.63	30	C	FMS	37.38	40.47	134	C	FMS	45.85	34.27	86	C	FMS	51.02	31.84	176	C
FMS	42.86	37.16	30	C	FMS	34.79	40.58	134	C	FMS	51.52	36.44	86	C	GFI	58.86	36.27	176	C
FMS	43.20	37.36	30	C	FMF	33.75	27.60	135	A	FMS	56.21	37.06	86	C	FMS	48.50	40.50	176	C
FMS	34.13	40.56	30	C	BO	33.72	27.75	135	C	FMS	44.05	37.59	86	C	FMS	32.84	40.76	176	C
FMS	44.00	41.30	30	C	FMS	32.63	28.92	135	C	BO	30.58	44.46	86	E	FMS	56.20	27.00	177	C
FMS	57.69	26.73	31	C	FMF	32.75	29.12	135	A	BO	33.82	27.37	87	B	FMS	55.23	27.97	177	C
FMS	51.07	30.90	31	C	FMA	35.35	31.30	135	D	BO	33.82	27.37	87	B	FMS	57.45	27.98	177	C
FMS	47.12	32.44	31	C	FMS	50.06	40.29	135	C	FMA	35.18	32.66	87	D	BO	31.41	32.12	177	D
FMS	46.96	32.87	31	C	FMS	36.90	40.55	135	C	FMA	35.21	32.66	87	D	FMS	43.62	35.77	177	C
FMS	32.92	34.69	31	C	FMS	30.56	40.72	135	E	FMA	35.17	32.68	87	D	FMS	35.18	36.79	177	C
FMS	57.22	35.85	31	C	FMS	30.10	40.75	135	C	FMS	49.81	36.61	87	C	FMS	37.12	37.27	177	C
FMS	53.72	36.13	31	C	FMS	33.70	41.10	135	C	FMS	49.61	36.84	87	C	FMS	43.94	37.28	177	C
FMS	34.35	36.79	31	C	GFI	36.34	35.09	136	B	BO	33.92	27.88	88	B	FMS	42.40	40.61	177	C
GFI	58.53	36.89	31	D	FMS	30.29	40.31	136	C	FMS	31.35	30.14	88	C	FMS	43.70	42.40	177	C
FMS	59.77	37.36	31	C	FMF	34.26	40.35	136	E	BO	48.00	32.24	88	A	FMS	45.00	42.50	177	C
FMS	36.38	37.55	31	C	FMF	29.12	40.66	136	A	FMS	30.98	32.54	88	C	FMS	33.82	27.54	178	C
GFI	30.30	37.71	31	E	FMS	33.11	40.70	136	C	FMA	34.56	33.04	88	D	FMS	57.49	27.91	178	C
FMS	39.52	43.39	31	C	FMS	29.99	40.75	136	C	FMF	42.20	36.40	88	E	FMS	56.18	28.01	178	C
FMS	47.20	32.30	32	C	FMS	34.00	41.00	136	D	BO	33.79	27.32	89	B	FMS	55.53	28.16	178	C
FMS	47.12	32.73	32	C	FMS	34.00	27.53	137	C	FMS	33.12	28.55	89	C	FMS	57.11	30.79	178	C
FMS	47.18	32.73	32	C	FMS	33.78	27.68	137	C	BO	32.19	31.78	89	C	FMS	48.73	33.74	178	C
FMS	47.77	32.78	32	C	FMS	34.78	29.27	137	C	FMS	61.19	35.90	89	C	FMS	57.19	38.07	178	C
FMS	47.22	33.20	32	C	FMS	46.84	38.36	137	C	BO	51.23	40.13	89	D	FMS	43.54	38.59	178	C
FMS	60.07	33.29	32	C	FMS	43.35	38.41	137	C	FMS	29.35	40.73	89	C	FMS	56.24	38.59	178	C
FMS	60.84	35.66	32	C	FMS	41.10	39.18	137	C	FMS	33.90	27.50	90	C	FMS	46.50	41.20	178	C
FMS	59.00	36.27	32	C	FMS	39.98	40.01	137	C	FMS	59.03	28.11	90	C	FMS	43.90	42.50	178	C
FMS	56.66	37.22	32	C	FMS	33.03	40.59	137	C	BO	31.21	31.82	90	D	FMS	33.99	27.53	179	C
FMS	42.46	37.23	32	C	FMA	47.90	40.90	137	D	FMS	45.62	34.77	90	C	FMS	33.60	27.70	179	C
FMS	57.20	37.44	32	C	FMS	34.91	26.74	138	C	BO	51.31	40.07	90	B	FMS	53.85	27.95	179	C
FMS	57.54	37.99	32	C	FMS	33.92	27.49	138	C	BO	51.16	40.18	90	D	FMS	56.74	28.05	179	C
FMS	30.56	38.23	32	C	FMS	33.76	27.64	138	C	FMS	30.40	40.76	90	D	FMS	35.01	29.26	179	C
FMS	47.80	40.90	32	C	FMS	32.77	29.13	138	C	FMS	30.39	40.77	90	D	GFI	59.23	35.98	179	E
FMA	47.80	41.00	32	D	HF	49.66	32.93	138	D	FMS	47.90	40.90	90	C	FMS	40.72	38.47	179	C
FMS	43.90	41.90	32	C	FMS	47.79	38.10	138	C	FMS	33.48	41.01	90	C	FMS	42.66	41.96	179	C
FMS	43.44	42.66	32	C	FMS	34.55	40.58	138	C	FMS	45.50	42.20	90	C	FMS	53.93	26.75	180	C
BO	31.45	32.35	33	E	FMS	36.85	27.96	139	C	BO	30.55	44.41	90	C	GFS	34.95	29.53	180	C
DIF	31.45	32.35	33	E	FMS	33.67	28.00	139	C	FMS	32.10	30.18	91	C	FMS	50.97	31.74	180	C
FMS	46.95	32.73	33	C	FMA	35.48	31.10	139	D	FMS	51.51	36.42	91	C	FMS	53.00	36.56	180	C
GFI	60.12	35.25	33	D	FMA	35.50	31.10	139	D	FMS	29.52	39.22	91	C	FMS	43.94	37.30	180	C
FMS	58.80	35.50	33	C	FMS	35.41	32.29	139	C	BO	51.34	40.03	91	D	FMS	57.57	38.18	180	C
FMS	45.00	36.72	33	C	GFI	36.13	33.77	139	B	BO	32.11	31.86	92	D	FMS	43.37	38.74	180	C
FMS	43.00	42.30	33	C	FMS	46.74	38.47	139	C	FMA	35.39	32.12	92	D	FMS	49.30	40.10	180	C
FMA	48.50	41.50	92	D	FMS	44.20	41.40	180	C	FMS	57.49	37.52	92	C	FMS	34.47	40.42	180	C
FMS	43.70	42.40	180	C	FMS	44.30	41.90	180	C										

Appendix A) Table S3-GPS data (input):

E_lon_deg	N_lat_deg	v_E_mmpa	v_N_mmpa v	E_sigma v	N_sigma co	correlation	reference site
50.05	34.68	0.52	11.82	0.41	0.41	0.002	EU
48.53	34.87	1.19	13.25	0.42	0.30	0.003	EU
51.81	34.98	0.75	9.68	0.77	0.76	0.040	EU
51.80	35.05	-0.31	11.23	0.22	0.26	0.003	EU
50.99	35.09	-0.83	11.11	0.18	0.16	0.004	EU
49.85	35.14	0.62	13.25	0.74	0.72	0.001	EU
51.17	35.20	-0.03	11.94	0.45	0.46	0.010	EU
51.89	35.22	0.52	8.96	0.77	0.76	0.000	EU
50.54	35.23	-0.41	11.08	0.43	0.43	0.001	EU
52.12	35.26	-1.29	10.61	0.36	0.36	0.001	EU
51.88	35.28	-0.14	12.23	0.17	0.16	0.005	EU
51.63	35.34	-0.13	11.67	0.25	0.63	0.001	EU
51.38	35.37	-0.13	11.80	0.48	0.49	0.010	EU
51.17	35.41	-0.90	12.20	0.73	0.74	0.000	EU
52.04	35.49	-0.21	8.93	0.36	0.36	0.011	EU
51.00	35.49	-0.39	12.16	0.70	0.70	0.020	EU
51.28	35.49	-0.03	11.15	0.44	0.43	0.001	EU
51.41	35.50	-0.64	12.25	0.46	0.47	0.010	EU
51.72	35.55	0.18	10.26	0.40	0.40	0.011	EU
51.71	35.57	-0.58	9.85	0.30	0.19	0.003	EU
50.60	35.59	-1.07	10.69	0.24	0.18	0.003	EU
51.97	35.63	0.07	8.59	0.25	0.31	0.002	EU
51.52	35.63	0.33	10.37	0.49	0.50	0.010	EU
51.89	35.65	-0.77	9.85	0.32	0.32	0.002	EU
52.09	35.66	-1.29	7.28	0.14	0.19	0.006	EU
51.96	35.68	-0.67	8.94	0.42	0.42	0.001	EU
51.33	35.70	-0.94	10.82	0.22	0.14	0.022	EU
52.06	35.70	-1.90	7.93	0.38	0.38	0.000	EU
51.67	35.72	-0.54	10.88	0.33	0.33	0.002	EU
51.81	35.73	-0.99	9.57	0.36	0.34	0.002	EU
51.39	35.75	-0.01	11.89	0.79	0.75	0.010	EU
51.11	35.75	-0.80	9.84	0.32	0.33	0.002	EU
51.99	35.76	-1.11	8.68	0.47	0.48	0.011	EU
50.84	35.77	-0.95	10.74	0.37	0.20	0.002	EU
51.52	35.77	-1.06	11.32	0.41	0.41	0.011	EU
51.99	35.79	-1.12	8.91	0.58	0.58	0.001	EU
51.80	35.80	-0.32	9.35	0.33	0.33	0.002	EU
51.57	35.81	-2.56	10.39	0.51	0.52	0.010	EU
51.26	35.81	-0.97	11.85	0.42	0.42	0.011	EU
51.43	35.83	-0.61	11.52	0.50	0.50	0.010	EU
52.06	35.85	-1.67	8.45	0.23	0.29	0.003	EU
52.16	35.87	-0.75	6.79	0.52	0.52	0.000	EU
51.41	35.88	-1.71	10.12	0.55	0.55	0.001	EU
52.01	35.90	0.23	7.71	0.33	0.34	0.002	EU
51.08	35.93	-0.97	9.99	0.23	0.21	0.003	EU
51.65	35.99	-1.46	9.76	0.20	0.36	0.002	EU
51.61	35.99	-1.73	10.61	0.33	0.33	-0.008	EU
50.75	36.01	-1.33	10.39	0.18	0.21	0.003	EU
50.63	36.01	-0.49	10.50	0.44	0.44	0.001	EU
50.75	36.14	-2.12	10.81	0.48	0.37	0.001	EU
51.32	36.15	-0.50	11.00	0.54	0.54	0.010	EU
44.01	36.16	-3.88	17.75	0.22	0.41	0.001	EU
49.21	36.20	0.99	9.75	0.61	0.61	0.001	EU
51.83	36.21	-1.41	9.23	0.36	0.36	0.002	EU
52.31	36.21	-1.83	8.99	0.58	0.56	0.020	EU
51.83	36.21	-1.28	8.71	0.49	0.31	0.001	EU

E_lon_deg	N_lat_deg	v_E_mmpa	v_N_mmpa v	E_sigma v	N_sigma co	correlation	reference site
47.93	36.23	0.82	13.05	0.39	0.39	0.001	EU
51.30	36.39	-1.89	10.45	0.46	0.47	0.001	EU
50.05	36.40	-1.65	10.36	0.76	0.80	0.000	EU
51.57	36.40	-1.67	8.48	0.39	0.33	0.001	EU
51.77	36.59	-3.98	10.81	1.21	0.90	0.008	EU
48.18	36.61	-0.51	11.43	0.66	0.69	0.009	EU
50.73	36.62	-0.79	10.25	0.74	0.76	0.000	EU
51.31	36.69	-3.07	7.76	0.66	0.49	0.001	EU
49.81	36.70	0.03	12.16	0.68	0.71	0.002	EU
48.81	36.76	-1.00	11.02	0.39	0.39	0.000	EU
50.93	36.79	-2.56	9.08	0.24	0.26	0.002	EU
46.16	36.91	1.11	13.50	0.41	0.39	0.000	EU
46.01	36.93	3.55	14.55	1.29	0.26	0.001	EU
50.10	37.16	-0.91	12.73	2.09	2.08	0.026	EU
48.01	37.17	-0.20	11.85	0.53	0.54	0.010	EU
48.89	37.19	-1.12	10.80	0.74	0.77	0.010	EU
49.62	37.32	0.85	12.41	0.19	0.33	0.004	EU
47.12	37.37	1.57	12.78	0.60	0.61	0.009	EU
42.46	37.53	-7.14	14.51	2.07	0.95	0.000	EU
44.75	37.53	2.42	14.96	0.59	0.60	0.010	EU
47.09	37.58	0.04	12.90	0.69	0.69	0.001	EU
48.92	37.76	1.74	11.77	0.44	0.46	-0.020	EU
47.65	37.83	0.17	11.76	0.26	0.40	0.004	EU
47.29	37.92	0.55	12.28	0.38	0.21	0.004	EU
47.87	37.93	2.42	12.94	0.57	0.58	0.005	EU
46.12	37.93	-0.92	12.76	0.28	0.56	0.002	EU
44.77	37.99	0.58	9.82	2.43	0.97	0.000	EU
48.46	38.00	2.97	11.28	0.78	0.83	0.017	EU
46.34	38.06	-0.77	12.65	0.26	0.43	0.002	EU
46.60	38.15	1.60	9.84	0.71	0.72	0.001	EU
46.60	38.18	1.49	11.62	0.46	0.46	0.004	EU
44.95	38.21	1.87	13.08	0.69	0.70	0.002	EU
45.89	38.23	0.63	11.88	0.41	0.41	0.004	EU
46.16	38.23	0.59	10.84	0.25	0.18	0.007	EU
47.27	38.27	2.29	11.24	0.54	0.56	0.004	EU
45.36	38.32	-0.68	12.72	0.20	0.33	0.006	EU
44.55	38.45	-0.71	12.19	0.64	0.64	0.001	EU
47.05	38.47	0.93	8.98	0.18	0.25	0.006	EU
48.23	38.48	3.47	11.48	0.40	0.40	0.000	EU
42.55	38.49	-6.28	13.43	0.95	0.75	0.000	EU
44.43	38.49	0.79	11.66	0.59	0.60	0.040	EU
45.19	38.49	1.94	13.69	0.26	0.29	0.004	EU
43.34	38.55	-5.72	12.51	0.66	0.65	0.000	EU
45.41	38.67	3.24	9.78	0.51	0.36	0.003	EU
45.73	38.67	3.13	10.19	0.37	0.22	0.004	EU
48.42	38.71	4.68	11.65	0.43	0.40	0.001	EU
46.27	38.74	4.60	8.97	0.60	0.61	0.010	EU
39.91	38.74	-16.02	10.66	0.55	0.54	0.000	EU
41.79	38.75	-5.25	13.91	0.45	0.39	0.000	EU
40.58	38.76	-6.92	18.46	0.78	0.68	0.000	EU
47.03	38.87	3.72	11.73	0.69	0.69	0.001	EU
45.61	38.95	3.09	10.39	0.60	0.61	0.008	EU
48.39	38.95	4.98	12.10	0.43	0.41	0.001	EU
41.06	38.96	-6.14	13.56	0.60	0.59	0.000	EU
40.05	38.96	-16.27	9.31	0.60	0.60	0.000	EU
47.16	38.98	3.75	11.29	0.59	0.60	0.005	EU
43.76	39.00	-5.78	10.84	1.33	0.89	0.000	EU
45.11	39.00	3.03	8.10	0.69	0.69	0.001	EU
48.05	39.01	4.69	10.44	0.77	0.81	0.012	EU

E_lon_deg	N_lat_deg	v_E_mmpa	v_N_mmpa v	E_sigma v	N_sigma co	correlation	reference site
44.57	39.03	2.53	11.80	0.79	0.80	0.002	EU
39.52	39.07	-17.77	11.42	0.91	0.81	0.000	EU
46.16	39.13	0.52	13.86	1.33	0.86	0.000	EU
41.45	39.19	-6.66	10.14	1.28	0.81	0.000	EU
42.91	39.23	-2.62	8.84	0.38	0.32	0.001	EU
45.05	39.30	4.15	9.51	0.57	0.58	0.003	EU
46.46	39.32	3.54	11.91	1.32	0.83	0.000	EU
44.16	39.33	4.45	9.22	0.83	0.83	0.001	EU
39.26	39.35	-18.68	7.46	1.78	2.15	0.000	EU
45.06	39.35	3.42	9.47	0.20	0.22	0.007	EU
44.39	39.38	3.55	9.22	0.63	0.63	0.001	EU
49.24	39.40	1.86	3.46	0.35	0.35	0.040	EU
48.72	39.50	5.68	11.78	0.36	0.35	0.001	EU
46.37	39.51	4.82	10.28	0.36	0.36	0.001	EU
47.74	39.51	6.16	13.53	0.35	0.34	0.003	EU
46.09	39.54	3.84	9.76	0.41	0.40	0.001	EU
44.15	39.56	-1.60	6.47	1.34	0.80	0.000	EU
41.51	39.64	-2.84	3.80	1.13	0.76	0.000	EU
49.02	39.68	6.35	5.88	1.38	1.41	0.000	EU
42.15	39.71	-1.83	8.22	0.86	0.77	0.000	EU
43.03	39.72	0.30	8.07	0.42	0.40	0.000	EU
40.25	39.73	-3.38	5.24	0.46	0.41	0.000	EU
46.76	39.75	4.43	10.33	0.44	0.42	0.001	EU
49.24	39.82	4.68	6.15	1.46	1.48	0.000	EU
39.52	39.82	-6.80	0.52	1.60	1.92	0.000	EU
45.66	39.84	4.35	9.46	0.34	0.34	0.001	EU
41.30	39.97	-1.26	5.32	0.40	0.39	0.000	EU
45.34	40.12	2.37	8.89	1.60	1.11	0.000	EU
44.74	40.15	2.25	9.10	0.48	0.43	0.000	EU
44.11	40.18	1.83	7.23	0.64	0.63	0.000	EU
46.76	40.18	3.54	10.59	0.74	0.66	0.000	EU
44.50	40.23	2.09	6.96	0.13	0.12	0.030	EU
48.15	40.33	3.76	9.36	0.76	0.66	0.000	EU
40.81	40.44	0.15	2.78	0.44	0.40	0.000	EU
44.86	40.53	0.80	4.77	0.86	0.65	0.000	EU
41.99	40.55	1.40	4.50	0.72	0.69	0.000	EU
43.95	40.61	1.42	7.55	0.64	0.63	0.000	EU
48.55	40.61	2.11	1.10	0.68	0.61	0.000	EU
43.17	40.69	0.98	5.32	0.46	0.40	0.000	EU
45.14	40.91	3.27	6.96	0.49	0.47	0.000	EU
43.77	40.97	0.85	5.99	0.71	0.65	0.000	EU
39.70	40.97	0.14	2.06	0.37	0.36	0.000	EU
47.86	40.98	0.09	3.44	0.51	0.50	0.001	EU
39.78	41.00	-0.76	2.09	0.14	0.12	0.017	EU
44.36	41.03	3.06	5.46	0.65	0.61	0.000	EU
42.76	41.13	0.66	4.48	1.35	1.06	0.012	EU
47.25	41.13	0.58	5.00	0.50	0.50	0.001	EU
47.18	41.22	0.01	4.98	0.25	0.15	0.018	EU
41.34	41.37	-1.05	2.29	0.69	0.68	0.000	EU
44.83	41.38	8.22	4.63	2.05	1.30	0.000	EU
43.89	41.54	0.98	4.01	0.49	0.46	0.000	EU
48.53	41.60	0.20	0.64	0.74	0.66	0.000	EU
42.13	41.65	-1.06	4.61	0.51	0.51	0.000	EU
46.51	41.65	0.54	4.56	0.49	0.49	0.000	EU
44.53	41.83	0.98	5.94	0.45	0.43	0.000	EU
45.80	41.95	-0.78	4.79	0.56	0.53	0.000	EU
42.47	42.02	1.69	3.60	0.58	0.54	0.000	EU
43.40	42.35	2.07	5.38	0.54	0.47	0.000	EU
44.49	42.45	0.28	3.32	0.46	0.45	0.000	EU

E_lon_deg	N_lat_deg	v_E_mmpa	v_N_mmpa v	E_sigma v	N_sigma co	correlation	reference site
43.14	42.47	0.55	3.38	0.66	0.55	0.000	EU
48.80	38.64	4.20	12.10	1.80	1.90	0.004	EU
48.99	40.87	0.70	2.10	0.90	0.80	0.005	EU
45.65	40.10	4.10	8.30	0.60	0.60	0.004	EU
44.68	39.84	5.70	6.40	0.60	0.60	0.000	EU
43.78	41.12	1.70	6.50	0.30	0.30	0.000	EU
43.78	41.12	2.10	5.40	0.60	0.60	0.000	EU
44.29	40.38	2.00	7.00	0.40	0.40	-0.012	EU
44.29	40.38	2.30	6.70	0.60	0.60	-0.017	EU
44.28	40.74	1.60	7.30	0.40	0.40	-0.006	EU
44.28	40.74	1.50	6.20	0.70	0.70	-0.011	EU
45.21	40.20	2.90	8.60	0.40	0.40	0.002	EU
45.21	40.20	3.40	8.40	0.60	0.60	0.005	EU
44.66	40.10	2.00	7.40	0.60	0.60	-0.003	EU
44.58	39.88	2.70	6.80	1.40	1.30	0.044	EU
44.19	41.19	1.80	4.90	0.40	0.40	-0.006	EU
44.19	41.19	1.90	4.70	0.60	0.60	-0.015	EU
44.59	41.06	2.80	6.20	0.60	0.60	-0.004	EU
44.55	40.84	2.40	6.10	0.60	0.60	-0.006	EU
44.72	40.52	2.20	6.90	0.70	0.70	-0.006	EU
43.95	40.11	2.30	7.20	0.40	0.30	0.000	EU
43.95	40.11	2.90	6.20	0.60	0.60	0.000	EU
43.81	40.10	2.60	6.50	0.40	0.40	-0.002	EU
43.81	40.10	2.80	5.40	0.60	0.60	-0.001	EU
44.53	40.75	2.70	5.90	0.60	0.60	-0.003	EU
45.06	40.31	2.40	8.20	0.60	0.60	-0.004	EU
45.91	40.20	4.80	8.70	0.60	0.60	-0.002	EU
43.68	40.27	1.10	-1.59	1.70	1.43	0.006	EU
43.79	41.57	-0.13	0.71	0.10	0.08	0.001	EU
42.97	41.63	0.71	2.78	0.20	0.28	0.002	EU
42.72	42.06	-1.22	2.86	0.56	0.56	-0.003	EU
41.65	42.13	-1.37	4.73	0.71	0.71	-0.008	EU
43.35	42.20	-1.10	-0.59	0.89	0.87	-0.005	EU
42.02	42.47	1.25	2.20	0.67	0.78	-0.086	EU

